Matti Järveläinen

Towards In Situ Methods for Characterization of Porous Materials

Matti Järveläinen

Towards In Situ Methods for Characterization of Porous Materials

Thesis for the degree of Doctor of Science in Technology to be presented with due permission for public examination and criticism in Festia Building, Auditorium Pieni Sali 1, at Tampere University of Technology, on the 16th of September 2016, at 12 noon.

Matti Järveläinen

Towards In Situ Methods for Characterization of Porous Materials

Thesis for the degree of Doctor of Science in Technology to be presented with due permission for public examination and criticism in Festia Building, Auditorium Pieni Sali 1, at Tampere University of Technology, on the 16th of September 2016, at 12 noon.

Abstract

Automation is becoming ever more important in production processes. But its progress is being hampered because a large part of process control is currently based on tacit knowledge, which is lost when plant operators retire. To offset this fading of knowledge, process variables must be quantified, because another change underway is the evident shift from conventional mass production to lean and green production, which promotes ordered production flow and rational process optimization by minimizing non-value-added work. Both of these changes have affected the analysis of materials and necessitated in situ study of processes through their material properties.

All the developed in situ methods in this thesis embody analysis of porous ceramics of different composition and pore structure, or the extent of added value in unfinished ceramic structures during powder compression [VII] and colloidal processing [V], in finished ceramic components in unsintered, high porosity fiber structures [I, III, VI], in ceramics composed of sintered, low porosity solids [II], and in oriented, lamellar structures [IV]. From the materials science perspective, the study of these porous ceramics provides information on their mechanical behavior in relation to pore structure: the effect of porosity changes in powder structure [VII], the effect of sintering in fibrous structure [III], and the effect of pore orientation in lamellar structure [IV]. The second investigated regime is the behavior of electrical signals in a porous material in sintered structure [II], and in suspensions [V]. Third regime is the investigation of local permeability of a fibrous structure [I, VI].

Whereas this thesis work focused mostly on the concrete development of 6 different characterization methods—thermal flow permeametry, grit blast-analysis, electrical pore analysis, adaptive image analysis, and granule bed compression—the results in the introduction demonstrate a systematic approach to developing process integrable in situ methods and discuss the relative importance of the methods' robustness, integrability, reliability, and comprehensiveness. In the regime of materials science, this work contributes to the analysis of pore characteristics and the effects of pores by showing results of granule bed strength measurement, the effect of the pore parameter on compressive strength, the concept of fiber free length, and a strong hypothesis about the reactions of material interfaces with electrical signals.

Preface

I've understood that everything can be predicted with a hundred percent certainty given that all the variables are known (Laplace's demon). My take on this are the in situ methods that measure some occurrences better than anything there was before them. Still, I do not claim to understand the real world very well, but have made it more predictable. This has not been my thrive in personal life as I like surprises but the industrial processes are better without them.

About the publications

Articles [I, III, VI] are based on experiments done in a project that was funded by a customer. The project was carried out during 2010-2014 and aimed to increase the understanding of variables that dominate the lifespan of fibrous hot gas filter elements, which are industrially used. A secondary objective was to develop methods, such as those published, which could be used to analyze the remaining lifetime.

Articles [II, V] are based on experiments done in a project that was carried out during 2012-2014 and funded by the Finnish Funding Agency for Innovation (TEKES) and steered by Finnish industrial partners Nordkalk, IDO and Outotec. The project focused on material responses to a multifrequency signal and aimed to develop on site methods for analysis of industrially produced or industrially used products measuring the functioning of filters, drying of ceramics, homogeneity of powders, and porosity and specific surface area of materials.

Article [IV] is a collaborative effort with the main author from Stockholm University. Article [VII] is based on the development of a method directly funded by an industrial customer. Because all the industrially funded work was carried out under a non-disclosure agreement, the names of some companies, their processes, and the producers of the studied materials cannot be revealed.

Support

Contents

List of Figures

List of Diagrams

List of Tables

List of Publications

This thesis is based on the publications listed below, which are later referred to in the following Roman numerals. The author's role is given after each publication entry.

I. Järveläinen, M., Keskinen, L., & Levänen, E. (2013). Use of thermal imaging in characterization of ceramic fiber structures. In *2nd International Conference on Competitive Materials and Technological Processes*. Miskolc: IOP Conf. Series: Materials Science and Engineering 47. Retrieved from http://iopscience.iop.org/1757-899X/47/1/012062

The author of this thesis was the corresponding author in writing this publication. He planned the experiments and developed the thermal flow procedure. In addition, he carried the research and experiments with the help of the second author and prepared and analyzed the results.

II. Järveläinen, M., Salpavaara, T., Seppälä, S., Roinila, T., Yli-Hallila, T., Levänen, E., & Vilkko, M. (2014). Characterization of Porous Ceramics by Using Frequency-Response Method. In *World Congress of the International Federation of Automatic Control* (pp. 10012–10017). Cape Town. http://doi.org/10.3182/20140824-6-ZA-1003.02423

The author of this thesis was the corresponding author in writing this publication. He wrote the sections on materials science together with the third author. He planned the experiments and analyzed the results on materials science. With the second author, he analyzed the link between material characteristics and the material's electrical response. Contributions other than those claimed for this thesis are likely to appear in a future doctoral thesis.

III. Järveläinen, M., Humalamäki, J., Laakso, J., & Levänen, E. (2015). Mechanical Characterization of Fiber Ceramics: Effect of Temperature. *Advanced Engineering Materials*. http://doi.org/http://dx.doi.org/10.1002/adem.201400512

The author of this thesis was the corresponding author for writing this publication. He planned the experiments and developed the grit blasting-procedure. He also participated in the experimental work, which was mainly carried out by the second author, with whom he analyzed the results.

IV.   Ojuva, A., Järveläinen, M., Bauer, M., Keskinen, L., Valkonen, M., Akhtar, F., … Bergström, L. (2015). The mechanical performance and CO2 uptake of ion-exchanged zeolite A structured by freeze-casting. *Journal of European Ceramic Society*, *35*(9), 2607–2618. http://doi.org/10.1016/j.jeurceramsoc.2015.03.001

The publication is a result of collaboration between the author of this thesis and Dr. Ojuva, who was responsible for writing this publication. The author of this thesis planned the experiments on mechanical measurements and the related image analyses in the publication. He also supervised the related experimental work, analyzed the results, and participated in writing these sections in the publication. Contributions other those claimed for this thesis were presented in Arto Ojuva's doctoral thesis.

V.   Salpavaara, T., Järveläinen, M., Seppälä, S., Yli-Hallila, T., Verho, J., Vilkko, M., … Levänen, E. (2015). Passive resonance sensor based method for monitoring particle suspensions. *Sensors & Actuators: B. Chemical.*, *219*, 324–330. http://doi.org/10.1016/j.snb.2015.04.121

The author of this thesis was responsible for the sections on materials science and wrote them together with the third author. In addition, he designed, planned, and carried out the related suspension measurements together with the main author and helped analyze the results. Contributions other than those claimed for this thesis are likely to appear in a future doctoral thesis.

VI.   Järveläinen, M., Keskinen, L., Heinonen, S., Kaleva, A., & Levänen, E. (2015). Thermal Flow Permeametry - A Rapid Method for Finding Local Changes in Flow Channels. *Composites Part A: Applied Science and Manufacturing*, *79*, 138–145. http://doi.org/10.1016/j.compositesa.2015.09.013

The author of this thesis was the corresponding author for writing this publication. He also planned the experiments and designed the method for thermal flow permeametry. He helped the second author carry out the measurement and analyzed the data.

VII.   Järveläinen, M., Kaleva, A., Kaitajärvi, A., Laakso, J., Kanerva, U., & Levänen, E. (2016). Compression curve analysis and compressive strength measurement of brittle granule beds in lieu of individual granule measurements. *Particuology.* http://doi.org/10.1016/j.partic.2015.10.006

The author of this thesis was the corresponding author for writing this publication, except for the experimental part, to which the second and the fifth author also contributed. With the fifth author, the author planned the experimental work and analyzed and formulated all experimental results. Contributions other than those claimed for this thesis are likely to appear in a future doctoral thesis.

Structure of this thesis and definitions of the developed methods

The work is arranged into five chapters (X) with sections (X.X) and subsections (X.X.X). Each chapter introduces the aims and relevance of its sections, and, similarly, each section the aims and relevance of its subsections.

Many chapters in this thesis are collated in a detailed diagram for the reader to quickly visualize the junctions of its topics. In the end, the thesis is summarized in a collective diagram of all its components.

The thesis introduces six in situ methods, which the author developed in cooperation with other researchers at TUT:

1. *Thermal flow permemetry (TFP):* this method allows hot air to flow through a flow porous structure, whose surface heating is measured with a thermal camera to detect local differences in permeability.
2. *PRBS porosity analyzer* is an electrical impedance analyzer, in which an electrical signal in the form of a pseudo-random binary sequence (PRBS) is injected into a porous structure to analyze its porosity.'
3. *Grit blaster for fiber structure thermal history*: in this method glass grit collides with a porous fiber net to measure its rigidization. Rigidization is linked with maximum temperature, to which the structure has been subjected.
4. *Non-contact suspension analyzers*: in this method, a high frequency AC-electrical field is sent to a suspension. Particles in the suspension change the resonation frequency of the electrical field, yielding different suspension characteristics linked with the electrical charging of the surfaces.
5. *Automatic pore parameter analyzer:* In this method a 2d-image of pores is automatically segmented and feature extracted to find relevant pore parameters.
6. *Granule strength measurement*: in this method, a granule bed is uniaxially compressed, and individual granule strength is calculated by analyzing the compression curve.

1   Lean, in situ -measurements and this thesis

This introduction is an overview of the topics of this thesis. Section 1.1, Shift to lean process control, aims to give a broad perspective on the increasing need for in situ measurements and to help understand the requirements of current methods.

The section on In situ process measurements focuses on the concrete matter of this thesis and defines and describes the benefits and obstacles, many of them also seen in my publications, of in situ measurement. The section continues to present the development of sensors that form the core of each measurement and concludes with a literature review of current in situ measurements and the fields they are used in and opens up a relatively unstudied field of in situ measurements related to porosity.

The introduction continues with section 1.3, Area of the thesis, which gives the purview of this thesis, its focus, research approach, and specific challenges. Finally, section 1.4, Work environment, allows the reader to assess the possible outside incentives to this work.

The following diagram shows the areas covered in this thesis.
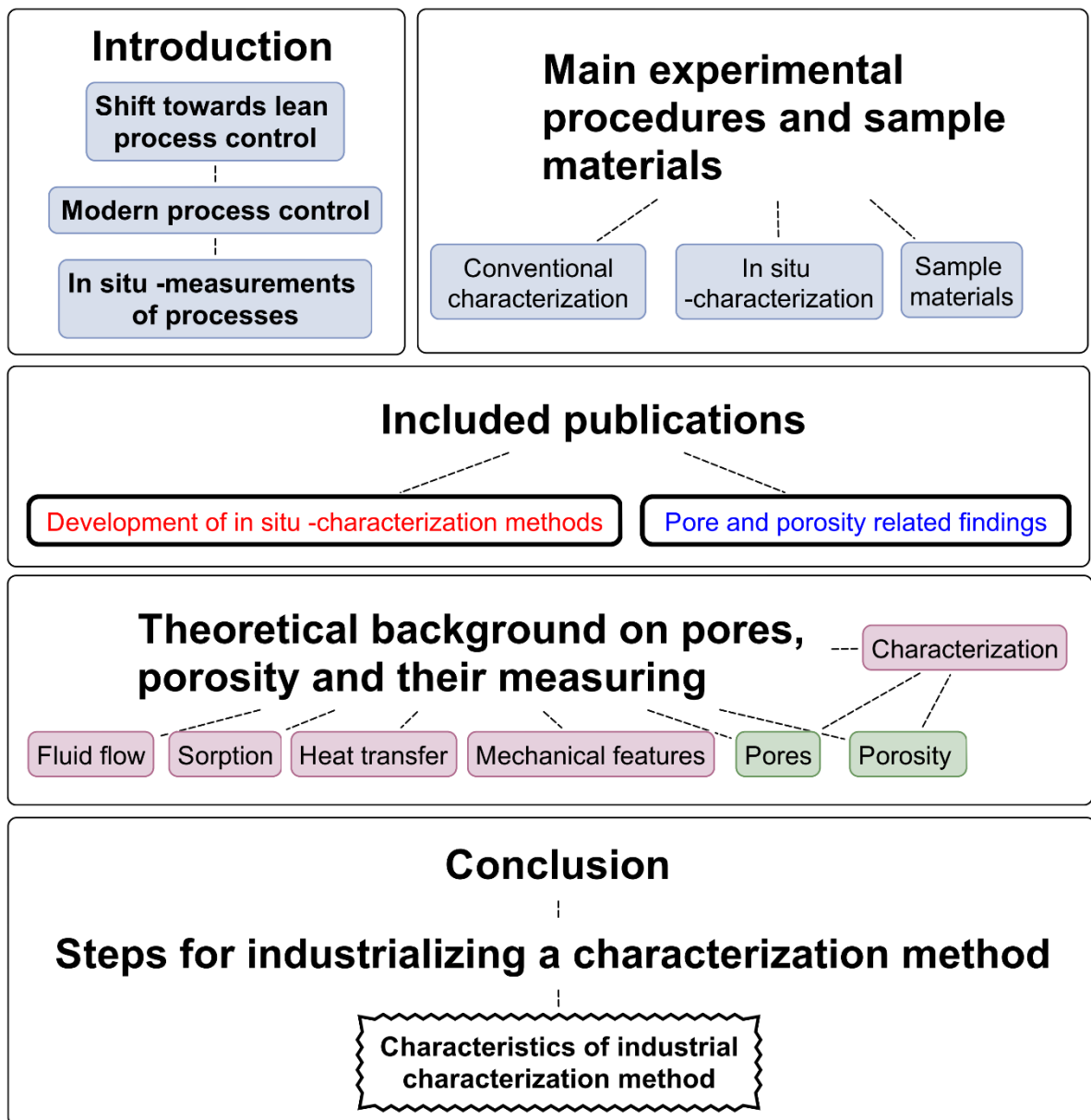
Diagram 1: Thesis coverage.

1.1 Shift to lean process control

This subsection gives an overview of how modern production processes are controlled, how they have been influenced by lean thinking, and how lean thinking is related to in situ measurement, one of the topics of this thesis (Diagram 2).

The subsection explains what is meant by process control and lean and how they have evolved and where they are used. Then it discusses the benefits of lean and, finally, links lean with in situ measurement.

The objective here is to help better understand and explain the root cause and principal ideas that affect in situ measurement.
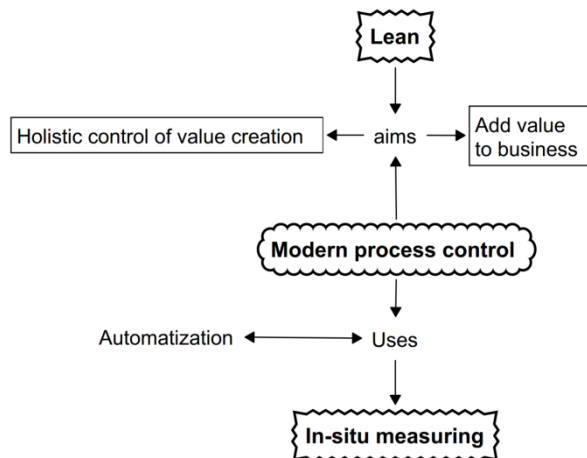
Diagram 2: Process control/Lean and in situ measurement.

1.1.1 An overview of process control

To understand why in situ measurements must have certain characteristics, it is first worth taking a look at modern process control, what it is and how it has changed over the past few years.

In its modern meaning, process control signifies adjusting the value creation process of a product from raw materials to a finished and valuable product. Control here aims to optimize the process to spare resources while lowering emissions and enhancing product quality, process safety, reliability, and plant availability. Increasing the level of automation aims at a holistic approach to the quality, cost, and time issues of processes. [1] Many of these factors are mentioned in the context of the benefits of lean production; thus integrating automation to production and business operations [1] is in good agreement with lean.

When automation is integrated with business, in addition to controlling the processes, automation aims to optimize, schedule, and plan the processes. This is possible only if appropriate parameters are measured, operational situations are analyzed, and the most profitable opportunities are exploited while plant personnel are being informed

and their knowledge put to good use. [2] In the core of these multiple operations lies information on the processes, collected using in situ measurement tools.

1.1.1.1 Development of automation

In industrialized countries, the volume of automation has been increasing in the process industry. Chemical, power generation, and petrochemical industries have the highest volume demand for process automation, but in the pharmaceutical industry it is increasing the most rapidly [1]. This is evident in the literature review in subsection 1.2.3.

Automation is currently being integrated with the whole supply chain [1] comprising users, vendors, consultants, and third parties [2]. Artificial intelligence is moving to field level automation; i.e., actuators and sensors, must now support maintenance and monitoring tasks. In the future, sensors will measure the health of the process, not by managing abnormal situation but by preventing them. [1] These are the straightforward motivations for developing new in situ tools to support lean principles.

1.1.2 Definition, aim and use of lean

As hinted in the previous subsection, process control often links well with the ideology of lean that is based on Toyota production system, developed after Ford commenced mass production. Thus many companies have adapted the lean methodology using the Toyota Production System as a role model [3]. According to NIST [4], lean is an "improvement model that strives to eliminate non-value-added activities" by continuous improvement, production of materials only on order, and an error-free process. Consequently, lean manufacturing does not rely on long production runs but on a smooth production flow [5] that reduces inventories, lead-times, and altogether yields improved productivity and quality [6], which have proved universally applicable. Lean has been found to provide the means to economically produce large variety in small volumes [7] and therefore, it has been adopted by a wide range of industries, and it is currently the "best practice" [8] in developed manufacturing industries [9]. The lean ideology is shown in Diagram 3.
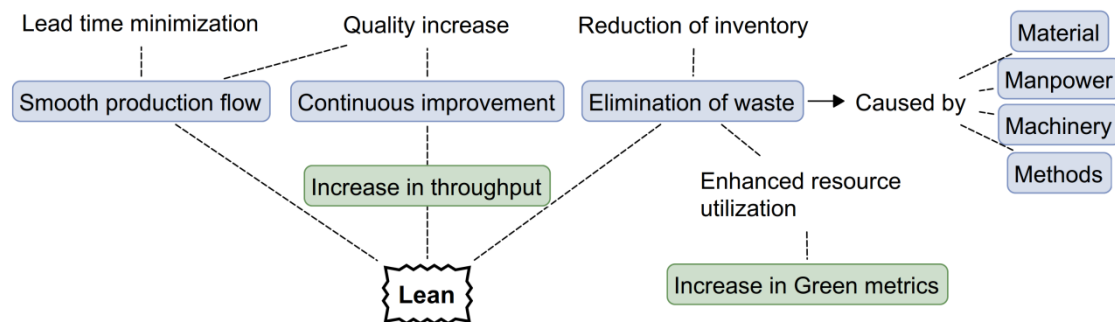
Diagram 3: Aim and use of lean.

In addition, lean has recently been linked with the paradigm of green production, which seeks to limit the environmental risks [6] caused by manufacturing. This aligns well with the lean goal of zero waste, efficient use of resources, and prevention of recurrent problems. [9]

1.1.2.1 Current use of Lean

In [10] the lean is viewed to have been developed from a set of shop-floor techniques to a holistic corporation culture. According to [6], lean is most actively researched and developed in the manufacturing sector, but as seen in history and suggested in some publications in [6], the paradigm will subsequently be adopted in other sectors as well. Quite recently, companies that use lean have started to expand the ideology to their supply chains [5]–[7], [10]. Lean is especially effective near the beginning of supply chain where the fluctuation of demand and over production have less crucial consequences. Closer to the final customer, systems such as agile can yield benefits by increasing the responsiveness to market demand [11].

Independent of the methods, quality and efficiency are necessary in production facilities; thus the technical performance of production equipment must be maximized, production disturbances removed, and rapid development of automation and sensors given better possibilities for advanced maintenance [12]. With that in mind, this thesis introduces in situ methods to assure material stability in raw materials [VII] and during production [I;V;VI], in the quality of the finished product [I-II;IV;VI], and in the inspection of current conditions [III]. The thesis in general focuses on the process of creating modern in situ methods that aim to analyze the production process in support of lean ideology. These methods are mostly used in the upstream of the supply chain where the benefits of lean are also most prominent.

5

1.1.3 Lean benefits of in situ measurement

A publication by Forrester et al. [8] points out factors that make companies lean. Among others, they include elimination of non-value-added activities, pursuance of zero defects, and pull-order of materials in production. All this calls for redesigning of factories [5], including the way processes are analyzed and corrected.[1]

Focusing on the factors that need redesigning, Sundar et al. [13] list non-value-adding activities as transportation, inventory, motion, waiting, overproduction, over processing, and defects. In situ measurements seek to eliminate the last two items that cause symptoms such as [5]

- "The reaction stage is typically complete within minutes, yet we continue to process for hours or days",

- We have in-process controls that never show a failure, and

- (overprocessing is caused by) delay of documents to accompany finished product.

Melton describes a typical example of laboratory analysis, which is necessary for a particular product but which turns out to be a bottle neck that does not support lean thinking. The process should be continually monitored for abnormalities and variation, and the whole production inspected in real-time [13] with the idea that no defects are passed downstream in the production chain [9]. <u>I claim that these are symptoms of an incapability to analyze the process in situ.</u>

The above symptoms derive from time-dependent process variations caused by [14]

- Changes in process input raw materials,

- Process fouling,

- Abrasion of mechanic components,

- Changes in catalyst activity,

- Production of different quality grades,

- Changes in the external environment,

---

[1] The new methods of analysis presented in this thesis concern this change.

which cause unnecessary usage of material and energy, both identified by Kurdve et al. [3] as blind spots in today's application of lean. <u>I claim that many of these blind spots could be exposed in in situ measurement.</u>

In a more holistic view, [10] acknowledges that in addition to reducing process costs, lean can increase the perceived customer value that is also addressed as in situ measuring increases the product quality and decreases the production time.

1.1.3.1 Lean and in situ measurement

The following is a synopsis to help crystallize the strong bond between production processes, lean thinking, and in situ measurement. Plainly, process control is increasingly driven by lean principles and needs automation. Automation in turn needs in situ measurements. This is shown in Diagram 4 and collated in the following list.

- Quality is a function of how well the process is understood.
    - To be able to understand, one must be able to quantify.
- Quantification is also needed in automation,
    - computers cannot make qualitative decisions.
- In lean manufacturing, products must be produced smoothly and only on order.
    - This means that the supply chain must be agile: in situ methods give direct feedback to, e.g., suppliers of raw materials.
- For zero defects, one must understand where they come from.
    - root cause analysis in situ on the product line is needed.
- in situ measurements support lean ideology:
    - No post-manufacture,
    - No quality checks of finished product.
- Lot sampling is not effective:
    - Natural materials vary and must be measured constantly.

Lean

Holistic control of value creation ← aims → Add value to business

Product quality
Process safety
Reliability
Availability
Resource utilization
Energy savings
Emission control

4. Process analysis & informatics
3. Supply chain integration
2. Business integration
1. Process integration

Modern process control

Atmosphere changes   Changes in catalyst

needed because --- Processes are not stable

Raw material changes

Process fouling   Machinery abrasion

Automatization ← → Uses

In situ -measuring

Diagram 4: Synergy of lean, process control, and in situ measurement.

1.2 In situ process measurements

The previous section discussed the importance of in situ measurement for a great many companies producing on lean principles. This section deals with in situ – measurement, its meaning, benefits, and barriers, which are important to recognize for the design of new methods. The section continues to review the recent development of sensors, which are in the core of these measurements, and ends with a structured literature review of in situ measurements of materials.

This section seeks to further the understanding of the modern use and benefits of in situ measurements (as shown in Diagram 5) and to introduce recent work focused particularly on pharmaceutics.

8

High pressure   High or low temperatures   Unstable samples   Kinetic reactions

When samples are dangerous

When offline samples don't represent the real material

Replaces traditional offline equipment

When samples are unreachable

When rapid sampling is needed

When samples can't be perturbed

Characterization of Industrial characterization method

Integrated

Compre-hensive

Sensitive   Reliable   Online   Onsite

Robust   Simple

Need calibration   Rough atmosphere   usability

Needs sensors

In situ -measuring

Recognize abnormalities and find root-cause

bring quality control closer to production

Verify process   Help scaling up

Monitoring the process   Undestanding the process   Process controlling

Assure quality

Increased safety   Reduction in time and cost

Early stage process development

Ultimate goal is self-adjusting process

In situ -measurements of processes

Diagram 5: Characteristics and benefits of in situ measurements and their comparison with traditional offline measurements.

1.2.1   Definition and use of in situ measurements

As explained above, process control is realized through quantitative feedback, which in [15] is divided into continuous measurement at a high sampling frequency, delayed measurements from analytical devices at a fixed sampling rate, and manual laboratory measurements available at unequal intervals. The first two fall into the domain of in situ measurement, which is defined by Chanda et al. [16] as something that *reveals physi-*

9

cal or chemical aspects of materials inline, online, or at the production site,[2] as opposed to laboratory measurement, which is conducted away from the production site.

Compared to laboratory measurements, in situ measurements characteristically

- measure a relatively large proportion of produced materials, which means that
  - they must be rapid,
    - measure only a short spectrum, and
    - be highly sensitive to only the variables relevant to effective quality, and thus
  - give a more comprehensive picture of production than lot-sampling.
- are (partly) integrable with the production process and often
  - customized,
  - use probes and
  - need calibration.
- must be
  - robust, because of rough industrial atmospheres,
  - reliable, because processes are expensive to interrupt at false alarms, and
  - simple so that shop floor staff can be easily trained to use them.

1.2.1.1 Benefits of in situ measurement

The reason for in situ -measuring is that "[Monitoring product quality] online is the key issue in producing higher quality products, optimizing the production chain, and thereby improving efficiency." [1] In continuous processes, latency, e.g., end-to-end delay associated with communication, computation, and actuation, affects the quality and performance of the process [2], and conventional off-line, lot-sampling, laboratory measurements lead to inconsistencies, especially in batch-operations [16]. Online measurement is also advantageous because it does not require difficult sample preparation and thus eliminates sample representability and markedly increases the sampling rate. [17] In situ measurement improves or enables [16] study of kinetic reactions, measuring of hazardous materials and measuring systems that should not be perturbed. These (1) improve process understanding and help create new processes, (2) scale up smaller ones, and (3) optimize already established ones. In addition, (4) processes can be monitored with in situ measurements, which help detect faults, ensure product quality and throughput, and, finally, enable (5) process control [18].

---

[2] Direct measurements of temperature, pressure, and flow, as they are routine measurements, are excluded from in situ measurements.

1.2.1.2 Barriers of in situ measurement

Apart from regulatory elements and attitudes, the biggest obstacle to in situ measurements is the difficulty to integrate them in production processes because both the hardware integration of sensors and later methods integration to a production system are hurdles to overcome. Sensors in industry come with problems such as their robustness in hazardous processing environments and implementation of sampling probes in a process stream. Such problems are currently encountered with dip-tubes [19] and bottom [20] or side valves of vessels [21]. Wireless technologies will undoubtedly play a role in this regard. The latter challenges are briefly addressed in the conclusions, but they are no major problems for in situ measurement developers,[3] especially in light of a third concern, which is the investment cost associated with integrating measurements, and whether it pays off in lean manufacturing.

The above delimits in brief the domain of in situ measurement and the new methods presented in this thesis, and focuses on the direct and concrete benefits and barriers of in situ measurements to give a perspective on how such measurements should be designed. The following provides added insight by introducing the Process Analytical Technique (PAT) as an apposite frame for in situ measurement.[4]

1.2.1.3 Process Analytical Technique

In situ process control has been affected by the guidance given in PAT terms and first introduced in pharmaceutical development by the United States Food and Drug Administration (FDA). This guidance was formulated to address problems with process instability and quality, which had become increasingly complex because of multi-factorial production systems [17]. PAT defines systems that focus on online measurements of raw materials, intermediates or products and aims to measure the key process parameters affecting the efficiency of the process or final product quality [17].

PAT uses integrated tools of quality analysis through [22] (1) data analysis with process analytical tools, (2) process monitoring and continuous feedback with the aim to change time-fixed processing to product-state-fixed processing. [22] This again comes back to the idea of lean production.

---

[3] In industry, engineers must carry out some of this work, for they are already beginning to understand the possibilities of modern in situ measurement.

[4] PAT seems perfectly to match the approach in this thesis in terms of theoretical conjunctions, research approach, and contents.

According to [17], most PAT applications are still in R&D.[5] The PAT trend is increasing [18] in the pharmaceutical industry, but a similar shift is likely to be seen elsewhere. The companies mentioned in Preface seem to be in the vanguard of this paradigm shift towards in situ measurement in their own industries.

1.2.2 Sensors

The above topics addressed in situ measurement as a whole. The following two sub-sections focus on the core of in situ measurement, the sensors, and conduct the reader into the core of this thesis.

In general, sensors are becoming increasingly miniaturized and wireless, followed by lower installation costs and massive amounts of data to process. As a result, many complex processes are turned from model- to data-driven mode. [23] Consequently, even more sensing will happen in the future [2]. This again will generate a new wave of sensors with low-cost microcontrollers providing the necessary functions to create smart sensors capable of connecting wirelessly to a network and enabling further sensor applications [24], such as those used already to benefit mobility, redundancy, and compactness[6]. [24] Recently, wireless networks have been emerging in industrial production systems [24], and I claim that this sensor development has opened a door to devices, such as those presented in this thesis, suitable for in situ measurements.

In production, sensing is divided into soft and hard sensing, both aimed at real-time quality and process control [25]. Soft sensing means combining sensory feedback, often measured with conventional sensors, by mathematical means and aiming at comprehensive feedback on dynamic industrial processes. Soft sensing, much like hard sensing, is used to support fault detection, diagnosis, and product control and monitoring [26]. However, I claim that combining conventional process measurements in a new way is not enough to characterize materials, especially when processes are new and incompletely understood. This is the reason for developing process-integrated hard sensors that focus on characterizing a direct phenomenon in contrast to relying on derived parameters from existing sensors. Hard sensors precede soft sensors (not studied in this thesis), especially in developing new processes, as discussed in publications [I; III-IV; VI-VII].

---

[5] Such as the techniques presented in this thesis.

[6] Typical examples are the consumer goods industry, environmental monitoring, smart structures entailing home and building automation, and medical and health care. [26]

The following review helps the reader contextualize the study of hard sensors and understand the materials and structural parameters the sensors can characterize.

1.2.3 Literature survey of in situ analysis

The following is an organized literature review using Sciencedirect, Scopus, and Google Scholar. The review focuses on recent findings on the use of in situ methods for materials. Many findings are also listed in [17], which is a multi-authored review of recent PAT technologies. Articles are categorized first according to industries or domains the authors targeted (when possible) and then divided into the parameters they studied and classified by the principle method their application is based on. In situ methods about the process manufacturing industry[7] are omitted on the basis that they measured material in a flow state with well-established methods.

The list below classifies the fields mentioned in the articles in the literature survey.

- In general, industries that use or produce particulate matter [17], [21], [27]–[29]
- chemical industries [17], [30]–[36]
- bio-process monitoring [17]
- sterile product production [17]
- film coating [17]
- pharmaceutical production [17], [21], [30], [32], [33], [35]–[50]
- food and nutrition industry[30], [35], [36], [51]
- agro-chemistry [30]
- oil and petroleum industry [28], [52]

The list below classifies the methods on the basis of the parameters the authors studied as classified on their basic measuring principle:

- Ultrasonic sensors [27], [30]
  - to study crystallization: liquid concentration, crystal size (in the range of 100 - 800 um), and suspension density (5-40 wt %).
  - ultrasonic resonators are used in drug quantification [37], dispersion stability studies [37], and in particle size studies [53]
- Dielectric constant sensor to detect
  - phase separations [52] and
  - solubility [31]
- Conduction sensors for
  - concentration control [32]
- Imaging methods such as

---

[7] Term "process manufacturing" is used as an opposite of piece goods production. A typical process manufacturing industry is, for example, the oil industry, where the product is flowing material, such as continuous suspension or liquid.

- o endoscopes
  - ▪ to monitor crystallization [33] and particle parameters [39], [54]
- o diffusing wave spectroscopy: laser technique to measure scattered light intensity
  - ▪ to monitor rheological parameters of emulsions [40], and
  - ▪ particle dynamics [51]
- Photometric stereo imaging
  - o to study granulation (granule growth) [21] and
  - o drying characteristics [41]
- Photofluorecense [55]
  - o to monitor particle parameters
- Computed tomography
  - o to analyze solidifying microstructure [56]–[59]
  - o to analyze the deformation behavior of materials [57], [59], [60]
- NMRI
  - o to study suspensions [61, pp. 103–106]
  - o to study properties of liquids [62]
- Photoacoustic methods
  - o for gas analysis [28]
- Magnetic methods using Hall-effect
  - o to analyze the properties of magnetic particles [63], [64]
- Capacitive sensing
  - o to detect voids and defects in concrete [65], [66]
- Spectroscopic sensors based on
  - o IR-spectroscopy for reaction analysis [22] in adsorption study [34], supersaturation [35], and concentration [67],
  - o terahertz (far-infrared) spectroscopy to study intermolecular structures, trace gases, and human imaging [68]
  - o Raman spectroscopy to study super saturation [68], exothermic reactions [42], and particle size [69]
  - o ultraviolet–visible light spectroscopy to monitor reaction completion [16]
  - o mass spectrometry to analyze gas [16], and
  - o nuclear magnetic resonance spectroscopy to analyze chemical reaction [51]
  - o electrical impedance spectroscopy [70] to study defects in concrete.

The above methods are mostly under in R&D, though some have already been integrated. For example, in [36], multiple in situ methods were used in unison to control automation. The methods monitor crystal size, shape, and quality, and the parameters are linked with the production system that controls the process. This is a mature condition for these in situ methods yet a long way ahead of typical cases, such as those presented in the enclosed articles.

1.2.3.1 In situ methods for analyzing pores and porosity

The in situ methods in the enclosed articles were developed to analyze pores or their direct effects on material. Recent and prior contributions to that topic appear in Bawuah et al., who studied a terahertz transmission pulse and light reflection to quantify the

bulk microstructure of pharmaceutical tablets and measured their weight [44] and porosity [44] in-line. Also Lecreps et al. used combination of pressure and flow measurements with extensive modeling to demonstrate porosity gradients of particles during their flow in a pipe [29]. Other properties indirectly related to porosity and analyzed in situ are

- pharmaceutical tablet surface smoothness by Raman spectroscopy [45] or Near-IR absorbency [49] and its correlation to tablet crushing strength [45] or hardness [49],
- pore network analysis with nMRI [71], computed tomography [72], and mechanical and thermal behavior of materials in situ [72]
- use of acoustic vibration methods to find structural surface defects [46], Young's modulus, and Poisson's ratio [47], and
- use of ultrasonic to measure Young's modulus [48], and
- use of acoustic emission to identify phenomena (granular rearrangement and fragmentation) that take place during powder compaction [50].

1.2.3.2 Observations from the literature review

In conclusion of the above, relatively many methods have been employed for in situ analysis of material composition, chemical structure, particle size, or chemical reactions but rather few to characterize pores on site, let alone analyze them online, especially outside the pharmaceutical industry. The literature survey is very centered on the latter industry, because in situ measurements of process manufacturing were omitted from the review.

With respect to the latter finding I have identified a lack of in situ measurements particularly in piece goods production industries other than pharmaceutics.

1.3 Research area and method of the thesis

The above sections outlined the need for and current state of in situ measurements, and now it is time to concentrate on the specific focus and research method used in this thesis. The next subsections 1.3.1. (In situ measurements in the ceramics industry) and 1.3.2 (Contribution of this thesis) state the special focus of the thesis and the reason for it. Subsection 1.3.3. (Specific challenges and research questions in the thesis) gives a detailed description of the problem while subsection 1.3.4. (Research approach) elaborates on the approach applied and inspired by systems theory to systematically approach the industrialization of laboratory measurements, i.e., to make laboratory measurements in situ. The section is concluded by subtopic 1.3.5 (Innovation man-

agement) which introduces the strategic level in developing in situ devices as well as using the devices later to improve industrial processes.

This section aims to enhance the reader's understanding of the compass of this work, the sectors of in situ measurements addressed, and the manner of the measurements.

1.3.1 In situ measurements in the ceramics industry

The above section identified a lack in in situ method applications in piece goods production in industries other than pharmaceutics. Ceramics is a particularly interesting industry in that, to my knowledge, it has not to any large extent adopted in situ methodologies; rather, the industry is accustomed to performing functional analyses of finished goods on the lot principle. Although some leading enterprises in the industry may use rudimentary in situ methods, such as viscosity meters in the process stage, they produce rather conventional and indirect functional parameters, which are far from the real and dominant material parameters. Solid-state in situ analyses are very rare, a situation that makes the industry an interesting and relatively open play ground for testing them.

According to a report written by the European Ceramic Industry Association [73], the European ceramic industry is a global industry leader with some 200 000 workers and a strategic and future-oriented sector in Europe, aiming in the future to embrace resource-efficient and low-emission practices. These goals are achieved by moving away from the traditional energy sources with process optimization as one key technology. The report stresses that this is strongly impacted by academic studies geared to breakthrough technologies.

The above, combined with my personal experience, render ceramic industry a "new pharmaceutics"—a second industry ready for a wave of in situ process equipment. The industry welcomes cooperation with universities and is looking for breakthrough technologies and new energy sources, both of which call for close understanding of processes in the commissioning stage. Above all, process control has been mentioned as a key technology to be developed.

1.3.2 Contribution of this thesis

The publications enclosed in this thesis focus on making laboratory measurements accessible to scaled-up production volumes, paying attention to finding methods that can be integrated in an industrial process or at least methods that are simple or robust enough to be used on production sites. The links of the enclosed articles with the

16

above objective are shown in Diagram 6. One aim of the methods is that they must be comprehensive wide-enough view of the production process.

To keep the developed techniques within a phenomenologically and scientifically comprehensible frame, I have focused in cases characterizing pores or their effect on the properties of products. This choice was made based on the fact that pores and porosity encompass—like it or not—all ceramic materials and are the single most important reasons for the functional and mechanical properties of ceramics.

The thesis thus contributes in two ways to

1. guinea pigging the possibilities and providing examples of the ways to tailor industrial in situ methods to answer
   a. what characteristics are important in in situ methods,
   b. what kind of approach can work in developing the methods, and
2. giving some new knowledge to understand the mechanical and functional effects of pores in ceramic materials
   a. on how pore parameters affect mechanical features,
   b. on how electrical signals change in porous ceramics, and
   c. on the permeability of fibrous structures.

In summary, all the topics in this thesis aim to create an in situ characterization measurement that measures an aspect related to porosity, pores, or their affects. Individual challenges are discussed in 1.3.3. (Specific challenges and research questions in the thesis).

Included publications

I: Use of thermal imaging in characterization of ceramic fiber structures

II: Characterization of Porous Ceramics by Using Frequency-Response Method

III: Mechanical Characterization of Fiber Ceramics: Effect of Temperature

IV: The mechanical performance and CO2 uptake of ion-exchanged zeolite A structured by freeze-casting

V: Passive resonance sensor based method for monitoring particle suspensions

VI: Thermal Flow Permeametry - A Rapid Characterization Method for Local Changes in Gas Permeability

VII: Compression curve analysis and compressive strength measurement of brittle granule beds in lieu of individual granule measurements

Strength - - - - - - - - - - - - - - - - - - Characterization - - - - - - Functional Features

In-situ characterization of pores and properties linked with pores

Diagram 6: Organization of the enclosed publications and their links to the framework.

1.3.3 Specific challenges and research questions in the thesis

Many industries use various material characterization methods, but they are typically laboratory measurements, which means that samples are very small in size and results are not in real time. In addition, laboratory measurement measure too many characteristics of samples, for example: the process engineer might need to know only the biggest pore but mercury porosimetry gives redundant parameters, which are useful for scientific research, but which complicate the measurement process and lack robustness. In addition, these lot measurements measure only a small volume of the total process and make it doubtful if the results can be extrapolated. To overcome these challenges, the enclosed publications target the following processes:

1. preparation of porous structures, focusing on
   a. powder mechanics [VII]
   b. suspension characteristics [V]
2. analysis of mechanical features of porous structures, focusing on
   a. mechanical changes during sintering of fibrous structures [III]
   b. correlation of mechanical properties with pore parameters in oriented structures [IV]
3. non-destructive characterization of porous structures, focusing on

a. measuring changes in porosity [II]
b. finding changes in local permeability [I, VI]

Continuing with the topical classification, Table 1 breaks the enclosed articles down into primary questions about scientific attributes and application (in situ) novelty.

Table 1 Primary research questions in the enclosed publications.

Classification	Research aspect	Development aspect
1a	Can granule strength be measured from a granule bed instead of measuring a single granule?	Single granule strength measurement is not feasible/possible. In industrial production, a robust, comprehensive, and rapid method is needed.
1b	Can the flocculation of a suspension be measured during its preparation?	Flocculation, especially in thick suspensions, must be measured with laboratory devices; long response time is not possible in lean production.
2a	How can the rigidization of a fiber structure be linked with the structure's thermal history	Thermal history can be measured from a millimeter size sample with a dilatometer, but hardly at all in local rigidization in a large sample. A new in situ method is needed.
2b	What is the link between a structure's pore parameters and its crushing strength?	Pore structure can be characterized from a microscope image, but for quantified data with samples with many pores, analysis must be automated.
3a	Is it possible to nondestructively measure the porosity of a ceramic sample?	Porosity measurement with the Archimedean method or intrusion porosimeter method is laborious and slow and does not reveal closed porosity. A faster and integrated method is needed.
3b	Can local permeabilities of a fibrous ceramic structure be analyzed from a hot air permeability measurement using an IR-camera?	Permeametry can be used to analyze local variation in a sample, but it is very slow and difficult to integrate.

Collating all the topical questions, this introduction to the thesis focuses on the following three main research questions:

1. In situ measurement of processes through materials:

   a. Can material characterization be systematically tailored for in situ measurement?

   b. How does the robustness, integrability, reliability, and comprehensiveness of in situ measurement devices affect the route from design table to use in processes?

2. Can porosity, pores, and changes in them that affect the functionality and mechanical properties of structured materials be analyzed in situ?

1.3.4 Research approach

In the above, some similarities were identified between in situ methods, which can be refined to a systematic research methodology. The main task is to find a parameter that dominates the value creating features in production process.

I used a systematic approach (in Fig. 1) to develop the in situ methods in this thesis. The process involved simple steps, starting from understanding the variables of a production process and finding their effect on the material parameters of the products. Then the key material parameters were pinpointed and a way was determined to comprehensively and robustly measure them, and only them. The new method was then tested in a laboratory and finally integrated into a production system.
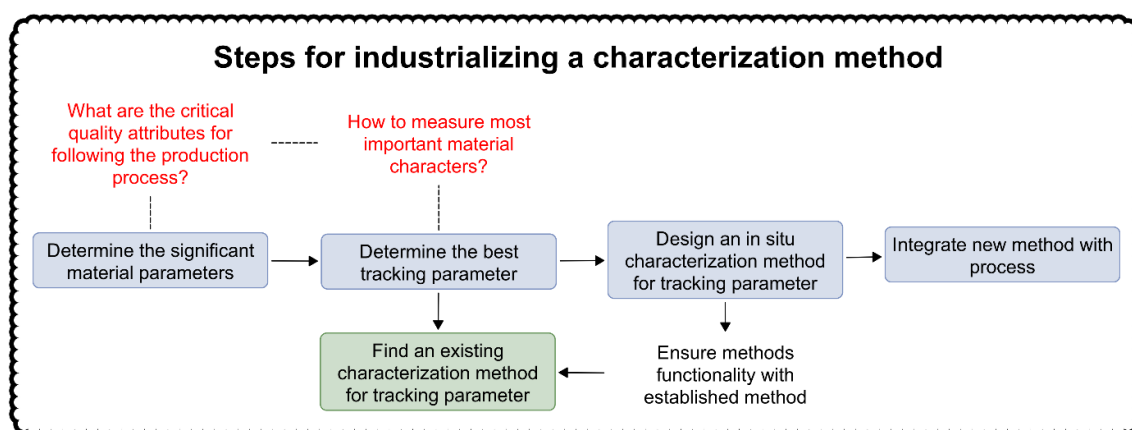
Figure 1 Systematic approach used to develop in situ methods.

The approach is a variant of the process described in [17], aimed to develop a PAT tool for pharmaceutical production. The process used in this thesis emphasizes an aspect

of materials science in favor of process engineering and while the focus is in the formal development method of in situ devices, there is evidently a need for certain innovative tasks in the development process. These are touched in the following subtopic.

1.3.4.1 Innovation management

To elevate the development of in situ –devices and industrial processes to a broader context this subsection mentions some existing theories related to innovation and their management.

According to Bessant and Phillips in [74] managing an innovation is possible with certain approaches that support the process. Innovations could be approached systematically, like the in situ device development in Fig. 1. Thus innovating could be a learned capability for a company given that the ability is flexible, especially in the case of disruptive innovations where the firm must focus in changing their value network, engineering new processes, finding new supply chains, etc. Teece [75] conceptualized this potency by introducing an idea of dynamic capabilities that refers to enterprise's ability to adapt when facing e.g. new technological opportunities or customer requirements. Dynamically capable companies can develop processes that enable them to change and develop together with the changes in their business environment [76]. The capability is driven in by implementing an innovative culture that counters the difficulty of codifying the innovation process. For example O'Connor in [76] presents such non-routine elements and state that caressing them, rather than pursuing a systemic codification for the process, could better keep the enterprises dynamically capable. This is especially important in technology driven businesses where innovation is a necessity.

To further incorporate the innovative culture, Bergman and Hagan [77] propose a technology-driven business strategy, where instead of viewing technologies merely as enabler, they are considered a core input that is taken into an account in strategy formulation in a same level as the customers, markets and competitors. This emphasizes the exploration of new disruptive technologies even in uncharted business areas. Other practical methods focus on combining internal and external factors with the aims to build a rich innovation network that pursues a coordinated knowledge flow combining [74]: science, technology, market needs, manufacturing capabilities, competitor behavior and regulatory issues. However, this may lead to adapting and improving ideas that have been developed elsewhere, possibly raising a risk of losing valuable technological assets. This risk can be controlled with governance structures, controlling the alliance scope and careful partner selection [78].

While not the focus of this thesis the innovation processes explained in this subsection have been carried out both during the development of in situ –methods and by the companies who have worked with us. This subtopic might thus help the reader to understand the angle from which the development processes have been addressed. However, this will not be discussed further in the thesis. The next subtopic finalizes this chapter by describing the working environment where the in situ –methods were developed.

1.3.5 TUT and the ceramics laboratory

This subsection describes the department and laboratory, in which I worked on this thesis. Articles [I-III; V-VI] were parts of long, industrial projects, whereas [IV; VII] were smaller projects. The aim is to introduce the work environment for some background and perspective for the experiments and research conducted there.

All the contributions to the enclosed articles and this thesis were written during my employment at Tampere University of Technology (TUT). The TUT strategy for 2013–2016 calls for "Technology for the benefit of people and the environment", and its mission is to be "at the leading edge of technology development and a sought-after collaboration partner among the scientific and business communities. The University produces competent graduates who enter careers in the different sectors of society". The TUT values are "Courage, responsibility, and community spirit". Since 2010, TUT has been a foundation-based university with a total funding in 2013 of 157.7 M€, about 50% of it from external sources. In 2013, TUT had over 10 000 students and almost 2000 employees.

This work was carried out in the Department of Materials Science (DMS), which receives most of its funding from industry or external sources, and which covers all material groups: metals, ceramics, polymers, and composites. Its 2015 turnover was 9.2 M€, of which 68 % was external funding. The department has about 100 academic employees, 36 of them post-doctoral students.

2 Theoretical background on pores, porosity and their measurement

This thesis is weighed towards applicative approaches for tailoring in situ - measurements to be used for the reason, and in the areas, described in the earlier chapter. Each of the presented method has a scientific background in pore and porosity -related matters and owing to that, this chapter encloses a theoretical overview of pores, porosity, their measuring and their effects from the materials science point of view.

The chapter does not aim to be an exhaustive review explaining all the latest theories but to work as a supportive base against which the results of in situ measurements can be examined. As such the following theories are a truncated summary of the most abundant ideas relating to the topics enclosed in the articles, also discussing shortly on the present research around it.

The chapter is divided in to four separate sections that address the theoretical background of enclosed articles [I-VII]. The chapter are related to the enclosed articles accordingly:

1. **Pores and porosity**, is a general chapter laying definitions but in sub-chapter 2.1.3 porosity links with
   a. sintered materials [II]
      i. Manufacturing methods: powder [VII], slip casting [II] and colloidal processing [V]
   b. porous crystals [IV], and
   c. fiber materials [I, III, VI]

2. **Effect of pores and porosity to mechanical properties**, opens with a general explanation of how porosity affects material strength but then focuses in pore characteristics at:
    a. oriented materials [IV]
    b. granular materials [VII]
    c. fibrous materials [III]
3. **Fluid flow in porous media,** focusing mainly in determination of permeability in the context of
    a. fibrous materials [I, VII] and their measuring with thermal flow permeametry,
    b. oriented materials [IV]
4. **Characterization of pores**, is limited to the methods used in the enclosed articles
    a. Porosity
        i. Archimedean method [II]
        ii. Porosimeter [I, III]
        iii. Porometer [I, III]
    b. Permeability
        i. Permeameter [III]
    c. Pore shape
        i. Image analysis [II, IV, VII].

The chapters are somewhat separate from each other because the ground for this work is not in theoretical inspection of pores and porosity but in in situ -measuring only focusing on themes that are included in the following theoretical frameworks. Still, all effort is made to categorize and progress the chapter in a non-disruptive flow. The topics are presented in Diagram 7.
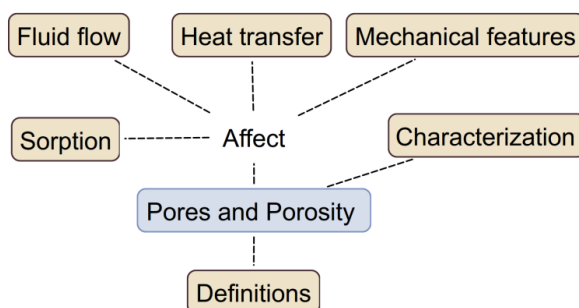
Diagram 7: Pores, porosity, and their measurement (concise version).

2.1   Pores and porosity

Apart from the nature materials porous structures are fabricated by man. The scope of this thesis covers the latter focusing on technical ceramics in the form of sintered components made by slip casting [II] or powder compaction [VII], fibrous [I, III, VI] and hierarchical structures [V].

The following sub-chapters define and introduce pores in general and then, acknowledging that the nature of pores in all of the previously mentioned ceramic structures is different, the chapter continues by focusing on the special characteristics in separate sub-chapters. In the sub-chapter on sintered ceramics their processing is also addressed to clarify the background for articles [II, V, VII].

In different fields, the terminology surrounding pores varies without a clear consensus. This thesis pursues to follow the common terminology used in materials science and adapts some terms from soil engineering if necessary.

Objective of this chapter is to define the main scientific topics in the thesis, namely pores, and build a shared background for the results presented later. The topics are visualized in Diagram 8.
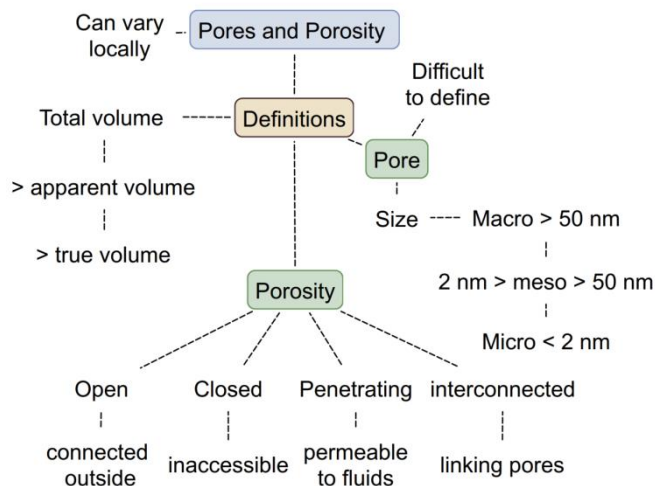
Diagram 8: Topics and details in section Pores and porosity

2.1.1   Pores

According to [79], pore is a relatively small solid-free space or void imbedded in a solid or semisolid matrix. When pores are fabricated into material its properties change:

density decreases while specific surface area increases. [80] These changes introduce functional properties: such as selective fluid permeability [I, III, VI], thermal and acoustic insulation, or sorption [IV]; but at the same time change the mechanical properties [III, IV, VII].

In a microscopic sense, pores can be classified by their network topologies, connectivity, and pore topology. [79] A text-book example of pore contains a cavity which is the relatively wide part in comparison to the narrow portion that is the pore opening separating the bodies and controlling the fluid flow [81]. In reality pore shapes are numerous and in actual cases many shapes are present at different sizes as in [IV]. In order to differentiate pores by size ranges they are categorized by width in IUPAC [82] accordingly:

- Macropore: larger than 50 nm[8]
- Mesopore: between 50 nm and 2 nm
- Micropore: below 2 nm

Pore width is the radius of the pore's body or its neck [81] depending on the way the pores are analyzed. The pore sizes are often given as a size distribution diagram that according to IUPAC [83] is "a distribution of pore volume (or area) with respect to pore size".

For further characterization, a structure may consist of open porosity[9], accessible to outside and closed, inaccessible porosity [83] that may contain fluids [80, p. 1]. In [83] the open porosity is distinguished by its interconnectivity, i.e. separating the special pores that have at least two openings on other sides of the structure. These are called penetrating pores and they make the porous structure permeable by letting fluids to pass through it and thus, especially when used for filtration, they are known as flow pores. The difference between pore types is shown in Fig. 2.

---

[8] Most of the study in this thesis is focused on macropores.
[9] A special case of open pores is dead-end (blind) pores that are interconnected only from one side of the medium.
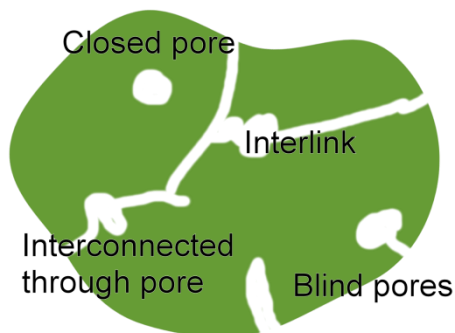
Figure 2 Pore types.

The most trivial characteristic of a porous material is the total volume fraction of pores, i.e. porosity that is calculated by dividing the volume of pores by the volume of bulk [81]. Based on the total volume of different pore types, the following classification is used [83]:

- Bulk or total volume: measured by the external dimensions
- True volume is the total volume minus the volume of open and closed pores
- Apparent volume is the bulk volume minus the volume of open porosity

Another common characteristic of porous material is the surface area of the pores which is often given as a comparative number by stating the specific surface area that is the interstitial area of pore surfaces per unit mass or volume[10]. The surface area is significant to all reactions, such as adsorption [IV] or surface charging [V], that take place on the surfaces; and affects the fluid flow through porous media [VI]. [79]

2.1.2 Challenge of defining a pore

In light of the previous, determining pore parameters, like has been done in [I-IV; VI-VII], is relatively straight forward, but as pores may be invisible to the naked eye they need to be analyzed by experimental techniques yielding macroscopic parameters, such as

---

[10] As stated by Dr. Arto Ojuva: "Surface area might be tricky, since you don't know directly if you are measuring the inside or the outside. Especially with nanoparticles the external surface area is often a significant fraction of the total pore area. Also, surface area is heavily dependent on the probe molecule (molecule used in surface area measurement). I'm trying to say that you cannot inherently claim that the reported surface area is "the interstitial area of pore surfaces" (whatever that means...)

[79]: porosity, pore size, specific surface area or permeability which describe the type of pores in the measured sample, and depend on the method of characterization.

The conventional characterization methods are further discussed in section 2.4. Characterization of pores, but as an example, a method called intrusion porosimetry that measures the volume of infiltrated liquid at a certain pressure and calculates the volume distribution of the sample may not lead to a clear correlation of pore volumes because the macroscopic parameters represent average behavior of a model sample [79] and easily underestimate and neglect certain pore characteristics.

The topics in this thesis include structures with heterogeneous pores [I; III; VI; VII] that are difficult to describe, and when averaging may lead to great errors. The problem is often evaded by measuring functionally important pore features for instance using an extrusion porometer instead of mercury porosimeter for structures where fluid flow is important[11].

In real materials the pore morphology may also vary spatially, like in [I, III, VI, VII], meaning that in certain areas porosity is different. This can be caused e.g. by the manufacturing method [79, p. 32] and lead to doubts on representativeness of a sample unless these heterogeneities are systematic that is the case in "anisotropic" structures in [IV]. This question of representativeness is often linked with manufacturing and can be countered with in situ -measuring.

A main challenge in microscopic pore analysis has been the definition of a pore. [79] defines a pore as "a portion of pore space bounded by solid surfaces and by planes erected where the hydraulic radius[12] of the pore space exhibits minima". This indicates that "a pore" may often be an artificial concept. Such as in the enclosed articles that study open porous structures composed of fibers [I; III; VII] and sintered aluminium oxide [II]. The pore size alone does not describe the structure but merely works as a guideline which is also perceivable when looking at the example images of real structures in the following chapters.

---

[11] Fluid flow depends mostly on the dimensions of the most constricted part of interconnected pores and not their total volume or properties of blind pores which the extrusion porosimeter measures.

[12] The book [79] uses hydraulic radius in the meaning of minimum value of area of cross section divided by the length of perimeter of cross section [79, p. 30].

2.1.3 Porosity in real life

Leaving aside the often simplistic way of defining materials by indirectly measured pore parameters, the following sub-chapters describe the real ceramic structures encountered in this thesis.

For sintered ceramics the sub-chapter is written from manufacturing perspective to retain coherency with articles [II, V] that cover related in situ -methods. Other sub-chapters on porous crystals [IV] and fibrous ceramics [I, III, VI] describe the structures in general and in comparative manner.

2.1.3.1 Porosity in partially sintered ceramics

In sintered ceramics, conventionally the effort is to reach dense solids as the mechanical properties strongly depend on the porosity. [79, p. 86] Yet, if functionality, like fluid permeability is striven, pores are fabricated in the material.

Each method under this topic, as the name implies, has a stage where the structure is sintered but before that the raw material forming is carried out with different manners. Typical ones include powder compaction and slip casting and both of them, as well as the majority of all ceramic production methods, exploit raw materials as fine colloids, susceptible to agglomeration. These finally determine the pore amounts, shapes, and sizes [80, pp. 13–14].

Sintering

Sintering of a particulate material inflicts particle bonding, neck growth, pore channel closure, pore rounding and shrinking. Sintering needs to be controlled as for example due to statistical laws, when porosity decreases under 10 percent, mostly ineffective porosity is left. [79] Fig. 3 shows how the microstructure changes when sintering temperature is increased. This phenomena, delimiting the functional use of the structure, is seen in our publication [II] that studies the possibility to use electrical agitation for online analysis of different porosity levels.
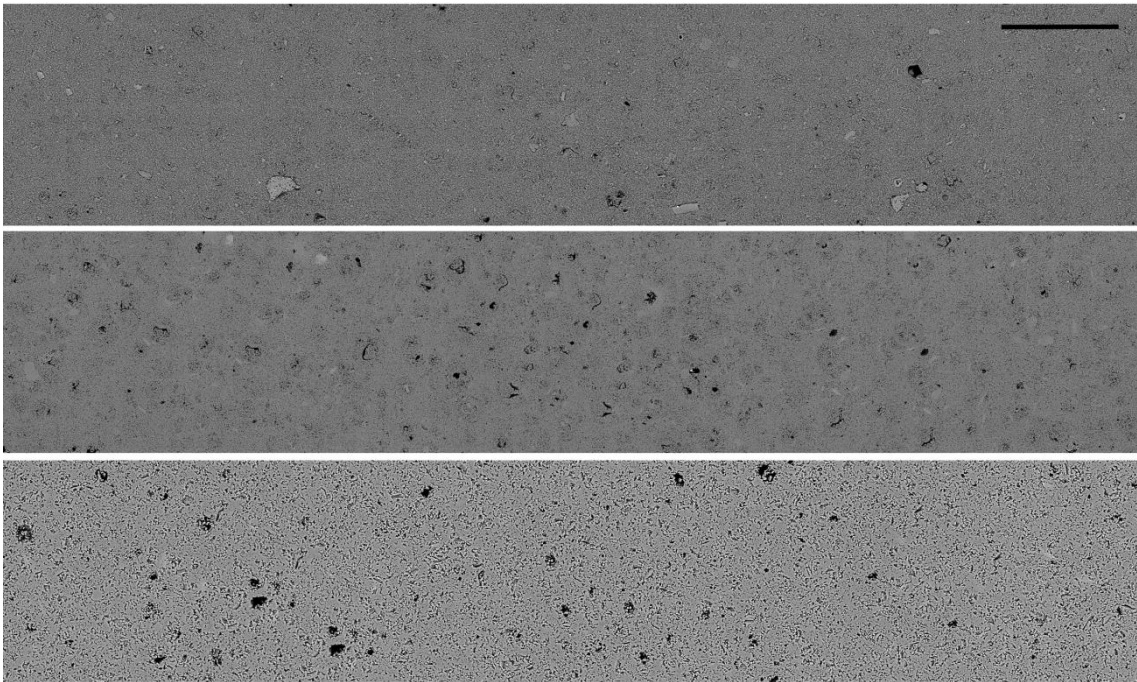
Figure 3 Sintered alumina structures with different total porosities from top to bottom 33, 18, and 3 % total porosity. Scale bar length is 130 µm.

Powder compaction

Ceramics with sub-millimeter or sub-micrometer pore size are typically produced by powder compaction [80, p. 12]. These structures are used for instance for filters, catalysis beds and gas sensors. In order to control the pore properties of the finalized ceramics the understanding of powder forming process is important [80, p. 12]. Powder compaction process is studied in [VII]. Granules and their internal porosity is shown in Fig 4.
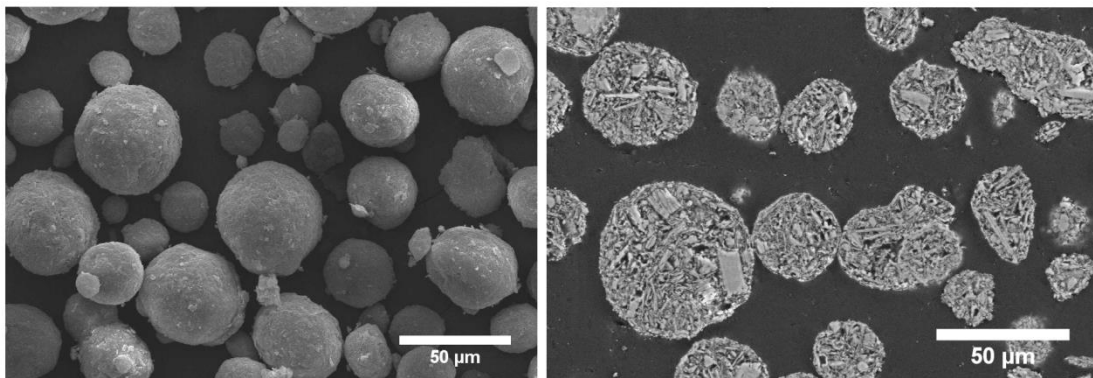
Figure 4 Kaolinite powder. Granule surface and cross sections.

Colloidal processing

Another typical forming method for sintered ceramics that was used for sample materials in [II] is slip casting. In slip casting, where the particles are suspended in a liquid solution, their surface properties influence the suspension characteristics. Phenomena surrounding particle-particle interactions are encountered in colloidal processing that is a typical step when manufacturing porous materials.

Colloid is a heterogeneous mixture of continuous dispersant and discontinuous phase that classically has a size of 1-1000 nm. For practical reasons the range is often extended with the main focus in the interactions of particles.[13] These interactions result from the particles being larger than molecules, so that they do not behave like a true solution, but at the same time being smaller than macroscopic particles[14], so that classical physics cannot be applied, and for instance gravitational force is not great enough to cause sedimentation. [84]

The above insinuates that non-classical forces act on the particles in a colloidal suspension. In addition to gravity, the particles can move because of forces caused by convection or Brownian motion but the electrical charges in a stable suspension prevents the sedimentation of the particles. These charges are caused by the inherent property of the surfaces of inorganic particles to charge in solutions. This invokes countering ions from the solution to bond on the particle surface which further induce a loosely bound diffusion layer of cations and anions to surround the particle and the primary, strongly bound ion layer. Now, the particles with ions surrounding them in a double layer, repel each other [85]. The electrical interaction between particles affected by temperature, acidity, and ions in the liquid; are a sum of double layer repulsion and van-der Waal's attraction. The mentioned variables are exploited when controlling suspension stability, [85] and they are studied by measuring the electrokinetic potential between the particle including the double layer, and the suspending liquid. Common device to measure this is zeta potentiometer. [86] Certain results in [IV] imply that an electrical resonance measurement can be used to study these forces in a suspension in an online manner.

---

[13] According to [85], in a system where solid particles are dispersed in a liquid, colloidal forces are significant below 40 µm particles.

[14] Those visible to the naked eye.

2.1.3.2 Porosity in porous crystals

Porosity in sorption materials is typically distinguished by the molecular size pores within the crystals that the structure is composed of. These materials are used for ion-exchanging, catalysts, molecular sieving or sorption. The intracrystalline porosity is classified by type into layered, isolated, channeled and interconnected pores [79, p. 89]. Interconnectivity in certain structures, mainly zeolites, is exploited in selective gas sorption that can be controlled by tailoring the intracrystalline pores.

In article [IV] a zeolite powder was structured for more efficient CO_2-capture. An example of structured zeolite is presented in Fig. 5. A zeolite crystal has an inherent pore in its lattice and the size of this pore typically varies within 0.3 and 1.0 nanometers. The zeolites are composed of silicon and oxygen with some aluminum and the lattice pore size can be controlled with doping. [87, pp. 5–8]
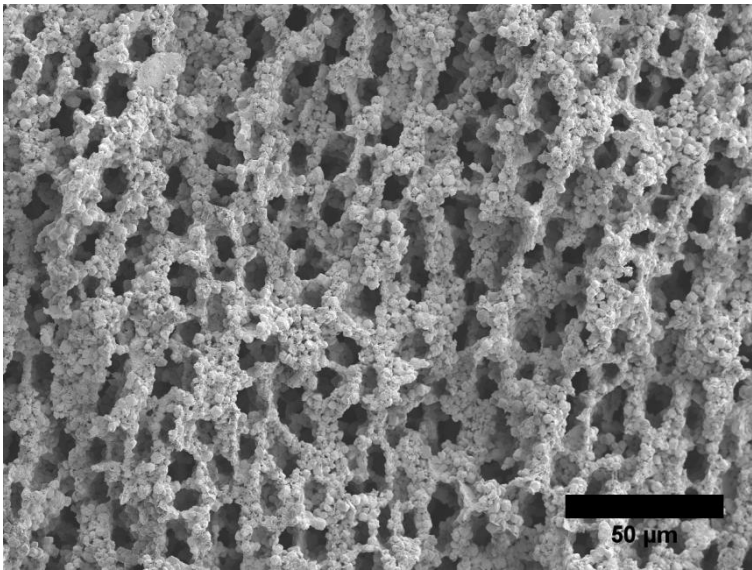
Figure 5 Structured zeolite.

2.1.3.3 Porosity in fibrous ceramics

A good and well-studied example of a fibrous and porous material is paper. It is distinct with a large amount of interconnected porosity and usually characterized in terms of pore radius using air permeability or pore size distribution with different fluid intrusion and extrusion techniques. [79, pp. 82–83]

Many ceramic fiber structures, included the one present in this thesis (Fig. 7), have remarkable similarities with the structure of paper but they are far more stable in high

temperatures and chemically aggressive atmospheres. Consequently they are used in hot gas filtration [68] and furnace linings [88].

A distinct demand in filter application is the filter's efficiency to remove particles of certain size. That depends on the pore size distribution rather than the equivalent pore radius that is calculated from the permeability. The latter does not reflect the size of the pores - few large pores have the same equivalent pore size as many small pores. [79, p. 83] In situ -method in [I; VI] aim to offer a tool for quick verification of existence of areas with larger porosity. The publication [III] aims to understand why this kind of a structure turns rigid when heated.
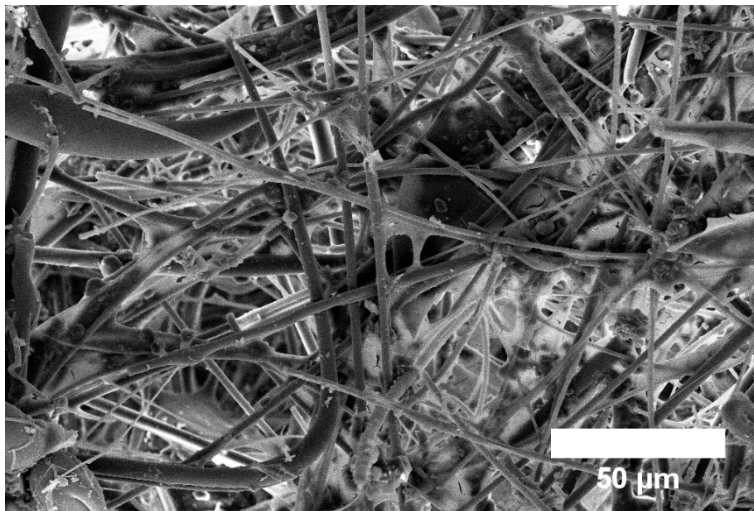
Figure 6 Ceramic fiber structure.

2.2 Effect of pores and porosity to mechanical features

As the previous introductory sections on pores and porosity clarified, the porosity, pore geometry, and pore size are known to have a major effect on the properties of porous material [80]. The features under interest on the enclosed publications are mechanical strength [III, IV, VII] and permeability [I, IV, VI]. The theoretical background of the firstly mentioned is examined in this section (visualized in Diagram 9) and the second in the following one.

Objective of this section is to display common theories related to how change in porosity or pore characteristics affect the compressive strength of heterogeneous structures and how a granule bed behaves under compression while its porosity is decreasing,

and finally inspect how a fibrous structure can be modeled explaining its strength and elasticity changes when it is heated.

Cellular structures	Fibrous structures	Granule bed compression
Oriented pores = anisotropic behavior Porosity = less material = lower strength	New connections in fiber network change force distribution	Large volume = high probability of catastrophic discontinuity

Mechanical features ---- Griffith --- Discontinuities (e.g. pores) affect force distribution ---------------- Weibull

Diagram 9: Pore effects on mechanical features.

2.2.1 Effect of porosity to mechanical features

Amount of porosity has an effect to mechanical properties such as strength and tensile modulus. This is seen in [IV] and [89], and in plain: increasing porosity means less material to carry the loading and subsequent decrease in component strength. This simplification has led to numerous studies such as [90] that relate porosity with a mechanical property. Still, most of the parametric relations presented in these studies have an empirical constant that has to be varied when material or manufacturing method is changed. The empirical factor is needed because the total porosity is not the only contributor to the mechanical characteristics [91] which is clearly seen in [IV], where a structure containing oriented porosity was found to carry load at in-plane axial compression five times higher with only changing the structure of pores while keeping the porosity constant.

To inspect this a little deeper, Griffith [92] explained that strength and amount of discontinuities in brittle materials are linked by how the stress is concentrated at the location of these discontinuities. In other words, the force applied to a structure can only be conducted through a solid phase and it has to go around or transmit through each discontinuity causing force concentration in the vicinity of discontinuities (see Fig 7). The conduction of force and its concentration close to discontinuities leads to idea, also originating from Griffith, that the discontinuity's shape and alignment with respect to the applied load affects the concentration of force as shown in the Figure 7. This concentration takes place also in porous materials and is dependent on the pore shape, size and orientation. We have used this principle when explaining the strength changes in [III, IV, VII].
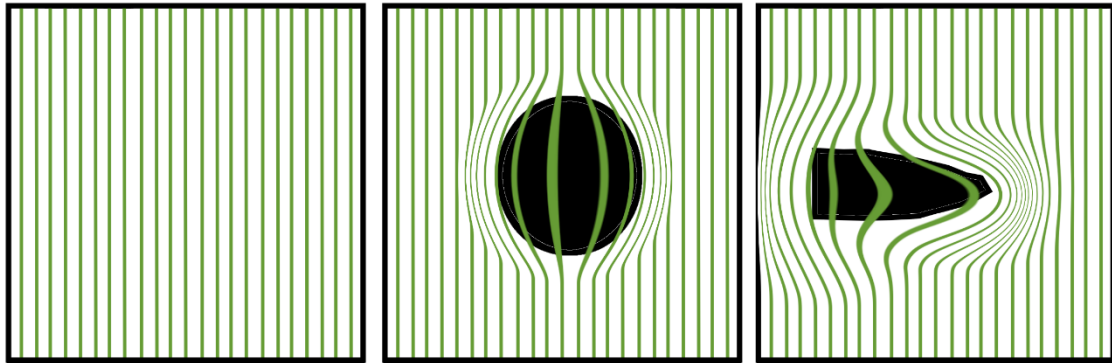
Figure 7 Stress concentration caused by different discontinuities. Lines indicate a stress field while black areas are the discontinuities. Stress concentrates on the tip of the discontinuity in the right-most picture.

2.2.2 Effect of pore characteristics to mechanical strength

Looking more closely in the pore characteristics, other than overall porosity, it is quickly evident that a porous material has to be viewed as a multiphase composite. When it is strained, the internal stress field is not constant [93, Ch. 1.2] and even the macroscopic behavior of the structure can vary according to direction and location of the strain. This is called anisotropic behavior and a typical example of it is a unidirectional fiber composite that has a stiffness of fiber in direction of their axis and stiffness of matrix against it [94]. In [III], although quite random, the fibers are oriented in certain layers causing non-linear behavior. Another example of nonlinearity is the oriented zeolite structure whose compressive strength was modeled in [IV].

2.2.2.1 Modeling of mechanical features

Approaches to model mechanical features are divided as [95]:

1. Composite theory, which is the basic approach in micromechanics, analyzing heterogeneous materials on the basis of their geometries and properties of each separate phase [93, Ch. 1.2]. In context of porous materials this approach is applied by considering pores as one of the phases of the composite.

2. Cellular solids is an approach that assumes the composite possessing a repeating structure that can be defined as a cell, following that the behavior of such composite is a function of each cells together. The structure is studied in multiple scales[15].

---

[15] But the methods in this category can either be homogenized, such as in [158], or they can be modeled with different generalization methods [95].

3. Minimum solid area approach assumes that a mechanical parameter can be calculated as a ratio of respective solid and the studied component which is directly proportional to the minimum ratio between solid contact area and the total cross-sectional area.[16]

In [IV] we have modeled compressive strength of an oriented structure using a cellular solids approach. When the above approaches were compared the choice was made based on that the one in question had been used before for such structures [91], [96] and the fact that our structure was very distinct with separate cells fitting easily to the framework that is explained in the following.

2.2.2.2 Geometric model for open cellular structures

Our approach in [IV] was to use the model originally published by Ashby [91]. The model views the cells composed of repeating structures and is mostly aimed for low-density open-pore cellular solids. It is derived from dimensional parameters of idealized structure composed of struts, not by modeling real pores. The model is semi-empirical but it has been fitted with extensive number of different structures.

Basis of the model, described better in [91], is to account for three variables classified as: material properties, topology of the cells, and relative density of the structure. The structures are classified either being stretching or bending dominated in which the differences are that the strut structure, considered to have locked joints, in a bending dominated type divides the force in a manner where the struts bend whereas in the other type they stretch. Focusing on the bending dominated structures; they are defined by low connectivity of the cell joints inducing three competing yield mechanisms: plastic yield, buckling, or fracture. The failure mechanisms can be predicted when the cell unit size and the strut modulus are known. The bending dominated structures are typically weaker especially if they break before their fracture strength which is seen in [IV] and further modeled using Euler-buckling principle.

2.2.3 Strength of a granular bed under compression

Moving now from mechanics of cellular structures to a structure that is somewhat similar - composed of repeating units - but is in a dynamic state during application of force, the modeling becomes more difficult.

---

[16] In addition to pore volume fraction, the approach uses parameters that describe pore morphology and packing [159] from the principle that structures become weak when the solid contact in highly porous structure minimizes [157].

The article [VII] addresses the measuring of granule bed strength that is relevant in certain processing steps when introducing porosity to materials. The theory in powder compression is relatively well understood but with brittle and small granules the interpretation of the compression curve has been unclear.

The following presents related theories in a broader sense in comparison to the article, acknowledging the different behavior of rigid granules and uses the earlier presented force field approach.

2.2.3.1 Compaction stages in compression of brittle granules

The difference between plastic and rigid granules is that the plastic granules deform during compression. This causes differences in their manner of yielding but certain similarities prevail. For instance in [97], the compression is found to take place in stages where the granules rearrange and deform, but these do not take place in as distinct steps as in brittle compression where distinct yield stages can be seen in a compression curve. The curve plots compressive pressure against strain in a steady-state compression and it is presented in a half-logarithmic scale to emphasize the relative changes. An example of the stages is seen in Fig. 8.
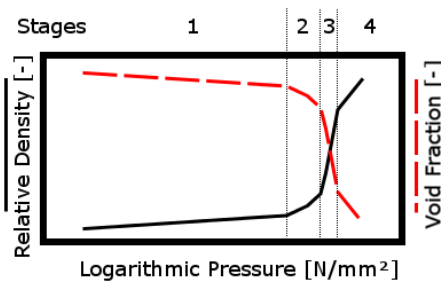
Figure 8 Granule yield stages in [VII].

During the first stage in the curve the granules deform elastically, pack, and rearrange. When the rearrangement takes place, the relative density decreases as the granules achieve a denser packing. During the second stage the compressive strength of the granules exceeds and they break mainly by fracturing and attrition [98]. The breakage probability can be described by Weibull-statistics [99] leading to the fact that smaller granules are relatively stronger and that the steepness and length of the curved region is affected. A high weibull modulus [100], small size distribution, high packing density and homogeneity of granules, lead to a steep and short second stage as the granules break at the same load. [101] The curve is not affected by granule size distribution provided that the strength of each size is equal [102] but their shape may change it because it changes the initial relative density [103]. During the third stage the fractured

granules rearrange under similar laws as in the first stage and in the final <u>fourth stage</u> the granule bed has no, or very limited amount of, voids left and the primary particles and pieces of granules can no longer rearrange. [104] Finally after the compression the relief of pressure causes the release of elastic transformation leading to a small decrease in compact density [105].

2.2.3.2 Force distribution links the bed strength to strength of individual granule

Correlating the granule strength of a single granule measurement with a granule bed measurement [106] is difficult but not always necessary if a relative analysis is enough. In single compression, force is transmitted to the granule by a controlled manner in which the granule is subjected to the most stressed condition by inducing the stress from its opposite poles [102]. This is not always the case in bed compression where the division of load is governed by how the force field divides across the granules. Still, in the both cases the granule breakage is influenced by the same factor that is the size and orientation of intragranular discontinuities, such as primary particle boundaries, binder-particle-interfaces, pores, and cracks which function as stress condensers.

The previously mentioned force field division in bed compression is controlled by shapes and sizes of granules and eventually affected by the partial yield of the bed. When granules fracture and their size becomes smaller they can divide the stress more evenly to bigger granules but themselves are exposed to a higher stress level, because of fewer contact points. [100], [102] As a countering effect the granules undergo size hardening that is linked with a weibull volume effect rendering the smaller granules relatively stronger [98].

Because of the above the changes in bed compression curve are smooth as the granule breakage only causes more force to divide to other nearby granules and adding to that also the punch geometry and granule's friction against other granules and the die walls affects the measured compressive strength. The stress is the highest close to geometric discontinuities of the die and close to the compressing punch. According to [107] the friction between the die wall and the granules is a more dominant feature than granule-granule friction. This can lead to unequal force distribution creating local regions of high-stress areas [97].

In [VII] an in situ -measuring method for measuring the bed strength of rigid granules is refined for being semi-automatized.

2.2.4 Mechanical aspects in fibrous materials

Theories on oriented structure made of powder and powder compression have now been presented. In the first cases it was possible, to some extent, model the structure but the previous modeling is more difficult as the modeled entities are moving during compression. In the following, the difficulty comes from the heterogeneity of fiber structure making the parameterizing enormously difficult.

Fiber structure studied in this thesis [I, III, VI] was a complex network of randomly oriented and kinked fibers that varied in diameter and length. In addition, it contained other strength increasing phases, such as binder and chopped fibers whose distribution was not even. Ultimately, the structure was so heterogeneous that no proper models were found to describe it and it was not totally clear what the results of conventional mechanical tests indicated.

In the beginning, the problem was compartmentalized via basic approaches to study fibrous networks [108, p. 28], [109, p. 4]:

- Network models: studying typical fiber deformation of a macroscopic entity studying for instance the effect of fiber orientation to the structure. In network model the individual fibers and their connections are modeled.
- Continuum models treat the fiber structure as a planar entity assuming that a representative volume of fibers and their connections can be studied as a continuum, i.e. structure can be homogenized.
- Molecular model studies the mechanical properties via the physics of molecular bonds omitting the structure's geometrics.

From these approaches the continuum idea was an obvious choice for the simple reason that the modeling of this structure was so complex that network model or molecular models were considered to need too much detail[17]. The work did not include modeling but touched the aspect by proposing a new feature "fiber free length" that is presented in the following.

2.2.4.1 Continuum model for fiber networks

To explain why a complex fibrous network turns rigid when heated, the network was studied in the paradigm of continuum modeling, focusing on a mesomechanic approach where a single fiber, with all its connection to nearby fibers, was chosen as a mesoelement as in [108, pp. 28–29]. Such a mesoelement is depicted in the Fig. 9 with

---

[17] It could be modeled but the main effort of the project where the study was carried out was not that.

red (the fiber) and green (fiber connections). Because the connection of a standard mesoelement are multiple and in different angles the strain for one fiber is not uniform. The free distance of the fiber in the figure is colored with deep red, it is the distance between the two adjacent connections. When this distance is small in comparison to fiber width the fibers shear under a load whereas with long distance they are more prone to bending [108, p. 29]. A similar observation was made in [III].
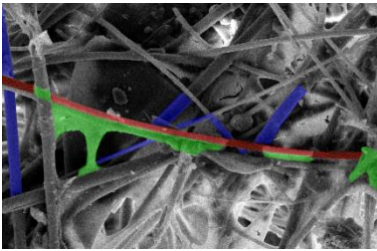
Figure 9 Fiber bonding in [III].

2.3 Effect of pores and porosity to fluid permeability

The mechanical aspects related to thesis have now been reviewed and next in line are the matters related to fluid permeability (visualized in Diagram 10) to which the present chapter focuses. That is an important functionality pursued by adding interconnected porosity to materials.

The chapter opens with a general sub-chapter presenting the field of fluid flow in porous media but focuses quickly on permeability models relevant for [I, VI], that study the porous structure of fibrous hot gas filters. In more detail the publications study permeability and its relation to pore structure and link those by measuring the heat transfer of hot gas flowing through the pores. For that reason, heat transfer in porous structure is also discussed in subsection Thermal measurement of permeability.

Permeability is also under investigation in the structure presented in paper [IV]. The structure is aimed for CO_2-sorption that is controlled by the nanoporosity in the crystalline structure of the studied zeolite. The kinetics of sorption processes are affected by the permeability of larger size flow channels providing the gas on the sorption frontier.

Objective of this chapter is to build a theoretical base on thermal flow permeametry measurement [I, VI] and as a side note explain how sorption is partially controlled by permeability. The latter is not in the main focus of this thesis but closely related and more thoroughly presented in [IV].
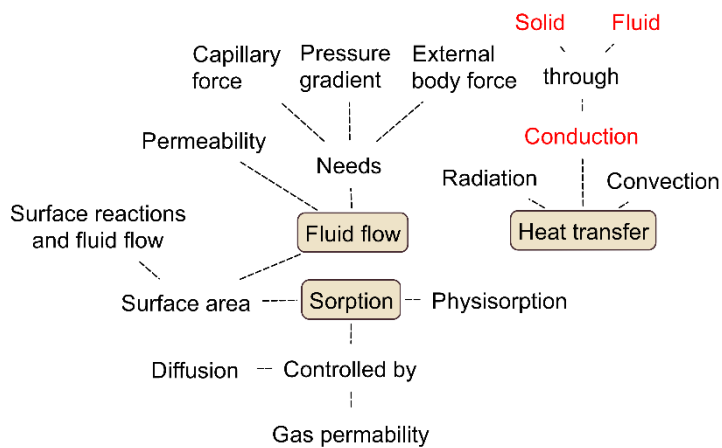
Diagram 10: Pore effects on fluid permeability.

2.3.1 Fluid flow in porous media

Fluid flow in porous and heterogeneous materials is seen in nature and technological areas where the most studied are the extraction of oil and gas, spreading of contaminants in fluid-saturated soils, separation processes such as filtration [110, p. 1], and substance transport in biological systems [111]. Many of the theories a rooted from research on those areas.

A detailed investigation of fluid flow through porous material can be complex because of heterogeneous microstructure in porous media giving rise to effective fluid flow properties [110, p. 1]. In plain, flow of fluid through a porous media is governed by:

- temperature and pressure dependent external factors such as:
  - the flow speed of fluid and
  - the fluid's viscosity, and
- structure dependent internal factors such as:
  - pore tortuousness
  - specific surface area per unit volume[18], and the
  - structure's thickness.

A fluid can flow through a porous media because of pressure gradient, external body force or capillary force. [110, p. 5] This thesis is confined to the firstly mentioned, whose modeling is studied via the most typical material property related to fluid flow -- permeability.

---

[18] The specific surface area is affected by the pore shape, size and topology.

2.3.2 Fluid permeability

In this thesis modeling of the flow through a porous media is confined in measuring the permeability of fibrous network [VI] and roughly predicting its structure on basis of that. Also zeolite structure is touched [IV].

Permeability[19] is the ability of material to transmit fluids [110]. The basis of fluid flow modeling comes from microscopic level Navier-Stokes equation describing the motion of newtonian substances. Continuing from that to the macroscopic level Hagen-Poiseuille equation gives the pressure drop in an incompressible and newtonian fluid in laminar flow through a long cylindrical pipe of constant cross section. This has then been refined to describe the flow of fluid through a porous medium showing how the discharge rate through the pores is proportional to the structures permeability, cross-sectional area and pressure drop; divided by the length of structure and viscosity of fluid. This is known as Darcy's law that for incompressible fluid in its integrated form shows the total discharge rate Q [m^3/s]:

$$Q = \frac{-\kappa A(p_b - p_a)}{\mu L},$$ when κ = permeability of the medium [m^2], A = cross-sectional area to

flow [m^2], p_b-p_a = pressure drop over the medium [Pa], μ = viscosity of the flowing medium [Pa · s], and L is the thickness of the medium [m]

2.3.2.1 Modeling permeability

Permeability of a structure can be predicted with Kozeny-Carman equation [112] that is a derived equation for fluid velocity coming from experimental modeling of voids in bulk material.

The equation is analytical and is based on Hagen-Poiseuille making an assumption that the flow goes through many parallel channels [113] that have the total internal surface equal to particle or pore surfaces. Equation has an empirical coefficient that depends on the porous path [29] and it was generated to predict permeability of a packed bed, being thus most accurate for a certain particle size distribution and particle shapes close to spheres [29] in a steady state flow [114]. The Kozeny-Carman equation shows the permeability Δp [pa] related to medium height L [m]:

---

[19] Permeability is considered to be a material property but some fluids may interact with the materials changing its permeability [110, p. 7] thus some references report "specific permeabilities" when measuring with a dedicated fluid.

$$\frac{\Delta p}{L} = \frac{180\mu}{\Phi_s^2 D_p^2} \frac{(1-\varepsilon)^2}{\varepsilon^3} \upsilon_s,$$ when μ = viscosity of the flowing medium Φ_s^2 = sphericity of the flow channels D_p^2 = diameter of flow channels ε = porosity of the medium υ_s = superficial flow velocity

In [114] the equation is refined to apply also for turbulent flow, obtaining a general equation for pressure drop through a fixed bed of different shaped material and a wide flow range. Certain analytical models have been prepared especially for fluid flow in fibrous materials but they are mostly based on simplified geometries where the fibers are considered as cylindrical rods parallel or against the flow in 2- [115] or 3-dimensions [116]. In fibrous systems the fibers are taken into account by adding their volume fractions, fiber diameter and orientation to flow [111].[20]

2.3.2.2 Washburn equation

Permeability of a structure can be used to measure its pore parameters with liquid intrusion and extrusion techniques that are both based on measuring a pressure needed to replace or displace the analyzed pores with a measuring liquid. This enables the quantification of pore sizes by using a Washburn equation that links the pressure and pore diameter with surface tension[21] and contact angle between the liquid used for measuring and the specimen. In extrusion porometry a wetting liquid with very small contact angle is used whereas intrusion porosimetry uses a liquid, typically mercury, that has a high contact angle. The Washburn equation shows pore cross-section diameter D:

$$D = 4\frac{\gamma \cos(\theta)}{P},$$ when γ = surface tension of the measuring liquid, θ = contact angle of the liquid, P = applied pressure

In the equation a circular pore cross-section and straight flow channels are assumed but linear correction factors for them can be used. [117]

---

[20] Because the models are very simplified but still need a lot of parametric information, quite impossible to obtain from the heterogeneous fiber structure, and because the function of this thesis is not to build permeability models, we are confined in the original KC-equation using it to roughly predict the flow channel-permeability -correlation.

[21] The capability of the surface to resist external force. Typically measured in dynes/cm: for water 72 dyn/cm, for wetting liquid 16 dyn/cm [117], and for mercury 486 dyn/cm.

2.3.3 Thermal measurement of permeability

In [I, VI] a fibrous structure that is very heterogeneous is analyzed using a flow of hot air through it and measuring that with a thermal camera in order to locate the areas of high permeability seen by the certain area heating faster. The method needs a small theoretical background on heat transfer in porous structures.

The following is based on a study of heat transfer in stone wool [118] which has a similar composition and structure in comparison to the one studied in [I, III, IV].

Heat transfer through porous materials in static situation takes place with four mechanisms [118]:

1. Conduction through solid medium
2. Conduction through gas medium
3. Convection due to air in pores
4. Radiation through material and pores

The importance of convection is normally very minimal, and in temperatures below 100 °C, such as in our case, the relative importance of radiation is also very small, so the both factors can be omitted. The dominating factors are conduction through gas and fibers which are found equally important to heat transfer [118] in situation where conduction through gas takes place in non-flow situation. On part of fiber conduction, it is determined by fiber orientation and the pore shape which affect the heat transfer, especially when porosity increases [119] but in order to focus on locating the local permeability we have minimized the effect of heat conduction through fibers by using a dynamic situation inducing a flow of hot gas through the media in [I, VI].

2.3.4 Permeability connection to sorption

In paper [IV] a zeolite powder was structured for more efficient CO_2-capture. The capture takes place mostly by physisorption directly from a gas flow making the efficiency of adsorption-desorption cycle important. The efficiency is retarded by intracrystalline diffusion of gas to active sorption-sites [120]. In simple, the aim was to increase the effective surface area by having a high permeability to allow large gas volumes to reach multiple adsorption sites.

The approach in [IV] was to craft oriented flow channels that have higher permeability than a simple bed of granules. The structure contained laminated walls, thin enough for rapid adsorption, and so close to each other that no surface area was wasted [87]. The replacement of powder bed with a structure that had ordered flow channels affected the

permeability by lowering the flow channel tortuosity. The effect of tortuosity is seen in Kozeny-Carman equation in subsection Fluid permeability.

2.4 Characterization of pores

The theoretical areas: effect of pores to strength and fluid flow, have now been covered and the final section of this chapter follows. The section is written to support the aim of this work: development of in situ -methods for measuring pore related factors. The functionality of these in situ -methods was ensured by comparing the results by the conventional methods presented in this chapter. The links between the methods are visualized in Diagram 11.

The section also finalizes the theoretical chapter linking the definitions of pore and porosity presented in the beginning by the methods with which they are acquired. The review is limited to characterization methods that are used to acquire the results presented in the enclosed publications.

Objective of this chapter is to give an overall description of some important methods used for characterizing pores. Aim is also to qualitatively compare the characteristics of different methods.
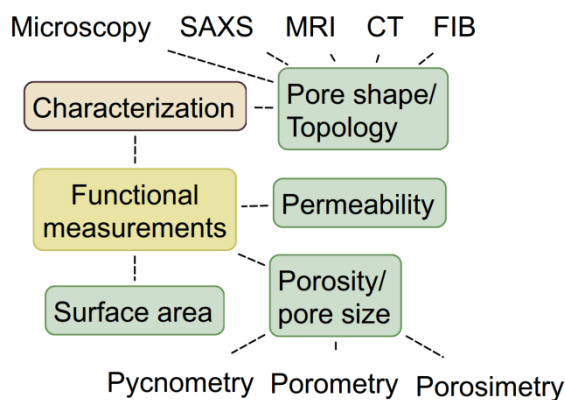
Diagram 11: Pore characterization.

2.4.1 Porosity and pore size distribution

Porosity and pore size distribution is measured indirectly with functional measurements by a priori assumption made of pore structure, i.e. assuming the pores are all cylindrical. [79]

Typical methods for measuring the distribution are mercury porosimetry and different extrusion porometers. The mentioned methods measure only the interconnected porosity but certain methods, based on diffraction or scattering can be used to gain information about the closed pores and pore structure of a sample [79]. Also pycnometrical methods such as Archimedean method can be used to measure the total porosity but it does not yield the distribution.

As various techniques measure different pore size ranges and some can measure the closed porosity as well, using multiple methods, like intrusion porosimetry, small angle X-ray scattering, and gas adsorption for pore characterization is useful in some occasions [82].

2.4.1.1 Pycnometry

Measures the volume of fluid displaced on submersion of the sample. Idea originates from Archimedes' principle with the exception that the measurement may carried out with gas, such as air [121], but the most typical procedure is to calculate the porosity simply by measuring the mass of a water saturated sample [79] minus the mass of dry sample divided by the density of saturating liquid giving the liquid volume that, when divided by sample volume, gives the sample's porosity. [81] This Archimedean method was used in [II].

2.4.1.2 Porosimetry

Porosimetry is a popular method for characterizing meso- and macroporous structures [122]. It is an intrusion method where a non-wetting fluid [122] is forced in to pores of the sample incrementally by external pressure, meanwhile recording the relation between the intruded amount and the pressure [81]. Typically the sample is first degassed to remove gas in pores that would hinder the intrusion [123]. Low external pressures fill only the large pores and progressive pressure increase fills the smaller one. Pore volume distribution can be calculated from the amount of intruded liquid [79]. By using the Washburn equation [123] also the cumulative pore diameters, mean diameter, pore surface area, based on an idealized cylindrical pore, can be derived [122], [123]. Based on the sample mass, and the density of mercury, also bulk and skeletal densities[22] of the specimen can be measured [123]. The technique is sensitive to con-

---

[22] Skeletal density is calculated from maximum mercury intrusion volume so it does not include closed pores but pores down to minimum measuring range defined by the maximum pressure that can be used [123].

tact angle between the intrusion liquid and the measured sample and because of that the most common intrusion liquid is mercury that has a high surface tension and a large contact angle with most of the materials, assuring it does not intrude the sample without external pressure [79].

Because intrusion porosimetry is based on the dynamic accessibility of liquid in to pores that is controlled by the pore opening [81] the method is known to underestimate the void sizes. This is caused by the shielded pores[23], but using a model in interpretation of the results can increase the accuracy [122]. However, the Washburn model offers no distinction between a long cylindrical pore or multiple shorter pores of the same size. Other challenges in the method are that the sample preparation (drying and air evacuation) or intrusion liquid pressure [124] may interact with sample and affect the porosity and typically the sample size is very small. Mercury porosimetry was used in [II, VI].

2.4.1.3 Porometry

Porometry[24] is a method where a low surface tension wetting liquid is let to spontaneously fill the pores of a measured specimen followed by its extrusion from the saturated specimen with a gas pressure induced from one side. In the measurement of saturated wet sample, no flow takes place until the biggest pore releases the liquid and bubbling point is reached. Progressively smaller pores are emptied and gas flow increases till the earlier measured dry and wet curves converge, showing all the pores are empty.

To determine the distribution of interconnected pore throat diameters Washburn equation [123] is used. From the wet curve a largest through pore is calculated from the initiation of flow, while mean flow pore size is determined from the intersection of half-dry curve[25] and wet curve, and smallest pore is calculated from the intersection of dry and wet curves [125].

Porometry typically exaggerates the number of smaller pores and mostly omits the shielded pores rendering the method more applicable for measuring samples, such as filters, whose flow channel size is the most important. [122] Only the pores smaller than

---

[23] Such as those shaped like an ink bottle but rather a large network of pores that is interconnected with a small opening. [160]
[24] Also known as extrusion porometry or flow permporometry.
[25] Mathematical half of the dry curve

bubble point[26] can be determined and the method is similarly sensitive to how the wetting liquid interacts with the sample as porosimetry. [122] Extrusion porometry was used in [II, VI]

2.4.2 Permeability

Measurement of permeability or permeametry can be carried out with various ways, for example as in ASTM standard [126]. The methods can be classified according to the fluid that is used. With gas challenges arise from its compressibility and with liquids from their susceptibility to interact with the measured material.

Basic principle in measuring is that a fluid is ejected through porous material with different flow rates meanwhile measuring the pressure drop over the sample. [79] Using Darcy's equation the permeability can be calculated.

Also estimates of porosity, mean pore or particle/fiber size, or specific surface area, can be derived from the measurements by applying derivatives of Kozeny-Carman function. Both are done in [VI].

2.4.3 Pore shape and topology

Pore shape and topology is difficult to address with functional methods presented earlier, though some information on that can be received by comparing the same sample with intrusion porosimetry and extrusion porometer or modeling permeability to give some indication on the tortuosity of the flow channel.

Also careful analysis on physical sorption-isotherms, a technique not presented in this thesis[27], can give information on pore shape [127]. Yet, direct measurement of pore shape and connectivity is carried out by microscopy techniques that offer a high resolution with the cost of losing spatial information. Measuring the pore size from two dimensional image typically underestimates it because the 2d-slice often does not go through the widest part of the pore. Also the pervasiveness and thus the representativeness of the method cannot be ushered [81].

---

[26] The point at which the first and the largest flow pore opens.

[27] The gas adsorption was not used because most of the effective pore sizes in this thesis are in micron-level whereas the method is most suitable for measuring sizes below 200 nm [120].

More pervasive methods that also offer topological information on the structure have a lower resolution in comparison to microscopy. These techniques are such as computed tomography [128], magnetic resonance imaging [128], small angle x-ray scattering [129], and focused ion beam scanning electron microscopy [122]. Also the modern high-resolution electron microscopy has been used to measure structural features such as pore shape and connectivity [130]. Most of these techniques, that for characterization in materials science are relatively new, are delimited with small scanning volumes and long measuring times. Although computed tomography and magnetic resonance imaging was tried they were found non-suitable for the samples that in most of the cases had spatial variation and could not be measured in large volumes.

In the enclosed articles [I, IV, VI, VII] analytical techniques were used to quantitatively measure properties of micrographs obtained by scanning electron microscopes or thermal camera.

2.4.3.1 Image analysis

In [131] image analysis is defined as "the set of computer processes designed to codify a real image, to recognize the most interesting elements, and to highlight the necessary information". The purpose of image analysis is to quantitatively analyze micrographs [122]. It is useful when analyzing a large set of details in multiple images when doing this by hand would be too time-consuming and tedious or even impossible [132].

Images can be analyzed in 2- or 3-dimension, in grey-scale or in color and the capabilities of analyzing them are diverse [133]. Maybe the most abundant possibility, also abused in the enclosed articles [I,IV,VI], is the feature extraction where a quantified and meaningful features are extracted and numerically presented from an image [132]. Such a feature can for example be pore length [IV] or spatial pixel intensity correlating with temperature [VI].

The process of image analysis is confined in four steps that are completed with different methods beyond the topic of this thesis, the step are [131]:

1. image acquisition: carried out e.g. with a microscope and a camera,

2. image processing: typically using filters to remove artifacts or to highlight specific image characteristics,

3. image segmentation: identification and isolation of pixels belonging to same category, and

4. feature extraction.

Methodological measures have to be used to [131] ensure that the image size can be compared to the structure and spatial position, and in homogeneous materials the observation scale has to be set according to observed feature: pixel size small enough to detect finest details but magnification on the level for comprehensive analysis.

3 Main experimental procedures and sample materials

The following is a standalone chapter shortly visiting some of the methods and devices used in the enclosed articles. Not all of them are presented, only those that were used in more than one article or were notably important from the aspect of characterization of pores and porosity. The chapter is divided into three sections of which the first one 3.1. Conventional characterization methods presents the common commercial methods that were used, the second 3.2. In situ -characterization methods present in-house crafted in situ -measuring methods, and the third 3.3 Sample materials used in testing the characterization methods, describes the materials that were used to test the in-situ methods.

The aim of the whole chapter is to give a general understanding on the devices and parameters that were used to run them in the experiments on the enclosed articles. The reader is referred to study the enclosed articles for mode detailed descriptions. Diagram 12 recaps the methods and materials presented in this chapter.

Main experimental procedures and sample materials in the thesis
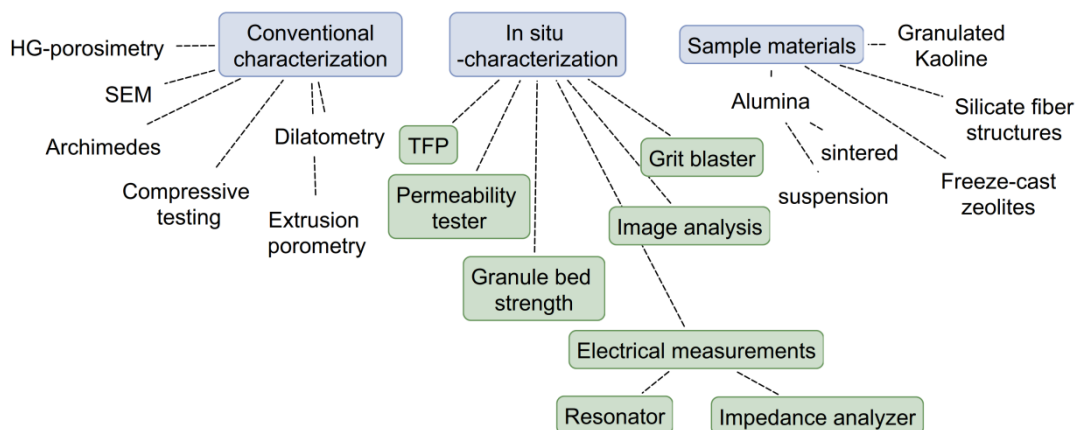
Diagram 12: Experimental procedures and Materials.

3.1 Conventional characterization methods

The following describes the most important commercial characterization methods that were used in the enclosed articles. The chapter has sub-chapters withholding microscopy and mechanical testing; pore parameter analysis by archimedean method, mercury porosimetry and extrusion porometry; and finally a description on thermal analysis by dilatometry.

3.1.1 General Characterization

3.1.1.1 Scanning electron microscopy

All the related microscopical analyzes in [I-VII] were carried out with scanning electron microscopes. Models that were used were Jeol JSM 6360LV, ULTRAplus; Phillips XL-30; Carl Zeiss Microscopy GmbH (Germany); JEOL JSM-7001F (Jeol Ltd., Tokyo, Japan); Hitachi Analytical TableTop Microscope TM3000 (Hitachi High-Technologies Europe GmbH, Krefeld, Germany).

Prior to imaging, the specimens were prepared by cutting them with suitable tools or pouring a suitable amount of powder on to a conductive adhesive, and enabling electrical conductance from top of the sample to the sample holder using conductive carbon cement or copper tape and coating the analyzed surface with carbon or gold using an evaporator or a sputter. Some samples were also analyzed using Energy-dispersive X-ray Spectroscopy coupled with the electron microscopes.

3.1.1.2 Mechanical testing devices

Compressive materials testing was used in [III, IV, VII]. Testers that were used in the measurements were Instron 5967 universal testing machine (Instron, Norwood, MA, USA) and Instron 4505 (Instron Industrial Products, England).

With the devices a load cell having a maximum capacity close to the measured strength was used when possible to improve accuracy. The compressive testing was carried out with suitable tools, for instance the granules in [VII] were compressed with a jig presented in subsection Granule bed compression.

3.1.2 Functional pore characterization

3.1.2.1 Archimedean method

The density and porosity of sintered ceramics were determined by Archimedes method in [II]. This was performed according to ASTM standard [134]. In the standard a specimen is first dried to constant mass and weighed, then saturated by boiling and soaking in water, and weighed under water, and finally in air. The above weights are used to determine the porosity and density.

3.1.2.2 Mercury porosimetry

In [I; VI] the pore volume distribution was measured with Micrometrics poresizer 9320 (Micromeritics Instrument Corporation, USA). In the method a small specimen was first dried and then placed in to a measuring chamber that was filled with mercury. Pressure in the chamber was first decreased to evacuate air and then mercury was introduced and pressure increased and the volume of intruded mercury was measured so that the corresponding pore volume could be calculated. [123] The applied measuring range was up to 200 MPa that is equal to 0.006 um pore size.

3.1.2.3 Extrusion porometry

In [I; VI] a capillary flow porometer (Porous Materials Inc., Ithaca, NY, USA) was used to measure the size of flow pores. The measurements were carried out at Porous Materials Inc[28]. headquarters where the filter element specimens' dry and wet flow rates with respective pressures were measured to calculate the corresponding pore throat

---

[28] Porous Materials Inc. Analytical Services Division. 20 Dutch Mill Rd. Ithaca, NY 14850, USA.

diameters [120]. In the measurement a wetting liquid (Galwick, surface tension 15.9 dynes/cm) was used to infiltrate the specimen and tortuosity factor of 0.715 was used to correct the pore size. Depending on the specimen a maximum pressure from 46-60 kPa correlating to a 1.0-0.8 um pore throat diameter was used.

3.1.3 Dilatometry

In [III, VII] a dilatometer (Model DI-24, Adamel Lhomargy, Roissy en Brie, France) was used in dynamic mode to measure length changes caused by temperature.

In a dilatometer measurement a specimen cut or compressed into shape of a cylinder with approximately 20 mm in length was placed between a measuring rod that followed the change in the specimen length with respect to temperature. After omitting the thermal expansion caused by the measuring rod the results were plotted with temperature against relative length, and e.g., sintering behavior (initiation temperature and extent) could be analyzed.

3.2 In situ -characterization methods

Having described all the commercial methods used in more than one of the enclosed articles in the following all the in situ measurements developed in-house and presented in the enclosed articles are described.

3.2.1 Grit blasting

In [III] a grit blasting test was devised to gain more understanding about the rigidization of ceramic fiber structures. In the test, momentum of round 150 - 250 µm glass grit was adjusted by controlling the feeding pressure so that it eroded a reference sample at a moderate rate. The erosion was caused by the grit breaking the fibers.

In the method a specimen was placed at a 90° angle towards a grit blaster (model FG Ghiotto 28HSS with a bottom container) that was used to eject glass grit for 5 seconds to erode a crater on the sample. Feeding was smoothed with a vibrator and the depth of the grater was measured using a sliding gauge to observe differences with specimen that had varying thermal histories. A schematic drawing of the method is shown in Fig. 10.
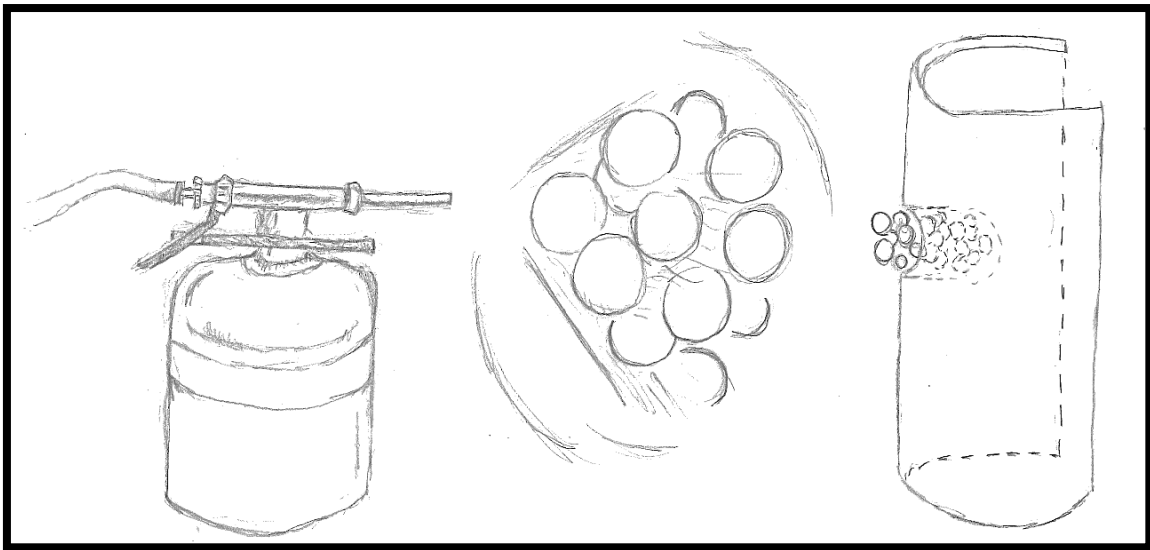
Figure 10 Sketch of grit blaster.

3.2.2 Permeability

In [VI] in-house designed conventional permeameter was used to link the thermal per-meametry results with permeability. The device had a gate valve for adjusting a laminar filtered flow that was measured with a flow velocity meter (Schmidt SS30.302, SCHMIDT Technology) while recording the pressure difference over the specimen with a manometer (DP measurement TT570SV, UK) connected on the sub-pressure side. Total measuring error of the unit was experimentally found to be 10 percent of the reading.

With the device, permeability was measured by drawing air through the component while the pressure drop over the studied specimen was changed in steps adjusting it with the gate valve. The measured flow velocity was divided by the specimen's outer surface area to calculate facial velocity, independent of component size. A schematic drawing of the method is shown in Fig. 11.
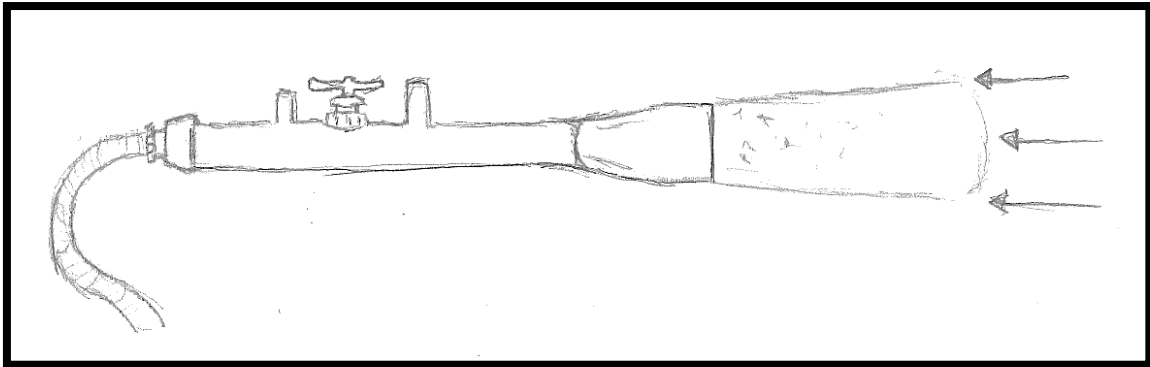
Figure 11 Sketch of sub-pressure tester.

3.2.3   Thermal flow permeameter

A thermal flow permeameter (TFP) whose development was the focus in [I; VI] consisted of a thermal camera (FLIR Thermacam PM595, FLIR Systems, Inc., USA), a length scale made of metallic rods that are visible in IR-images, and an adjustable gas inlet able to feed air up to 2000 l/min. During the measurement, air at 25 °C was let to flow through a heater and finally through the monitored specimen. The heater unit could be heated up to 400 °C but 100 °C air was mostly used with an average face velocity of 5.5 cm/s which in combination caused the specimen to heat between atmospheric temperature and 70 °C depending on the local permeability. A schematic drawing of the method is shown in Fig. 12.

The resulting thermal images were analyzed with ImageJ as explained in the subsection Image analysis.
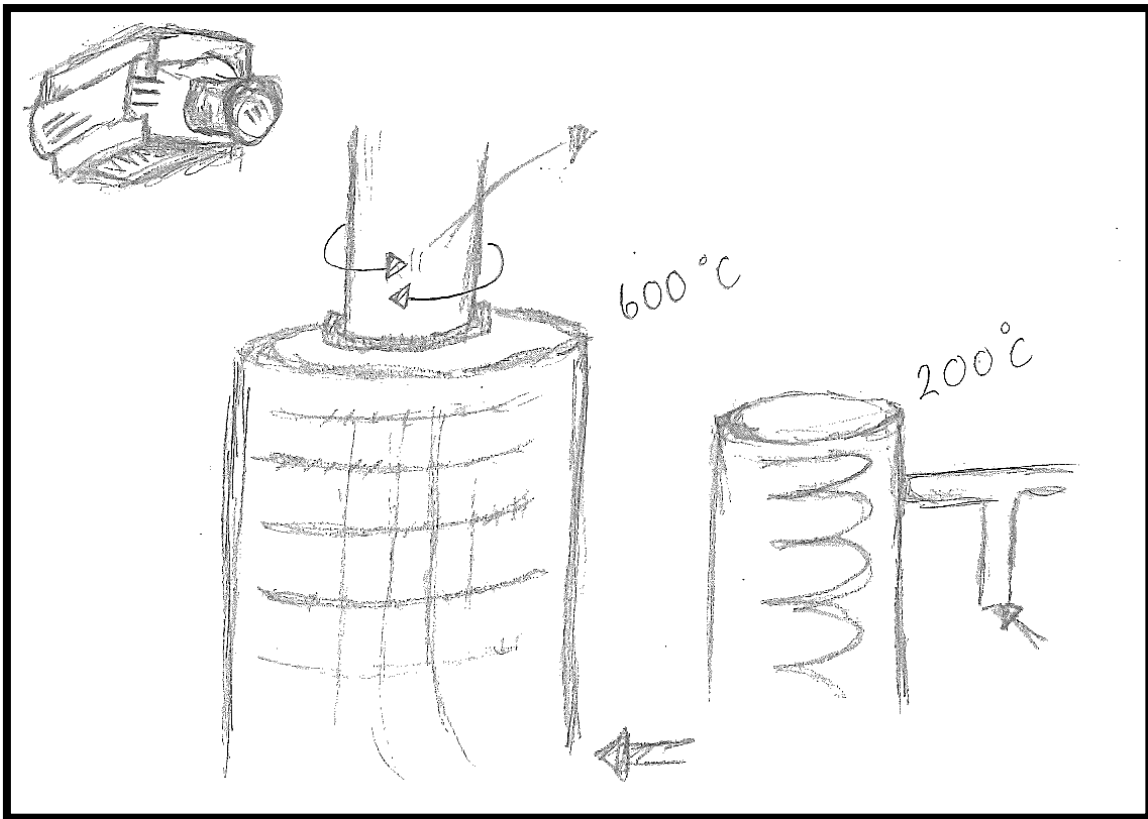
Figure 12 Sketch of Thermal flow permeameter.

3.2.4 Image analysis

To analyze images of thermal camera in [VI] and granules in [VII] a freeware application, ImageJ, was used but for pore parameter analysis in the publication [IV] a special algorithm was coded in an MSc thesis by Masi Valkonen [135].

3.2.4.1 Thermal image analysis

The thermal images were quantified using the following approach. The images, in which the temperatures were exhibited as brightness variations, were converted to gray scale and their gray value[29] was calculated with image analysis software, ImageJ [136]. Thus, the gray value could be related directly to the surface temperature of the imaged component and when using the external scale, the selected point or a selected area could be identified.

---

[29] A unitless indicator of the luminescence, or brightness, of a pixel varying from 0 (black) to 254 (white).

3.2.4.2 Granule size and relative density

In [VII] the SEM-micrographs of polished cross sections of granule specimen were analyzed to find out if the two size ranges of granules had a different shape or apparent density. To do this a baseline image was converted in to binary with automatic thresholding, and the granules were sectioned according to cross-sectional area using an algorithm provided in ImageJ. Then the average circularities[30] and aspect ratios[31] of the sections were analyzed omitting the granules reaching over the image borders. The intragranular apparent density was estimated from SEM-image by similarly sectioning the size fractions and measuring the average gray values[32].

3.2.4.3 Pore characteristics analysis

In [IV] the effort was to link pore parameters such as pore area, alignment and roundness with the compressive strength of a cellular structure. This was carried out using an adaptive algorithm that first converted a grayscale SEM-image into a binary one containing empty pores and dense walls. Then using morphological dilation[33] any unrealistically small features and noise was removed, and an algorithm for a principal component analysis was used to find the main axis and the center point of the pore. Orthogonal major and minor axes were then calculated from the pore center point, and used to draw ellipsoids for each pore in order to quantify the cross-sectional pore width, pore area, and pore aspect ratio.

3.2.5 Granule bed compression

In [VII] a special tool was used to measure a bed strength of rigid granules. The granules were compressed with linear plate heads with a uniaxial compression tool. The apparatus consisted of a top punch, bottom punch and a cylindrical die, with a diameter of 19.5 mm, where the tested material was poured. The moving surfaces of the tool were first sprayed with silicone and wiped to control wall friction. The mechanical yield of the compression tool in the studied range up to 10 kN was negligible. A schematic drawing of the method is shown in Fig. 13.

---

[30] $4\pi \times$ [Area] / [Perimeter], unity resembling a perfect circle

[31] Longest diameter / shortest diameter, unity resembling a perfect circle

[32] the sum of the gray values of all the pixels in the selection divided by the number of pixels

[33] Dilation signifies the procedure in which a value of output pixel is changed to the maximum value of all the pixels in the input pixel's neighborhood.
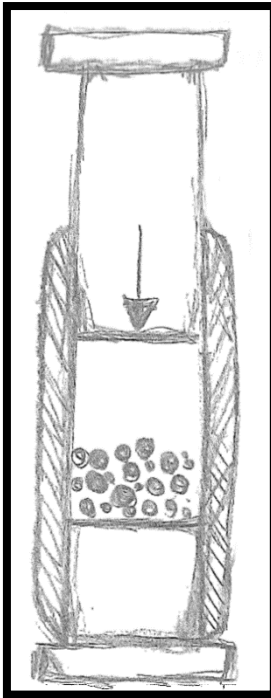
Figure 13 Sketch of compression tool.

3.2.6 Electrical measurements

Electrical devices were used to quantify porosity in sintered aluminum oxide by an impedance analyzer using a maximum-length binary sequence signal [II]; and to measure electrical response of particulate suspension using a resonator [V].

3.2.6.1 Impedance spectroscope

The method for measuring porosity was based on the electric frequency-response where the analyzed specimen was placed between capacitor plates so that it changed the permittivity of the capacitor thus porosity changes in dielectric ceramics affecting their relative permittivities changed the system's frequency response.

The system was built on National Instrument's PCI-6052E measurement card that was used to send and measure an excitation and to receive the output signal. The system consisted of a 1-MΩ resistor and a capacitor that formed a first-order low-pass-filter[34], whose output was buffered with an amplifier.

---

[34] A low-pass filter is a filter that passes signals with a frequency lower than a certain cutoff frequency and attenuates signals with frequencies higher than the cutoff frequency.

The capacitor was designed to fit a 12 mm thick ceramic specimen between the 3x3 cm electrode areas on both side made of circuit board material. A ground plane on top of the specimen and under the electrode area, on the other side of the capacitor plane, made the total capacitance of the system to include that of the capacitor plus the constant stray capacitances of the system.

The input signal was in the form of maximum frequency binary sequence [137] with a length of 16,383-bit, having an amplitude of 1 V. The sampling rate was 100 kHz. The input signal was injected into the system four times and a cross-correlation function was used to compute the frequency response. To eliminate transience and reduce deviation in the measurements, the frequency response was calculated from the mean of the last three of those signals and their responses. A schematic drawing of the method is shown in Fig. 14.
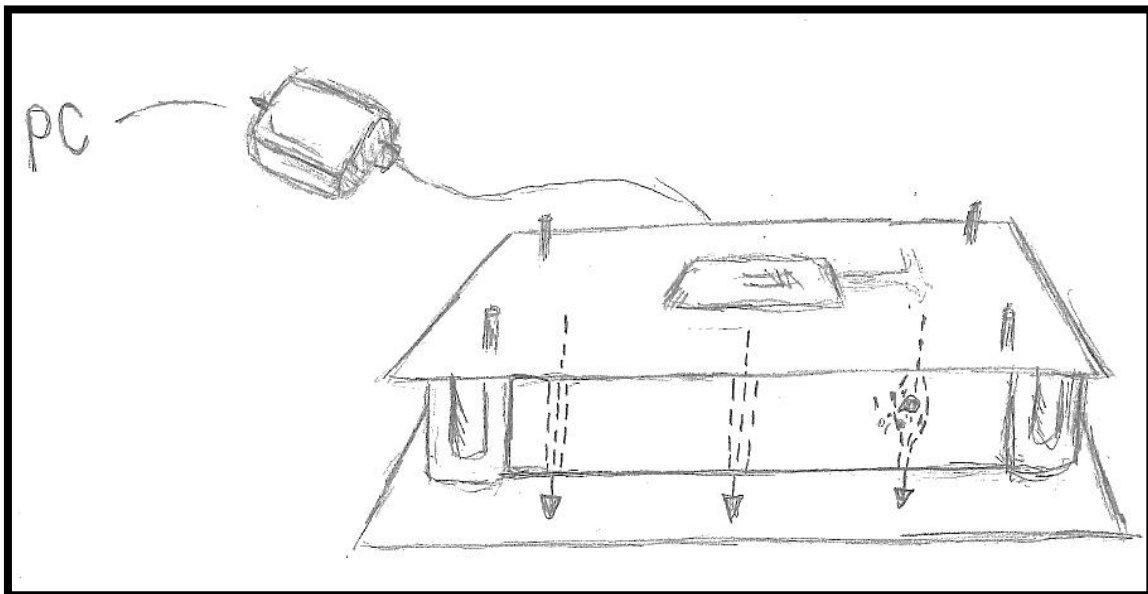
Figure 14 Sketch of impedance analyzer.

3.2.6.2 Resonator

The method of measuring electrical response of a colloidal suspension was based on a resonator that had an inductor (coil) - capacitor circuit i.e. LC-circuit that was made of a 7 μm thick etched aluminum pattern that was laminated between two 80 μm thick PET films. The pattern included a rectangular coil with three turns and two rectangular 1 cm^2 surfaces forming a parallel plate capacitor as the laminated film was folded in two and glued together. The capacitance and the resonance frequency are sensitive to permit-

tivity changes making it possible to measure materials brought into close proximity of the resonator.

To measure suspensions, the resonator circuit was embedded in the bottom of a glass container and measured by a one-turn reader coil under the container. The reader coil was connected to a measuring device with a coaxial cable and the measurement was carried out with an in-house reader device that generated the excitation and reference signals. The excitation signal was fed to the reader coil and compared against the reference. The resonator measured the magnitude ratio or gain/loss and the phase difference between two inputs yielding a resonance curve peaking at a frequency defined by: the sensor material, design, and the surrounding materials (specimen). The permittivity of the measured specimen altered the position and shape of the resonance curve. A schematic drawing of the method is shown in Fig. 15.

The measurements were done by using a 2000-point frequency sweep, ranging from 70 MHz to 90 MHz, the sweep was repeated twice per second. By using this configuration in the selected frequency range, it was possible to measure materials whose permittivity ranged from air to water.

A feature extraction process was used to capture the essential information from the measured gain response curves consisting of gain values at discrete frequencies. Polynomial regression was used to describe the shape of the curve in order to locate essential areas linking the changes in the curve to characterized features. Two baseline ripped features were extracted from a polynomial model: a frequency and a bandwidth of a dip in the resonance curve. First feature was strongly affected by the relative permittivity of the specimen and the other was linked with dielectric losses.
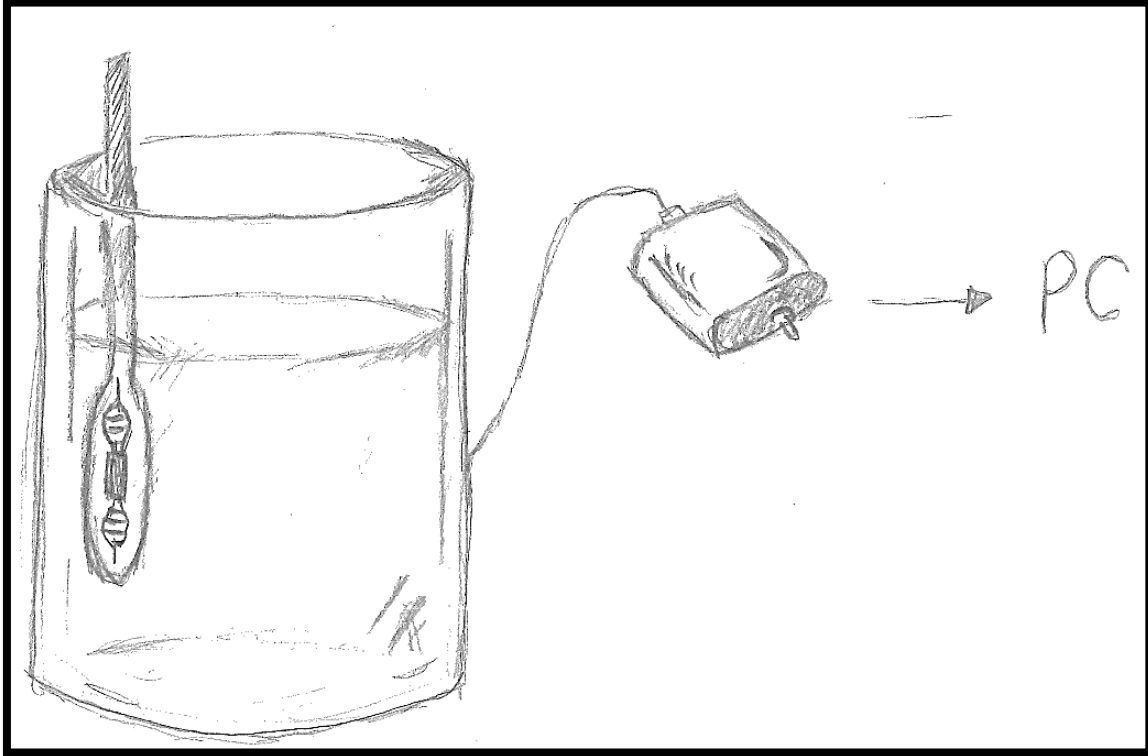
Figure 15 Sketch of resonator.

3.3 Sample materials used in testing the characterization methods

This chapter describes the materials that were used to test the in-situ measuring methods.

1. The publications I, III and VI had the same silicate-based fiber structure used for hot gas filtration,
2. material used in IV was zeolite 4A that was freeze-cast to achieve structured flow channels.
3. The aluminium oxide suspension in V was the base used for slip casting the sintered aluminium oxide pieces in II.
4. The granules tested in VII were made of kaolinite.

3.3.1 Silicate fiber structure I/III/VI

The structure that was tested in I, III and VI was composed of non-oriented fibers with improperly molten material at the tips of some of the fibers. The fibers were composed of amorphous alumina silicate with crystalline regions of alfa-alumina as the main

phase. Composition of the fibers given by a manufacturer, and supported by our analysis, as 45–60 weight percent SiO_2 and 40–55 weight percent Al_2O_3. The fibers were bound together with silica. Fiber diameters varied at 1-10 um while the diameters of improperly molten parts at the tips of the fibers varied from 10 um to 300 um. Fiber lengths varied from 100 um to 800 um. Mean flow pore size and the average pore size were both 4 um, indicating all the pores in the average range go through the structure. The largest flow channel was 39 um in diameters, and open porosity was 80 percent. Thermal diffusivity was 0.3 mm^2/s.

A representative image of the structure can be seen in subsection 2.1.3.3.

3.3.2 Freeze-cast zeolite structure IV

Freeze-cast structures in IV were prepared at Stockholm University by Dr. Arto Ojuva with a method presented in [138]. The area covered in this thesis was their compressive strength and how it changed as a function of pore parameters which varied as the cooling rate of the freeze casting apparatus was changed.

"Composite monoliths with a lamellar porous structure were prepared from aqueous suspensions of zeolite A, bentonite and polyethylene glycol (PEG). The suspensions were frozen unidirectionally, starting from the bottom of a cylindrical die that was set to cool at a constant rate. After freezing, the ice was sublimed in a freeze-dryer and the remaining compact powder body was thermally treated to obtain a mechanically strong monolith with a continuous and directional porosity" [IV]

A representative image of the structure can be seen in subsection Porosity in porous crystals.

3.3.3 Aluminium oxide suspension and sintered aluminium oxide V/II

In publications V and II aluminium oxide suspension (slurry) was prepared. In V its solid and dispersing agent content was analyzed with a resonator. In II the suspension was slip cast and then the cast pieces were sintered at different temperatures to gain varying pore structures to test an impedance analyzer.

3.3.3.1 Suspension

Suspensions were made of Al_2O_3 powder, deionized water, and dispersing agent. Dispersing agent was first mixed with water and then alumina powder was added to the mixture in small increments. The alumina powder had a particle distribution between 0.1 um and 3 um. Suspension with discrete intervals of dispersing agent and particle

amount was tested. The final viscosity of the suspension measured at the shear rate of 10 1/s was 1.2 Pa s. The tested suspensions were shear thinning.

A representative image of the suspension preparation and online resonator measurement can be seen in subsection Electical measurements.

3.3.3.2 Slip casting and sintering

The suspension for slip cast pieces was prepared as described above but after homogenizing the dispersing agent-aluminum oxide -suspension a binder was added to increase pre-sintering strength of the component and polyethylene glycol was stirred into the slip to increase processability. The prepared suspension was poured into a gypsum mold, where the solids compacted to the mold walls as water was removed by capillary action. The compacted pieces were dried before pre-processing after which the pieces were sintered at different temperatures to gain varying pore structures.

A representative image of the structures after different sintering temperatures can be seen in subsection Porosity in partially sintered ceramics.

3.3.4 Granulated kaolinite VII

In VII we tested a common industrially spray-dried granulated kaolinite powder that was received in a non-sintered state and heat-treated in different temperatures to achieve comparative test materials. Average size of the granules was close to 40 µm. Based on image analysis granules above 45 µm were less round than granules below that but both fractions appeared equally dense when examined from cross sectional cuts under a scanning electron microscope.

A representative image of the studied granules can be seen in subsection Porosity in partially sintered ceramics.

4 Comparative summary of the results of the articles

In the following, the results collated from the enclosed articles [I-VII] are presented from two perspectives. The first section views the results as comparative value analysis of in situ measurements by first making its way to each methods and then contrasting them, as developed in the enclosed articles, with their laboratory counterparts. In other words, the chapter is written from the practical angle to demonstrate the special capabilities and uses of the new methods. The content of this chapter is visualized Diagram 13.

Although the articles contribute mostly to new applications in industrial characterization, some fundamental discoveries were also made about pores, porosity, and their effects on materials.[35] They are discussed from the materials science perspective in section 4.2. on Pore and porosity related findings.

---

[35] By accident.
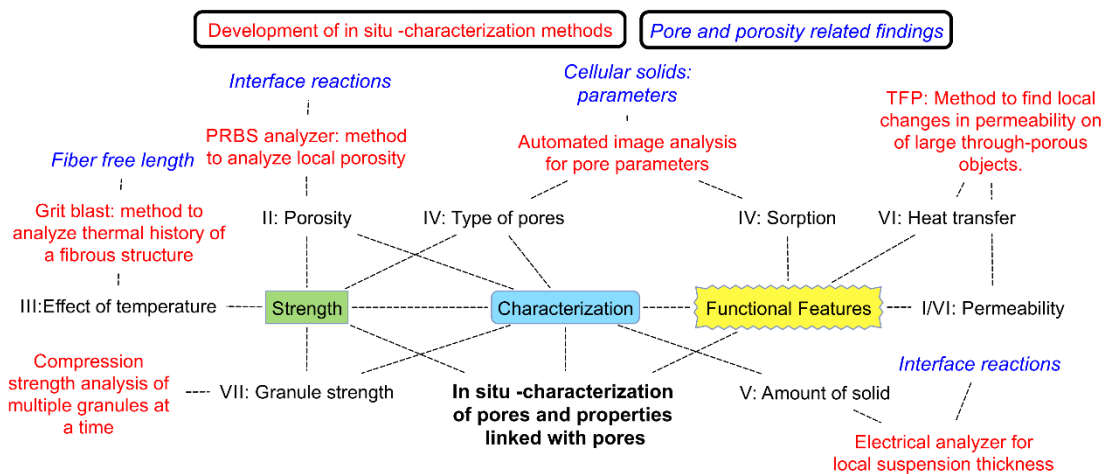
Diagram 13: Comparative summary.

4.1 Development of in situ characterization methods

The main results in the enclosed articles, except [IV], were used for in situ analysis and defined to analyze the properties of pores or pore-related functional features. The objective in [IV] was to understand the compressive strength of a porous structure with well-defined pores. The task was carried out with an imaging method similar to that used in [VII] with its attributes aimed at in situ.

The following summarizes the results of the enclosed articles one by one from the industrial angle. For coherent discussion, the summary is structured so that it first presents the relevance of each characterization method[36] from the system approach angle[37] presented in Research Approach, then proceeds to the concrete aims of the methods, and finally compares a laboratory relative to the industrialized method and simultaneously introduces the novelties of the new methods. The next section focuses on the contribution of the articles to materials science.

As discussed in chapter 1 (Lean, in situ measurements and this thesis), in situ characterization must be

     1. robust,

---

[36] Note that understanding the relevance was part of the results.

[37] Find a material parameter, determine the tracking and reference parameter, and design an industrial characterization method.

2. integrable/on site,
3. reliable, and
4. comprehensive.

These features are separately compared with a corresponding laboratory measurement.

In subsection 1.3.3. (Specific challenges and research questions in the thesis), the research topics of each publication were described from the in situ perspective, as below in table 2. Answers to the questions are individually given in the following subsections.

Table 2: In situ development aspects in the enclosed publications.

Sub-chapter	Development aspect
4.1.1. Thermal flow permeametry I/VI	Permeametry can be used to analyze local variation in a sample, but it is very slow and difficult to integrate.
4.1.2. PRBS Porosity analyzer II	Porosity measurement with the Archimedean method or intrusion porosimeter method is laborious and slow and does not reveal closed porosity. A faster and integrated method is needed.
4.1.3 Grit blaster for fiber structure thermal history III	Thermal history can be measured from a millimeter size sample with a dilatometer, but hardly at all in local rigidization in a large sample. A new in situ method is needed.
4.1.4 Automatic pore parameter analyzer IV/VII	Pore structure can be characterized from a microscope image but for quantified data with samples with many pores, analysis must be automated.
4.1.5. Non-contact suspension analyzer V	Flocculation, especially in thick suspensions, must be measured with laboratory devices; long response time is not possible in lean production.
4.1.6. Granule strength measurement VII	Single granule strength measurement is not feasible/possible. In industrial production, a robust, comprehensive and rapid method is needed.

4.1.1 Thermal flow permeametry I/VI

Relevance

In our industrially funded project, fiber structures were previously analyzed by measuring the total pressure drop over the structure, but it was soon discovered in [I] that the structure had local variations in permeability, which affected flow properties through the structure. Later, the mechanical properties were also found to differ locally [III], and

local variation in permeability was recognized as the most significant variable for a tracking parameter for the outlined features.

Evidently, a permeameter could not be used to measure local permeability, because measurement had to be carried out by blocking and unblocking the structure, which would have been very laborious. The permeameter was chosen as a reference method, and a thermal flow permeametry (TFP)[38] was developed.

Aim

The focus of TFP was to locate a difference in local permeability in a structure with permeating porosity. Articles [I, VI] showed that this can be done with the simple approach of measuring how a hot air flow heats the surface of a structure.

A particular difficulty in this case was that conduction through fiber and gas are equally dominant in heat transfer [118]; however, we wanted to measure only conduction through gas and thus link it with the permeability of the structure. We achieved this by choosing the correct measuring parameters and assuring that conduction through fibers could be ignored.

The method aimed at quick analysis of hot gas filter elements whose permeability was not always even due to inexact manufacturing or patchy cleaning [139] during use.

Laboratory counterparts of the method

The method's closest laboratory counterparts are different permeameters, such as those in [126]. The principle of permeameters is presented in subsection 2.4.2 (Permeability), but, in short, permeability is measured by drawing or pushing fluid through a specimen while the pressure difference caused by the specimen at a specific flow velocity is measured. If permeability is needed over a certain section of the specimen, the other areas must be blocked or a device such as the miniporopermeameter [140] must be used.

In addition, extrusion porometers and intrusion porosimeters are sometimes used for similar purposes, although they aim at quantifiable results with hundred-fold smaller specimens.

---

[38] A method called thermoporometry [161] should not be confused with TFP.

Comparison

The research problem and reason for developing TFP was that "permeametry can be used to analyze local variation in a sample, but it is very slow and difficult to integrate." The following compares the characteristics of TFP to its laboratory counterparts.

Robustness

A thermal image can be acquired from a distance, thus increasing work safety. This does not need human involvement and no hazardous substances such as mercury. The method is robust because it is simple and because it uses only a thermal camera and hot air flow.

Integrability

Furthermore, the method is non-destructive in contrast to a mercury porosimeter or extrusion porometry, which may require glue to clamp the sample. Moreover, methods that use liquids cannot be used with certain specimens.

TFP is quick, though the intention in the articles was not to optimize time, it took only 40 seconds per measurement,[39] which facilitates integration into a rapid production process. Methods such as mercury porosimetry or extrusion porometer take several minutes for measure a sample plus time to prepare it.

The method can be fully automated, and if hot air must anyway be pushed through the structure,[40] it can be synergistically implemented with production only by adding thermal imaging to the process.

Reliability

Air, being a fluid used for measuring, gives more functional results in certain applications, such as hot gas filter elements. This is due to the specimen's possible reactions with liquids, should they be used in the measurement.

Air pressure is the only variable in the process. Other than that, the method has no consumable parts which increases its reliability.

---

[39] This could be cut down even further if necessary.
[40] For instance, to release the component from a mold.

The method can measure large material volumes, as shown in our measurement, in which we used over a 2-m tall component with an outer dimension of 0.15 m. In comparison, mercury porosimetry uses samples in a size range of one cubic centimeter. [128]

The TFP method can locate differences in permeability in a single measurement through the whole structure, whereas the conventional methods require multiple sample analyses or blocking of certain sample areas, and the miniporopermeameter is capable of characterizing only the surface.

4.1.2 PRBS Porosity analyzer II

Relevance

Heat treatment temperature and the duration of sintering together with the initial composition and grain size affect the evolution of the porosity of a structure, which in turn affects the strength and functional properties of porous ceramics. Porosity is thus a significant material parameter, but typical methods, such as Archimedean or mercury methods, which use water buoyancy or liquid intrusion as the tracking parameter, are not industrially feasible, though they could be used as a reference.

Electrical capacitance, a tracking parameter quicker and more non-destructive than the above, was chosen, and an in situ method was developed to measure it.

Aim

In porosity analysis, the focus was to find an in situ method that could be used for non-destructive analysis of the total porosity of a ceramic component. Article [II] shows how an in-house built capacitive measuring device, which used a pseudo-random binary sequence, could distinguish components whose total porosities were 3, 18, and 33 %.

During its development, the method had no dedicated application; it was developed in general to analyze changes in porosity in different manufacturing steps, such as sintering, or to analyze the density of, e.g., mining filters.

Laboratory counterparts of the method

The method's closest laboratory counterpart is the Archimedean method, which was used to certify the functionality of the electrical method. In addition, mercury porosime-

try is related but aims at more quantifiable results. Both related methods are presented in subsection 2.4.1 Porosity and pore size distribution.

Comparison

Measuring porosity with the Archimedean method or the intrusion porosimeter is laborious and slow and does not reveal closed porosity. Therefore, a faster and more integrated method is necessary.

Robustness

Electrical sensors can be built on nearly any non-porous, electrically insulating material. Only the electrodes must be exposed to the outside atmosphere.

Integrability

A specimen is measured by placing it between two electrode plates and measuring it for a couple of seconds. The procedure can be automated and the plates integrated, e.g., into the transfer clamps used to move the product. With a pseudo-random binary-sequence signal, measurement can be done in a couple of seconds compared to a regular frequency sweep, which can take minutes. This enables integrating the measurement into rapid production flow.

Measuring porosity with the Archimedean method takes more than 30 hours according to the standard in [134], with at least an hour of direct labor time, which renders the method unsuitable for in situ measurement. Mercury porosimetry uses a toxic fluid and applies high pressure to the specimen and thus cannot be considered an in situ method at all.

Reliability

Our method is currently in its early stages of development, but it is expected to measure the whole porosity by analyzing the total permeability of the sample. Air in the pores lowers permeability, but also water may interact with the specimen. These effects can hopefully be counteracted in the future by changing the measuring frequencies so that the specimen need not be dried and that the original specimen can be measured without evacuation or submersion in liquid. However, [124] questions whether the mercury porosimeter measure the original structure or an altered sample that may have been changed in preparation or during measurement. Furthermore, mercury porosimetry calculations are based on cylindrical ideal pores, which commonly leads to underestimation of pore size [141].

Our method could give information of a 5 cm x 5 cm x 1 cm specimen and could probably be scaled to measure larger components. In contrast, mercury porosimetry is limited to a maximum of not more than about 1 square centimeter [141] specimen size.

4.1.3 Grit blaster for fiber structure thermal history III

Relevance

Fibrous structures, studied in [I, III, VI], are known to rigidize in use at high temperatures. Regardless of the reason, rigidization limits the life time of fibrous structures, and as it takes place locally and in seemingly random areas, a method was needed for in situ analysis. We hypothesized that rigidization was caused by fibers sintering to each other, and because of that material elasticity was chosen as the relevant characteristic to be studied. Rigidization was studied by mechanical testing and resonant frequency damping analysis but these techniques were not sensitive to rigidization. XRD could show when amorphous fibers crystallized, but rigidization started before that. Finally, grit blasting turned out to be sensitive to elasticity changes.

A grit blast, adjusted to break only fibers of low elasticity and thus cause deep dimples in rigidized structures, was seen to link with the reference sample's heat treatment temperature and dilatometer measurement, which were chosen as reference measurements. Dimple depth was chosen as the tracking parameter.

Aim

The grit blaster was designed to be a method that could easily be applied on site to quickly scan a large area of a fiber structure to determine if it had sustained temperatures beyond its thermal tolerance. The method was based on the idea that the rigidization of a fiber network causes the same grit flow to create deep craters in a specimen that had sustained high temperatures.

The method was needed for quick in situ analysis of hot gas filter elements, which had to be changed at the end of their life cycle. Initially, the method had been used to analyze samples from a lot where changes signifying the end of an element's life time were seen only in certain areas of the filter element, but which were impossible to detect with methods that could analyze only a fraction of the total specimen volume.

Laboratory counterparts of the method

The closest laboratory counterpart was a dilatometer experiment, which I had also developed at TUT, and which could also estimate the highest temperature to which the specimen had been subjected. A dilatometer measures the initiation point of sintering. In the structure studied in [III], certain phase changes could also be used as internal markers to indicate if a structure had been heated above a certain temperature, these changes could be seen with x-ray diffraction.

Comparison

<u>Thermal history can be measured from a millimeter size sample with a dilatometer, but when local rigidization takes place in a large sample, it is almost impossible to measure the history. Therefore, a new in situ method is necessary.</u>

<u>Robustness</u>

The method used an industrial grade grit blaster and glass grit that was ejected with compressed air, making the device applicable also at industrial atmosphere. A challenge with the test setup used in [III] was that the grit blaster could not provide a steady grit flow for more than 5 seconds; thus we could not use a continuous grit flow for measurement. This difficulty could have been avoided with a better feed system. In addition, grit moisture was seen to affect flowability. Otherwise, the system was very robust and applicable on site.

<u>Integrability</u>

The method was initially intended for an automated testing rig, where the grit blasting erosion capability would have been adjusted to erode only a specimen with no life time left. As such, it could be used in the plant for non-destructive analysis, but for now the method is applicable for destructive lot sample testing on site. Compared to the dilatometer, this is still good progress, because the dilatometer had to be used in a laboratory and needed sample preparation.

<u>Reliability</u>

The reliability of this method was tested by heating a similar specimen at a different temperature at 100-200 °C intervals from 400 °C up to 1050 °C. The specimens were easily distinguishable as they showed a minimal variation in crater depth. Certain reliability problems were encountered with a relatively inexpensive grit blaster, leading to an

unsteady grit flow during long blasting sessions. The problem was tackled by limiting the blasts to five-second bursts.

<u>Comprehensiveness</u>

The method was developed primarily to increase the comprehensiveness of the test in comparison to dilatometer measurement. In dilatometer measurement, a 20-mm, rod-shaped sample was heated and cooled while following its length changes. Sample preparation took about 15 minutes, and a single measurement 7 hours. In grit blasting, no sample preparation was needed, and one measurement took 5 seconds, plus a couple of seconds to measure the crater depth. Thus a whole 2-m filter element could be tested in one axial direction, whereas with a dilatometer the measurement location had to be guessed, based on how the element looked or felt.

4.1.4 Automatic pore parameter analyzer IV

Relevance

In [IV], it was discovered that with the same porosity, certain structures fabricated with different parameters had markedly different strength. Closely studied, the structures revealed that their pores differed in shape from that of the studied material parameter. The tracking parameter was set as the pore aspect ratio and strength was used as reference. Pore properties had to be extracted from SEM images, a task beyond human capability, so a method with in situ characteristics had to be engineered.

Aim

An in-house algorithm was used to analyze images in [IV]. Analysis was based on automatic segmentation, followed by feature extraction. This procedure was developed to increase precision in images of hundreds of analyzed objects to obtain quantitative results by feature analysis. In analytically more straightforward cases in [VI,VII], imageJ [136] was used, but the zeolite structures in [IV] could not have been easily analyzed without an adaptive filter and dedicated feature extraction, which are presented in [135].

Laboratory counterparts of the method

The only counterpart of image analysis is to measure features in images by hand, which is impossible or at least cumbersome with images with many features. In [IV], different pore size parameters were analyzed from samples, which had straight and even capillaries; consequently, poro- and porosimeters can be considered counterparts here, though the two approaches are basically different (as described in Characteriza-

tion of pores) when more heterogeneous structures are compared. Two-dimensional image analysis should thus be viewed mostly as a method to analyze pore shape, which we aimed to quantify.

Comparison

Pore structures can be characterized from a microscope image, but since in situ analysis aims at quantified data, analysis must be automated.

Robustness

Images used for analysis were automatically preprocessed to enhance their contrast via adaptive histogram equalization and to remove noise from the images. This method had an adaptive algorithm, which allowed analysis of difficult images with changes in contrast or intensity. In addition, supervised learning, a method that taught the algorithm to spot interesting objects in an image, was used to further the applicability of the method.

Integrability

Extracting features, such as pore dimensions or particle size, from a preprocessed and segmented image yielded numerical results, which could be directly incorporated in the work flow after image analysis.

Reliability

To assure the user of the results, the algorithm showed how it recognized pores. In fact, when tested, the algorithm recognized pores more consistently than any human being.

Comprehensiveness

The method analyzes a whole set of multiple images at once and yields features such as pore orientation or shape. Similar analysis cannot be carried out by hand.

4.1.5 Non-contact suspension analyzer V

Relevance

Colloidal particles are separated due to electrical fields around them. When particles stick together, gravity causes sedimentation, and the suspension can no longer remain homogenous. To study the homogeneity of a suspension, the solid content at the bottom was chosen as the material parameters and tracked with changes in resonant frequency, applied with an in-house built LC-circuit. The frequency was referenced with the amount of added solids and viscosity of the suspension.

Aim

Suspension analysis aimed at in situ measurement of suspensions. Initially, this technique was tested by measuring the amount of aluminum oxide and dispersing agent in an aqueous suspension to engineer a method that could be used, e.g., to detect agglomeration or unattached dispersing agent molecules to improve slurry processes. The first publication on the topic, [V], demonstrated how a feature calculated from a resonance signal was linked with the amounts of dispersing agent and aluminum oxide to yield an online method for measuring the relative amounts of both ingredients. If multiple measuring points could be fixed at different levels, the homogeneity of a suspension could be analyzed. One publication has been written in Finnish to describe and market the idea [142].

Laboratory counterparts of the method

Suspensions are analyzed with functional and quantitative methods. Functional methods, such as rheometry, study the viscosity of a suspension and link it with solid content and suspension state. Other methods, such as turbidity meters, measure the suspension's solid content usually through changes in the intensity of a light beam. These methods do not focus on the charges on the surface of particles, whereas the zeta potentiometer measures that by focusing on the difference in the electrical potential between a fluid and the electrical double layer surrounding a colloidal particle. However, in [V], we may have linked some high frequency electrical phenomenon with the quantity of the examined species to electrically measure the percentile amount of aluminum oxide or dispersing agent.

Comparison

Flocculation, especially in thick suspensions, must be measured with laboratory devices; however, long response time is not possible in lean production.

<u>Robustness</u>

Measurement was arranged in a non-contact manner so that an electrode used was embedded inside the suspension vessel, and so that it could be read through the vessel chassis from outside. We did not need to touch or disturb the process in any way, which helped maintain sensor integrity.

<u>Integrability</u>

A measurement arranged in a non-contact manner and read through a non-conductive material can be easily integrated. Raw data can be analyzed using an algorithm to extract features and thus to automate measurement and give it boundaries to determine the preferred state of the suspension.

<u>Reliability</u>

The reliability of the method is seen in [V] when reference measurements with isopropanol were made between each measurement. The measurement could be easily repeated. However, long-term contamination or colloid agglomeration on the electrode may cause difficulty.

<u>Comprehensiveness</u>

The method can be directly incorporated in a suspension vessel, obviating thus lot sampling, which might alter the suspension. The measurement gives readings only of the vicinity of the electrode, but multiple electrodes can be placed in various parts of the container to determine the homogeneity of the suspension.

4.1.6 Granule strength measurement VII

Relevance

Powders are granulated for numerous reasons, and one important feature of a granule is its durability in the intended use. Granules have usually plastic binders, which alter their behavior from rigid granules studied in [VII]. Granules are studied in situ with methods that focus mainly on flowability [143], shape, or size. Yet granule strength is one important measure that can be studied by compressing a single granule. This does not give a very comprehensive picture of how granules behave, nor is it possible with small granules. Therefore, the compressive strength of a bed of granules was chosen as the tracking parameter, linked with the breakage of individual granules and using particle size and SEM images for reference.

Aim

In [VII], an in situ measurement method was refined for further semi-automatization for the bed strength of rigid granules. A large amount of granules was compressed with a piston to gain a curve that, when examined in a half-logarithmic plot, showed certain areas linked with granule rearrangement, breakage, and rearrangement of primary particles.

Laboratory counterparts of the method

Granule strength is studied mainly by individually compressing granules [144], and studies on bed compression have been limited to non-rigid granules [145]. In situ studies of granule strength focus on process-relevant dynamic testing methods [143]; thus their closest counterpart is single granule compression.

Comparison

The strength of a single granule cannot be measured. In industrial production, a robust, comprehensive, and rapid method is thus necessary.

Robustness

The method uses a simple piston-cylinder tool, which can be inserted in any material testing device. Interpretation of the results ignores any noise caused by the alignment or wear of the measuring tool.

Integrability

The compression procedure could be automated and integrated into a granulation unit. In addition, analysis of the compression curve can be automated with tangential fitting (presented in [146]).

Reliability

The reliability of the method was addressed in [VII] by measuring the observational error as 0.5 MPa for compression granulated kaolinite powder with an average strength of 3.3 MPa. The measured bed strength was affected by granule shape, size, and density; consequently, whenever the strength must be changed, measurements should be accompanied by other type of analysis, e.g., SEM.

Comprehensiveness

Granules are normally produced by the kilo or ton, and measurement is tailored to approximately 1 gram of granulated powder, which is a lot type measurement. However, in comparison to crushing one granule under a microscope, the method can be used with a robust compression tool, whereby crushing a gram of micron-size granules easily adds up to crushing millions of granules at a time.

4.2 Pore- and porosity-related findings

An added contribution to materials science is provided in articles [II-V; VII] (as [I; VI] are purely application oriented). Their contribution is basically related to pores, porosity, and their affect.

In 1.3.3 (Specific challenges and research questions in the thesis), each publication topic was introduced in terms of research and described as below. The questions are individually addressed in the following subsections, which are organized first to summarize and then discuss each result.

Table 3 Sections and research aspects.

Section	Research aspect
4.2.1. Reaction of interfaces to electrical signals II/V	Is it possible to nondestructively measure the porosity of a ceramic sample? Can the flocculation of a suspension be measured during its preparation?
4.2.2. Fiber-free length III	How can the rigidization of a fiber structure be linked with the structure's thermal history
4.2.3. Effect of pore parameters on compression strength IV	What is the link between a structure's pore parameters and its crushing strength?
4.2.4 Strength of rigid granules VII	Can granule strength be measured from a granule bed instead of measuring a single granule?

4.2.1 Reaction of interfaces to electrical signals II/V

Results of capacitive porosity measurements

Publication [II] focused on using a frequency-response method with a capacitor-type measuring device. Sintered aluminum oxide plates were placed in the electric field of a

capacitor so that the electrical permittivity of the plates affected the capacitance of the measuring device. The plates were fabricated with an identical slip casting process, but when sintering temperature was altered, changes appeared in the measured capacitance, this was linked with the amount of total porosity measured with on the Archimedean principle.

Discussion of capacitive porosity measurements

From the correlation between porosity and capacitance, we deduced that with alumina samples sintered at a low temperature capacitance dropped because of increasing porosity. This indicated that the dielectric constant of the measured sample was affected by the volume average of the dielectric constants of the materials between the capacitor plates. In alumina samples with low porosity, a high volume of empty space, i.e., pores, containing air lowered the dielectric constant.

Results of resonance-based suspension measurements

Publication [V] focused on using a resonance-based sensor to study the solid content and the content of dispersing agent in a traditional aqueous suspension. Results show that the place of the dip in the resonator gain-frequency curve was dominated by the amount of alumina particles in the suspension, whereas its width was dominated by the amount of steric dispersing agent. This result was assumed to derive from resonating ions.

Discussion of resonance-based suspension measurements

In simple terms, the suspension double layer presumably resonates with a high-frequency electrical field, and the resonance frequency changes with the local amount of net charge, i.e., the amount of particle surface near the electric field used to probe the suspension. In detail, the electrical charges of a suspension depend on how particles and the double layer surrounding them are affected by the balancing ions from the suspending liquid. Present models and theories also acknowledge non-equilibrium reactions affecting the charging and the counter-ions added by the particles and point out that time-dependent relaxation may be seen with high frequency electric fields. [147]

4.2.2 Fiber-free length III

Results

Publication [III] sought to determine the mechanical characteristics that are linked with the effect of temperatures lower than those causing crystallization on a fibrous alumi-

num silicate structure. This was earlier linked with material phase changes [148], [149], which could be analyzed by measuring the crystalline structure of material. Methods that were used to collate a specimen by its mechanical characteristics when heat-treated at different temperatures were resonant frequency damping analysis, c-ring compression, and grit blasting. The first two turned out insensitive to the heat treatment temperature, but grit blasting was highly sensitive with a low deviation in reference samples. When grit was blasted with identical parameters, the dimple became deeper at high treatment temperatures.

Discussion

The study of fiber networks in this thesis was confined to creating a mechanical method for detecting changes in fiber-free length, which was further hypothesized to be linked with thermal history and presumed to be caused by fibers sintering to each other. The hypothesis was that the number of contact points increased, which was seen as rigidization of the fibrous structure, which the mesomechanic model [108, p. 32] explains by bonds in a single fiber reinforcing and stiffening the structure.

4.2.3   Effect of pore parameters on compression strength IV

Results

Publication [IV] focused on finding a relationship between the pore characteristics and compressive strength of a structure with oriented porosity. Pore diameters and shapes of different types were characterized with a microscope, and an adaptive image analysis algorithm and the results were used to explain the changes in the compressive strengths of corresponding structures. A buckling model predicted reasonably well the evolution of compressive strength with changing pore parameters.

Discussion

Though all the tested structures were rigid, buckling may have been possible because the cell wall was much longer than its thickness, and because it was not well supported. Consequently, the cellular solid approach with buckling behavior in [IV] could be modeled on the Euler principle [150, pp. 635–636] adapted from [96].

4.2.4   Strength of rigid granules VII

Results

Publication [VII] studied if the bed compressive strength of micron size and rigid ceramic granules could be derived from load-displacement measurement in cylindrical uniaxial compression. This was found to be possible when the load displacement curve was first converted to pressure-relative density, and when pressure was presented on a logarithmic scale to highlight regions in the curve. The compression curve had the highest curvature in the region where the granules broke. Granule breakage was inspected with particle size measurement before and after passing the region and by inspecting microscope images before and after the region.

Discussion

Similar regional behavior as predicted by theory in subsection 2.2.3. (Strength of a granular bed under compression) was seen in the pressure-relative density curve, indicating that uniaxial compression can be applied to rigid and small granules. A method, using linear fitting and suggested in [VII], shows approximated bed crushing strength and can be used as a qualitative characteristic for granule strength. Though we must keep in mind that in reality granules do not yield to a singular stress but to a stress span dictated by the uneven stress distribution in the granule bed during the compression. Stress distribution is affected by range of granule size, shape and strength of individual granules.

5 Conclusions: in situ measurement of pore-related characteristics

This chapter concludes the introduction to this thesis. The first section concludes in situ development, and the next one continues with a materials science perspective on the pore and porosity related part covered by the research linked with this thesis. The subsections answer the research questions and give recommendations for further research. The chapter ends with a final executive summary of the whole introduction.

The thesis features 14 diagrams from the empty Diagram 1 with all the topics to be covered and then filling the empty domains with topical diagrams 2-13. All these diagrams are collated in Diagram 14 on the next spread.

Theoretical background on pores, porosity and their measuring
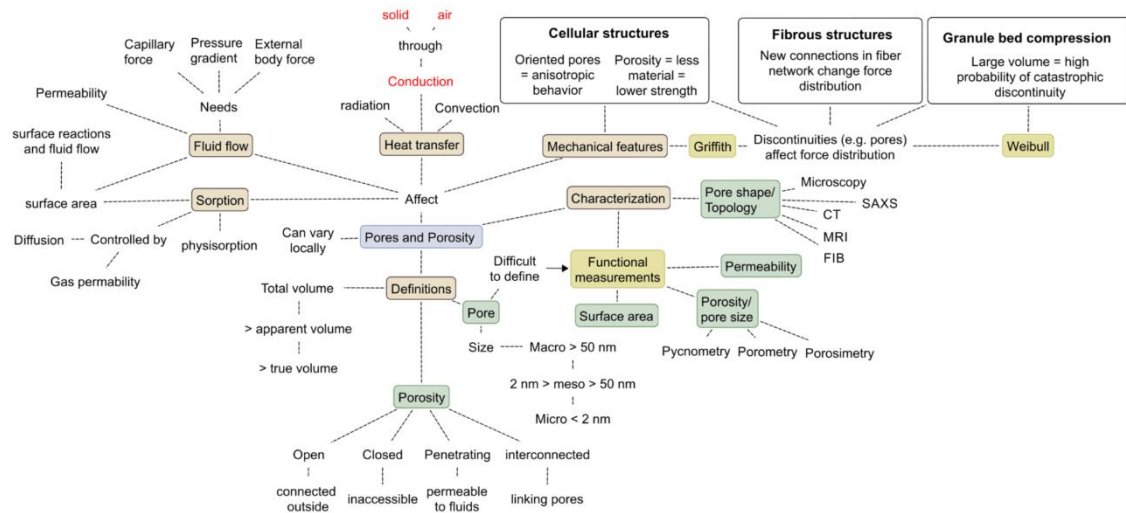
Main experimental procedures and sample materials
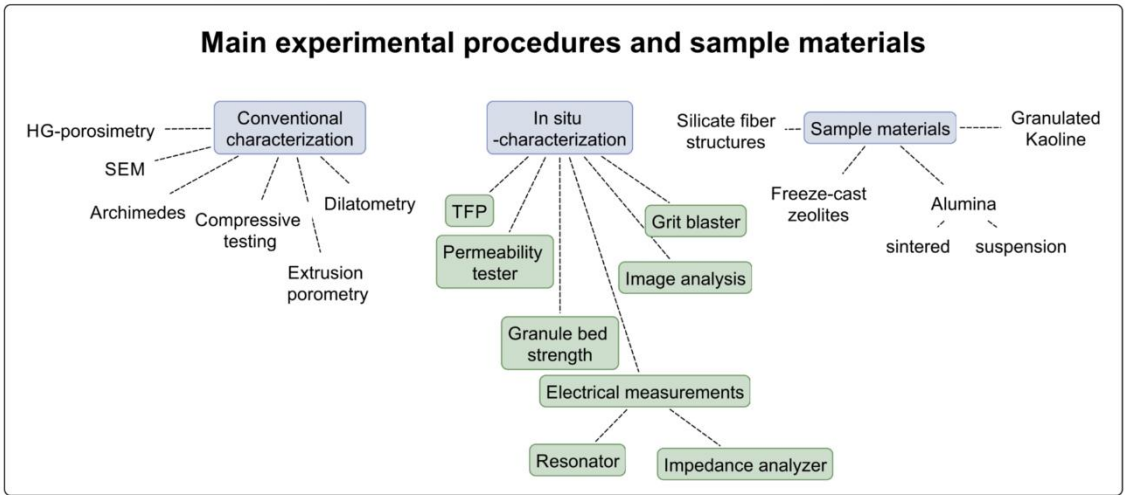
Included publications

I: Use of thermal imaging in characterization of ceramic fiber structures

II: Characterization of Porous Ceramics by Using Frequency-Response Method

III: Mechanical Characterization of Fiber Ceramics: Effect of Temperature

IV: The mechanical performance and CO2 uptake of ion-exchanged zeolite A structured by freeze-casting

V: Passive resonance sensor based method for monitoring particle suspensions

VI: Thermal Flow Permeametry - A Rapid Characterization Method for Local Changes in Gas Permeability

VII: Compression curve analysis and compressive strength measurement of brittle granule beds in lieu of individual granule measurements

Diagram 14: All diagrams.

Interface reactions

PRBS analyzer: method to analyze local porosity

Fiber free length

Grit blast: method to analyze thermal history of a fibrous structure

Cellular solids: parameters

Automated image analysis for pore parameters

TFP: Method to find local changes in permeability on of large through-porous objects.

II:Porosity   IV: Type of pores   IV: So VI: Heat transfer

III:Effect of temperature   **Strength**   **Characterization**   **Functional Features**   I/VI: Permability

Compresion strength analysis of multiple granules at a time

VII: Granule strength

In-situ characterization of pores and properties linked with pores

V: Amount of solid

Interface reactions

Electrical analyzer for local suspension thickness

Steps for Industrializing a characterization method

What are the critical quality attributes for following the production process?

How to measure most important material characters?

Determine the significant material parameters → Determine the best tracking parameter → Design an in situ characterization method for tracking parameter → Integrate new method with process

Find an existing characterization method for tracking parameter ← Ensure methods functionality with established method

Kinetic reactions

When offline samples don't represent the real material

Unstable samples

When rapid sampling is needed

When samples are unreachable

When samples are dangerous

High pressure   High or low temperatures

Replaces traditional offline equipment

When samples can't be perturbed

Characteristics of Industrial characterization method

Integrated
Compre-hensive

Sensitive   Reliable   Online   Onsite

Need calibration   Rough atmosphere   Robust   Simple

usability

In situ -measurements of processes

Verity process

Monitoring the process

Increased safety

Help scaling up

ssure quality

Understaring the process

Reduction in time and cost

Early stage process development

Process controlling

Ultimate goal is self adjusting -process

In situ -measuring

Needs sensors

Recognize abnormalities and find root-cause

bring quality control closer to production

4. Process integration
3. Supply chain integration
2. Business integration
1. Process integration

Automatization

Modern process control

Uses

aims

needed because

Processes are not stable

Raw material changes

Atmosphere changes   Changes in catalyst

Process fouling

Machinery abrasion

Holistic control of value creation

Add value to business

Product quality
Process safety
Reliability
Availability
Resource utilization
Energy savings
Emission control

Lean

Shift towards lean process control

Lead time minimization

Smooth production flow

Continuous improvement

Quality increase

Increase in throughput

Elimination of waste

Reduction of inventory

Enhanced resource utilization

Increase in green metrics

Methods   Material

Machinery   Manpower

Caused by

85

5.1 In situ measurements with a systematic approach

In situ measurement is sought for lean production. The first subsection concludes the systematic approach to in situ measurement and answers research question 1a: "Can material characterization be systematically tailored for in situ measurement?" Subsection 5.1.1 (Systematic approach to making a characterization method in situ) collates and grades the in situ methods developed in this thesis. Subsection 5.1.2 (Observations of the in situ methods in publications I-VII) suggests how the methods here could be further developed for use in a process environment and points out the common characteristics of the methods' attributes and maturity. The last subsection collates and generalizes the characteristics of the presented in situ methods and answers research question 1b: "How do the robustness, integrability, reliability, and comprehensiveness of in situ measurement devices affect the route from design table to use in processes?"

The following subsections are limited to examining the applicability of the methods in general, though equally important is to understand where process control can be assisted with in situ measurements. According to [17], many PAT (in situ) techniques are used in R&D to help understand and perhaps scale up a production process. Such assistance is necessary in relatively new processes, whereas in older and better understood processes in situ measurements can help optimize and automatically control them. An added incentive for in situ measurements may also come from certain regulatory authorities that are actively monitoring some processes [18].

5.1.1 Systematic approach to developing an in situ characterization method

A systematic approach used in developing in situ methods was described in subsection 1.3.4. (Research Approach). The following table summarizes the approach and gives a concrete example of the development steps taken in V (non-contact suspension analyzer).

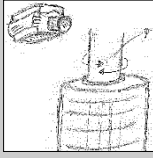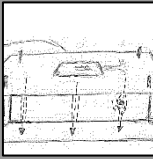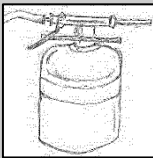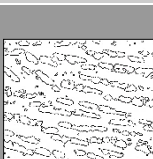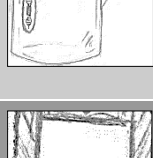Table 4 Summary and example of the systematic approach.

Steps in developing an in situ characterization method	Example from a publication
A manufacture process is studied from a material perspective and the most significant material properties of the process are pointed out.	The homogeneity of a ceramic product is dominated by its suspension stability. Stability is determined by interfacial electrical charges. Unstable suspensions flocculate and cause sedimentation. A sedimented suspension has more solids on the bottom. Materials parameter: solid content on bottom in comparison to that on the surface.
Proper tracking parameter(s) are chosen for property(ies).	A solid content can be tracked online with a resonator, which interacts probably with the surface charges of colloidal particles. This interaction affects resonant frequency, which was chosen as the tracking parameter.
The most suitable characterization method is chosen for the tracking parameter.	The local resonant frequency of a suspension can be measured with an LC-circuit that is design to probe a limited volume of material surrounding it.
A new method, better suited for following the tracking parameter and capable of in online measurement of a large sample area in an industrial environment, is developed. The new method ignores irrelevant properties.	An LC-resonator with a sensor that can be inserted in a suspension is designed with a view to its usability in a production facility atmosphere. Resonant frequency features are studied and a certain change in the frequency curve is linked with a local solid content.
The method's functionality is ensured by comparing measured changes in the tracking parameter with the existing method.	Other parameters linked with solid content are suspension viscosity and simply the amount of solids added in the suspension. Electrical measurement is tested and adjusted in laboratory to correlate results with viscosity and amount of solids.
The new method is integrated into the industrial process.	The integration of the measuring device is discussed in [142].

The same approach was used to develop all the devices. It proved applicable to the task giving a positive answer to the research question 1a. In addition it shows a one possible approach to others who strive to develop similar in situ measurements.

5.1.2 Observations of the in situ methods in publications I-VII

Chapter I explained how industrial production facilities benefit from in-situ methods featuring robustness, integrability, reliability, and comprehensiveness. In section IV, I presented six methods, developed at TUT in cooperation with other researchers, which exhibit these features in different degrees. The following Table 1 lists the methods and compares their features to the features of the devices that are currently used for the same task. The comparison intends to show the success of the development of the methods, disclose their current state of development, and point the way to their continued integration, the topic of the next subsection.

Table 5 Comparison of in-situ methods. Methods are evaluated from 1-3 (bullets, 3 being the highest grade) on four different attributes. Type & Route columns are highlighted in red, yellow (italics), or green (bold) according to the readiness of the device for in situ measurements in an industrial process.

		In-situ features					
		robust-ness	integra-ble	reliable	compre-hensive	TYPE	Route
	I/VI Thermal Flow Perme-ametry	●●	●●	●●●	●●●	**Continu-ous non-intrusive, online**	**Direct integ-ration**
	II PRBS Porosity analyzer	●	●	●●●	●●●	*Discrete, online*	Increase robust., Lab testing
	III blaster for fiber thermal history	●●●	●	●●	●●	Discrete, near produc-tion	*Increase reliability*
	IV Auto pore parame-ter ana-lyzer	●●	●	●●●	●●●	Discrete, on product lab	**Increase integrabili-ty, direct integrat.**
	V Non-contact suspen-sion analyzer	●●●	●●●	●	●●	**Continu-ous, non-intrusive online**	**Increase reliability, direct integrat.**
	VII Granule strength measu-ment	●●	●	●●	●●	Discrete, near produc-tion	Increase robust. and reliability lab testing

5.1.3 Route from laboratory to process

This subsection discusses the choice of the best route for in situ devices from laboratory testing to process. The route begins with a systematic approach to developing a method and continues to, and later depends on, the method's balance between robustness, integrability, reliability, and comprehensiveness.

89

5.1.3.1   Route of an in situ device from design to use in processes

This thesis is mostly limited to the development steps of new in situ methods, but the different integration routes of the methods are compared in the following for future reference (the reader is referred to "Table 2: Comparison of in-situ methods"):

- I/VI: the method is the most comprehensive on the list for quickly measuring a whole product, and it can be easily integrated to its intended use[41]. Its reliability is high with a direct route to process integration. The challenge in integration is clear presentation of data and setting acceptable quality limits, which must be carried out at the production plant.

- II: compared to existing methods, the porosity analyzer is comprehensive. In its intended use, it can scan a whole product but has problems with integrability issues coming from the shape limits of the measured pieces[42]. The system is also quite delicate. For production use, the device must be more robust in mechanical design and its integration must be dealt with. The route is to increase its robustness, develop a systematic way of contact with the measured product, and then in the production facility laboratory, test the system in a simulated process environment. It would also help to directly link the cut-off frequency with the measured sample's dielectric constant and to understand the interfacial effect of water on measurement.

- III: The grit blaster is a robust tool with no special attention necessary in use. Because it is a destructive method, it is clearly not an online tool, but it can be used next to a production line. However, it has some reliability issues with uneven grit flow and with erosion of the measured structure, which in long term use must be examined for variables other than temperature. Its route to a production line needs laboratory testing for an even grit flow and clarification of the erosion process. After that, it can be quickly applied on a production line.

- IV: From the method's perspective, the auto pore parameter analyzer is comprehensive, as it analyzes a whole microscope image at a time. Its reliability has also been found to be high. It is difficult to integrate into a production process, but in production laboratories, it makes the work flow leaner, especially because it is robust with its self-adaptive algorithm taking care of, e.g., variations in contrast. The route to its in situ use is to hone its user interface for easy introduction to the personnel.

- V: The suspension analyzer is a robust and integrable device. The sensor can be directly implanted in a process stream, or it can be used to measure through a container. Its reliability, however, is an issue, since its long-term use may cause dirt to accumulate on the sensors or the container wall. Another issue is that the processes and the measured quantity are not well un-

---

[41] Hot air is anyway ejected through the structure during manufacturing.

[42] The contact between the measuring electrode and the measured product affects measurement results.

derstood. Its comprehensiveness depends on how many sensors are used at a time. Its route is to increase reliability in direct production line testing and scouting for phenomena that affect the electrical response of the suspension. Research is also needed to understand the reason behind the changes in resonant frequency when particles with surface charges or ions are added in the suspension.

- VII: The granule bed strength device is a destructive tool that can be used next to a production line. It is semiautomated, and effort has been made to automate the compression curve analysis. In contrast to measuring one granule at a time, it is quite comprehensive, measuring a statistically significant number of granules. Its reliability is quite good, but some of its components depend on the user. Its route to production is to automate it further and build a working user interface to increase its robustness and reliability. The method has been used in [151].

The next subsection concludes on the importance of the different characteristics based on six case examples.

5.1.4 Importance of the characteristics of in situ measurement

In-situ measurement has clear benefits in industry: faster reaction times yield savings in sample preparation, transport, and analysis. Integrated characterization also links with the lean principle of minimizing non-value adding tasks and finding the root causes for process phenomena. The latter means that a direct measurement reveals the process in more detail[43], helps understand it more deeply, improves product quality, consistency, and process efficiency, which all contribute to less process waste.

Yet benefits must exceed risks for the industrial partners to be interested in them. Risks come from investing in a new characterization method that has purchase, installation, and service costs. To minimize these risks, the route and the way the system is combined with an in situ device must be aligned with the state of maturity of the device. To answer research question 1b, the following list acknowledges that in situ methods contain to a degree the following attributes, which affect their development route in the following manner:

- **Robustness**. Robustness of devices is a key issue when the device is installed in production. High robustness results in no need of special attention paid to the surroundings and to the safety/use training of personnel. Instead, highly robust devices can be straightforwardly incorporated in the process.

---

[43] For example, controlling a process based on time or temperature relies on historical data, whereas direct measurement of a process state takes into account variations in the process.

91

<u>Robust devices need less protection when brought near a process.</u> The need, of course, varies with the severity of the production atmosphere

- **Integrability** issues determine if the method can be used online or at-line and also interfere with the compatibility of process control and the way data output is handled and results presented. It is also linked with the ease of installation. <u>High integrability devices can work online naturally as part of the process[44].</u>

- **Reliability** is divided into the reliability of the device itself—can it measure what it is supposed to measure—and the reliability of the results: does it measure what it is intended for. This means that the measurement uses a frequency high enough to measure changes, but also that the measured quantity and its relation to the process state is well-understood. Normal fluctuation can thus be distinguished from real changes in the process. In addition, the deterioration of the device and how that affects the measurement must also be understood. <u>If reliability is good, the technique can be integrated with process control, depending on integrability.</u>

- **Comprehensiveness** is a key to lean production. It is gained by measuring only the necessary information but measuring it on a scale large enough to truly represent the chosen product state variable[45]. It also means that the time-scale of the measured changes is smaller than the measurement frequency so that changes can be detected. The <u>aim is to measure the whole production volume, though compromises may have to be made.</u>

5.2 Theoretical implications about pore and porosity related findings

This thesis contributes mostly to the far end of applications, but section 4.2. (Pore- and porosity-related findings) presented some findings on a more scientific paradigm.

In short, besides mechanical properties, pores and porosity affect many functional properties of a structure and their effects, whether on a manufacturing state or a complete product, must be well understood through characterization. Characterization is a demanding task, and linking whatever is defined as a pore with the functional features of the structure is a complex matter. Yet it can be greatly simplified with methods that focus on the functional definitions of the structure. To do that, one must understand what to look for with the functionality created with a porous structure. Even with proper

---

[44] Less integrability means in situ devices that can only work near a production line, e.g., measuring a production side stream.

[45] In some situations, the process has been instrumented with a device that measures too small a volume to represent variations in the whole product.

methods, local characterization challenges may arise from the homogenization of the structure, because measuring a relatively small volume of the whole can lead to misjudging the real variation, which can later result in inferior products.

With the above boundary conditions, the answer to research question 2 "can porosity, pores, and changes in them that affect the functionality and mechanical properties of structured materials be analyzed in situ?" is positive, because the result with all the developed in situ devices were successful.

The following briefly concludes the findings on pore and porosity and gives recommendations for further research on the topics.

5.2.1 Conclusions about the reaction of interfaces with electrical signals II/V

Both of the following cases are important mostly for the manufacturing and quality assurance of porous materials.

An impedance analyzer, capable of distinguishing between aluminium oxide plates with different porosity, was developed in [II]. The reason for the correlation between impedance and porosity was not studied, but probably the amount of pore interface or simply the different ratio of air and aluminium oxide affected the permeability of the plates. Our further studies, yet to be published, report how minute amounts of moisture can cause what we believe is a form of MWS polarization [152]. This finding may be used to analyze the amount of effective surface area.

A Resonator, whose capacitance was sensitive to changes in permittivity in the surrounding environment, was used in [V]. Changing permittivity changed the position and shape of the resonance curve, and the changes were clearly linked with the number of dispersing agent molecules and aluminium oxide particles. An electric field with a frequency close to $8 * 10^7$ Hz seemed to interact with the substances and possibly make them resonate in some mode to affect dielectric losses in the resonator. Interestingly, this frequency occurred at the far end of the molecular polarization frequency [153, p. 8], leaving a question open as to whether the connection between polar dispersing agent molecules and aluminium oxide particles could be monitored as a change in resonation frequency. This is definitely an interesting topic for future research.

5.2.2 Conclusions about fiber structure studies III

Fiber-free length refers to fiber mechanics, and we offered it to explain why thermal treatment rigidifies a fiber network. To continue modeling this (not included in the the-

sis), the degree of contact between fibers or a relative bonded area could be stochastically calculated by determining the network's porosity [154] or by applying image analysis to fiber cross-sections [155]. Fiber networks could also be schematically modeled [154] or studied by computer simulation [156]. Results thereof could directly help optimize the binder used in fibrous structures, but they could also help understand the origin of the mechanical strength of fibrous networks.

Flow in a fiber network. An interesting further research angle that has only recently been brought up with the development of computer sciences is the modeling of fluid flow in complex pore structures. It has been studied by modeling an imaged microstructure [110] and by artificially generating non-isotropic fiber networks with the finite element method [111]. The random structure of a fibrous hot gas filter element provides a truly challenging study, but it could also be used to optimize flow channels by studying how the structure changes when the fibers are oriented or changed in size.

5.2.3 Conclusions about the effect of pore parameters on the compression strength of oriented cellular structures IV

The buckling of rigid structures is not an undisputed idea but may be possible especially on the micron scale. The structure under compression in [IV] consisted of struts that were only a few microns thick but whose length may reach millimeters and be supported by vertical beams, which also formed due to ice templating. An added incentive to modeling the behavior of oriented cellular structures is to use digital microstructure models [157], which until very recently have been limited by imaging resolution and computational challenges. Our 2d-pore parameter algorithm showed that the pore aspect ratio was in this case the parameter that best linked with compressive strength. I assume that this was due to the aspect ratio changing systematically with the increasing number of support struts, which added to compressive strength.

5.2.4 Conclusions about the strength of rigid granules VII

Optimizing granule production aims to understand the production parameters that affect characteristics such as the compressive strength, shape, and size of granules. The granules studied in [VII] varied in their characteristics, necessitating measurement of a representative number of granules. The publication focused mostly on compressive analysis of multiple granules, moving towards analysis of the compression curve, where the average compressive force was located based on changes in the compression rate of the curve. The curve was analyzed semi-automatically on a half-logarithmic scale, and a correlation with the sintering temperature and a chosen feature in the curve suggested that the feature could be used to indicate comparative compression

strength. The novelty here was that our research proved that analysis could be done with small and brittle granules. However, parameters such as granule shape and size affect the feature so that the method may not function universally. Finding means to calculate the derivate of the compression pressure-relative density curve might help discover a more precise feature and set research towards automated data analytics.

5.3 Summary

This introduction presented seven peer reviewed articles focused mainly on novel characterization methods to analyze pores [IV], porosity [II], and the effect of pores on mechanical parameters [III, IV, VII] and permeability [I, VI], and to characterize the evolution of material parameters in the manufacture of porous materials [V, VII]. Fig. 16 shows the different pore structures of the materials used in the case studies.

The viewpoint of the introduction was written from in situ characterization. In situ measurement was defined as something that could be carried out in-line, online, or at least on a production site. The choice of the viewpoint was clear, since all the characterization methods aimed at robust and comprehensive industrial measurement in exchange for precise and meticulous laboratory analysis. The pharmaceutical industry was the first to see the need for in situ measurements, but it has been argued that as production goes lean, the accompanying straightforward process control requires necessarily robust, integrable, reliable, and comprehensive in situ measurement and process sensing. Fig. 16 shows the developed in situ methods.
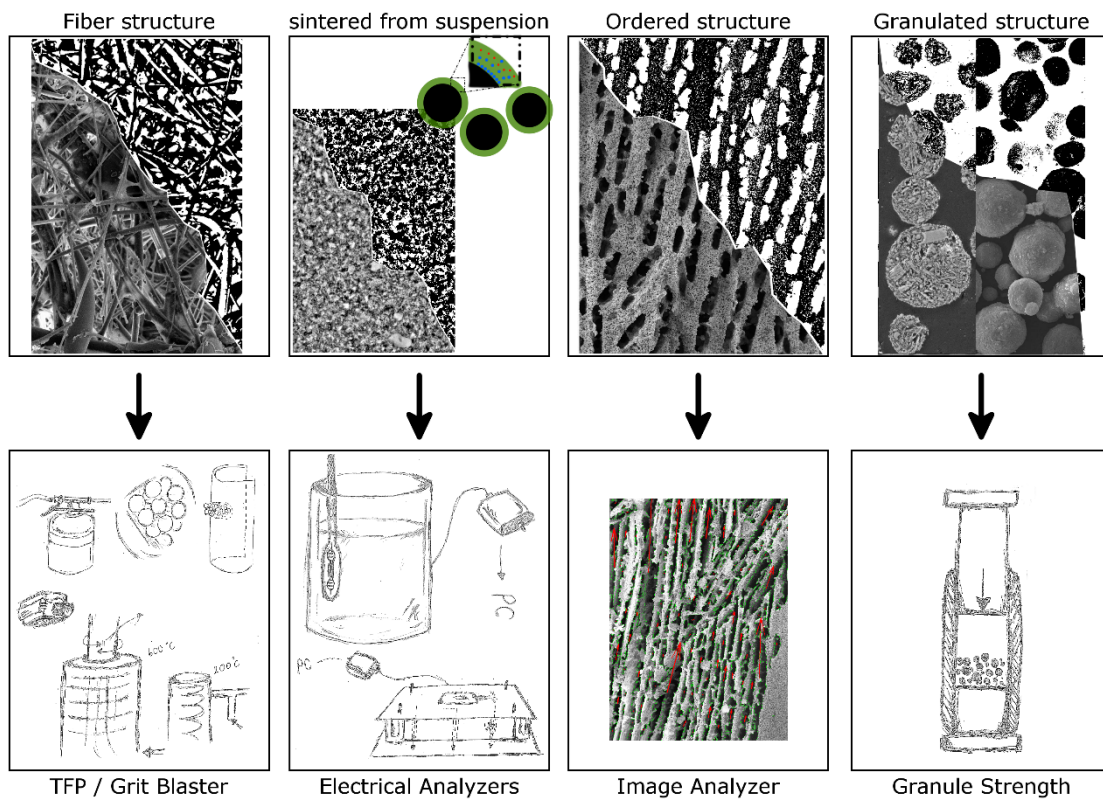
Figure 16: Sample materials and in situ methods.

The methods were developed systematically in steps that started from understanding the material parameters linked with the quality of the process and finding a parameter to track it. The parameter had to be such that it could be measured in situ. The same approach was used to develop all the methods, proving that it was applicable to the development task. The methods reached varying states of maturity as to robustness, integratability, reliability, and comprehensiveness, which determined the way to integrate and use measurements. In total, the development task was an interdisciplinary mission, covering such matters as process control issues, materials science, and automation.

The methods presented in the enclosed publications were developed with industrial partners for a particular task, but they can all be extended to characterize the local permeability and mechanical properties of fibrous structures, the colloidal state of suspensions, the porosity of consolidated materials, to automatically define a pore parameter in 2d-images, and to measure the strength of rigid granules. Some fundamental ideas in materials science were also covered, such as the connection between fiber-free length and the rigidity of a fibrous structure, interface reactions of materials and

electrical signals, a link between pore parameters, and compressive strength in oriented structures.

I believe that the methods here are now at a stage in which industrial partners are necessary for their further development and validation. Thus I end this summary with a challenge for industry to continue building the characterization methods and this ideology with us. I believe that, especially with smart sensors, lean, and industrial internet, a change in paradigm from industrial laboratory analysis to in situ measurement is virtually inevitable.

References

[1]   S.-L. Jämsä-Jounela, "Future trends in process automation," *Annual Reviews in Control*, vol. 31, no. 2, pp. 211–220, 2007.

[2]   T. Samad, P. McLaughlin, and J. Lu, "System architecture for process automation: Review and trends," *Journal of Process Control*, vol. 17, no. 3, pp. 191–201, 2007.

[3]   M. Kurdve, M. Zackrisson, M. Wiktorsson, and U. Harlin, "Lean and green integration into production system models - experiences from Swedish industry," *Journal of Cleaner Production*, vol. 85, pp. 180–190, 2014.

[4]   The National Institute of Standards and Technology (NIST), "Lean and Continuous Improvement," *Services and Initiatives*. [Online]. Available: http://www.nist.gov/mep/services/continuous-improvement/index.cfm. [Accessed: 26-Jun-2015].

[5]   T. Melton, "The Benefits of Lean Manufacturing," *Chemical Engineering Research and Design*, vol. 83, no. 6, pp. 662–673, 2005.

[6]   J. A. Garza-Reyes, "Lean and green – a systematic review of the state of the art literature," *Journal of Cleaner Production*, vol. 102, pp. 18–29, 2015.

[7]   M. Holweg, "The genealogy of lean production," *Journal of Operations Management*, vol. 25, no. 2, pp. 420–437, 2007.

[8]   P. Forrester, U. Shimizu, H. Soriano-Meier, J. Garza-Reyes, and L. Basso, "Lean production, market share and value creation in the agricultural machinery sector in Brazil," *Journal of Manufacturing Technology Management*, vol. 21, no. 7, pp. 853–871, 2010.

[9]   P. J. Martínez-Jurado and J. Moyano-Fuentes, "Lean Management, Supply Chain Management and Sustainability: A Literature Review," *Journal of Cleaner Production*, vol. 85, pp. 134–150, 2013.

[10]   P. Hines, M. Holweg, and N. Rich, *Learning to evolve: A review of contemporary lean thinking*, vol. 24, no. 10. 2004.

[11]   J. Ben Naylor, M. Naim, and D. Berry, "Leagility: integrating the lean and agile manufacturing in the total supply chain," *International Journal of Production Economics*, vol. 62, pp. 107–118, 1999.

[12]   J. Riezebos, W. Klingenberg, and C. Hicks, "Lean Production and information technology: Connection or contradiction?," *Computers in Industry*, vol. 60, no. 4, pp. 237–247, 2009.

[13]   R. Sundar, a. N. Balaji, and R. M. S. Kumar, "A Review on Lean Manufacturing Implementation Techniques," *Procedia Engineering*, vol. 97, pp. 1875–1885, 2014.

[14]   P. Kadlec, R. Grbić, and B. Gabrys, "Review of adaptation mechanisms for data-driven soft sensors," *Computers and Chemical Engineering*, vol. 35, no. 1, pp. 1–24, 2011.

[15]   T. S. Schei, "On-line estimation for process control and optimization applications," *Journal of Process Control*, vol. 18, no. 9, pp. 821–828, 2008.

[16]   A. Chanda, A. M. Daly, D. a. Foley, M. a. LaPack, S. Mukherjee, J. D. Orr, G. L. Reid, D. R. Thompson, and H. W. Ward, "Industry Perspectives on Process Analytical Technology: Tools and Applications in API Development," *Organic Process Research & Development*, 2014.

[17]   L. L. Simon, H. Pataki, G. Marosi, F. Meemken, K. Hungerbu, A. Baiker, S. Tummala, B. Glennon, M. Kuentz, G. Steele, H. J. M. Kramer, J. W. Rydzak, Z.

Chen, J. Morris, F. Kjell, R. Singh, K. V Gernaey, M. Louhi-kultanen, J. O. Reilly, N. Sandler, O. Antikainen, J. Yliruusi, P. Frohberg, J. Ulrich, R. D. Braatz, T. Leyssens, M. Von Stosch, R. Oliveira, R. B. H. Tan, H. Wu, M. Khan, D. O. Grady, A. Pandey, R. Westra, E. Delle-case, and D. Pape, "Assessment of Recent Process Analytical Technology (PAT) Trends: A Multiauthor Review," *Organic Process Research & Development*, vol. 19, pp. 3–62, 2015.

[18] L. L. Simon, "2014: The PAT Trend Is Still Bullish," *Organic Process Research & Development*, vol. 19, no. 1, pp. 1–2, 2015.

[19] F. Sistare, L. Pierre Berry, and C. . Mojica, "Process analytical technology: An investment in process knowledge," *Organic Process Research & Development*, vol. 9, no. 38, 2005.

[20] T. Lopez, "Robust Dynamic State Estimation of Nonlinear Plants," *AlChE Journal*, vol. 45, no. 1, 1999.

[21] T. Närvänen, K. Seppälä, O. Antikainen, and J. Yliruusi, "A new rapid on-line imaging method to determine particle size distribution of granules.," *AAPS PharmSciTech*, vol. 9, no. 1, pp. 282–287, 2008.

[22] R. C. Willis, "Process Analytical Technology," pp. 21–22, 2004.

[23] S. Yin, S. X. Ding, A. Haghani, H. Hao, and P. Zhang, "A comparison study of basic data-driven fault diagnosis and process monitoring methods on the benchmark Tennessee Eastman process," *Journal of Process Control*, vol. 22, no. 9, pp. 1567–1581, 2012.

[24] A. Flammini, P. Ferrari, D. Marioli, E. Sisinni, and A. Taroni, "Wired and wireless sensor networks for industrial applications," *Microelectronics Journal*, vol. 40, no. 9, pp. 1322–1336, 2009.

[25] A. Alawi, J. Zhang, and J. Morris, "Multiscale Multiblock Batch Monitoring : Sensor and Process Drift and Degradation," *Organic Process Research & Development*, vol. 19, pp. 145–157, 2015.

[26] S. J. Qin, "Survey on data-driven industrial process monitoring and diagnosis," *Annual Reviews in Control*, vol. 36, no. 2, pp. 220–234, 2012.

[27] D. Pertig, R. Buchfink, S. Petersen, T. Stelzer, and J. Ulrich, "Inline analyzing of industrial crystallization processes by an innovative ultrasonic probe technique," *Chemical Engineering and Technology*, vol. 34, no. 4, pp. 639–646, 2011.

[28] V. Hanyecz, Á. Mohácsi, A. Pogány, A. Varga, Z. Bozóki, I. Kovács, and G. Szabó, "Multi-component photoacoustic gas analyzer for industrial applications," *Vibrational Spectroscopy*, vol. 52, no. 1, pp. 63–68, 2010.

[29] I. Lecreps, O. Orozovic, M. Eisenmenger, M. G. Jones, and K. Sommer, "Methods for in-situ porosity determination of moving porous columns and application to horizontal slug flow pneumatic conveying," *Powder Technology*, vol. 253, pp. 710–721, 2014.

[30] J. Ulrich and P. Frohberg, "Problems, potentials and future of industrial crystallization," *Frontiers of Chemical Science and Engineering*, vol. 7, no. 1, pp. 1–8, 2013.

[31] A. Hourri, M. St-Arnaud, and T. K. Bose, "Solubility of solids in supercritical fluids from the measurements of the dielectric constant: Application to CO_2–naphthalene," *Review of Scientific Instruments*, vol. 69, no. 7, p. 2732, 1998.

[32] M. Wijaya Hermanto, A. Phua, P. Shan Chow, and R. B. H. Tan, "Improved C-control of crystallization with reduced calibration effort via conductometry," *Chemical Engineering Science*, vol. 97, pp. 126–138, 2013.

[33] L. L. Simon, T. Merz, S. Dubuis, A. Lieb, and K. Hungerbuhler, "In-situ monitoring of pharmaceutical and specialty chemicals crystallization processes

using endoscopy-stroboscopy and multivariate image analysis," *Chemical Engineering Research and Design*, vol. 90, no. 11, pp. 1847–1855, 2012.

[34] J.-M. Andanson and A. Baiker, "Exploring catalytic solid/liquid interfaces by in situ attenuated total reflection infrared spectroscopy.," *Chemical Society reviews*, vol. 39, no. 12, pp. 4571–4584, 2010.

[35] D. D. Dunuwila and K. A. Berglund, "ATR FTIR spectroscopy for in situ measurement of supersaturation," *Journal of Crystal Growth*, vol. 179, no. 1–2, pp. 185–193, 1997.

[36] Z. K. Nagy and R. D. Braatz, "Advances and New Directions in Crystallization Control," *Annual Review of Chemical and Biomolecular Engineering*, vol. 3, no. 1, pp. 55–75, 2012.

[37] J. Medendorp, R. G. Buice, and R. a Lodder, "Acoustic-resonance spectrometry as a process analytical technology for the quantification of active pharmaceutical ingredient in semi-solids.," *AAPS PharmSciTech*, vol. 7, no. 3, p. 59, 2006.

[38] A. Niederquell and M. Kuentz, "Proposal of stability categories for nano-dispersions obtained from pharmaceutical self-emulsifying formulations," *International Journal of Pharmaceutics*, vol. 446, no. 1–2, pp. 70–80, 2013.

[39] L. Simon and A. S. Myerson, "Continuous antisolvent plug-flow crystallization of a fast growing API," *International Symposium on Industrial Crystallization*, pp. 3–6, 2011.

[40] A. Niederquell, A. C. Völker, and M. Kuentz, "Introduction of diffusing wave spectroscopy to study self-emulsifying drug delivery systems with respect to liquid filling of capsules," *International Journal of Pharmaceutics*, vol. 426, no. 1–2. pp. 144–152, 2012.

[41] A. Burggraeve, N. Sandler, J. Heinämäki, H. Räikkönen, J. P. Remon, C. Vervaet, T. De Beer, and J. Yliruusi, "Real-time image-based investigation of spheronization and drying phenomena using different pellet formulations," *European Journal of Pharmaceutical Sciences*, vol. 44, no. 5, pp. 635–642, 2011.

[42] I. Csontos, H. Pataki, A. Farkas, H. Bata, B. Vajna, Z. K. Nagy, G. Keglevich, and G. J. Marosi, "Feedback control of oximation reaction by inline Raman spectroscopy," *Organic Process Research & Development*, p. 140318112940008, 2014.

[43] P. Bawuah, P. Silfsten, T. Ervasti, J. Ketolainen, J. A. Zeitler, and K.-E. Peiponen, "Non-contact weight measurement of flat-faced pharmaceutical tablets using terahertz transmission pulse delay measurements.," *International Journal of Pharmaceutics*, vol. 476, no. 1–2, pp. 16–22, 2014.

[44] P. Bawuah, A. Pierotic Mendia, P. Silfsten, P. Pääkkönen, T. Ervasti, J. Ketolainen, J. A. Zeitler, and K. E. Peiponen, "Detection of porosity of pharmaceutical compacts by terahertz radiation transmission and light reflection measurement techniques," *International Journal of Pharmaceutics*, vol. 465, no. 1–2, pp. 70–76, 2014.

[45] S. Virtanen, O. Antikainen, and J. Yliruusi, "Determination of the crushing strength of intact tablets using Raman spectroscopy," *International Journal of Pharmaceutics*, vol. 360, no. 1–2, pp. 40–46, 2008.

[46] I. Akseli, G. N. Mani, and C. Cetinkaya, "Non-destructive acoustic defect detection in drug tablets," *International Journal of Pharmaceutics*, vol. 360, no. 1–2, pp. 65–76, 2008.

[47] I. Akseli and C. Cetinkaya, "Air-coupled non-contact mechanical property determination of drug tablets," *International Journal of Pharmaceutics*, vol. 359, no. 1–2, pp. 25–34, 2008.

[48]   I. Akseli, D. C. Becker, and C. Cetinkaya, "Ultrasonic determination of Young's moduli of the coat and core materials of a drug tablet," *International Journal of Pharmaceutics*, vol. 370, no. 1–2, pp. 17–25, 2009.

[49]   M. J. Taylor, S. Tanna, and T. Sahota, "In vivo study of a polymeric glucose-sensitive insulin delivery system using a rat model.," *Journal of pharmaceutical sciences*, vol. 99, no. 10, pp. 4215–4227, 2010.

[50]   E. Serris, L. Perier-Camby, G. Thomas, M. Desfontaines, and G. Fantozzi, "Acoustic emission of pharmaceutical powders during compaction," *Powder Technology*, vol. 128, no. 2–3, pp. 296–299, 2002.

[51]   M. Alexander and D. G. Dalgleish, "Diffusing Wave Spectroscopy of aggregating and gelling systems," *Current Opinion in Colloid and Interface Science*, vol. 12, no. 4–5, pp. 179–186, 2007.

[52]   A. R. . Goodwin and M. R. Moldover, "Phase border and density determinations in the critical region of (carbon dioxide+ethane) determined from dielectric permittivity measurements," *The Journal of Chemical Thermodynamics*, vol. 29, no. 12, pp. 1481–1494, 1997.

[53]   L. S. Ferreira and J. O. Trierweiler, "Modeling and simulation of the polymeric nanocapsule formation process," *IFAC Proceedings Volumes (IFAC-PapersOnline)*, vol. 7, no. PART 1, pp. 405–410, 2009.

[54]   S. Watano and K. Miyanami, "Image processing for on-line monitoring of granule size distribution and shape in fluidized bed granulation," *Powder Technology*, vol. 83, no. 1, pp. 55–60, 1995.

[55]   E. N. Kaufman and T. C. Scott, "In situ visualization of coal particle distribution in a liquid fluidized bed using fluorescence microscopy," *Powder Technology*, vol. 78, no. 3, pp. 239–246, 1994.

[56]   N. Limodin, L. Salvo, E. Boller, M. Suéry, M. Felberbaum, S. Gailliègue, and K. Madi, "In situ and real-time 3-D microtomography investigation of dendritic solidification in an Al–10wt.% Cu alloy," *Acta Materialia*, vol. 57, no. 7, pp. 2300–2310, Apr. 2009.

[57]   N. Limodin, L. Salvo, M. Suéry, and M. DiMichiel, "In situ investigation by X-ray tomography of the overall and local microstructural changes occurring during partial remelting of an Al–15.8wt.% Cu alloy," *Acta Materialia*, vol. 55, no. 9, pp. 3177–3191, May 2007.

[58]   S. Terzi, L. Salvo, M. Suéry, N. Limodin, J. Adrien, E. Maire, Y. Pannier, M. Bornert, D. Bernard, and M. Felberbaum, "In situ X-ray tomography observation of inhomogeneous deformation in semi-solid aluminium alloys," *Scripta Materialia*, vol. 61, no. 5, pp. 449–452, Sep. 2009.

[59]   S. Terzi, L. Salvo, M. Suéry, and E. Boller, "In situ X-ray microtomography characterization of the entrapped liquid formed during partial remelting of a cold-rolled Al–8 wt.% Cu alloy," *Scripta Materialia*, vol. 60, no. 8, pp. 671–674, Apr. 2009.

[60]   S. S. Singh, J. J. Williams, P. Hruby, X. Xiao, F. De Carlo, and N. Chawla, "In situ experimental techniques to study the mechanical behavior of materials using X-ray synchrotron tomography," *Integrating Materials and Manufacturing Innovation*, vol. 3, no. 1, p. 9, Apr. 2014.

[61]   E. Kissa, *Dispersions: Characterization, Testing, and Measurement*. CRC Press, 1999.

[62]   H. N. Bachman, J. Lavigne, R. Leveridge, N. Heaton, M. D. Hürlimann, W. J. Looyestijn, and J. White, "Nucear Magnetic Resonance Comes Out of Its Shell," *Oilfield Review*, vol. 20, no. 4, pp. 4–23, 2008.

[63] T. Takamura, P. Ko, J. Sharma, R. Yukino, S. Ishizawa, and A. Sandhu, "Magnetic-Particle-Sensing Based Diagnostic Protocols and Applications," *Sensors*, vol. 15, no. 6, pp. 12983–12998, 2015.

[64] C. Chaiyachit, S. Satthamsakul, W. Sriratana, and T. Suesut, "Hall Effect Sensor for Measuring Metal Particles in Lubricant," in *Proceedings of the International MultiConference of Engineers and Computer Scientists 2012 Vol II*, 2012, vol. II, no. 2, pp. 14–17.

[65] D. Sharma, "Non-destructive Testing of Materials using Capacitive Sensing Technique," *MIT International Journal of Electronics and Communication Engineering*, vol. 1, no. 2, pp. 73–77, 2011.

[66] X. Yin, D. a. Hutchins, G. G. Diamond, and P. Purnell, "Non-destructive evaluation of concrete using a capacitive imaging technique: preliminary modelling and experiments," *Cement and Concrete Research*, vol. 40, no. 12, pp. 1734–1743, 2010.

[67] T. Togkalidou, M. Fujiwara, S. Patel, and R. D. Braatz, "Solute concentration prediction using chemometrics and ATR-FTIR spectroscopy," *Journal of Crystal Growth*, vol. 231, no. 4, pp. 534–543, 2001.

[68] D. Duffy, M. Barrett, and B. Glennon, "Novel, calibration-free strategies for supersaturation control in antisolvent crystallization processes," *Crystal Growth and Design*, vol. 13, no. 8, pp. 3321–3332, 2013.

[69] Y. Hu, H. Wikström, S. R. Byrn, and L. S. Taylor, "Analysis of the Effect of Particle Size on Polymorphic Quantitation by Raman Spectroscopy," *Applied Spectroscopy*, vol. 60, pp. 977–984, 2006.

[70] T. Zhang, L. Zhou, H. Ammari, and J. Seo, "Electrical Impedance Spectroscopy-Based Defect Sensing Technique in Estimating Cracks," *Sensors*, vol. 15, no. 5, pp. 10909–10922, 2015.

[71] J. B. Wachtman, "Molecular Diffusion to Determine Pore Size Distribution in Porous Solids," in *15th Annual Conference on Composites and Advanced Ceramic Materials*, 2009, p. 668.

[72] L. Salvo, P. Cloetens, E. Maire, S. Zabler, J. J. Blandin, J. Y. Buffière, W. Ludwig, E. Boller, D. Bellet, and C. Josserond, "X-ray micro-tomography an attractive characterisation technique in materials science," *Nuclear Instruments and Methods in Physics Research, Section B: Beam Interactions with Materials and Atoms*, vol. 200, pp. 273–286, 2003.

[73] Ceramic Unie, "Paving the way to 2050," 2012.

[74] J. Bessant and W. Phillips, "Innovation management and dynamic capability," in *The SAGE handbook of strategic supply management*, London: Sage Publications Ltd, 2013, pp. 353–371.

[75] D. J. Teece, "Explicating dynamic capabilities: the nature and microfoundations of (sustainable) enterprise performance," *Strategic Management Journal*, vol. 28, pp. 1319–1350, 2007.

[76] G. C. O'Connor, "Major Innovation as a Dynamic Capability: A System Approach," *Journal of product innovation management*, vol. 25, no. 4, pp. 313–330, 2008.

[77] S. J. Berman and J. Hagan, "How technology-driven business strategy can spur innovation and growth," *IEEE Engineering Management Review*, vol. 34, no. 3, pp. 31–37, 2006.

[78] D. Li, L. Eden, M. Hitt, and D. Ireland, "Friends , Acquaintances or Strangers ? Partner Selection in R & D Alliances Bush School Working Paper # 589," *Academy of Management Journal*, vol. 51, no. 1, pp. 315–334, 2008.

[79] F. A. L. Dullien, *Porous Media Fluid Transport and Pore Structure*, Second Edi. San Diego, California: Academic Press, 1991.

[80] I. Kozo, K. Sridhar, and N. Makoto, *Porous Materials*. Springer Science & Business Media Dordrecht, 1998.

[81] J. R. Nimmo, "Porosity and pore size distribution," *Encyclopedia of Soils in the Environment*, pp. 295–303, 2004.

[82] A. D. McNaught and A. Wilkinson, Eds., *on-line corrected version: Compendium of Chemical Terminology the "Gold Book,"* 2nd verson. Oxford: Blackwell Scientific Publications.

[83] R. Asthana, A. Kumar, and N. B. Dahotre, "Pore Characterization," in *Materials Processing and Manufacturing Science*, Burlington, MA, USA: Academic Press, 2006, pp. 224–227.

[84] L. L. Schramm, "Suspension," Saskatchewan, 2014.

[85] R. G. Holdich, "Colloids and agglomeration," in *Fundamentals of particle technology*, Loughborough: Midland Information Technology and Publishing, 2002, pp. 1–16.

[86] I. Zeta-Meter, "Zeta Potential : A Complete Course in 5 Minutes," *Zeta-Meter Inc.* Staunton, USA, pp. 1–8.

[87] A. Ojuva, "Processing and performance of zeolites for efficient carbon dioxide separation," Stockholm University, Doctoral Thesis, 2015.

[88] ASM, "Monolithic and Fibrous Refractories," in *ASM Engineered Materials Handbook*, ASM Desk E., ASM International, in ASM Handbooks online, 1995.

[89] X. Chen, S. Wu, and J. Zhou, "Influence of porosity on compressive and tensile strength of cement mortar," *Construction and Building Materials*, vol. 40, pp. 869–874, 2013.

[90] E. Ryshkewitch, "Compression Strength of Porous Sintered Alumina and Zirconia," *Journal of the American Ceramic Society*, vol. 36, pp. 65–68, 1953.

[91] M. F. Ashby, "The properties of foams and lattices.," *Philosophical transactions. Series A, Mathematical, physical, and engineering sciences*, vol. 364, no. 1838, pp. 15–30, 2006.

[92] A. A. Griffith, "The Phenomena of Rupture and Flow in Solids," *Philosophical Transactions of the Royal Society A: Mathematical, Physical and Engineering Sciences*, vol. 221, no. 582–593. pp. 163–198, 1921.

[93] J. Aboudi, S. M. Arnold, and B. A. Bednarcyk, *Micromechanics of Composite Materials: A Generalized Multiscale Analysis Approach*. 2012.

[94] Z. Hashin, "Analysis of composite materials," *ASME J. Appl. Mech.*, vol. 50, no. September, pp. 481–504, 1983.

[95] R. Haj-Ali and J. Aboudi, "Nonlinear micromechanical formulation of the high fidelity generalized method of cells," *International Journal of Solids and Structures*, vol. 46, no. 13, pp. 2577–2592, 2009.

[96] M. M. Porter, R. Imperio, M. Wen, M. a. Meyers, and J. McKittrick, "Bioinspired scaffolds with varying pore architectures and mechanical properties," *Advanced Functional Materials*, vol. 24, no. 14, pp. 1978–1987, 2014.

[97] G. Aryanpour and M. Farzaneh, "Application of a piston equation to describe die compaction of powders," *Powder Technology*, 2015.

[98] R. Pitchumani, O. Zhupanska, G. M. H. Meesters, and B. Scarlett, "Measurement and characterization of particle strength using a new robotic compression tester," *Powder Technology*, vol. 143–144, pp. 56–64, 2004.

[99] S. Antonyuk, J. Tomas, S. Heinrich, and L. Mörl, "Breakage behaviour of spherical granulates by compression," *Chemical Engineering Science*, vol. 60,

pp. 4031–4044, 2005.

[100] G. R. McDowell, "ON THE YIELDING AND PLASTIC COMPRESSION OF SAND," *Journal of the Japanese Geotechnical Society : soils and foundation*, vol. 42, no. 1, pp. 139–145, 2002.

[101] J.-H. Song and J. R. G. Evans, "A Die pressing Test for the Estimation of Agglomerate Strength," *Journal of the American Ceramic Society*, vol. 77, no. 3, pp. 806–814, 1994.

[102] G. R. McDowell and J. P. de Bono, "On the micro mechanics of one-dimensional normal compression," *Géotechnique*, vol. 63, no. 11, pp. 895–908, 2013.

[103] J. P. de Bono and G. R. McDowell, "An insight into the yielding and normal compression of sand with irregularly-shaped particles using DEM," *Powder Technology*, vol. 271, pp. 270–277, 2015.

[104] B. J. Briscoe and N. Özkan, "Compaction behaviour of agglomerated alumina powders," *Powder Technology*, vol. 90, pp. 195–203, 1997.

[105] R. D. Carneim and G. L. Messing, "Response of granular powders to uniaxial loading and unloading," *Powder Technology*, vol. 115, pp. 131–138, 2001.

[106] M. G. C. Couroyer Z. Ning, C. Couroyer, Z. Ning, and M. Ghadiri, "Distinct element analysis of bulk crushing: effect of particle properties and loading rate," *Powder Technol.*, vol. 109, pp. 241–254, 2000.

[107] F. Güner, Ö. N. Cora, and H. Sofuoğlu, "Numerical modeling of cold powder compaction using multi particle and continuum media approaches," *Powder Technology*, vol. 271, pp. 238–247, 2015.

[108] R. E. Mark, C. C. Habeger, J. Borch, and M. B. Lyne, *Handbook of physical testing of paper*, 2nd ed. New York/Basel: Marcel Dekker INC, 2001.

[109] J. Tryding, "In-plane fracture of paper," *Report: Lund University of Technology*, 1996. [Online]. Available: http://www.lth.se/fileadmin/byggnadsmekanik/publications/tvsm1000/web1008.pdf. [Accessed: 14-Mar-2016].

[110] V. Koivu, "Analysis of Fluid Flow Through Porous Media Based on X-Ray," University of Oulu, Doctroal Thesis, 2010.

[111] T. Stylianopoulos, A. Yeckel, J. J. Derby, X. J. Luo, M. S. Shephard, E. a. Sander, and V. H. Barocas, "Permeability calculations in three-dimensional isotropic and oriented fiber networks," *Physics of Fluids*, vol. 20, no. 12, pp. 1–10, 2008.

[112] P. C. Carman, "Fluid flow through granular beds," *Transactions of the Institution of Chemical Engineers.*, vol. 15, pp. S32–S48, 1937.

[113] R. G. Holdich, "Fluid flow in porous media," in *Fundamentals of particle technology*, Loughborough: Midland Information Technology and Publishing, 2002, pp. 21–28.

[114] S. Ergun and a. a. Orning, "Fluid Flow through Randomly Packed Columns and Fluidized Beds," *Industrial & Engineering Chemistry*, vol. 41, no. 6, pp. 1179–1184, 1949.

[115] J. Happel, "Viscous flow relative to arrays of cylinders," *American Institute of Chemical Engineers*, vol. 5, no. 2, pp. 174–177, 1959.

[116] G. W. Jackson and D. F. James, "The permeability of fibrous porous media," *Canadian Society for Chemical Engineering*, vol. 64, no. 6, pp. 364–374, 1986.

[117] B. Rimez, "Calculations used in porometry." Porometer, EKE, Belgium, pp. 1–4, 2013.

[118] A. Karamanos, A. Papadopoulos, and D. Anastasellos, "Heat transfer phenomena in fibrous insulating materials," *Mechanical Engineering*, 2006.

[Online]. Available: http://www.geolan.gr/sappek/docs/publications/article_6.pdf. [Accessed: 14-Mar-2016].

[119] J. Ordonez-Miranda and J. J. Alvarado-Gil, "Effect of the pore shape on the thermal conductivity of porous media," *Journal of Materials Science*, vol. 47, no. 18, pp. 6733–6740, 2012.

[120] J. C. Groen, L. a a Peffer, and J. Pérez-Ramírez, "Pore size determination in modified micro- and mesoporous materials. Pitfalls and limitations in gas adsorption data analysis," *Microporous and Mesoporous Materials*, vol. 60, no. 1–3, pp. 1–17, 2003.

[121] L. Ruggieri, T. Gea, A. Artola, and A. Sánchez, "Air filled porosity measurements by air pycnometry in the composting process: A review and a correlation analysis," *Bioresource Technology*, vol. 100, no. 10, pp. 2655–2666, 2009.

[122] C. M. Gribble, G. P. Matthews, G. M. Laudone, A. Turner, C. J. Ridgway, J. Schoelkopf, and P. a C. Gane, "Porometry, porosimetry, image analysis and void network modelling in the study of the pore-level properties of filters," *Chemical Engineering Science*, vol. 66, no. 16, pp. 3701–3709, 2011.

[123] P. A. Webb, "Poresizer 9320 Data collection, Reduction and Presentation." Micromeritics, pp. 1–17, 1993.

[124] S. Chatterji, "A discussion of the paper 'Mercury porosimetry—an inappropriate method for the measurement of pore size distributions in cement-based materials' by S. Diamond," *Cement and Concrete Research*, vol. 31, no. 11, pp. 1657–1658, 2001.

[125] Porous Materials INC, "PMI capillary flow porometer," *Product brochure*, 2015. [Online]. Available: http://www.pmiapp.com/products/productPages/capFlow.html. [Accessed: 14-Mar-2016].

[126] ASTM F778, *Standard Methods for Gas Flow Resistance Testing of Filtration Media*. ASTM, 2007.

[127] Micromeritics, "Gas sorption Analyses," *Product brochure*, 2012. [Online]. Available: http://www.micromeritics.com/Product-Showcase.aspx. [Accessed: 14-Mar-2016].

[128] W. C. Bae, S. Patil, R. Biswas, S. Li, E. Y. Chang, S. Statum, D. D. D'Lima, C. B. Chung, and J. Du, "Magnetic resonance imaging assessed cortical porosity is highly correlated with µCT porosity," *Bone*, vol. 66, pp. 56–61, 2014.

[129] G. N. Okolo, R. C. Everson, H. W. J. P. Neomagus, M. J. Roberts, and R. Sakurovs, "Comparing the porosity and surface areas of coal as measured by gas adsorption, mercury intrusion and SAXS techniques," *Fuel*, vol. 141, pp. 293–304, 2015.

[130] Y. Sakamoto, M. Kaneda, O. Terasaki, D. Y. Zhao, J. M. Kim, G. Stucky, H. J. Shin, and R. Ryoo, "Direct imaging of the pores and cages of three-dimensional mesoporous materials.," *Nature*, vol. 408, no. 6811, pp. 449–453, 2000.

[131] J. Martínez-Martínez, D. Benavente, and M. a. García del Cura, "Petrographic quantification of brecciated rocks by image analysis. Application to the interpretation of elastic wave velocities," *Engineering Geology*, vol. 90, no. 1–2, pp. 41–54, 2007.

[132] J. Ghiasi-Freez, I. Soleimanpour, A. Kadkhodaie-Ilkhchi, M. Ziaii, M. Sedighi, and A. Hatampour, "Semi-automated porosity identification from thin section images using image analysis and intelligent discriminant classifiers," *Computers and Geosciences*, vol. 45, pp. 36–45, 2012.

[133] J. M. Prats-Montalbán, a. de Juan, and a. Ferrer, "Multivariate image analysis: A review with applications," *Chemometrics and Intelligent Laboratory Systems*,

vol. 107, no. 1, pp. 1–23, 2011.

[134] ASTM, "C373 - 88 Standard Test Method for Water Absorption, Bulk Density, Apparent Porosity, and Apparent Specific Gravity of Fired Whiteware Products." pp. 1–3, 1999.

[135] M. Valkonen, "Training based segmentation of electron microscope images," Tampere University of Technology, MSc Thesis, 2015.

[136] National Institutes of Health, "ImageJ," *Image Processing and Analysis in Java v 1.47J*, 2013. [Online]. Available: http://rsbweb.nih.gov/ij/index.html.

[137] M. Vilkko and T. Roinila, "Designing Maximum Length Sequence Signal for Frequency Response Measurement of Switched Mode Converters," in *Nordic Workshop on Power and Industrial Electronics*, 2008, pp. 1–6.

[138] A. Ojuva, F. Akhtar, A. P. Tomsia, and L. Bergström, "Laminated adsorbents with very rapid CO2 uptake by freeze-casting of zeolites," *ACS Applied Materials and Interfaces*, vol. 5, no. 7, pp. 2669–2676, 2013.

[139] J. Seville, T. G. Chuah, V. Sibanda, and P. Knight, "Gas cleaning at high temperatures using rigid ceramic filters," *Advanced Powder Technology*, vol. 14, no. 6, pp. 657–672, 2003.

[140] J. P. Heller and J. V. McLemore, "Miniporopermeameter," US patent 5,373,7271994.

[141] S. Diamond, "Mercury porosimetry An inappropriate method for the measurement of pore size distributions in cement-based materials," vol. 30, pp. 1517–1525, 2000.

[142] M. Järveläinen, T. Yli-hallila, T. Salpavaara, J. Verho, M. Vilkko, and E. Levänen, "Kolloidisten suspensioiden online -analysointi: tutkimuksesta liiketoimintaa," *Materia-lehti*, vol. 5. Vuorimiesyhdistys-Bergsmannaföreningen ry, pp. 54–57, 2015.

[143] J. Clayton, "Reviewing Current Practice in Powder Testing," *Organic Process Research & Development*, p. 140415130544007, 2014.

[144] P. Müller and J. Tomas, "Simulation and calibration of granules using the discrete element method," *Particuology*, vol. 12, no. 1, pp. 40–43, 2014.

[145] R.Thyagarajan, G. M. D. Cantin, B. P. Kashyap, and C. J. Bettles, "Modelling compaction behaviour of nickel–phosphorus and nickel–boron electroless coated titanium powders," *Powder Technology*, vol. 274, pp. 53–61, 2015.

[146] M. Järveläinen, E. Levänen, and T. Mäntylä, "Use of uniaxial compression in determining the fracture strength of granules in powders." ECerS XII, 12th Conference of the European Ceramic Society, Stockholm, 2011.

[147] F. Carrique, E. Ruiz-Reina, R. Roa, F. J. Arroyo, and Á. V. Delgado, "General electrokinetic model for concentrated suspensions in aqueous electrolyte solutions: Electrophoretic mobility and electrical conductivity in static electric fields," *Journal of Colloid and Interface Science*, vol. 455, no. July, pp. 46–54, 2015.

[148] V. Heuer, G. Walter, and I. Hutchings, "High temperature erosion of fibrous ceramic components by solid particle impact," *Wear*, pp. 257–262, 1999.

[149] V. Heuer, G. Walter, and I. . Hutchings, "A study of the erosive wear of fibrous ceramic components by solid particle impact," *Wear*, vol. 225–229, pp. 493–501, Apr. 1999.

[150] F. P. Beer, E. R. Johnston, J. T. DeWolf, and D. F. Mazurek, "Mechanics of Materials (Sixth Edition)," p. 838, 2012.

[151] U. Kanerva, T. Suhonen, J. Lagerbom, and E. Levänen, "Evaluation of crushing strength of spray-dried MgAl2O4 granule beds," *Ceramics International*, vol. 41,

no. 7, pp. 8494–8500, 2015.

[152] M. Samet, V. Levchenko, G. Boiteux, G. Seytre, a. Kallel, and a. Serghei, "Electrode polarization vs. Maxwell-Wagner-Sillars interfacial polarization in dielectric spectra of materials: Characteristic frequencies and scaling laws," *The Journal of Chemical Physics*, vol. 142, no. 19, p. 194703, 2015.

[153] Z. Ahmad, "Polymeric Dielectric Materials," in *Dielectric Material*, M. A. Silaghi, Ed. InTech, 2012, pp. 3–26.

[154] D. V. Wilbrink, L. A. A. Beex, and R. H. J. Peerlings, "A discrete network model for bond failure and frictional sliding in fibrous materials," *International Journal of Solids and Structures*, vol. 50, no. 9, pp. 1354–1363, May 2013.

[155] K. Niskanen and H. Rajatora, "Statistical geometry of paper cross-sections," *Journal of Pulp and Paper Science*, vol. 28, no. 7, p. 228, 2002.

[156] D. Tsarouchas and A. E. Markaki, "Extraction of fibre network architecture by X-ray tomography and prediction of elastic properties using an affine analytical model," *Acta Materialia*, vol. 59, no. 18, pp. 6989–7002, Oct. 2011.

[157] A. P. Roberts and E. J. Garboczi, "Elastic Properties of Model Porous Ceramics," *Journal of the American Ceramic Society*, vol. 83, no. 12, pp. 3041–3048, 2000.

[158] L. J. Gibson and M. F. Ashby, *Cellular Solids: Structure and Properties*, 2nd ed. Cambridge University Press, 1997.

[159] K. U. O'Kelly, a. J. Carr, and B. a O. McCormack, "Minimum solid area models applied to the prediction of Young's modulus for cancellous bone," *Journal of Materials Science: Materials in Medicine*, vol. 14, no. 4, pp. 379–384, 2003.

[160] S. Wild, "A discussion of the paper 'mercury porosimetry - An inappropriate method for the measurement of pore size distributions in cement-based materials' by S. Diamond [1] (multiple letters)," *Cement and Concrete Research*, vol. 31, no. 11, pp. 1653–1656, 2001.

[161] M. R. Landry, "Thermoporometry by differential scanning calorimetry: Experimental considerations and applications," *Thermochimica Acta*, vol. 433, no. 1–2, pp. 27–50, 2005.

Publication I

USE OF THERMAL IMAGING IN CHARACTERIZATION OF CE-RAMIC FIBER STRUCTURES

by

Järveläinen Matti, Keskinen Lassi & Levänen Erkki

Use of thermal imaging in characterization of ceramic fiber structures

Matti Järveläinen[1], Lassi Keskinen and Erkki Levänen
Department of Materials Science, Tampere University of Technology, P.O.Box 589, FIN-33101 Tampere, Finland

E-mail: matti.jarvelainen@tut.fi

Abstract. Fibrous bodies that contain open porosity can have a very heterogeneous structure that is difficult to characterize in terms of local flow resistance changes within the same sample. This article presents a method that is applicable for a quick analysis of flow distribution even with large samples. In this first attempt to understand how our flow distribution thermal imaging works, we present how the measuring parameters and the results correlate with sample's thickness and density. The results indicate that our method can quickly make a distinction between areas that have different flow resistances because of variations in the sample's density or wall thickness.

1. Introduction

Use of fibrous ceramics is widespread in high temperature applications such as furnace linings [1] and hot gas filter elements [2,3]. In some applications it is necessary to produce an even gas flow distribution within the same product because in the case of uneven flow distribution the product may malfunction. In filtration applications the filtration characteristics [4] and the cleaning of filter elements [5] depend on their structure. In addition, the mechanical characteristics of fibrous bodies are affected by uneven wall thickness and changes in bulk density, which are both difficult to measure.

Conventionally, a permeability measurement [6] is used to analyze the flow resistance and changes in it. While the conventional methods can be reliable and fast to analyze the sample as a whole, they cannot be easily used to find differences within a same sample. Because of this a method better than the conventional flow permeability measurement is needed for local permeability analysis.

Thermal imaging has been used in non-destructive testing before [7] but we have invented another way to take advantage of it. We have noticed that a randomly oriented fibrous structure heats faster in certain areas when hot air flows through it. This takes place due to local differences in the air permeability that in this case is mostly controlled by the wall thickness and bulk density of the sample.

2. Materials and Methods

2.1. Thermal imaging system

Measurement system that we used is presented in figure 1. The system included a thermal camera (FLIR Thermacam PM595), length scale, and an adjustable air inlet. Air was blown through a porous sample while its surface was imaged with thermal camera. Air temperature and velocity was varied in the experiments. Sample dimensions and its thermal diffusivity are presented in table 1.

---

[1] To whom any correspondence should be addressed.
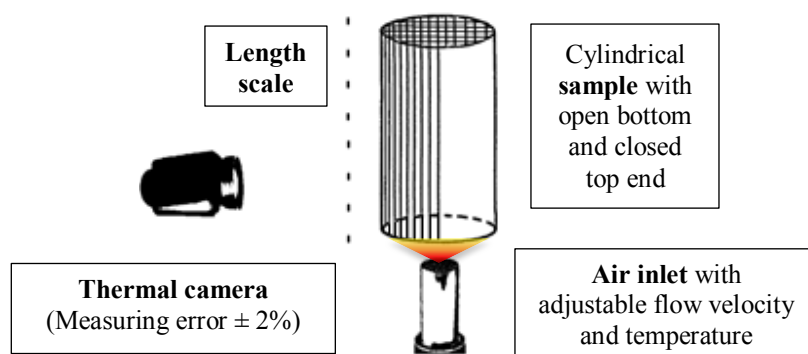
Figure 1. A schematic presentation of the thermal imaging setup.

2.2. Material

The materials in these experiments were composed of non-oriented, silicate based fibers, and some non-fibrous areas. An example of microstructure of the tested material is shown in figure 2. The fiber dimensions, size of non-fibrous parts, and material compositions are presented in table 1.
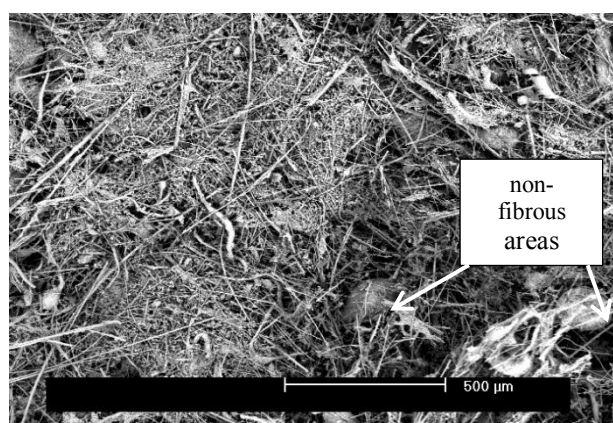
Figure 2. SE-image of the studied fiber structure.

The pore characterization was carried out with capillary flow porometry and mercury porosimetry. However the highly heterogeneous pore structure and a large size of the samples rendered the exact characterization of the material very difficult. Table 1 presents the measured pore characteristics.

Table 1. Approximate material parameters.

Dimensions	Length [m]	2.4
	Radius [m]	0.2
	Wall thickness [m]	0.02
Composition	mostly Al_2SiO_5, $CaSiO_3$ and amorphous SiO_2	
Microstructure	Fiber diameter [μm]	1 – 10
	Fiber length [μm]	below 1000
	Non-fibrous [μm]	10 – 500
Pore characteristics	Mean flow pore size [μm]	4[a]
	Average pore diameter [μm]	4[b]
	Largest through pore [μm]	39[a]
	Porosity [%]	80[b]
Thermal diffusivity	@200°C [mm^2/s]	0.3[c]

[a] PMI capillary flow porometer   [b] Micrometrics poresizer 9320   [c] NETZSCH 457 MicroFlash

3. Results
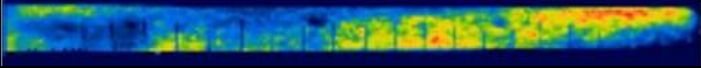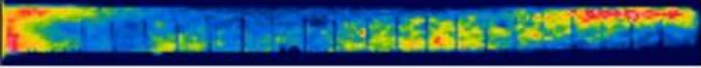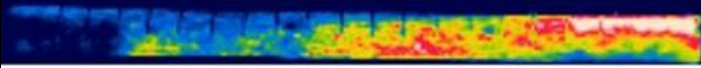
Tested samples behaved in two distinctive ways. In the first type 'striped' sample, hot air seemed to form stripes in the thermal images along the length of the sample, while in the second type 'spotted' sample, large cold and hot spots formed. Examples of the two types are presented in the figure 3. The 'spotted' type samples were mostly used in the studies but the 'striped' sample was used in the experiment in section 3.2 to show that wall thickness is not the only factor that determines the heating rate in the samples.
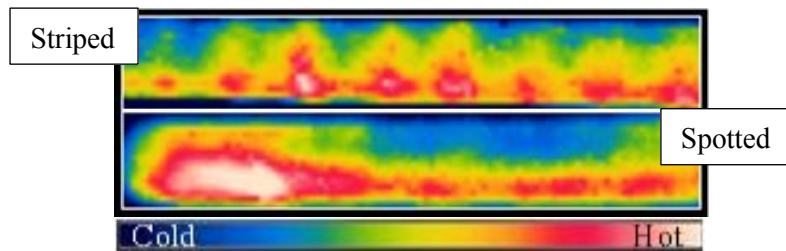
Figure 3. Thermal images of two sample types.

3.1. Effect of measuring variables

Preliminary measurements were carried out in order to see how the measuring variables, *air temperature* and *flow velocity*, affect the measurement. In figure 4 a same sample is first heated with a standard flow rate and temperature (reference), then with a flow velocity twice as high, then with temperature and flow velocity twice as high, and finally with the air flow from the opposite direction.

	Thermal Images	Parameters [°C]/ [l/min]	Time [sec]	Temp. [°C] Max/Min/ Ave
Ref.		100/500	535	69/22/56
2x Flow		100/1000	195	72/23/53
2x Flow 2x Temp		200/1000	90	88/33/63
Flow reversed		200/1000	120	106/51/70

Figure 4. Effect of changing measurement parameters. Time is heating time during image capture.

3.2. Correlation of thickness and temperature variations

Thickness changes and a thermal image of a 'spotted' sample are presented in figure 5a. Thickness is measured in seven places across the length of the sample. Another thickness correlation is presented in figure 5b where in the 'spotted' sample it is obvious that the faster heating rate on the left side is caused by smaller wall thickness and thus higher permeability, whereas in the 'striped' sample there is little correlation between the heating rate and wall thickness. In this case the heating rate differences have to be caused by some other factor, such as density variations between the cold and hot areas.
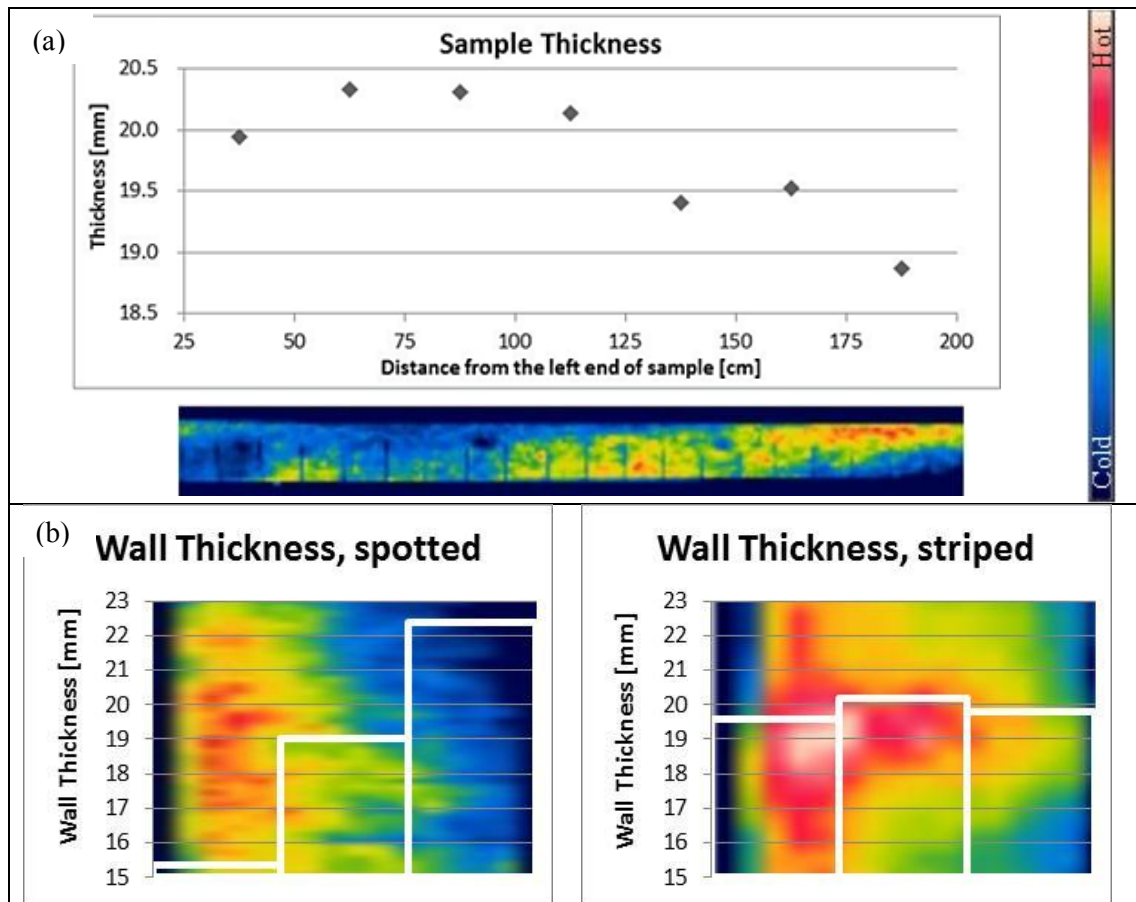
Figure 5a. Sample thicknesses and its thermal image aligned together.
5b. Wall thicknesses measured from three spots, thermal images aligned on the background.

3.3. Correlation of density and temperature variations

Bulk density and a thermal image of a 'spotted' sample are presented in figure 6. Density changes were calculated from weights and volume measurements that were carried out from dissected sample images using image processing methods.
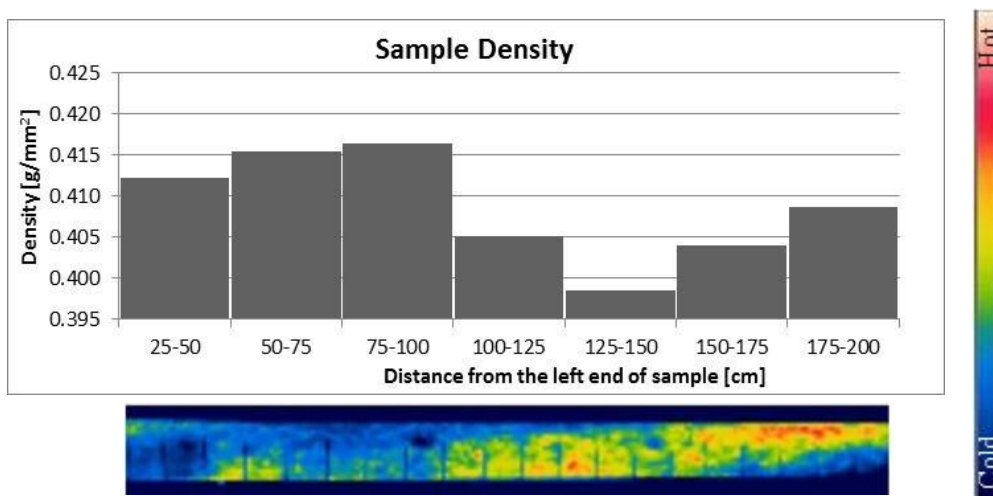
Figure 6. Sample density and its thermal image aligned together.

3.4. Correlation of density x thickness and temperature variations

Average thickness and density of a 'spotted' sample from the above figures 5A and 6 are multiplied and the result is plotted together with the thermal image in figure 7. This is done in order to find out if this rough estimate of permeability is a function of both the density and thickness. This estimate does not take into account the pore characteristics that will affect the permeability but it still leads to a higher correlation than the ones presented before. This is further discussed in section 4.
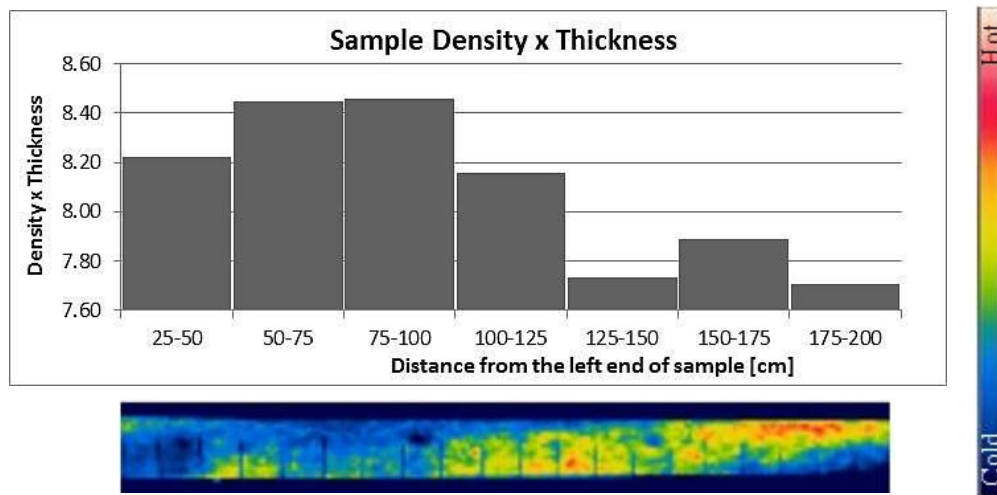
Figure 7. Sample density times thickness and its thermal image aligned together.

4. Discussion

First thing to notice in the above thermal images is that certain areas of the samples heat faster. In the section 3.1 we showed that this takes place regardless of the gas injection velocity, temperature, and direction of the gas flow. Together these prove that the heating rate differences are caused by certain characteristics of the sample, not the measuring setup. In order to find the dominant character that determines the heating rate in different areas, we visually correlated the thermal images with the local thickness and density of the samples. In the figure 5b the thermal image of a 'spotted' sample seemed to contain hot and cold areas as a result of the variation in thickness of the sample. However, in the thermal image of the 'striped' sample, in the same figure, hot and cold areas were seen regardless of the negligible changes in wall thickness. This led us to understand that the thickness is not the only factor that controls the heating. After that we studied how density affects the heating rate and the correlation is presented in figure 6. Visual correlation is a little higher with density than with the wall thickness that indicates that the density dominates the heating rate over the wall thickness in this study.

Yet even with a 'spotted' sample the correlation seems to be the highest with the computational factor "thickness times density" that is presented in figure 7. Thus it can be deducted that the heating rate, in our particular experiment, is fixed by the relative flow resistance of the sample that is, at least partially a combination of the samples thickness and density. In this study we examined the samples only in terms of density and thickness changes but it is obvious that also the factors related to pore characteristics have an important role in the flow resistance as is shown by [8]. These characteristics are unfortunately difficult to measure in the heterogeneous fiber bodies.

The measurements were carried out with a relatively cool air and high flow velocity which is especially important if the samples have high thermal diffusivity. With highly diffusive samples the high flow velocity eliminates the possibility of remarkable thermal diffusion [9] through the material which would have an effect on the measurements. In addition to choosing the right measuring parameters, we had samples that had a low thermal diffusivity as presented in table 1. Thus we believe that the differences in the heating rates are solely caused by differences in flow distribution of the

samples. This is simply the cause of more hot air flowing through the areas where the permeability is higher, and as the samples surface is comparatively even the more porous areas heat faster. The highest correlation would undoubtedly be found with the heating rate and permeability as it would also take into account the effect of pore characteristics. This is still to be studied and takes time because the local permeability distribution is difficult to measure.

5. Conclusions

In this article we presented a method for analysing flow distribution with thermal camera and hot gas. With the acquired results we have formed a basis for thermal permeability measuring. Comparing the new method to conventional permeability measurement that includes flow and pressure meters, the new one is faster and can possibly find smaller permeability differences if the measuring parameters are chosen correctly. Another strength of this investigated method, is that it can spot differences within the same sample. Even difficult, highly heterogeneous samples, such as the ones analysed in this article, can be measured.

With a small effort this method could be used for instance to ensure an even production quality in terms of permeability of the product or it could be used to analyse local permeability changes, for instance in filtration applications. Experiments presented in this article were carried out for silicate-based fibrous ceramics having low density and thermal diffusivity. The method would undoubtedly be applicable also for other samples if the ratio between the permeability and thermal diffusivity of the them is high enough. In the case of very low ratio, heat conducting through the sample might affect the results. Even in this case the method might be used if the imaged surface was first coated with highly heat absorbing material such as graphite that would promote the heating caused by permeability in favour of the heat conducting through the sample.

References

[1] ASM 1995 Monolithic and Fibrous Refractories *ASM Engineered Materials Handbook* (ASM International, in ASM Handbooks online)
[2] Heidenreich S 2013 Hot gas filtration – A review *Fuel* **104** 83–94
[3] Seville J, Chuah T G, Sibanda V and Knight P 2003 Gas cleaning at high temperatures using rigid ceramic filters *Advanced Powder Technology* **14** 657–72
[4] Sharma S D and Carras J N 2009 FUELS - HYDROGEN PRODUCTION | Gas Cleaning: Barrier Filters *Encyclopedia of Electrochemical Power Sources* ed J Garche (Amsterdam: Elsevier) pp 313–8
[5] Kanaoka C and Amornkitbamrung M 2001 Effect of filter permeability on the release of captured dust from a rigid ceramic filter surface *Powder Technology* **118** 113–20
[6] ASTM F778 2007 *Standard Methods for Gas Flow Resistance Testing of Filtration Media*
[7] Chrzanowski K and Park S 2001 Evaluation of thermal cameras for non-destructive thermal testing applications *Infrared physics & technology* **42** 101–5
[8] Mancin S, Zilio C, Cavallini A and Rossetto L 2010 Pressure drop during air flow in aluminum foams *International Journal of Heat and Mass Transfer* **53** 3121–30
[9] Maqsood A, Anis-ur-Rehman M and Gumen V 2000 Thermal conductivity of ceramic fibres as a function of temperature and press load *Journal of Physics D: Applied Physics* **33** 2057–63

Publication II

CHARACTERIZATION OF POROUS CERAMICS BY USING FRE-QUENCY-RESPONSE METHOD

by

Järveläinen Matti, Salpavaara Timo, Seppälä Sari, Roinila Tomi, Yli-Hallila Teemu,
Levänen Erkki & Vilkko Matti

Characterizing Porous Ceramics by Frequency-Response Method

M. Järveläinen* T. Salpavaara**
S. Seppälä* T. Roinila** T. Yli-Hallila**
E. Levänen* M. Vilkko**

*Department of Materials Science, Tampere University of Technology, P.O. Box 589, FI-33101 Tampere, Finland
** Department of Automation Science and Engineering, Tampere University of Technology, P.O. Box 692, FI-33101
Tampere, Finland

Abstract: Nondestructively determining pore properties of ceramic materials is essential in many industrial applications. There are several limitations in the existing characterization methods, so new techniques are required to meet the increasing demands of analysis. This paper examines the possible use of an electrical frequency-response method based on broadband excitation and Fourier techniques to characterize porous ceramic materials. The applied method provides a non-destructive, online characterization technique that is fast and can be applied inexpensively. In this article, ceramic samples with three different pore characteristics were measured by the frequency-response method that used a pseudo-random binary sequence. A sample of material was placed between the plates of a capacitor, and the capacitance was measured. Material properties, such as porosity, influence the permittivity value of the material. The samples with different porosities can be distinguished by analyzing the capacitance of the capacitor.

Keywords: capacitors, characterization, density measurements, frequency-response methods, impulse signals, permittivity, polarization analysis, pseudo random sequences, signal detection

1. INTRODUCTION

The number of ceramic materials used in functional and construction applications in industrial environments is continuously increasing. The main reason is their attractive properties, such as high temperature, chemical resistance, hardness, and the potential to easily tailor the pore characteristics in a controlled manner. Ceramic materials are used in critical process components in challenging environments, such as in the presence of corrosive acids and bases, because no other material can withstand the challenging atmospheres.

This study aims to develop a fast, continuous, online, and onsite pore characterization method, based on frequency-response measurements for ceramic materials in industrial applications. Traditional, nondestructive testing methods have limitations, such as cost, sample size, and slowness, so there is a strong need for the frequency-response technique. In an industrial process, this could mean improving quality control, safety, and efficiency. In addition to porosity measurements, this method could have other interesting applications. Porosity influences other important properties of ceramics, such as modulus of elasticity (Asmaniet al. 2001), strength (Coble et al. 1956), and thermal insulation ability (Sumirat et al. 2006). Furthermore, porosity has a functional purpose in many applications (Studart et al. 2006), such as ceramic bio-implants (Kamitakahara et al. 2008, Niemelä et al. 2011), membranes (Ciora et al. 2003, Garmash et al. 1995), drug delivery (Ahuja et al. 2009), solid oxide fuel cells (Sanson et al. 2008), and absorbent structures (Ojuva et al. 2013, Vasiliev et al. 2010).

The frequency-response method in this article is an electrical porosity measurement based on different polarization behaviors of materials in alternating electric fields. As Lira-Olivares et al. (2000) stated the following polarization types are encountered in ceramics: Electronic, ionic, dipolar orientation, and Maxwell-Wagner-Sillars (Lira-Olivares et al., 2000). According to Richerson (2006), atoms and their bonding types affect material polarization sensitivity and rate (Richerson, 2006). These physical phenomena should enable discrimination of two phases by analyzing the disturbances in a sample polarity. The applicability of the frequency-response method in porosity measurements is studied by measuring the behavior of ceramic materials in alternating electric fields. Vila et al. (1998) found that porosities and impurities in ceramics influence measured permittivity and dielectric loss (Vila et al., 1998). This study clarifies how changes in porosity, such as differences in amounts of air and solids, affect the measured electrical properties.

The proposed frequency-response analytical method has several attractive features, such as flexibility in industrial applications, fastness, size scaling, and potential use as a non-destructive online tool. An electrical impulse, required as an excitation signal, is easy and straightforward to generate and use. Calculating the responses is based on simple Fourier techniques so are easy to implement in practice. We used a maximum-length binary sequence (MLBS) excitation to quickly measure a wide frequency band of materials. The MLBS excitation method is interesting because the energy density of the excitation is very even across the whole measuring range. In addition, because the MLBS has only two different signal values, it can be easily implemented with a low-cost application.

There are no existing methods that fulfill all the above-mentioned requirements. Mercury porosimetry (Giesche, 2006) analyzes small sample sizes and is destructive. Computed tomography (Taud et al. 2005) and magnetic resonance imaging (Fagan et al. 2005) are non-destructive, but measurements are slow. The same applies to gas-adsorption methods (Sing et al. 1985). The traditional Archimedes method can be used for big samples, but the measurement is time consuming and laborious. None of these methods can be used for continuous analysis.

2. METHODS AND MATERIALS

For the frequency-response measurement, samples were manufactured and characterized by Archimedes measurement. This section is divided into three parts. The first part considers the sample manufacturing and characterization, the second part considers signal generation, and the last part considers the applied equipment and the idea of the electrical frequency-response method.

2.1 Manufacturing and characterization of alumina samples

To study the functionality and sensitivity of the frequency-response method to measure porosity, ceramic sample series with various porosity properties were manufactured and characterized by the Archimedes method. Samples were made of aluminum oxide (alumina), because it is a common technical ceramic with well-known properties. Alumina has high resistivity and is an electrical insulator. Microstructure and impurities affect the electrical properties of alumina.

The sample series were manufactured by slip casting. By using three different sintering temperatures, samples with three different porosities were achieved.

Slip casting of alumina samples. In slip casting, a ceramic component is produced from a slip containing ceramic powder, water, and additives. First a dispersing agent (Dispex A40) was stirred into the water. The dispersing agent worked as a stabilizer in the slip. Then alumina powder (Al_2O_3, Martinswerk MR70) was added to the mixture. After the powder was stirred until it was homogenous, a binder (Raisional 116) was added to increase pre-sintering strength of the component. Finally, polyethylene glycol was stirred into the slip to increase processability.

The prepared slip was poured into a gypsum mold, where the solid content compacted to the mold walls as water was removed by capillary action. When the component was solidified, the mold was removed. Before sintering, the component is known as a green body. To avoid cracking, the green body was dried before sintering for 24 hours at 45ºC, followed by 24 hours at 90ºC.

Sintering. After drying and processing, the green bodies were heated at high temperatures, where the structure of the ceramics became denser due to diffusion of atoms. This is called *sintering*. This also caused the component to shrink. We selected three different sintering temperatures: 1100ºC, 1300ºC, and 1550ºC. Heat treatment was carried out in two steps. First, the green bodies were heated at 1ºC/min up to 200ºC, with a 60-minute dwell. The ceramics were then heated at 1ºC/min up to the sintering temperature, with a 120-

minute dwell. The cooling rate after heating was 5ºC/minute. After sintering, the samples were characterized by the Archimedes method. Microstructures were studied by scanning electron microscopy (SEM) (Phillips XL-30).

Material characterization. Density and porosity properties of the samples were determined by the Archimedes method. The test was performed according to ASTM standard (ASTM Standard C373-88) to four representative samples from each sintering temperature. The test measured dry mass, saturated mass, and mass when the sample was suspended in water. From these values, porosities and densities were determined. Average values of the results are presented in Table 1. A theoretical density of 3.98g/cm^3 was used in the calculations.

Table 1. Results of Archimedes test; porosity properties of the samples.

Sintering temperature [°C]	Bulk density [g/cm^3]	Apparent density [g/cm^3]	Open porosity [%]	Total porosity [%]
1550	3.85	3.86	0.09	3.23
1300	3.27	3.89	15.78	17.94
1100	2.66	3.89	31.62	33.10

In addition to the Archimedes test, the samples were imaged by SEM. The samples were cut, ground, and polished. Fig. 1 shows the sintering shrinkages and microstructures of cross-sectional areas.
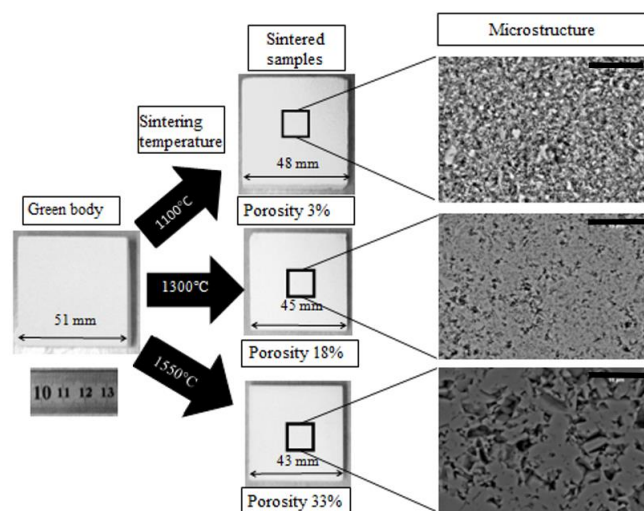

Fig. 1. Sample in green state and after sintering. The length of the black scale bars in the SEM-photos is 10 μm.

2.2 Frequency-response measurement

In steady state, for small-signal disturbances, the analyzed system is linear and time-invariant. According to basic control theory, this type of system is fully characterized by its impulse response in the time domain, which can be transformed to the frequency domain and presented as a frequency-response function.
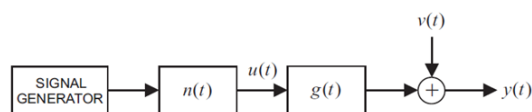

Fig. 2. Typical frequency-response-measurement setup.

Fig. 2 shows a typical frequency-response-measurement setup, in which the device under test, presented by the system impulse-response function $g(t)$, is to be identified. The designed excitation is first processed (filtered and amplified by $n[t]$), yielding the actual excitation $u(t)$. The device under test is then perturbed with $u(t)$, yielding the corresponding output response $y(t)$. The measured signal is corrupted with noise, presented by $v(t)$. The noise resembles white noise and is uncorrelated with $u(t)$ and $y(t)$. All the signals are assumed to be zero-mean sequences. Applying cross correlation between the sampled input and output responses, an estimate of the frequency-response function is obtained as:

$$G(e^{jw\,T_s}) = \frac{1}{\alpha} \sum_{k=0}^{M-1} R_{uy}(m) e^{-jkw\,T_s} \qquad (1)$$

where M, α, T_s, and $R_{uy}(m)$ respectively denote the total length of collected data, the variance of $u(m)$, the sampling interval, and the cross-correlation function between the input and output signals (James, 2004). The requirement in (1) is that the system is perturbed with a signal resembling white noise, such as with maximum-length binary sequence (MLBS) (Godfrey, 1993). Other frequency-response-computation techniques can be found (e.g., Pintelon et al., 2001).

2.3 Maximum-length binary sequence

Pseudo-random binary sequence (PRBS) is a periodic broadband signal with the following properties:

1. The signal has two levels and can switch the level only at certain event points $t = 0, \Delta t, 2\Delta t, ...$

2. The change of signal level is predetermined, so that PRBS is deterministic and experiments are repeatable.

3. The sequence is periodic with period $T = N\Delta t$, where N is an odd integer

4. Within one period, there are $(N + 1)/2$ intervals when the signal is at one level and $(N − 1)/2$ intervals when it is at the other.

A PRBS is based on a sequence of length N. The most commonly used signals are based on maximum-length sequences (maximum-length binary sequence [MLBS]). Such sequences exist for $N = 2^n − 1$, where n is an integer. They are popular because they can be generated using feedback shift register circuits, as shown in Fig. 3.
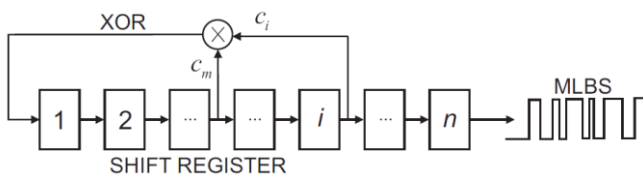
Fig. 3. *N*-bit shift register with XOR feedback for MLBS generation.

Table 2 shows an example of an output from a shift register circuit for generating an MLBS of length $2^4 − 1 = 15$. The feedback is generated from stages 1 and 4. All four columns in Table 1 produce the same MLBS. The register can be started with any number other than 0,0,0,0. In the example, the register starts from 0,0,0,1. Each binary number from 0,0,0,1 to 1,1,1,1 appears exactly once (the sequence starts repeating after 15 cycles). This is a general result for all MLBS (Godfrey, 1993). In practice, the values 0 and 1 are mapped to -1 and +1 to produce a symmetrical MLBS with an average close to zero.

Table 2: Maximum-length binary sequence from a four-stage shift register.

Shift	Stage 1	Stage 2	Stage 3	Stage 4
1	0	0	0	1
2	1	0	0	0
3	1	1	0	0
4	1	1	1	0
5	1	1	1	1
6	0	1	1	1
7	1	0	1	1
8	0	1	0	1
9	1	0	1	0
10	1	1	1	1
11	0	1	1	0
12	0	0	0	1
13	1	0	0	1
14	0	1	1	0
15	0	0	0	0
16	0	0	0	1

Selection of the feedback connections (stages) is important. Very few of the possible connections result in a sequence of the maximum length $2^n − 1$ (some sequences can be produced from several different stages). The linear feedback shift register can be described by a polynomial. The polynomial has a degree that equals the length of the register and has coefficients that are either 0 or 1 (depending on the applied stages). For example, the polynomial of the 15-bit-length MLBS (4-bit-length shift register) shown in Table 1 has a polynomial $x^4 + x + 1$ (the applied stages are 1 and 4; the 1 corresponds to the input of the first bit). A necessary, sufficient condition for the sequence to be maximal length is that the corresponding polynomial is primitive.

Fig. 4 shows the form of the power spectrum of the MLBS shown in Table 1. The sequence is generated at 10 kHz and has signal levels ±1 V. The power spectrum has an envelope and drops to zero at the generation frequency and its harmonics. The spectrum is given by

$$\Phi_{\mathrm{MLBS}}(q) = \frac{a^2\,(N+1)\sin^2\left(\pi q / N\right)}{N^2\left(\pi q / N\right)^2}, \quad q = \pm 1, \pm 2, ... \qquad (2)$$

where q denotes the sequence number of the spectral line, a is the signal amplitude, and N is the signal length.
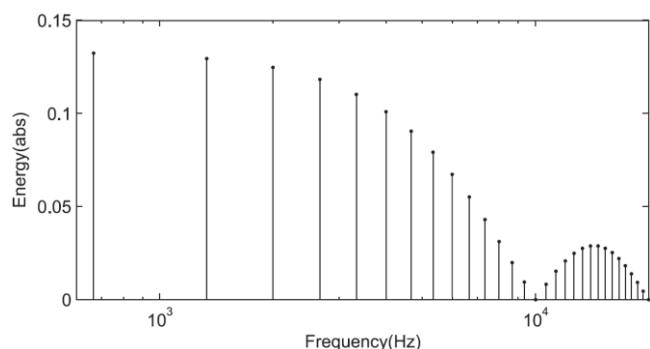
Fig. 4. Power spectrum of 15-bit-length MLBS generated at 10 kHz.

The MLBS x has the lowest possible peak factor $|x|_{peak}/x_{rms} = 1$ regardless of its length. Therefore, the sequence is well-suited for sensitive systems that require small-amplitude perturbation. Due to the deterministic nature of the sequence, the signal can be repeated and injected precisely, and the SNR can be increased by synchronous averaging of the response periods. Other advantages of the MLBS method include straightforward generation and design of the sequence. Because the MLBS has only two signal values, it can be generated with a low-cost application, the output of which can only cope with a small number of signal levels. This is not the case with multi-sine signals, which have an infinite number of signal levels.

2.4 Measurement system

The method for measuring porosity was based on the electric frequency-response measurement described in Section 2.2. The porosity affects the permittivity of a sample, altering the frequency response of the system. The required electronics of the measurement system were kept as simple as possible. The system was built to interface with National Instrument's PCI-6052E measurement card. The measurement card sent and measured an excitation of the system and also received the output signal of the system. The measurement system consisted of a resistor and a capacitor that formed a first-order low-pass-filter, presented in Fig. 5. The capacitor was designed so that the sample could be inserted between the capacitor plates in a controlled manner.

In the measurement, a sample was placed between the capacitor plates as a dielectric so that the relative permittivity of the sample affected the capacitor's capacitance. The ceramic samples were 12 mm thick and placed on a 3x3 cm electrode area that was made of circuit-board material. A ground plane was put on top of the sample. There was another ground plane under the electrode area on the other side of the capacitor plane. Due to the measurement arrangements, the total capacitance of the system consisted of both the capacitance of the sample capacitor and the system's stray capacitance, which was constant. The capacitor was connected to a 1-MΩ resistor to form a first-order low-pass filter, whose output was then buffered with an amplifier.
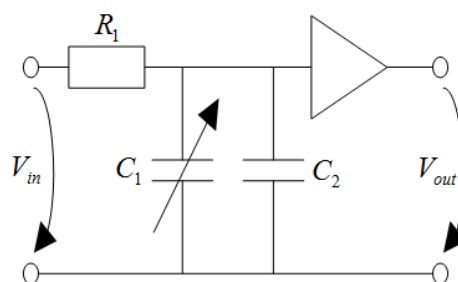
Fig. 5. First-order low-pass filter to measure the porosity of ceramics. The relative permittivity of samples affects the filter's capacitance, shown as C_1. C_2 represents the constant stray capacitance.

The MLBS was used as an input signal. The injection was 16,383-bit long and had amplitude of 1 V. The sampling rate was 100 kHz. The input signal was injected into the system four times and (1) was used to compute the frequency response. To eliminate transience and reduce deviation in the measurements, the frequency response was calculated from the mean of the last three of those signals and their responses. The higher sampling rate could have improved system performance, but the measurement card did not enable that.

3. RESULTS AND DISCUSSION

The frequency responses of alumina ceramics with different porosities were measured. After preparation, the samples were stored in room atmosphere. Before the measurements, all samples were oven-dried at 120°C for 24 hours to remove moisture, which would have interfered with measurements. After oven-drying, the samples were placed in a desiccator, where they were allowed to cool to air temperature. In addition to ceramic samples, the measurements were carried out with air and a reference sample made of polytetrafluoroethylene (PTFE). With these reference samples, the functionality of the measurement system was verified. The calculated magnitude responses are presented in Fig. 6. In the case of ceramic samples, the presented magnitude response was a mean of five measurements with different samples from each porosity group. PTFE was also measured five times. As presented in Fig. 6, the ceramic samples gave clearly distinguishable magnitude responses.
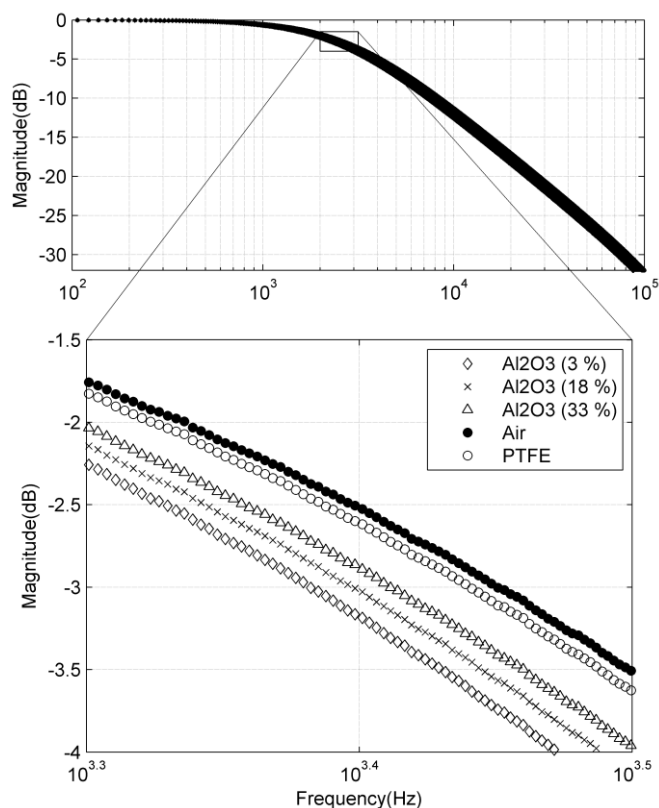
Fig. 6. Average magnitude responses of the three alumina groups having different porosities and the references, air and PTFE.

For further calculations, we chose the values of -3 dB cut-off frequencies, which are commonly used to describe the function of a low-pass filter. The system's total capacitance also can be determined from this value if resistance R is known. The total capacitance can be written as follows:

$$C = \frac{1}{2\pi R f} \qquad (3)$$

Cut-off frequencies and their standard deviations are presented in Table 3. Furthermore, an approximation of the capacitance caused by the sample was calculated. This was done by subtracting stray capacitance from the total capacitance. The stray capacitance was 55.7 pF from measurements.

Measurements of air, PTFE, and alumina produced expected results. The measurements showed that when the porosity increased, the cut-off frequency also increased, so the samples had lower capacitances. When measuring porous ceramics, there was more deviation than measuring nonporous materials such as PTFE. The porous samples were more prone to variations in air moisture and placement in the device.

Table 3. Cut-off frequencies of sample materials from magnitude responses in Fig. 6, -3 dB point, and calculated capacitances.

	Al_2O_3 3%	Al_2O_3 18%	Al_2O_3 33%	Air	PTFE
-3 dB cut-off frequency [Hz]	2412	2497	2580	2826	2759
Deviation of cut-off frequencies [Hz]	10.2	26.4	12.5	0.3	0.5
Total capacitance [pF]	66.0	63.7	61.7	56.3	57.7
Capacitance of the sample [pF]	10.3	8.1	6.0	0.7	2.0

The cut-off frequencies are presented as a function of the porosities in Fig. 7. There was a clear correlation between the magnitude response and the porosity. In addition to the relatively small measurement errors, variations were caused by the material. This is indicated by the horizontal error bars that denote the porosity variation.
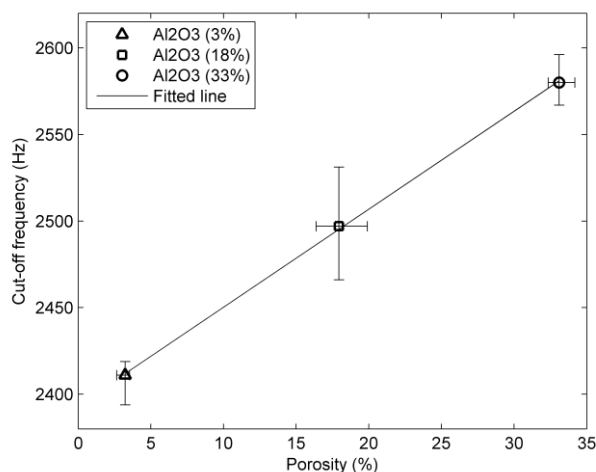
Fig. 7. Average, minimum, and maximum cut-off frequencies of each sample group, presented as a function of the total porosities from Table 1.

4. CONCLUSIONS

A frequency-response method, based on broadband excitation and Fourier techniques, was presented for characterizing porous ceramics. Series of measurements were performed with different alumina samples. The results included the cut-off frequencies, which were measured from individual ceramic samples. The relationship between the cut-off frequencies and porosities was studied.

There were three groups of samples with different porosities. The average porosities of the groups were 3 percent, 18 percent, and 33 percent. The results show that the resolution of the measurement system was sufficient to separate different porosity groups from each other. Still, the

performance of the measurement system must be increased if the system is to measure relative permittivity from different materials.

The presented frequency-response technique can be efficiently used as a non-destructive tool in online characterization of porous ceramics. Other advantages include flexibility, size scaling, and relatively simple computation algorithms required to compute the responses. Future research should study the influence of adsorbed water in porous structure on the electric frequency responses.

REFERENCES

Ahuja, G. and Pathak K. (2009). Porous carriers for controlled/modulated drug delivery. *Indian Journal of Pharmaceutical Sciences* Vol. 71, No. 6, 599–607.

Asmani, M., Kermel, C., Leriche, A., Ourak, M. (2001). Influence of porosity on Young's modulus and Poisson's ratio in alumina ceramics. *Journal of the European Ceramic Society* Vol. 21, 1081–1086.

ASTM Standard C373-88, Standard test method for water absorption, bulk density, apparent porosity, and apparent specific gravity of fired whiteware products.

Ciora, R. J. and Liu, P. K. T. (2003). Ceramic membranes for environmental related applications. *Fluid/Particle Separation Journal* Vol. 15, No. 1, 51–60.

Coble, R. L. and Kingery W. D. (1956). Effect of porosity on physical properties of sintered alumina. *Journal of American Ceramic Society* Vol. 39, No. 11, 377–385.

Fagan, A. J., Davies, G. R., Hutchison, J. M. S., et al. (2005). Development of a 3-D, multi-nuclear continuous wave NMR imaging system. *Journal of Magnetic Resonance* Vol. 176, No. 2, 140–150.

Garmash, E.P., Kryuchkov, Y. N. and Pavlikov, V.N. (1995). Ceramic membranes for ultra- and microfiltration (review). *Glass and Ceramics* Vol. 52, No. 6, 150–152.

Giesche, H. (2006). Mercury porosimetry: A general (practical) overview. *Particle & Particle Systems Characterization* Vol. 23, No. 1, 9–19.

Godfrey, K. (1991). Design and application of multifrequency signals. *Computing & Control Engineering Journal* Vol. 2, No. 4, 187–195.

Godfrey, K. (1993). *Perturbation Signals for System Identification*. Prentice Hall.

James, G. (2004). *Advanced Modern Engineering Mathematics. 3rd ed.* Pearson Education Limited.

Kamitakahara, M., Ohtsuki, C. and Miyazaki, T. (2008). Review paper: Behavior of ceramic biomaterials derived from tricalcium phosphate in physiological condition. *Journal of Biomaterials Application* Vol. 23, 197–212.

Lira-Olivares, J., Marcano, D., Lavelle, C. and Sánchez, F. G. (2000). Determination of porosity by dielectric permitivity measurements in porous ceramics. *Revista Latinoamericana de Metalurgia y Materiales* Vol. 20, No. 2, 68–79.

Niemelä, T., Aydogan, D. B., Hannula, M., et al. (2011). Determination of bioceramic filler distribution and porosity of self-reinforced bioabsorbable composites using micro-computed tomography. *Composites Part A: Applied Science and Manufacturing* Vol. 42, No. 5, 534–542.

Ojuva, A., Akhtar, F., Tomsia, A. P. and Bergström, L. (2013). Laminated adsorbents with very rapid CO_2 uptake by freeze-casting of zeolites. *ACS Applied Materials & Interfaces* Vol. 5, 2669–2676.

Pintelon, R., Schoukens, J. (2001). *System Identification: A Frequency Domain Approach*. IEEE Press.

Richerson, D. W. (2006). *Modern Ceramic Engineering: Properties, Processing, and Use in Design*. CRC Press.

Sanson, A., Pinasco, P. and Roncari, E. (2008). Influence of pore formers on slurry composition and microstructure of tape cast supporting anodes for SOFCs. *Journal of the European Ceramic Society* Vol. 28, No. 6, 1221–1226.

Sing, K. S., Everett, D., Haul, R. A., et al. (1985). Reporting physisorption data for gas/solid systems with special reference to the determination of surface area and porosity. *Pure & Applied Chemistry* Vol. 57, No. 4, 603–619.

Studart, A. R., Gonzenbach, U. T., Tervoort, E. and Gauckler, L. J. (2006). Processing routes to macroporous ceramics: A review. *Journal of the American Ceramic Society* Vol. 89, No. 6, 1771–1789.

Sumirat, I., Ando, Y. and Shimamura, S. (2006). Theoretical consideration of the effect of porosity on thermal conductivity of porous materials. *Journal of Porous Materials* Vol. 13, No. 3–4, 439–443.

Taud, H., Martinez-Angeles, R., Parrot, J. F. and Hernandez-Escobedo, L. (2005). Porosity estimation method by X-ray computed tomography. *Journal of Petroleum Science and Engineering* Vol. 47, No. 3–4, 209–217.

Vasiliev, P. O., Ojuva, A., Grins, J. and Bergström, L. (2010). The effect of temperature on the pulsed current processing behaviour and structural characteristics of porous ZSM-5 and zeolite Y monoliths. *Journal of the European Ceramic Society* Vol. 30, No. 14, 2977–2983.

Vila, R., Gonzalez, M., Molla, J. and Ibarra, A. (1998). Dielectric spectroscopy of alumina ceramics over a wide frequency range. *Journal of Nuclear Materials* Vol. 253, 141–148.

Publication III

MECHANICAL CHARACTERIZATION OF FIBER CERAMICS: EFFECT OF TEMPERATURE

by

Järveläinen Matti, Humalamäki Joonas, Laakso Jarmo & Levänen Erkki

Mechanical Characterization of Fiber Ceramics: Effect of Temperature[**]

By Matti Järveläinen,* Joonas Humalamäki, Jarmo Laakso and Erkki Levänen

1. Introduction

Ceramic fibers are used at high temperatures for thermal insulation and gas-solid separation. In several gas-filtration plants, the fiber ceramics have displaced the more advanced ceramic materials, such as silicon carbide,[1] because of their lower price and capability to form filter elements with lower pressure drop.[2] The use of fibers, instead of granular ceramics or metals,[2] in a filter element body is a relatively new approach that needs attention, especially in monitoring their service condition. New monitoring methods are needed because the phenomena controlling the lifetime of fibrous filter elements are different from granular elements. The differences are mostly caused by dissimilar manufacturing methods. The most basic differences are induced by how the main properties in granular filter elements, porosity, and mechanical strength, are generated. This is carried out by well understood control of granule size and sintering procedure. However, the elements composed of fibers are manufactured without sintering by using a slurry-based vacuum-forming process.[3] The sintering step with fibrous elements is obviated by using organic and inorganic binders dedicated to interlink the fibers to each other. Leaving out the sintering stage lowers the cost of fibrous elements, but leads to lowered mechanical properties.

Because of the relatively low mechanical properties of fibrous elements, it is important to understand how fibrous structures behave under mechanical load. Several studies have investigated that with conventional methods, such as mechanical testing by compressive and four-point bending tests.[4–6] However, due to the discontinuous and heterogeneous structure, it is unclear if conventional models, such as Weibull theory, are suitable to describe mechanical properties of these fibrous structures. Some authors have also attempted to characterize fibrous structures by mechanical modeling[7–9] but the downside of these discrete models is the rough assumption that fibrous structure consists of simple discrete elements connected by nodes. In reality, the structure is much

more complex as the fibers are often randomly oriented and kinked, and fiber diameter and length vary remarkably. In addition, other phases, such as binder can be present and are normally not evenly distributed (Figure 1). All of these factors impair the applicability of general models. It is also possible to measure the state of single fibers online,[10] but the applications for that are still far from commercial state.

Due to downsides of conventional mechanical testing and modeling, new mechanistic approaches have to be developed. We propose erosive-wear testing by grit blasting as a reliable experimental technique for characterizing these fibrous structures and demonstrate the technique's applicability to display the effect of thermal loading to fibrous aluminosilicates. Very few studies are focused on erosive wear of fibrous aluminosilicates.[11,12] Heuer et al. studied high temperature erosion of amorphous aluminosilicate fibers used in an insulation application. The insulator felts were either embrittled at high temperatures or only erosion-tested at high temperatures without prior embrittlening. In this case, embrittlement means that the fibrous structure becomes more brittle, that is, strain corresponding to ultimate strength decreases. Heuer noticed that erosion rate increased with temperature and concluded that there was a significant increase in erosion rate as the material was heated above 990 °C, which was above the temperature where mullite formed in the material he studied. Furthermore, when the material was embrittled by transforming amorphous aluminosilicates into cristobalite and mullite in 1,000 h heat treatment at 1,260 °C, the erosion rate was no longer after that affected by temperatures between 20 and 1,000 °C. Heuer did not show that high-temperature erosion tests can be used to predict ambient erosion of the samples' heat-treated at temperatures between 20 and 1,000 °C.

The previous studies clearly show that many fibrous structures undergo embrittlement at high temperatures.[4,5,11,12] We add to this by our present study where we performed room temperature grit blasting tests to heat-treated aluminosilicates in order to investigate if erosion rate is proportional to their thermal history, as Heuer et al stated. This work is also devoted to determine if mechanical properties measured by c-ring testing or acoustic response by resonant frequency testing can be linked with structural rigidization. Heuer's earlier article discusses embrittlement of the fibrous structures only after a phase change. We dispute that embrittlement is not just a high-temperature phenomenon linked to crystallization but also occurs at lower

[*] M. Järveläinen, J. Humalamäki, J. Laakso, E. Levänen
Department of Materials Science, Tampere University of Technology, P.O. Box 589 FIN-33101, Tampere, Finland
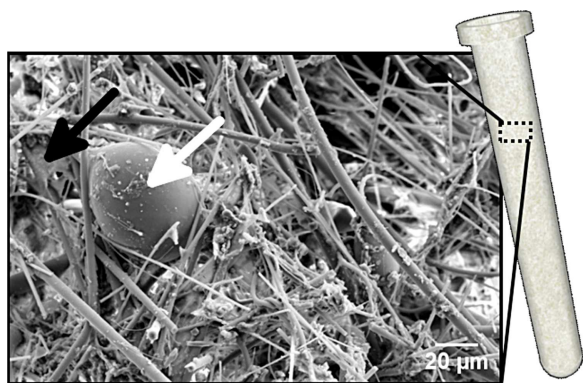E-mail: matti.jarvelainen@tut.fi

FULL PAPER

Fig. 1. Schematic of the studied filter element and a SEM image of the fibrous structure with inorganic binder (black arrow) and shot (white arrow).

temperatures by other mechanisms, such as sintering and viscous creep in amorphous materials. We propose that the fibers start to adhere by sintering with their neighbors at the different contact points which explains the structural embrittlement also observed below the crystallization temperature. This embrittlement is determined by the fiber's free length, that is, the average distance between its contact points.

2. Materials and Methods

2.1. Material

We demonstrated functionality of the studied methods with a tubular component for hot-gas filtration (schematic in Figure 1). According to manufacturer, the component consisted of tangled, mainly amorphous aluminosilicate fibers with a mass ratio of 51% SiO_2 and 49% Al_2O_3. The fibers were bound together with organic and inorganic (silica) binders. The structure was formed from flocked fiber-slurry by vacuum-process.[13]

Figure 1 shows the microstructure of the studied material. Due to the heterogeneity and large size of the investigated component, the characteristics below contain significant variations. The randomly oriented fibers were between 1 and 10 μm in diameter and shorter than 1,000 μm in length. The fibers were connected with an inorganic binder. The structure also contained improperly molten raw material ("shots," appearance of a drop), easily observed at the tips of some of the fibers ranging from 0 to 300 μm. Pores of the component where roughly characterized with a mercury porosimeter (Micromeritics poresizer 9320) by cutting three representative pieces (125 mm^3) from the component and measuring their effective porosity that was on average 80% (standard deviation 1.9). Average pore diameter was 4 μm (standard deviation 4.3) and the size distribution was wide from below 1 μm to above 110 μm.

2.2. Heat Treatments

Samples for c-ring testing, grit blasting, and impulse excitation were cut from the, initially cylindrical, fibrous aluminosilicate filter elements. After cutting to correct sample

sizes these specimen were heat-treated at 600, 700, 800, 900, and 1,050 °C for 10 h. The heating and cooling rates were 5 °C min^{-1}. These temperatures were selected to study if rigidization occurred at relatively low temperatures, especially those below mullite formation.

2.3. Material Characterization

2.3.1. Dilatometer

Dilatometer (Model DI-24, Adamel Lhomargy, Roissy en Brie, France) measurements with a 10-hour isotherm were carried out for each heat treatment temperatures to understand the sintering behavior of the samples. The samples were cut in radial direction of the filter element, and their size was the [sample wall thickness] $\times 7 \times 7$ mm^2. Wall thickness was 20.6 ± 3.3 mm.

2.3.2. XRD

In addition to dilatometer tests, XRD was used to study the changes in crystalline phases in the heat-treated samples. The measurements were carried out at room temperature between 10 and 80° angles by step size of 0.013°. The XRD measurements were carried out with a PAN analytical Empyrean X-ray diffractometer and monocromatized Cu(alfa) radiation. ICDD card files were used to analyze XRD data.

2.4. Methods

2.4.1. Grit Blasting

A sample from the filter element was axially cut into three 120° sections of 30 cm in length. The cut sections were heat-treated in a laboratory furnace. Figure 2 shows an overview of the grit-blasting apparatus. Tests were conducted in a cabinet (1). A 120°-cut sample (2) was attached to the sample holder (3) by Velcro tape (4). The grit-blasting gun was model FG Ghiotto 28HSS with a bottom container (5) and gun (6) units. The gun barrel (7) length was 83 mm and the inner diameter was 6 mm. Air pressure was limited to 0.65 bar, with an outward relief valve. Glass grit was sucked by this negative pressure from the can into the barrel and blasted at a 90° angle onto the sample surface in 5 s bursts. Blast onset and offset was manually controlled with a control valve (8).

Before each blast, the distance from the end of the gun barrel to the sample surface was adjusted to 35 mm. A 5 s-blast was applied to the sample with previous experimental parameters. Consistency of the blast was ensured with the following measures: A pressurized, air-operated vibrator to even grit flow; keeping the glass-grit surface at 60 mm from the mouth of the container; periodic blasting into the reference sample; and periodically mixing and replacing the grit. Finally, the depth of the each crater created by the blast was measured with a slide gauge with 0.01 mm accuracy.

The glass grit was round, with diameters between 150 and 250 μm. Mass flow of the glass grit was measured by performing 19 5 s blasts to a 45 μm sieve and weighting the mass gain of the sieve after each blast. Mass flow values varied
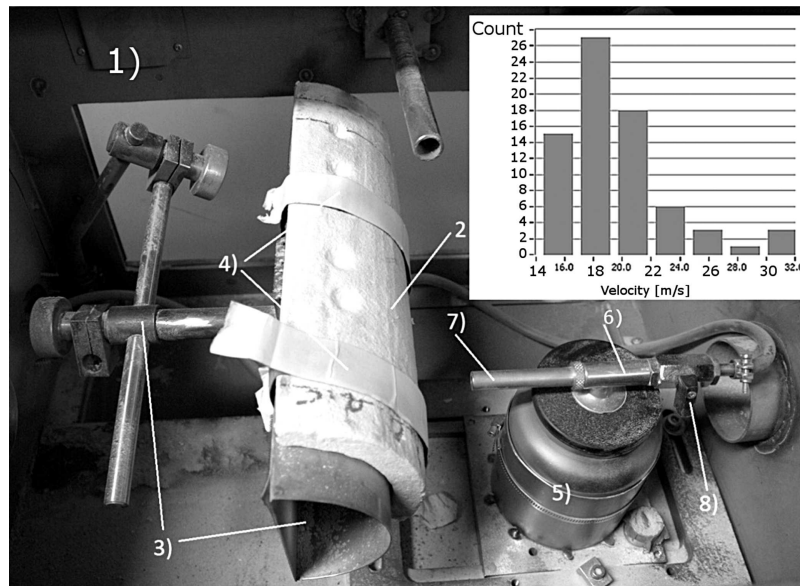
Fig. 2. Overview of the grit-blasting apparatus (1) with sample holder (3), sample (2), and grit-blasting gun with grit container (5). Particle velocity distribution in grit-blasting test on the up right corner.

from 1.68 to 2.78 $g\,s^{-1}$. Average values and standard deviations (SDs) were 2.16 and 0.27 $g\,s^{-1}$. The mass flow was not as steady in this grit-blasting setup, intended for on-site measurements, as it would have been in a laboratory-grade erosion system. However, this did not seem to affect the consistency of the crater depth values. Grit must have a certain momentum to erode material, but increasing mass flow does not noticeably affect crater depth.

Particle velocity was measured with a HiWatch camera and Oseir Spray Monitor software. Figure 2 shows particle-velocity distribution. Velocity of the majority of the particles was between 14 and 25 $m\,s^{-1}$. Some particles had higher velocities, up to 32 $m\,s^{-1}$. Average particle velocity was 19.8 ± 3.7 $m\,s^{-1}$.

2.5. Diametrically Compressive c-Ring Test

c-ring testing was carried out in accordance with ASTM C 1323-96.[14] The standard is intended to be used for monolithic advanced ceramics, but it was applied to fibrous ceramics due to the lack of suitable and reliable strength-testing procedures for heterogeneous materials. Figure 3 shows the schematic of the c-ring specimen and strength-test configuration. In our experiments, 50 circular specimens of 145.6 ± 6.3 mm outer diameter, 20.6 ± 3.3 mm wall thickness, and 20.6 ± 2.8 mm height (b) were cut out from the sample, and 10 circles were heat-treated at each temperature. The circular samples did not have exactly round cross-sections due to the manufacturing process. There were also variations in wall thicknesses. A slot (L) with length of at least that of the wall thickness was cut from the circle so that the part of the ring with the thinnest wall was on the opposite side of the slot. Maximum stress could be applied to the thinnest side of the ring, ensuring that all specimens broke down nearly at the same spot. During the test, the maximum tangential load was located at the outer

surface of the ring, as Figure 3 shows. As the samples broke at the same place, the calculated hoop strength was comparable between each specimen.

Material testing was carried out with an Instron 5967 universal testing machine with a 2 kN load cell, with technical accuracy of 0.05 N. A pre-tension of −2 N was used to fasten the sample between two metal plates, and another was attached to the load cell. The loading rate was 6 mm min^{-1}, and the test was terminated once there was a drastic drop in the force-displacement curve. Figure 3 shows an example of the stress-strain curve of the sample that was heat-treated at 900 °C for 10 h.

Strengths and apparent strains corresponding to ultimate tensile strength were determined from the compression data. Here, apparent strain means vertical displacement of the load cell during the experiment, rather than true strain, corresponding to ultimate strength of the c-ring specimen. Ultimate c-ring strength is given as hoop strength that is derived using curved-beam theory and calculated with Equation 1.

$$\sigma_{\theta max} = \frac{P * R}{bt(r_0)} \frac{(r_0) - (r_a)}{(r_a) - R}$$

Where
$$R = \frac{(r_0) - (r_i)}{ln\frac{(r_0)}{(r_i)}} \text{ and } r_a = \frac{(r_0)+(r_i)}{2}$$

In the equations, P is the applied compressive load, r_i is inner radius, r_0 is outer radius, r_a is average radius, b is the axial thickness shown in Figure 3, t is the radial thickness.[15] In the experiments, average radius, length, and thickness were used to calculate ultimate c-ring strengths. In addition to c-ring strength and apparent strain values, an apparent elastic modulus or effective rigidity value, given by the slope of linear region of the c-ring stress (in MPa) versus apparent
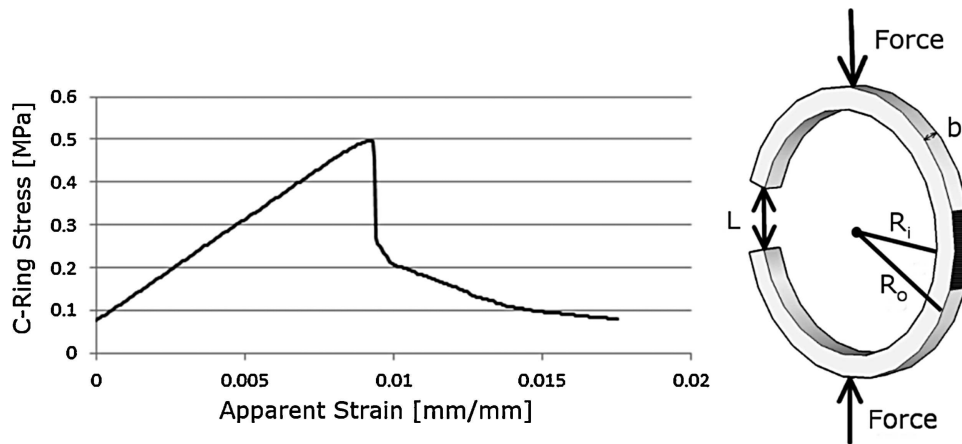
FULL PAPER

Fig. 3. On the left: Stress-strain-curve of the c-ring sample that was heat-treated at 900 °C. On the right: c-ring specimen according to ASTM C 1323-96.[14] Area of maximum stress rastered on the c-ring surface.[28]

strain (in mm/mm), was determined to evaluate the effective rigidity of the discontinuous fibrous material. Indeed, taking into account such a complex and heterogeneous microstructure, conventional methods of determination of true elastic constants were not adopted.

2.6. Impulse Excitation Technique

The impulse excitation technique[16] was used to determine resonant frequency values of the heat-treated samples prior to the grit-blasting experiments. Figure 4 shows the schematic of the resonant-frequency apparatus. Resonant frequency depends not only on the elastic behavior but is also linked to the size of specimen.[17] That is why samples were carefully machined to identical dimensions.

A concave (300 × 150 mm² × [wall thickness]) 120°-sample was cut from the original tubular component and it was placed on top of a piece of PU foam so that the concave side of the sample was lying against it. A microphone was placed at 30 mm from the other end of the 120° segment of the tubular specimen and a small rubber mallet was used as the impulse tool. The emitted frequencies were recorded, and dominant resonance frequency was analyzed with custom-made software. Dominant resonant frequency is the frequency peak in the spectrum with the highest amplitude. Dominant resonant frequencies were measured five times for each heat-treated and non-grit-blasted specimens. Figure 4 shows a schematic presentation of the measuring setup and dominant resonant frequency of the sample heat-treated at 800 °C for 10 h. Accuracy of the frequency measurement was experimentally found to be ± 0.1 Hz.

3. Results

3.1. Thermal Expansion and Shrinkage

Figure 5 shows relative length changes as a function of temperature for the samples that were heat-treated by holding them at target temperatures for 10 h at heating and cooling rates of 5 °C min⁻¹. Total shrinkage increased as the heat

treatment temperature increased. Furthermore, the 1,050 °C sample showed rapid change in the sintering curve, starting at about 970 °C and ending at about 1,020 °C. This was caused by a volumetric phase change to mullite.

Total shrinkage increased with temperature but the steady-state shrinkage rate was highest for the 900 °C sample. Presumably, the amount of softened phase increases at 900 °C, improving viscous flow and the phase's sintering rate. At 1,050 °C, the volumetric-phase change also hampered the shrinkage caused by sintering.

3.2. Crystal Structure

Figure 6 shows results of XRD analysis for the heat-treated samples. At 400 °C, α-alumina (A) was the main crystal phase. The structure also contained a phase at about 30° angle that could not be identified, which was possibly some crystalline silicate. This is indicated by (X). As heat treatment temperature increased to 800 °C, the amount of this unidentified phase gradually increased. At 900 °C, the phase was no longer visible. Mullite peaks were visible in the XRD pattern of the sample heat-treated at 1,050 °C, indicating that most of the mullite (M) crystallization took place at somewhere between 900 and 1,050 °C. XRD measurements also verified dilatometer data that indicated mullite formation started at about 1,000 °C. The results agreed with those of Takei et al,[18] who studied an aluminosilicate fiber with similar composition.

3.3. Grit-Blast Resistance

Results show the applicability of grit-blasting in determining thermal history of the studied fibrous bodies. We were interested if grit-blasting could also be used to study rigidization of samples that were heat-treated below mullite-formation temperature. Figure 10 shows crater depths, and their standard deviations, for the heat-treated samples. Crater depths increased as heat treatment temperature increased. Standard deviations were small, indicating good repeatability of the testing method and either homogeneity of the test material or insensibility of the test method to material
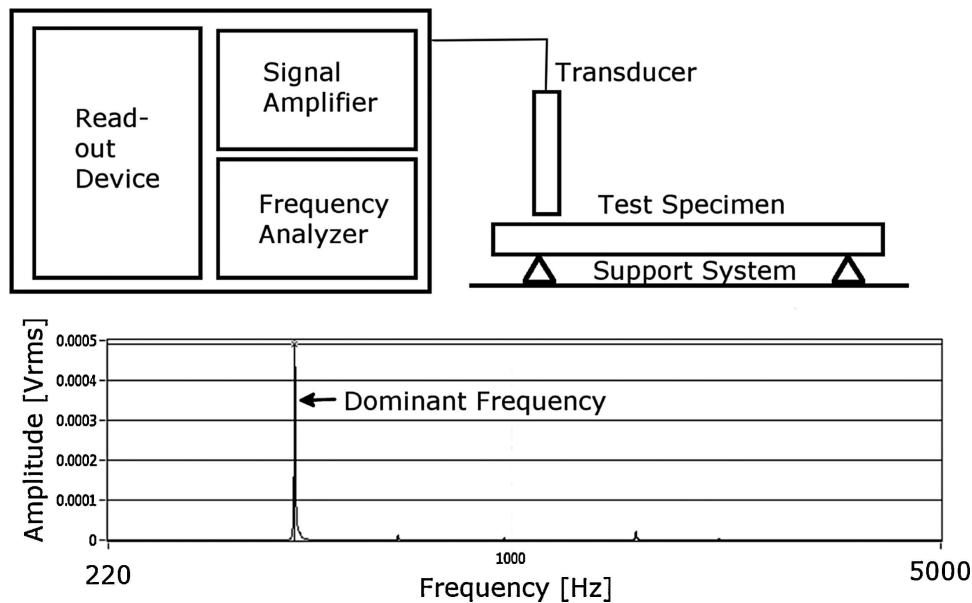
Fig. 4. Above: schematic of the equipment used to determine dominant-resonant frequencies of the heat-treated samples (ASTM C1259-01).[16] Below: Acoustic-response spectrum and determination of the dominant resonant frequency from the spectrum of the sample heat-treated at 800 °C for 10 h.

inhomogeneity. Craters created in samples heat-treated at 900 °C showed larger scattering in the crater depths, possibly implying that the material was less homogeneous than the other samples. Based on the experiments, grit blasting seems to be a promising method to determine thermal history of the elements.

3.4. Diametrically Compressive c-Ring Strength

Compressive c-ring tests were conducted on heat-treated samples to evaluate the sensitivity of this technique to thermal history of fibrous structures and if the samples rigidized when heat-treated. Figure 7 shows the results. Similar to grit-blasting tests, values increased as heat treatment temperature increased. However, samples heat-treated at 900 °C were an

exception and had lower than average strength than samples heat-treated at 800 or 1,050 °C. Strength scattering was large, and only 400 and 1,050 °C heat treatments could reliably be distinguished from each other in terms of strengths.

Figure 7 also plots the effective rigidity values extracted from the linear region of the stress–strain curve. The rigidity increased as heat treatment temperature increased. The values widely scattered, and sample heat treatment could not be evaluated based on them. However, temperature caused a slight increase in compressive c-ring strength and rigidity.

3.5. Resonant Frequencies

Similar to c-ring strength testing, impulse excitation can be used to estimate elastic modulus of a material. We were interested
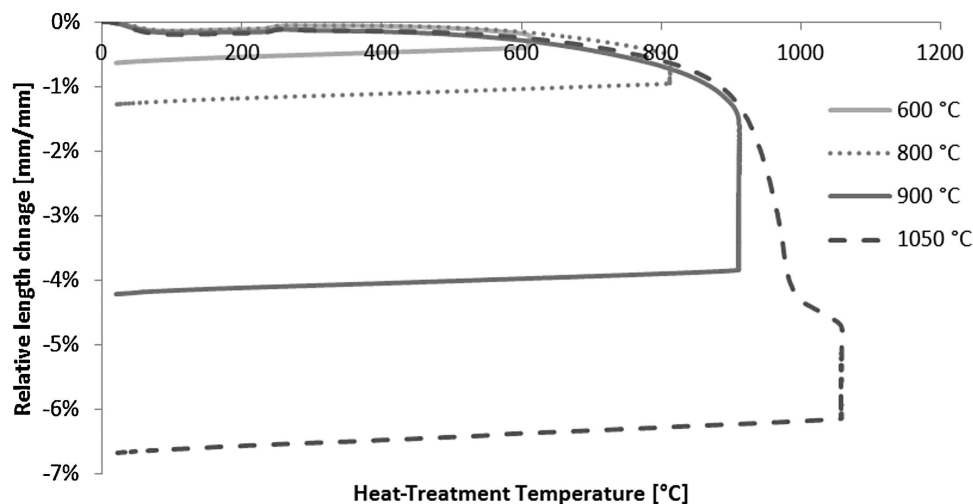
Fig. 5. Dilatometer measurement results.
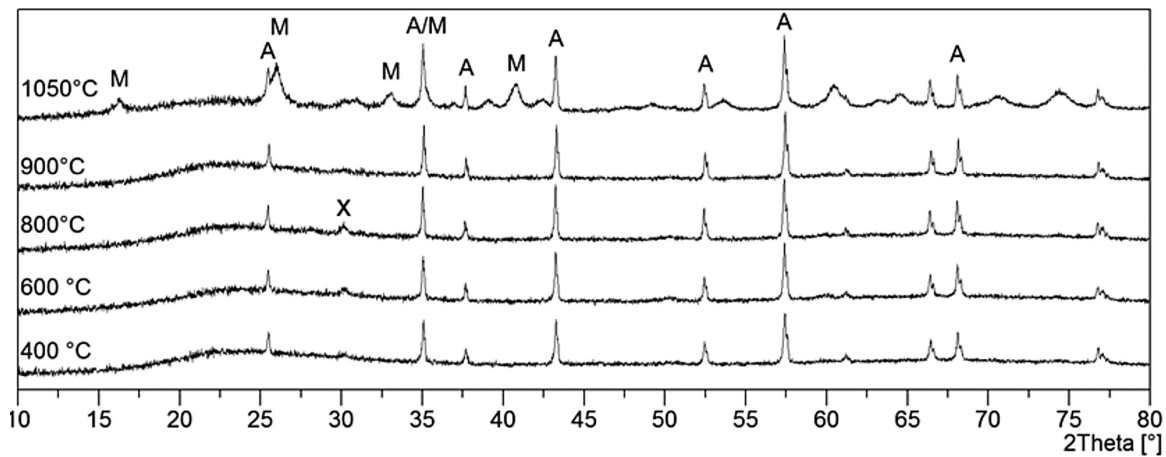
Fig. 6. XRD patterns of the heat-treated samples. A refers to α-alumina (Alumina [Rhombohedral]) ICDD no. 04-006-9730) and M to mullite (Mullite [Orthorhombic] ICDD no. 98-006-6445). X is an unidentified crystalline phase.

if there was a more accurate or repeatable method than the c-ring test to evaluate thermal history of fibrous structures. Frequencies reported in Figure 8 increased as heat treatment temperature increased, except for samples heat-treated at 400 or 600 °C, for which resonant frequency was roughly equal. Similar to c-ring testing, the resonant frequency of the sample heat-treated at 900 °C had a lower frequency than samples heat-treated at 800 or 1,050 °C. Resonant frequencies had low SD values, implying good repeatability of the test method. In addition, the location where the impulse tool hit the specimen did not affect dominant resonant frequency, further improving repeatability and reliability of the method.

3 *4. Discussion*

In this work, different on-site techniques for characterizing highly heterogeneous fibrous ceramics were presented and compared. The influence of heat treatment temperature (10 h, range: 400–1050 °C) on mechanical behavior was also examined. The general goal was to investigate if the methods can be used to

determine the maximum temperature the structure was subjected to as a result of the temperature-caused changes of mechanical properties that are closely related to microstructural evolution of such structures. Scaled results are presented in Figure 9. Resonant frequency testing had the best repeatability but temperature sensitivity was not good. This method could only roughly estimate the thermal history of the samples. Samples heat-treated at 400 and 600 °C show nearly equal resonant frequencies, indicating that the test method was not applicable to distinguish low-temperature heat treatments from each other. In the samples heat-treated at such low temperatures, minute variations in the composition, structure, and dimensions of the specimen most likely explained slightly larger resonant frequency of the sample heat-treated at 400 °C. Resonant frequency is only slightly dependent on the heat treatment temperature. Other factors, perhaps the evidenced phase change, determined the frequency.

Similar to resonant frequency tests, diametrically compressive c-ring strength increased as heat treatment temperature increased. Strength-test data scattering was large, indicating
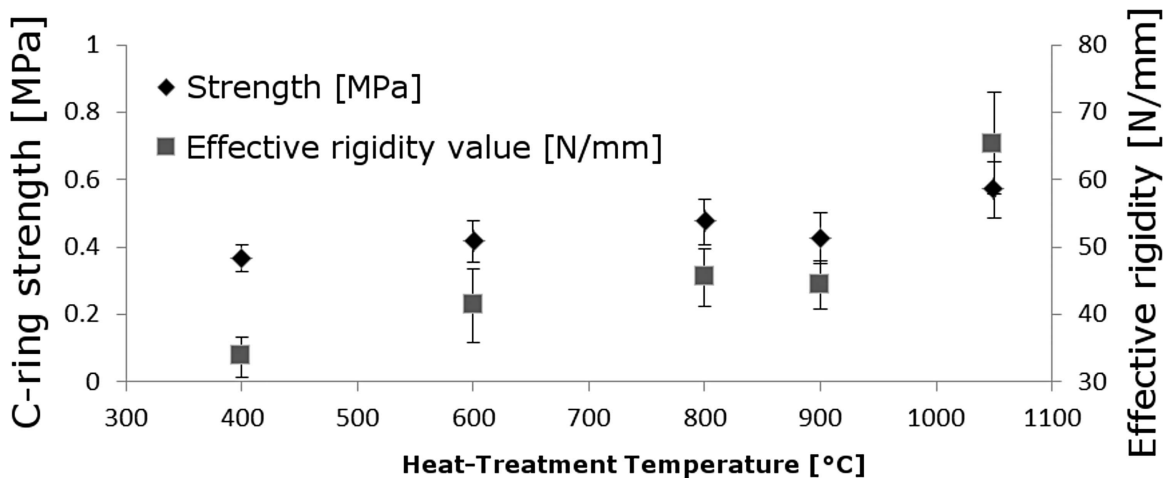
Fig. 7. c-ring strengths and effective rigidity parameter values (calculated from the slope of c-ring stress (MPa) vs. apparent strain [mm/mm]) for the samples heat-treated at different temperatures.
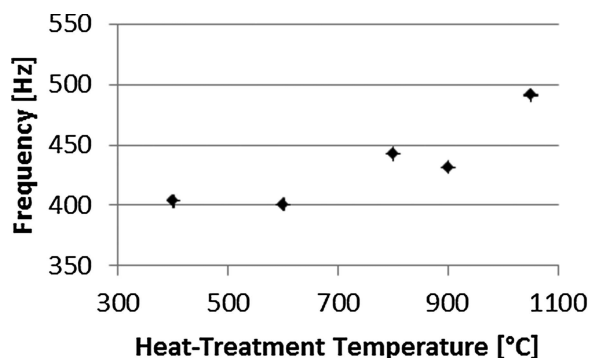
Fig. 8. Resonant frequencies of the samples heat-treated at different temperatures.

second-order polynomial regression as a function of heat treatment temperature by a coefficient of determination $R^2 = 0.9995$. The reason for this unexpectedly fine correlation with thermal history was that grit-blasting was the only method sensitive to microstructural changes in fiber free length, while results of the other methods were dominated by structural inhomogeneities, such as uneven binder distribution seen in Figure 1.

XRD measurements showed that the amount of unidentified crystalline phase increased at 400 to 800 °C. This may be partially responsible for increased strength, effective rigidity, and resonant-frequency values. The amount of amorphous phase increased at 900 °C, possibly promoting shrinkage via viscous flow and decreasing strength and resonant frequency. Dilatometer measurements furthermore supported this theory, as isothermal shrinkage rate was highest with the sample heat-treated at 900 °C. Mullite crystallization at 1,050 °C again increased strength and resonant frequency, but is responsible for the decrease in isothermal shrinkage as the viscous flow was hampered by the formed mullite. Even so, the grit-blasting strength was not affected by this phase change, but followed the sintering temperature. We believe this is due to decreased free length of the fibers.

that method repeatability in determining thermal history of fibrous structure is poor. A large number of samples needed to be tested to estimate the heat treatment temperature. The average elastic moduli in the c-ring test increased slightly as heat treatment temperature increased, implying structural embrittlement. However, result scattering was vast, which is why they could not identify thermal history of the sample. Still, both the elastic moduli and strength showed that the samples rigidize, especially when the heat treatment temperature exceeded the phase-change temperature.

However, the grit-blasting test showed high resolution for thermal-history distinction and its results had a very small variation. Crater depths gradually increased as heat treatment temperature increased. Crater-depth values followed a

4.1. Description of Fiber Free Length

C-ring and resonant frequency results can be partially explained with initial crystallization of an unidentified phase, followed by its disappearance that led to a decrease both in strength and resonant frequency at 900 °C, and finally an
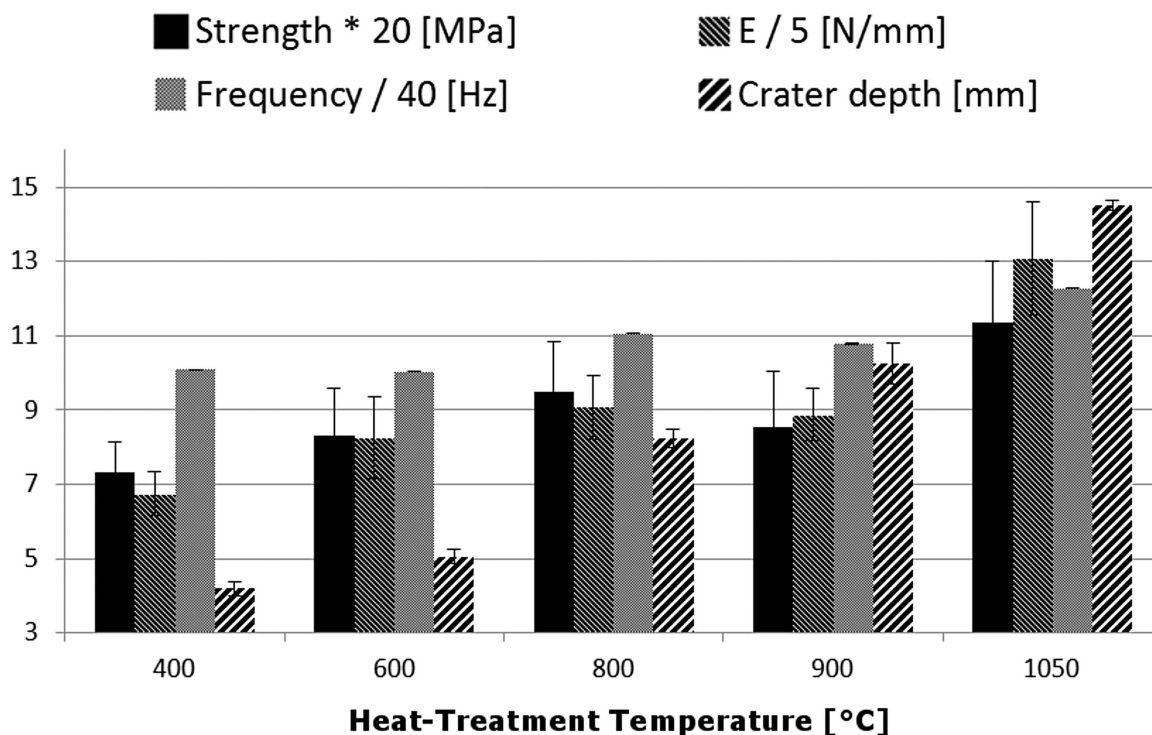
Fig. 9. Comparison of the average strengths, ultimate strains, resonant frequencies, and crater depths of the heat-treated samples. SDs of the average values are also plotted in the columns.

FULL PAPER
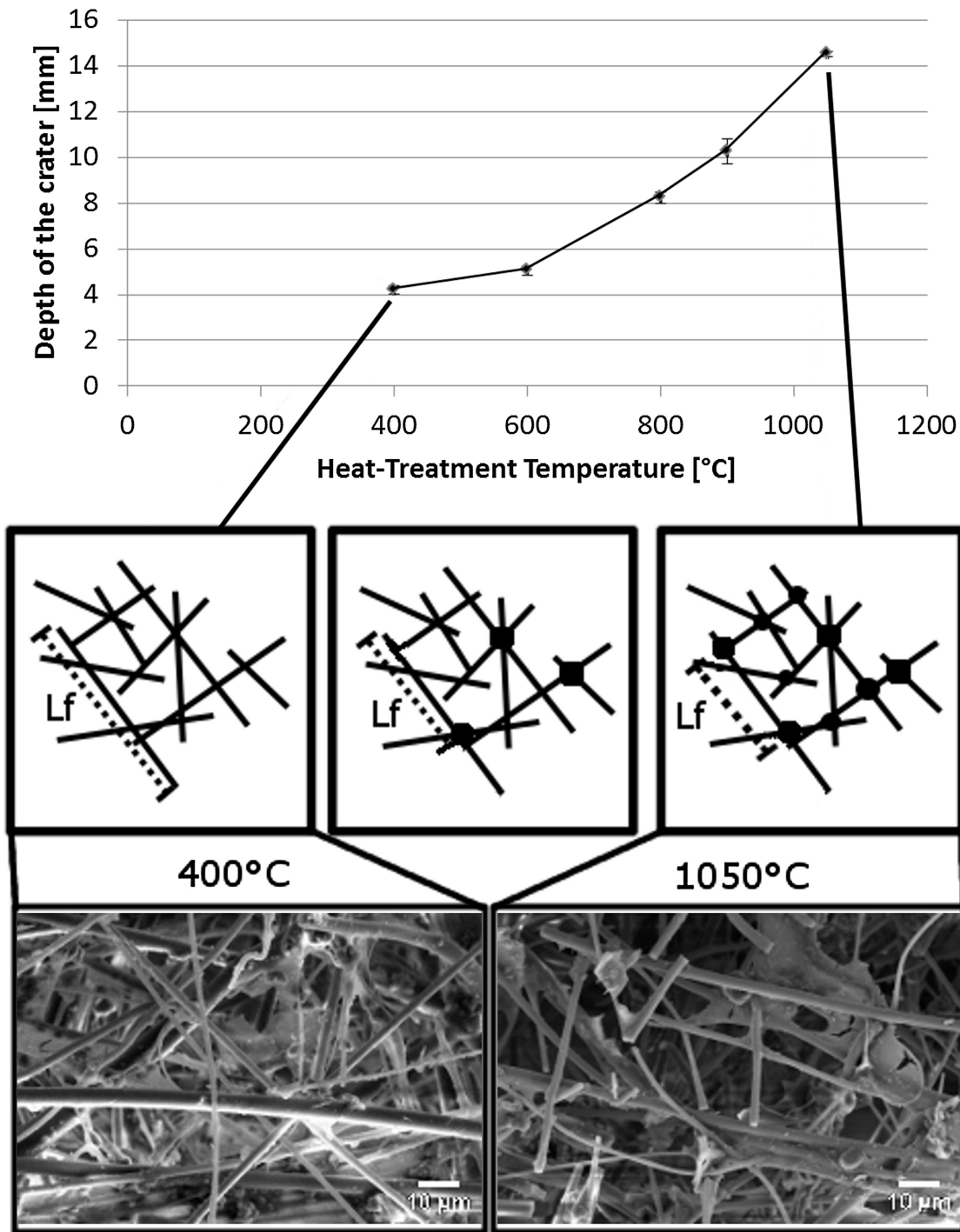
Fig. 10. Crater depths for the samples heat-treated at different temperatures for 10 h. Ten craters were blasted into the sample surface for those heat-treated at 400, 600, 800, and 900 °C. Fifteen craters were blasted into the sample heat-treated at 1,050 °C. Below is a schematic of the concept of fiber free length. The contact points (black dots) are caused by sintering of the inorganic glassy phase and are responsible for decreased free length. SEM images of the samples treated at 400 and 1,050 °C.

increase caused by mullite formation and severe sintering above 1,000 °C. However, unlike in c-ring and resonant-frequency tests, the sample heat-treated at 900 °C showed no decrease in crater depth. It means that this is a different mechanism from the crystallization which controlled the erosion rate. We believe that fibers sintered to each other and the increased erosion rates can mainly be explained by decreased fiber free length, that is, the decrease of the fiber's length that is between its contact points. Fiber free length decreased as they attached to each other via sintering between the contact points. The length of the fiber subjected to stress caused by impacting particles in grit-blasting testing decreased (Figure 10). When this free length decreased, a shorter section of the fiber was subjected to the same impact force. The

FULL PAPER

fibers' capability to absorb impact energy from the glass grit decreased and the probability of fibers breaking under erosion increased, leading to deeper craters. In a sense, grit-blasting measured the state of fiber stacks, whereas the other methods measured the mechanical integrity of the whole structure.

Craters created in the sample heat-treated at 900 °C exhibited larger SDs than those created in the samples heat-treated at lower temperatures. Phase change at 900 °C should produce a macroscopically heterogeneous structure because the overall composition in the sample is non-homogeneous and that explains larger variations in crater depths. At 1,050 °C, mullite formation was also responsible for structure embrittlement. At 1,050 °C, increased, accelerated erosion rate is caused by the sum of the structure embrittlement by mullite crystallization and a decrease of free length caused by sintering of the structure, which is the dominant feature. Sintering is an irreversible process, so the grit-blasting will show the peak temperature the structure has been subjected to.

5. Conclusion

We presented several methods to characterize fibrous aluminosilicate samples heat-treated for 10 h at temperatures ranging from 400 to 1,050 °C. This study's goal was to develop on-site methods to monitor changes of mechanical properties of products consisting of such structures. Studied methods included diametrically compressive c-ring strength test, resonant-frequency test, and erosion test by glass-grit blasting. The c-ring test showed an increase in a sample's average strength and rigidity as heat treatment temperature increased. Similarly, in the impulse-excitation technique, dominant resonant frequency of the sample increased as heat treatment temperature increased. Samples heat-treated at 900 °C showed lower strengths, moduli, and resonant frequencies than did samples heat-treated at 800 and 1,000 °C. This was explained by crystalline phase changes between the temperatures. However, both the c-ring test and resonant frequency test showed such a large scattering of the measured values that the thermal history could not be distinguished from the data. This was probably because the measurements were also affected by other factors such as structural defects within the structure.

Unlike the c-ring strength and resonant-frequency measurements, the grit-blasting test accurately and reproducibly distinguished between different heat treatments. The method was fast, accurate, and could probably also characterize how other fibrous ceramics sinter in the analyzed temperature range via linking the sintering with the concept of fiber free length that we proposed in this article. The concept explained the high sensitivity of the grit-blasting method. Free-length is the distance between the fiber contact points to neighboring fibers or other structures. The free length decreased when the sample's heat treatment temperature increased. This happened because the fibers sintered to each other, creating new contact points. When the free length decreased, the fibers had

fewer degrees of freedom to move when they were hit by glass grit. This was seen as an increase in crater depths in higher temperature.

This paper only discussed the effect of thermal load on mechanical properties of the elements. Also chemicals, especially alkalis, affect properties of fiber ceramics.[19–27] Further studies should investigate the applicability of the method when the fibers have been in contact with chemicals.

[1] S. Schaafhausen, E. Yazhenskikh, *J. Eur. Ceram. Soc.* **2014**, *34*, 575.

[2] S. Heidenreich, *Fuel* **2013**, *104*, 83.

[3] R. F. Allen, United States Patent Application Publication Number 2008/0314012 A1, 2008, US20080314012 A1.

[4] J. Humalamäki, *Mechanical Characterization of Fibrous Ceramic Filter Elements*, Tampere University of Technology, Tampere, Finland **2013**.

[5] P. Laihonen, *Evaluation of Mechanical Integrity of Fibrous Hot Gas Filter Elements*, Tampere University of Technology, Tampere, Finland **2012**.

[6] D. Muller, W. Acchar, G. M. C. Silva, E. A. Moreira, J. R. Coury, M. D. M. Innocentini, D. Hotza, C. R. Rambo, S. Carlos, *Cerâmica* **2009**, *55*, 318.

[7] D. V. Wilbrink, L. a. a. Beex, R. H. J. Peerlings, *Int. J. Solids Struct.* **2013**, *50*, 1354.

[8] D. Tsarouchas, a. E. Markaki, *Acta Mater.* **2011**, *59*, 6989.

[9] M. Delincé, F. Delannay, *Acta Mater.* **2004**, *52*, 1013.

[10] S. M. Toffoli, R. L. Lehman, *J. Am. Ceram.* **2001**, *28*, 123.

[11] V. Heuer, G. Walter, I. Hutchings, *Wear* **1999**, *225–229*, 493.

[12] V. Heuer, G. Walter, I. Hutchings, *Wear* **1999**, 257.

[13] J. S. Zievers, *Hot Gas Filter*, US Patent number 4, **1990**, *968*, 467.

[14] ASTM C 1323, *Ultimate Strenght of Advanced Ceramics with Diametrally Compressed C-Ring Specimens at Ambient Temperatures*, ASTM, West Conshohocken, PA **2014**.

[15] C. Brinkman, S. Duffy, *Life Prediction Methodologies and Data for Ceramic Materials*, ASTM International, Philadelphia, PA **1994**.

[16] ASTM C1259-01, *Standard Test Method for Dynamic Young's Modulus, Shear Modulus*, ASTM, West Conshohocken, PA **2014**.

[17] J. Mohapatra, Y. Kamada, H. Kikuchi, 212.8.206.21 **2011**, *21*, 159.

[18] Tt. Takei, A. Yasumori, K. Okada, *J. Am. Ceram. Soc.* **1999**, *82*, 2876.

[20] G. L. B. Stephen, C. Carniglia, in *Handb. Ind. Refract. Technol. Princ. Types, Prop. Appl.*, Noyes Publications, **1999**, 255.

[21] B. K. Novakovik, Rada, in *Adv. Ceram. Use Highly Oxid. or Corros. Environ.*, Trans Tech, Uetikon-Zuerich, Switerland; Enfield, NH **2001**, 121.

[22] J. C. Lee, H. J. Song, M. J. Park, H. I. Shin, *Colloids Surf. A Physicochem. Eng. Asp.* **2001**, *187–188*, 399.

[23] M. Schmucker, P. Mechnich, S. Zaefferer, H. Schneider, *J. Eur. Ceram. Soc.* **2008**, *28*, 425.

[24] Y. Wang, J. Liu, *Corros. Sci.* **2009**, *51*, 2126.

[25] S. L. Gao, E. Mäder, R. Plonka, *Acta Mater.* **2007**, *55*, 1043.

[26] M. R'Mili, J. Lamon, *Acta Mater.* **2011**, *59*, 2850.

[27] J. J. Haslam, F. F. Lange, *J. Am. Ceram. Soc.* **2006**, *89*, 985.

[28] S. Duffy, *J. Test. Eval.* **2005**, *33*, 6.

Publication IV

THE MECHANICAL PERFORMANCE AND CO2 UPTAKE OF ION-EXCHANGED ZEOLITE A STRUCTURED BY FREEZE-CASTING

by

Ojuva Arto, Järveläinen, Matti, Bauer Marcus, Keskinen Lassi, Valkonen Masi,
Akhtar Farid, Levänen Erkki & Bergström Lennart

Mechanical performance and CO_2 uptake of ion-exchanged zeolite A structured by freeze-casting

Arto Ojuva [a,b], Matti Järveläinen [c], Marcus Bauer [a], Lassi Keskinen [c], Masi Valkonen [d], Farid Akhtar [a,e], Erkki Levänen [c], Lennart Bergström [a,*]

[a] *Department of Materials and Environmental Chemistry, Stockholm University, SE-10691 Stockholm, Sweden*
[b] *Berzelii Center EXSELENT on Porous Materials, Stockholm University, SE-10691 Stockholm, Sweden*
[c] *Department of Materials Science, Tampere University of Technology, PO Box 589, FIN-33101 Tampere, Finland*
[d] *Department of Signal Processing, Tampere University of Technology, PO Box 589, FIN-33101 Tampere, Finland*
[e] *Division of Materials Science, Luleå University of Technology, SE-97187 Luleå, Sweden*

Abstract

Zeolite 4A has been freeze-cast into highly porous monoliths with a cylindrical shape. The brittle monoliths, with lamellar or columnar pores and wall thicknesses between 8 and 35 μm, show a compressive mechanical response along the main pore axis that could be modeled by a buckling behavior. The failure strength is proportional to the density and the amount of transverse bridging across lamella, which was shown to be related to the pore cross-sectional aspect ratio. Monoliths with highly anisotropic pores with a cross-sectional aspect ratio higher than 3 yielded sequentially from the top surface, whereas monoliths with a pore aspect ratio lower than 3 were found to delaminate into longitudinal splinters. The freeze-cast monoliths show a sharp gas breakthrough front with a 1:9 mixture of CO_2 and N_2, indicating rapid uptake kinetics of the lamellar structures.
© 2015 Elsevier Ltd. All rights reserved.

1. Introduction

The growing increase of the emission of anthropogenic carbon dioxide has put increasing pressure on developing technologies which can rapidly mitigate the emissions and are readily applicable to point sources of high emission density, e.g., coal-fired power plants.[1–4] The primary challenge in capturing CO_2 from a flue gas stream containing post-combustion products (mainly N_2 and CO_2) lies in the cost- and energy-efficient separation of very large volumes of CO_2 at a low partial pressure (0.10–0.15 bar) from mainly N_2.

While various technologies, such as cryogenic separation[5] and amine scrubbing,[6] have been proposed for the task, CO_2/N_2 separation using solid sorbents via the established temperature or pressure swing technologies is a promising route due to its low energy demand and material cost.[7] Although various promising sorbent materials have been studied, including metal-organic frameworks,[8,9] mesoporous silica,[10,11] microporous silicates,[12] polymers[13–15] and activated carbon,[16,17] zeolite adsorbents are a robust and widespread group of adsorbents already in use within many applications. The regeneration of the physically adsorbed gas demands relatively small amounts of energy, typically 40–50 kJ/mol depending on the loading.[18]

The separation in pressure or temperature swing processes using adsorbents is achieved by streaming the gas mixture through a long adsorbent column, often several cubic meters in volume, and controlling the adsorption affinity of one of the species by pressure or temperature. The adsorbent is often in the form of small extruded rods or beads (2–5 mm),[11,19] which are packed on trays or into a bed in the separation column in various sizes and shapes, depending on the application. The velocity of the adsorption front through the bed will govern the time

---

* Corresponding author. Tel.: +46 8 162368; fax: +46 8 152187.
E-mail address: lennart.bergstrom@mmk.su.se (L. Bergström).

allowed for adsorption: the gas flow will typically be stopped when the adsorbing species reaches the far end of the bed, the bed is purged from the adsorbed species, and a new separation cycle begins.

The efficiency, or the total time-dependent uptake, of the adsorbent bed is limited by the micropore diffusion within the adsorbent particles, which depends on the particle size and the thickness of the walls. The pressure profile along the bed should be kept uniform; a large gas flow is enabled by wide channels with low tortuosity. These demands call for an efficient adsorbent design to ensure both laminar flow and rapid micropore diffusion. Thin lamellar structure with sheet width and spacing at or less than 200 μm has been identified by Webley et al.[20,21] to enable a rapid and efficient uptake with minimum diffusion resistance and small pressure drop.

However, lamellar monoliths with sheet spacing under a millimeter are difficult or impossible to shape by extrusion; previous reports indicate that the smallest spacing for thin walled honeycombs is 700 μm.[22] Significant reduction of the wall spacing requires that alternative shaping methods are used. One promising approach is the solvent solidification route: we recently showed that freeze-casting of zeolites[23] could yield monoliths for rapid CO_2 uptake with a lamellar structure and sheet width and spacing below 35 μm. The monoliths were produced by directional freezing of an aqueous suspension containing zeolite 13X and a binder. After the suspension was completely frozen, the ice was removed by sublimation and the remaining lamellar structure was consolidated by thermal treatment. While zeolite 13X is a good adsorbent, it has a relatively low CO_2-over-N_2 selectivity compared with other zeolites, such as the zeolite A chosen for this study.[24]

The mechanical strength of the adsorbent monoliths needs to be sufficiently high to sustain stresses induced by handling and fluctuations in pressure and gas flow. Mechanically, a lamellar pore structure can be treated with same mathematical approximations as anisotropic open cellular solids, e.g., honeycomb ceramics and porous wood. These types of structures have been studied extensively, e.g., by Ashby and Gibson,[25] who have related the mechanical properties of porous structures to the properties of the bulk material, scaled by porosity.[26] With increasing porosity, a number of various failure mechanisms, such as buckling or bending, will dominate the mechanical response.

The mechanical properties of different types of low-density porous materials have recently been investigated; Donius et al. found the Gibson–Ashby scaling laws to accurately describe the compressive behavior of freeze-cast nanocellulose-clay aerogels.[27] Porter et al. found that the Euler buckling is the dominating mode of failure for freeze-cast porous titania bodies and related the axial compressive strength to the pore aspect ratio.[28] Introducing anisotropy in the cell walls by forming them out of flat platelets has also been attempted, and it was found that letting the platelets to assemble along the direction of the freezing front considerably enhanced the mechanical properties as compared to spherical particles.[29–32] In an interesting study, Tang et al.[33] froze a monolith in a cylindrical shape simultaneously from the bottom of a mold and radially inwards from its sides,

resulting in both axially and radially ordered structures, which nearly doubled the compressive strength in the radial direction as compared to monoliths with only axial ordering. However, little attention has been given to investigations of the mechanical properties of freeze-cast adsorbents produced from porous particles. The ambition to shape highly anisotropic hierarchically porous structures for gas separation applications requires that we understand the failure behavior in detail.

In this work, we have investigated how mechanically stable, anisotropically porous, composite monoliths can be produced by freeze-casting suspensions of zeolite A, bentonite clay and polyethylene glycol, and the subsequent removal of ice by sublimation and heat treatment at 1023 K. The mechanical properties of the anisotropically porous monoliths has been measured and discussed with respect to the dominating failure mechanism. We have analyzed cross-sectional images of the monoliths using a computer algorithm for principal component analysis in order to quantify the pore size and shape and related the pore anisotropy to the mechanical properties of the freeze-cast monoliths. We have also determined the suitability of freeze-cast monoliths based on LTA in its NaA-form (zeolite A) and two different potassium-exchanged NaKA-forms for CO_2/N_2 separation by determining the time-dependent gas breakthrough of CO_2.

2. Experimental

Zeolite with the framework Linde Type A (LTA) in its sodium-containing form, known as zeolite 4A or NaA, was obtained as a powder with an average particle size of 2–4 μm (Fig. 1) from Luoyang Jianlong Chemical Industrial Co., LTD (Yanshi, Henan, China). Bentonite, which was used as an inorganic binder, and polyethylene glycol (PEG, MW 8000), which was used as an intermittent binder, were both obtained from Sigma–Aldrich (Sigma–Aldrich Chemie GmbH, Buchs, Germany).

The ion-exchange process of NaA into NaKA, adapted from Cheung et al.,[34] was carried out in an aqueous mixture of the
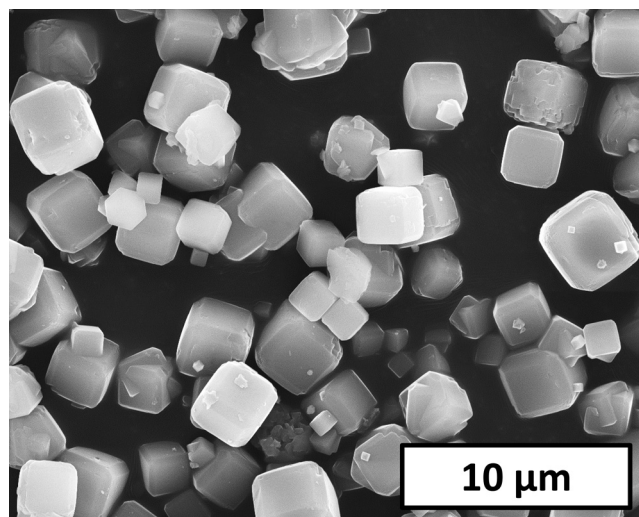

Fig. 1. SEM image of NaA (zeolite A) showing cubic particles with a size distribution of 2–4 μm.

zeolite and potassium salt: 10.0 g of zeolite was mixed in 1.00 dm^3 of de-ionized water in a vessel under continuous stirring. Then, depending on the intended exchange ratio, either 0.800 g of KCl (Sigma–Aldrich) to produce 17.6% K-exchanged or 0.400 g of KCl to produce 10.2% K-exchanged zeolite A (as determined by energy-dispersive X-ray spectroscopy, EDX), was added and the mixture was stirred for 30 min. The ion-exchanged zeolite was filtered and washed twice with de-ionized water, after which the retained powder was dried in an oven at 373 K overnight. The elemental composition of the powders was characterized in a scanning electron microscope with a field-emission gun (JEOL JSM-7001F, Jeol Ltd., Tokyo, Japan) by energy-dispersive X-ray spectroscopy.

The rheological measurements were performed at 298 K with a Paar Physica MCR301 rheometer (Anton Paar GmbH, Graz, Austria), using a concentric cylinder geometry. First a pre-shear at 50 s^{-1} was done during 120 s, after which the suspension was allowed to rest for 30 s before the shear viscosity was measured at a rate of 200 s^{-1} during 360 s.

Before they were freeze-cast, the zeolites were conditioned overnight in a constant climate chamber (KBF 115, Binder GmbH, Germany) at 303 K and 50% relative humidity. This conditioning was determined to stabilize the water content to 21.3 ± 0.7 wt%, determined by thermogravimetry from room temperature to 1173 K, at 10 K/min, using TGA 7 (PerkinElmer, Waltham, USA). The conditioned zeolites were mixed with PEG, bentonite and deionized water (see Table 1) in a milling flask with 5 mm zirconia milling balls and milled overnight in order to de-agglomerate the suspension. The suspension was de-aired under stirring at a low vacuum created by a water tap aspirator for 5 min.

The freeze-casting unit was identical to the one described in our previous work,[23] consisting of a liquid nitrogen vessel and a protruding copper rod with a thermocouple and a heater on the top, controlled by a control unit, Jumo cTron 08 (Jumo GmbH & Co. KG, Germany). The controller allowed the user to set a constant cooling rate during the casting. The suspension to be cast was poured in a cylindrical PTFE die with a copper bottom plate. The die had an inner diameter of 20.0 mm and two different heights: 20 and 40 mm. The former were used to prepare monoliths with a precise height for mechanical testing, and the latter to prepare tall monoliths (30–35 mm) for breakthrough measurements.

Table 1
The identity of the suspensions and their compositions.

Suspension ID	A20	A25	A30	A32
Total inorganic content (wt% dwb)	18.3	22.9	27.4	29.2
DI water (cm^3)	100	100	100	100
Zeolite A (g)	26.5	36.2	47.7	53.0
Bentonite (g)	3.61	4.95	6.51	7.21
PEG (g)	3.61	4.95	6.51	7.21

The mass reported on the row for zeolite A was the actual mass of the zeolite that had been conditioned in a climate chamber, containing 21.3 ± 0.7 wt% water. The relative amounts of bentonite and PEG to the zeolite were kept constant.

The frozen ice/powder compacts were sublimed in a freeze-dryer (Hetosicc, Heto lab equipment, Denmark) at 20–40 Pa for 2 days. The resulting porous powder bodies were thermally treated in a muffle furnace (Nabertherm GmbH, Lilienthal, Germany) under air. The powder bodies were first heated to 823 K at 2 K/min, where the temperature was kept constant for 2 h in order to remove the intermittent organic binder PEG, and then to 1023 K at 10 K/min with no holding time.

Scanning electron microscope images were obtained with a JEOL JSM-7001 F microscope (Jeol Ltd., Tokyo, Japan) and with a Hitachi Analytical TableTop Microscope TM3000 (Hitachi High-Technologies Europe GmbH, Krefeld, Germany). Representative pieces were prepared from the middle of the monolith and cut into a suitable size (a few mm) with a scalpel and placed on a conductive holder with Leit-C conductive carbon cement (Plano GmbH, Wetzlar, Germany). Finally the pieces were coated either with a thin layer of gold (JSM-7001F) or carbon (TM3000) prior to insertion into the microscope.

The mechanical tests were performed with an Instron 5967 (Instron, Norwood, MA, USA) mechanical testing device. The monoliths were placed on a metal plate in a small plastic bag between two rubber pieces to distribute the load more evenly. The monoliths were compressed with a 2 kN load cell at 10.0 mm/min while the applied force and piston movement was recorded. The compressive stress for each monolith was calculated by dividing the measured compressive force with the diameter of the monolith. The compressive strain was calculated by dividing the initial height of the monolith with its actual height that was read from the piston movement during compression. For standard tests, three monoliths from each composition were tested, and the averaged value reported. For Weibull analysis more monoliths were made from the highest and lowest concentration suspensions, i.e., A20 and A32, and frozen at either 1.5 or 10.0 K/min. For these measurements the plastic bag and the rubber pieces could be omitted as the top surfaces of the monoliths were made flat by grinding with fine sandpaper, and the compression speed was reduced to 0.50 mm/min. The Weibull analysis was performed on 3–10 monoliths of each identity.

The time-dependent gas breakthrough tests were performed on a stacked column of freeze-cast monoliths with a total column length of 15 cm, as shown in Fig. 2. The monoliths were activated under a flow of N$_2$ at a rate of 0.15 L/min at 573 K for 12 h. After activation, the monoliths were cooled to 298 K. At time zero, the gas feed was switched from N$_2$ to 0.15 L/min flow of 10% CO$_2$ in N$_2$ using a pneumatic switching valve. The switching time was less than 0.1 s. The concentration of CO$_2$ in the gas leaving the column was measured as a function of time using a CO$_2$ analyzer (IR 1507 fast response CO$_2$ infrared transducer).

3. Results and discussion

Composite monoliths with a lamellar porous structure were prepared from aqueous suspensions of zeolite A, bentonite and polyethylene glycol (PEG). The suspensions were frozen unidirectionally, starting from the bottom of a cylindrical die that was set to cool at a constant rate. After freezing, the ice was sublimed in a freeze-dryer and the remaining compact powder body was
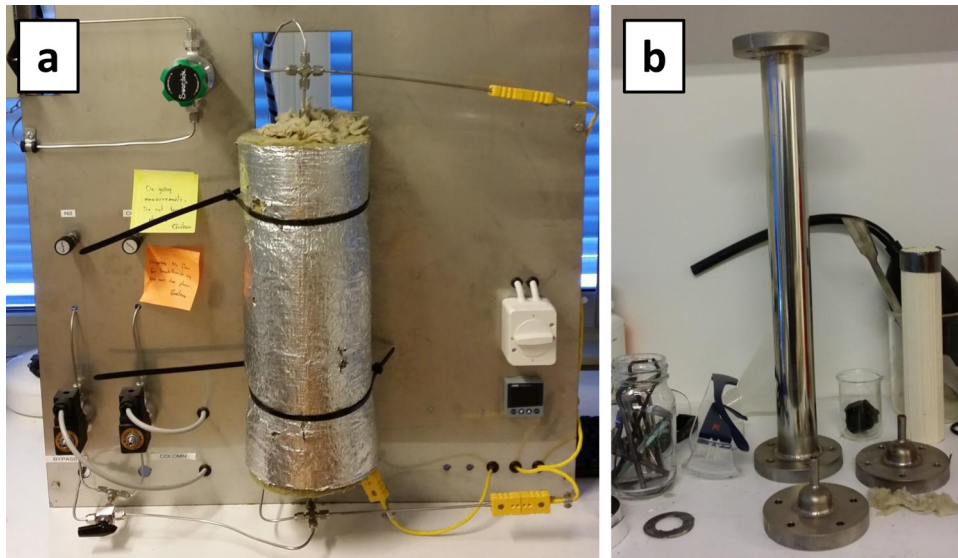
Fig. 2. Photograph of the gas breakthrough apparatus (a); and the column (b). The column consists of 6–7 monoliths, with a total length of 15 cm, of A20 with varying potassium loading frozen at 10 K/min. After activation with N_2, a gas mixture containing 10% CO_2 was let in the column at 150 ml/min, and the relative concentration of CO_2 was measured at the outlet.

thermally treated to obtain a mechanically strong monolith with a continuous and directional porosity.

The maximum suspension concentration was determined from rheological measurements. The maximum solids loading can be determined by:[35]

$$1 - \eta_r^{-1/n} = a'\phi + b' \tag{1}$$

where η_r is the relative viscosity (viscosity of the suspension divided by the viscosity of the solvent, water + PEG), n is a flow parameter, where we used a typical value of 2, φ is the solids loading of the suspension, and a' and b' are empirically determined parameters from the rheology measurements. Fig. 3 shows that the predicted maximum loading is 31.4 wt%; however suspensions with concentrations above 30 wt% were found to be too viscous for freeze-casting. The highest solids loading that we have used was 29.2 wt% dwb.

The crushing strength σ^* for a thick-walled anisotropic porous solid (e.g., a honeycomb) can, along its main axis, be described by:[36]

$$\sigma^* = \sigma_s \frac{\rho}{\rho_s} \tag{2}$$

where σ_s is the fracture strength of the (non-porous) bulk material and ρ/ρ_s is the relative density of the material. Isotropic brittle foams, where the cell walls also experience bending stress, can be described according to the expression by Ashby and Gibson:[25,26,37]

$$\sigma^* = \sigma_s C \left(\frac{\rho}{\rho_s} \right)^{3/2} \tag{3}$$

where C is an empirical constant relating to the dominant type of deformation, e.g., 0.65 for brittle foams.[37,38] Materials with a low elastic modulus E and a high length to thickness ratio can

fail before fracture at the elastic buckling strength, σ_{el}, according to[39]:

$$\sigma_{\text{el}} = EI \frac{\pi^2}{k'L^2} \tag{4}$$

where E is the elastic modulus of the material, L is the length of the buckling wall or beam, I is the area moment of inertia of the cross-section of the cell edge or wall[28] and k' describes the degree of constraints for the attachment points of the wall. The theoretical requirement for buckling to occur is for the failing element, such as a wall with a cross-sectional area A_w, to
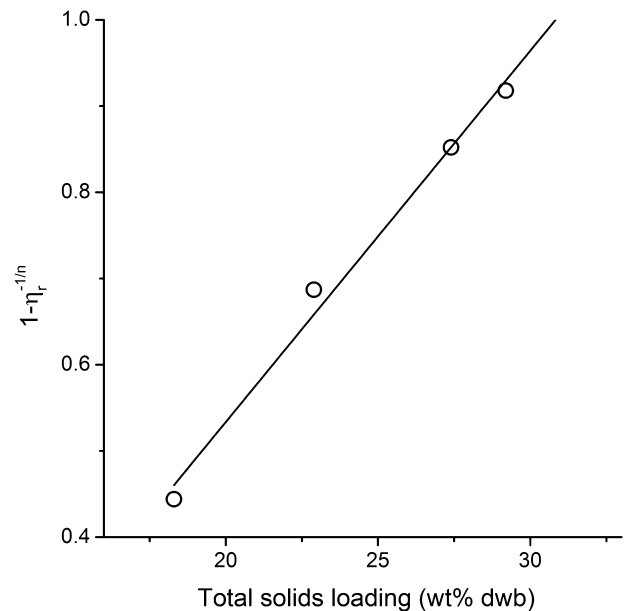
Fig. 3. Plot of $1-\eta_r^{-1/n}$ versus the total inorganic content for the zeolite-bentonite-PEG suspension. The circles show the measured values from the four suspensions (A20, A25, A30, A32) used in the preparation of the monoliths and the straight line is the linear least squares fit to the data.
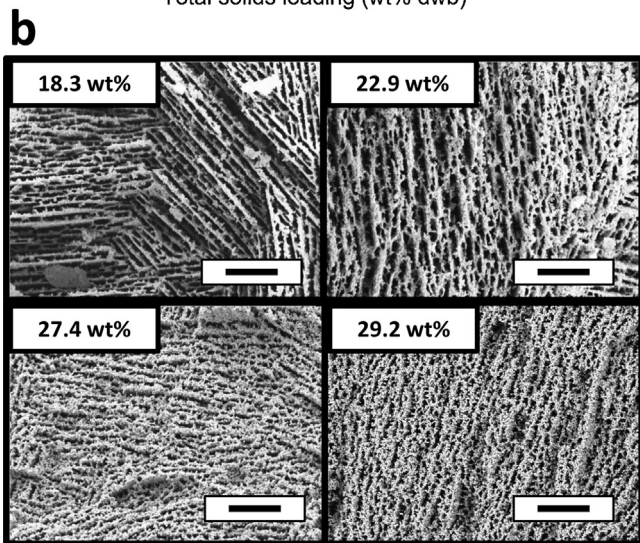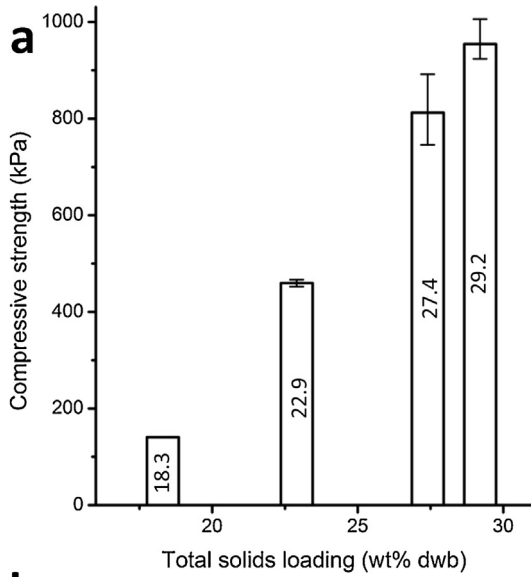
Fig. 4. Compressive strengths and microstructures of freeze-cast zeolite A-based monoliths prepared at a constant cooling rate of 10 K/min. (a) The compressive strengths of a series of monoliths made from suspensions with varying solids loadings, (b) the SEM graphs from the cross-sections of the monoliths for A20–A32. The scale bar is 100 μm.
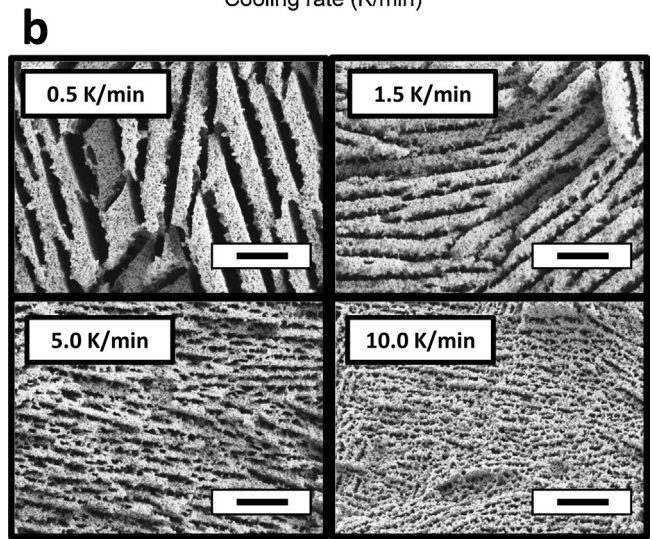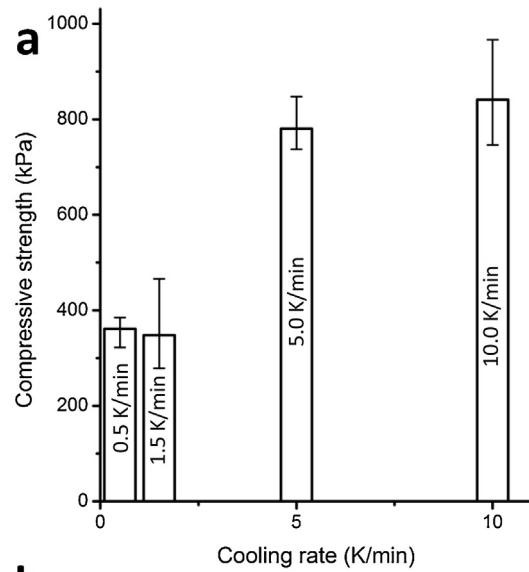

Fig. 5. Compressive strengths and microstructures of freeze-cast zeolite A-based monoliths prepared from A30-suspensions at cooling rates between 0.5 and 10 K/min, showing (a) the compressive strengths of a series of monoliths, and (b) SEM micrographs from the cross-sections of the monoliths. The scale bar is 100 μm.

have a slenderness ratio L/r, where $r = \sqrt{I/A_w}$, that exceeds a minimum value[39]:

$$\frac{L}{r} > \pi \sqrt{\frac{E}{\sigma^*}} \qquad (5)$$

Eq. (5) is satisfied for the freeze-cast monoliths when the length of a free wall section exceeds 200 μm, after which the brittle zeolite/bentonite composite wall will buckle during compression.

We have investigated the compressive strengths of several freeze-cast monoliths: first we tested two series, one series that focused on the influence of the density where monoliths freeze-cast at different suspension concentrations the same cooling rate, and another series that inspected the influence of the cooling rate, at a constant solids loading, on the strength.

Fig. 4 shows that the strength increases proportionally to the solids loading. This behavior is typical for brittle cellular solids without bending deformations and thick-walled honeycomb structures. Extending the linear relation to a dense material suggests that the maximum strength should be 1110 kPa, and extrapolating down to zero strength suggests the lowest limit for the solids loading is 16.5 wt%.

Fig. 5a shows that there is a significant difference in the compressive strengths between the monoliths freeze-cast at slow cooling rates (0.5 or 1.5 K/min) compared to the monoliths freeze-cast at high cooling rates (5.0 or 10.0 K/min): the compressive strength drops to approximately one half for the monoliths freeze-cast at slow cooling rates compared to the monoliths that were freeze-cast at high cooling rates. The visible differences in the scanning electron micrographs, Fig. 5b, show how the structure changes for the different cooling rates. Slow
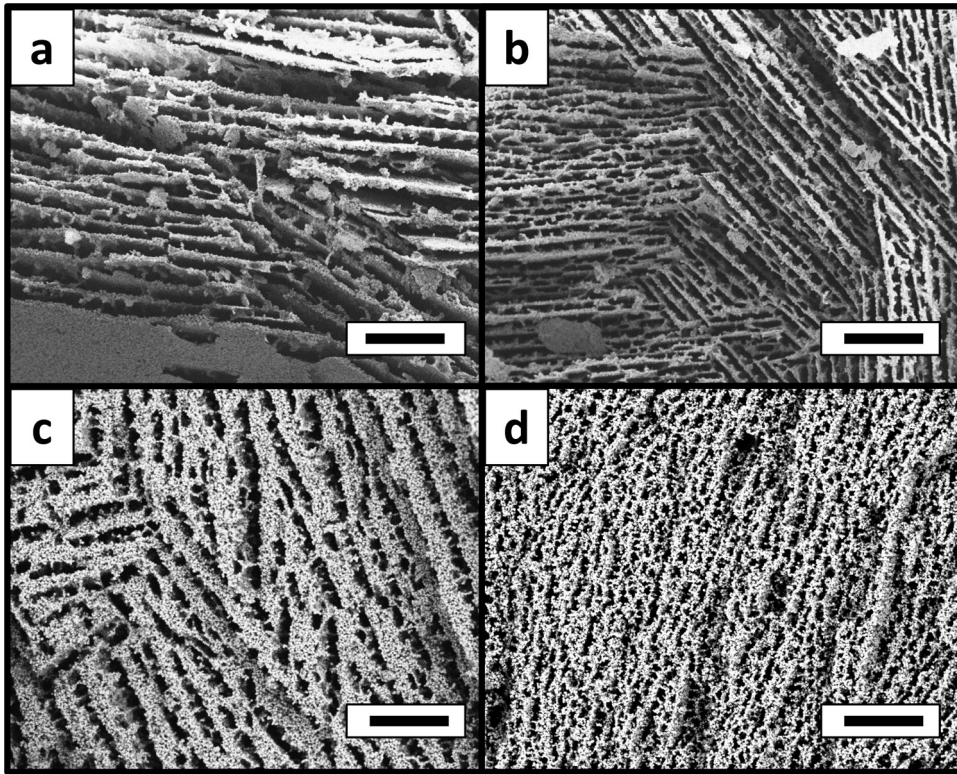
Fig. 6. SEM cross-sectional images of the four monoliths: (a) and (b) are A20 frozen at 1.5 and 10 K/min, respectively, and (c) and (d) are A32 frozen at 1.5 and 10 K/min, respectively. The scale bar is 100 μm.
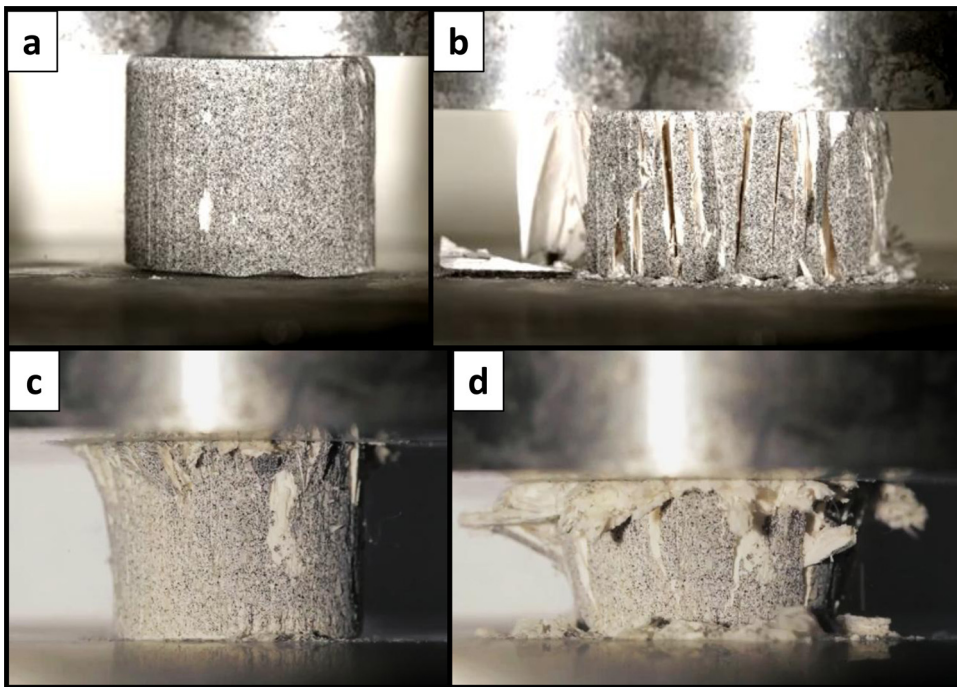

Fig. 7. Snapshots before (a, c), and after (b, d), of composite freeze-cast zeolite/bentonite monoliths subjected to a compressive strength test. Images (a) and (b) relate to monoliths made from suspension A32 by freezing at 1.5 K/min, and images (c) and (d) relate to monoliths made from suspension A20 by freezing at 1.5 K/min. The surface of the monoliths has been painted with small black dots in order to better follow the deformation of the surface.
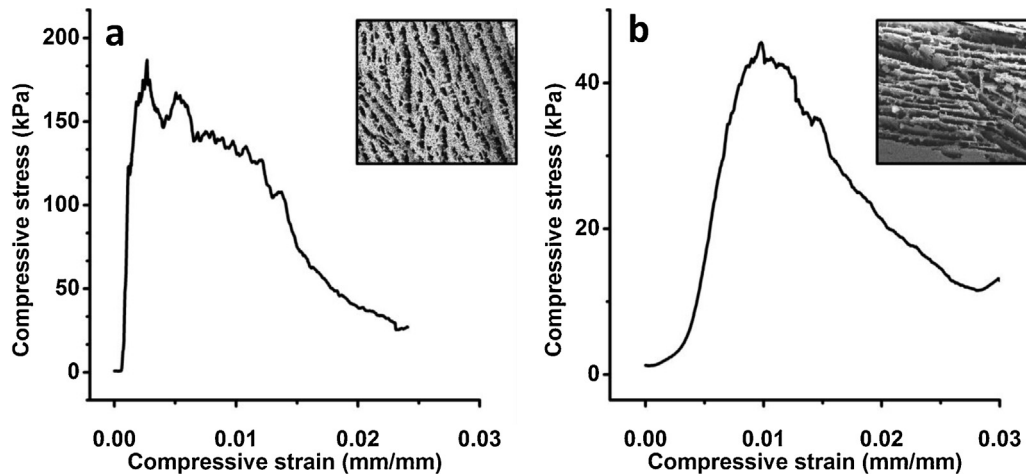
Fig. 8. Stress–strain curve for monoliths prepared from suspensions; (a) A32 and (b) A20 cooled at 1.5 K/min. The insets show typical SEM micrographs for the structures.

cooling of the suspensions leads to well-separated ice and zeolite/bentonite composite sheets, which creates a monolith with thick and clearly isolated lamella. On the other hand, rapid cooling reduces the lamella thickness and increases the number of transverse bridges or struts between them, to the point where, for the 10.0 K/min monolith, the pores are clearly more round than lamellar, and the structure is much more isotropic. The high number of struts will distribute the compressive stress to the adjoining lamella, whereas a limited number will result in a more localized fracture behavior of the individual lamella.

In order to further probe the stress-strain behavior of the monoliths, four monolith series were prepared from suspensions of both low and high solids loading at slow and fast cooling: A32 at 1.5 and 10.0 K/min and A20 at 1.5 and 10.0 K/min, as shown in Fig. 6.

The compression behavior of the freeze-cast monoliths under increasing load was carefully recorded with a high-speed camera; Fig. 7 shows snapshots before compression and during fracture of two of the monoliths. Their corresponding stress-strain curves in Fig. 8 show that elastic-brittle[26] failure is typical for freeze-cast monoliths: the linear elastic region at low stress is controlled by bending of cell walls, and at higher strains the material starts to collapse and the stress decreases sequentially. The compression experiment was terminated before the final region where the stress starts to increase again due to densification of the porous structure. Fig. 8 shows that the maximum stress occurs at a much smaller strain for the denser monolith (A32) compared to the less dense monoliths (A20). Fig. 7 shows that A32 holds together in a coherent piece, breaking gradually into thinner and thinner longitudinal splinters, whereas the much weaker monolith A20 collapse by a process where the thin, relatively isolated, lamella fail individually and crumble very close to the top of the monolith.

We have made an attempt to retrieve more quantitative information on the pore anisotropy from the SEM graphs with digital image analysis. A computer algorithm was used to convert the grayscale image into a binary one containing empty pores and dense walls. Morphological dilation smoothened out any unrealistically small features and noise, and an algorithm for a principal
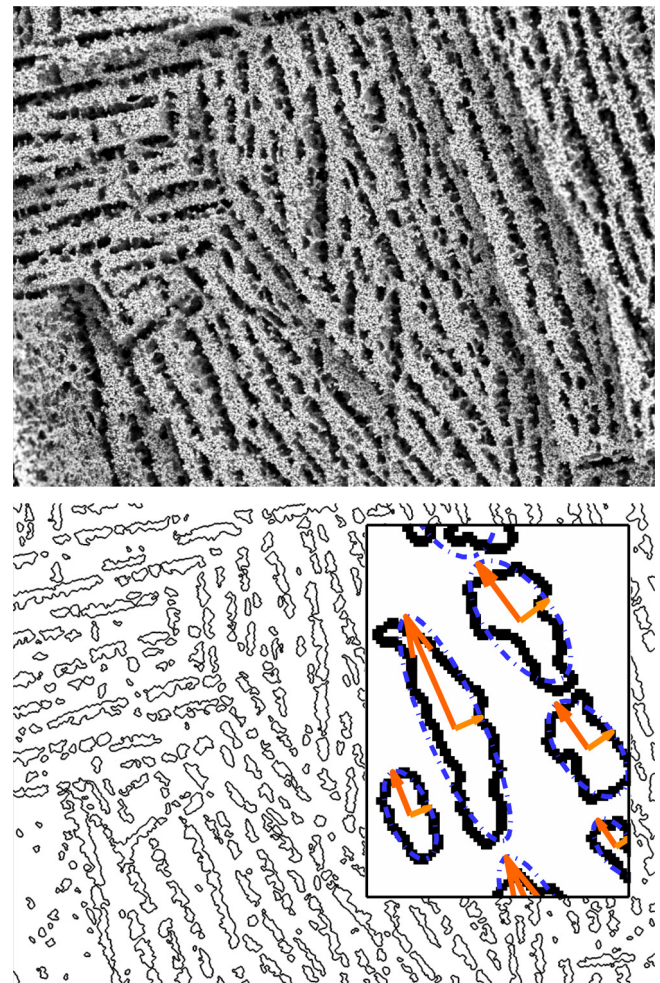

Fig. 9. Cross-sectional SEM images of a monolith frozen at 1.5 K/min from A32 suspension. The top images display the unprocessed cross-sectional SEM image, and the bottom image shows the result after image processing, outlining the pore boundaries. The inset in the bottom image shows details of ellipsoids that represent the pores, and the arrows are the semi-major and semi-minor axes of the ellipsoids, or half of the pore major and minor axis, respectively. An interactive version of the figure is available as supplementary information.
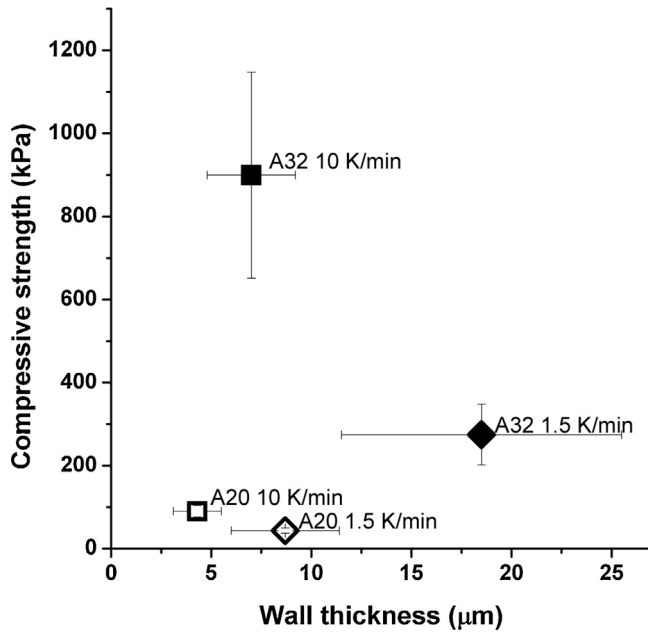
Fig. 10. The maximum compressive strengths of four monoliths with different wall thicknesses. Each point contains information on which dispersion (A20 (open symbols) and A32 (closed symbols)) and what cooling rate (1.5 K/min (diamonds) or 10 K/min (boxes)) the monoliths were freeze-cast at. The error bars are the standard deviations for the measured wall thicknesses (horizontal bars) and compressive strengths (vertical bars).
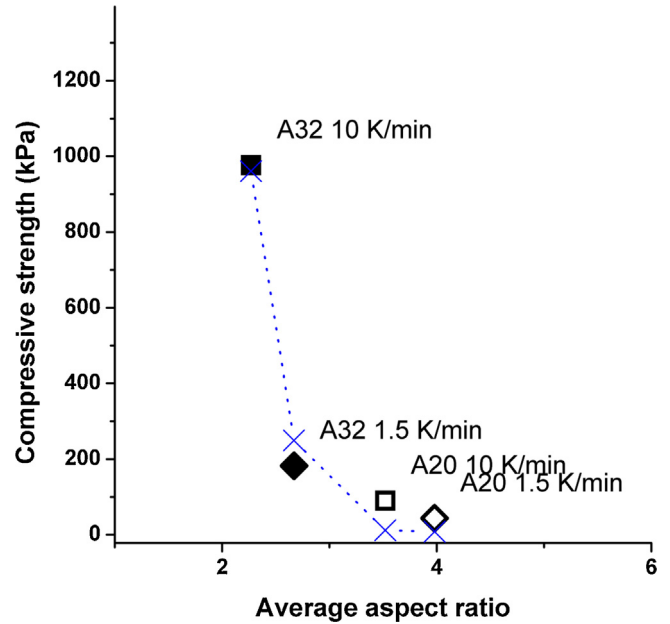

Fig. 11. The compressive mechanical strength σ^* versus the average cross-sectional pore aspect ratio of the freeze-cast monoliths. The open symbols denote low-density monoliths, cast from the A20 suspension, and the closed symbols denote high-density monoliths out of A32. Squares indicate a cooling rate of 10 K/min and diamonds 1.5 K/min. The blue crosses connected with a dotted line indicate the calculated compressive strengths according to Eq. (6) using data from Table 2.

component analysis was used to find the main axis and the center point of the pore. Orthogonal major and minor axes were then calculated from the pore center point, and used to draw ellipsoids for each pore in order to quantify the cross-sectional pore width, pore area, and pore aspect ratio, individually. A typical processed image is shown in Fig. 9.

As seen in Fig. 10, combining the estimates of wall thickness from the image analyses with the compressive strengths data shows that even if a high solids loading results in a high strength, a strong monolith can also be obtained by decreasing the wall thickness, i.e., by increasing the cooling rate. Increasing the cooling rate at constant solids loading, i.e., porosity, organize the lamella into several thin sections, that are much less likely to contain a flaw big enough to be critical for the entire volume under stress, analogous to the well-known effect in dense material where the strength increases as the characteristic length scale decreases.[40]

The influence of the pore morphology of freeze-cast monoliths on the strength was recently investigated by Porter et al.[28] who found a correlation between the compressive strength σ^* of the porous solid and the pore aspect ratio χ, and showed that the strength could be predicted with an expression based on the Euler buckling theory (Eq. (4)) by modifying the expression of inertia and adding a surface roughness parameter:

$$\sigma^* = \frac{\pi q^2 E}{(k'L)^2}\left(\frac{A_w^2}{3b^2}\left(\frac{1}{x}\right)^2 + \frac{A_w}{2}\left(\frac{1}{x}\right) + \frac{b^2}{4}\right) \qquad (6)$$

where q is an empirical factor relating to the surface roughness of the lamella, E is the elastic modulus, k' is a geometry parameter, L is the lamellar wall height, A_w is the wall cross-sectional area

($A_w = ad$, a is the pore main axis and d is the wall thickness) and b is the pore minor axis (Table 2).

Fig. 11 shows that the experimental data can be accurately described with Eq. (6), indicating that the dominating failure mechanism during fracture might indeed be buckling of the very thin and long lamella, even for the columnar monoliths. The measured compressive strength data was used to calculate the Weibull distribution (Fig. 12) for the probability of survival, P_S, of the monoliths[41]:

$$P_S = \exp\left[-\left(\frac{\sigma^*}{\sigma_0}\right)^m\right] \qquad (7)$$

where σ_0 is the characteristic strength of the monolith (the strength for which the P_S is $1/e$) and m is the Weibull modulus, determined from linear regressions of the series in Fig. 11a. The monoliths produced from the A32 suspensions at cooling rates of 1.5 and 10 K/min had a Weibull moduli of 2.3 and 3.4, respectively, while the weaker monoliths produced from the A 20 suspensions at cooling rates of 1.5 and 10 K/min had higher moduli, 6.9 and 7.1, respectively.

The Weibull survival probability plot in Fig. 12b shows that, although the Weibull modulus is comparatively high, the A20 monoliths will fail easily already at a low stress, and while the A32 have a higher average strength, the low Weibull modulus shows that the monolith may fail at stresses much lower than the average σ^*.

In summary, our results suggest that weaker A20 monolith fail at very low compressive stress due to the ease of bending and buckling of thin, isolated, laminate walls. The monolith A32

Table 2
Morphological and mechanical properties of monoliths prepared from suspensions with low (A20) and high (A32) concentrations, frozen at slow (1.5 K/min) and fast (10.0 K/min) cooling rates.

	A20 1.5 K/min	A20 10.0 K/min	A32 1.5 K/min	A32 10.0 K/min
Pore area A_P [μm^2]	438	112	298	106
Wall thickness d [μm]	8.70	4.33	18.5	7.03
Pore major axis a [μm]	45.1	23.6	32.6	20.2
Pore minor axis b [μm]	11.3	6.70	12.2	8.89
Aspect ratio χ	3.98	3.52	2.67	2.27
Elastic modulus E [kPa]	479	2270	5930	89,600
Compressive strength σ^* [kPa]	44.5	90.2	183	977

1.5 K/min has more bridges between the lamella and its failure is more dependent on crack propagation through an entire longitudinal section, ultimately depending on the arrangement of walls. The strongest monolith, A32 10.0 K/min, does not have any distinct lamella, and the compressive energy is dissipated more evenly, leading to the highest measured σ^* of the investigated monoliths.

The equilibrium uptake of CO_2 in consolidated zeolite NaA monoliths was determined to be 3.30 mmol/g. The 10.2% K-exchanged NaKA had a lower uptake, 2.91 mmol/g, most likely due to the decreased micropore volume after ion-exchange. The 17.6% K-exchanged monoliths a slow uptake where equilibrium was not reached after several days.

Time-dependent gas flow through a column filled with freeze-cast adsorbent monoliths is shown in Fig. 13. The initial flow of N_2 gas is replaced by a 1:9 CO_2:N_2 gas mixture at time zero and the concentration of CO_2 is monitored at the end of the column. The region of zero concentration in the gas breakthrough curve corresponds to the time during which CO_2 is completely adsorbed by the solid, and the region where the concentration

C/C_0 lies between zero and one, often called the mass transfer zone (MTZ), is the zone where some gas is being adsorbed while some gas is flowing past. In a separation column the gas flow would be turned off at the start of the MTZ, and its sharpness is an indication of how large portion of the bed is still unsaturated during the end of the adsorption cycle.

The breakthrough front for the freeze-cast zeolite monoliths shows a rapid increase in the relative CO_2 concentration indicating the low resistance to mass transfer and uniform gas flow.[42,43] The pure 4A monolith bed (black squares) takes 50 s until CO_2 is slipping through and a total of 100 s until the bed is saturated, while the 10.2% and 17.6% K-exchanged monoliths show first traces of CO_2 penetration at 30 s and saturation at 80 s (NaKA 10.2%) and 100 s (NaKA 17.6%). These results suggest that at a flow of 150 cm^3/min, 0.25 cm^3 (or 0.011 mmol) of CO_2 is adsorbed into a monolith with a volume of 47 cm^3 every second until breakthrough, corresponding to a CO_2 uptake rate of 230 g_{CO_2}/(s m^2).

The mass transfer coefficients were $k = 0.31$, 0.29 and 0.17 m/s for the monoliths with a degree of potassium exchange
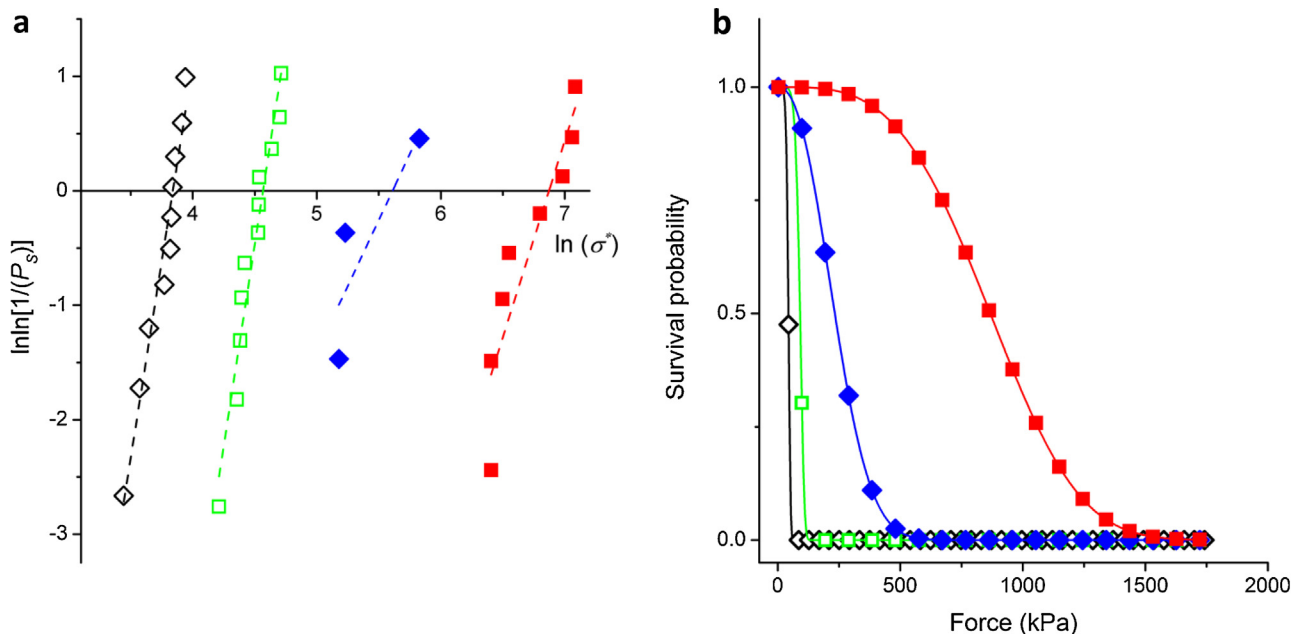

Fig. 12. The Weibull distribution for the compressive strength σ^* of freeze-cast monoliths. The Weibull moduli m for different monoliths was obtained using Eq. (6) on the data in (a) and are presented as a survival probability plot in (b). Black open diamonds: A20 1.5 K/min, green open squares: A20 10.0 K/min, blue diamonds: A32 1.5 K/min, red squares: A32 10.0 K/min. (For interpretation of the references to color in this figure legend, the reader is referred to the web version of this article.)
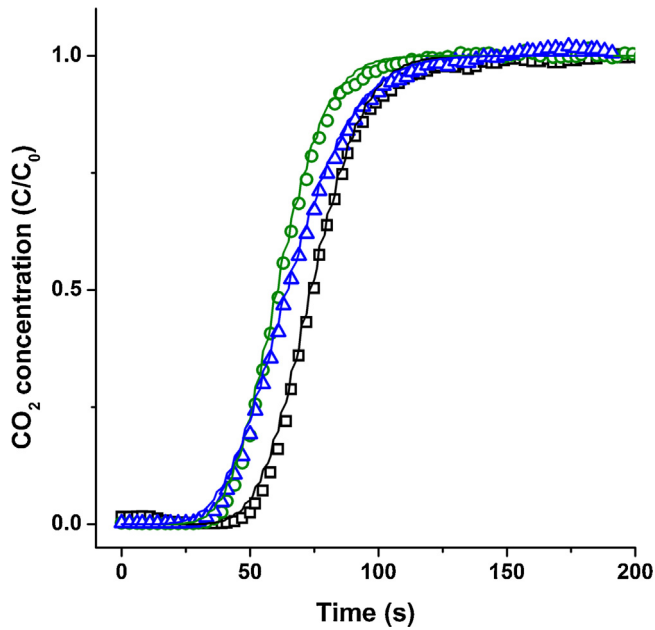
Fig. 13. CO_2 breakthrough curves for freeze-cast monoliths frozen at 10.0 K/min from an A20 suspension of zeolite NaA (black square), 10.2% K-exchanged NaKA (green circle) and 17.6% K-exchanged NaKA (blue triangle). (For interpretation of the references to color in this figure legend, the reader is referred to the web version of this article.)

of 0%, 10.2% and 17.6%, respectively. These mass transfer coefficients correspond to typical values for isothermal uptake (adsorbate concentration < 1%) of SO_2 in packed beds consisting of pellets with a diameter below 1 mm.[44] We can also calculate the effective diffusivities, which for the three different ion-exchanged adsorbent monoliths are $D_e = 2.3 \times 10^{-7}$, 2.2×10^{-7}, and 1.3×10^{-7} m²/s.

4. Conclusions

We have evaluated the fracture behavior of freeze-cast zeolite A composite monoliths under compressive loading for various pore structures and porosities, and their CO_2 uptake kinetics at different potassium exchange ratios. The compressive strength of the brittle freeze-cast monolith was found to follow the Euler buckling mechanism. The strength increases with increasing solids loading and decreasing cross-sectional pore aspect ratio, which was determined by image analysis. A Weibull analysis of the predicted survival probability at a characteristic strength revealed that there are two distinctly different Weibull moduli for the monoliths, one close to 3 and another close to 7. The former was linked to an average pore aspect ratio below 3, while the higher Weibull moduli relate to monoliths with a pore aspect ratio above 3.

We also determined the concentration limits of the aqueous zeolite-based powder suspension for successful freeze-casting. The lower zeolite concentration of the suspension was extrapolated from the compressive tests of monoliths frozen at 10 K/min, which were found to be linearly dependent on the solids loading, and a value of 16.5 wt% dwb was obtained. This is close to the

practical lower limit of 18.3 wt% that could be used to produce self-supporting, albeit very fragile, structures.

The sharp front in breakthrough experiments indicate that the freeze-cast monoliths have a low mass transfer resistance and promote a uniform gas flow along the macropore channels. The uptake of CO_2 from a 1:9 mixture of CO_2 and N_2 in a gas breakthrough experiment was found to be slower for 17.6% than for NaA (no ion exchange) or 10.2% K-exchanged zeolite A.

Appendix A. Appendix A Calculation of diffusion from breakthrough curves

In a parallel laminate system we assume that the axial dispersion is negligible, so the differential mass balance in a column of length z becomes

$$v\frac{\partial c}{\partial z} + \frac{\partial c}{\partial t} + \left(\frac{1-\in}{\in}\right)\frac{\partial q'}{\partial t} = 0 \tag{8}$$

where c is the concentration of the fluid, $\in$ is the total void fraction, q' is the loading of the adsorbate in the adsorbent and t is time.

The interstitial velocity v is:

$$v = \frac{Q_V \in}{S} \tag{9}$$

where Q_V is the volumetric flow rate of the fluid and S is the cross-sectional area of the bed.

The analytical solution to describe the concentration of the adsorbate at the end of the column in a breakthrough is adapted from Klinkenberg[46]:

$$\frac{c}{c_0} = \frac{1}{2} \cdot erfc\left(\sqrt{\xi} - \sqrt{\tau} - \frac{\sqrt{\xi}}{8} - \frac{\sqrt{\tau}}{8}\right) \tag{10}$$

where the dimensionless bed length ξ is

$$\xi = \frac{kKz}{v}\left(\frac{1-\in}{\in}\right) \tag{11}$$

where k is the mass-transfer coefficient and K is the Henry constant of the adsorbate. The dimensionless time τ is

$$\tau = k\left(t - \frac{z}{v}\right) \tag{12}$$

If we assume that the diffusion in the macropores is much faster than the diffusion in the micropores, then the time at which the adsorbate reaches the end of the column is governed by the uptake kinetics and capacity of the adsorbate, which at fast diffusion and low partial pressures are expressed by the Henry constant K. The steepness of the curve, i.e., the time it takes to saturate the entire column, is controlled by the mass transfer resistance of the lamellae and expressed by the mass-transfer

coefficient k. The mass transfer coefficients for the monoliths with three degrees of potassium exchange become $k = 0.31$, 0.29 and 0.17 m/s for 0%, 10.2% and 17.6% NaKA, respectively. This corresponds to typical values for isothermal uptake (adsorbate concentration < 1%) of SO_2 in packed beds consisting of pellets with a diameter below 1 mm.[44] At 10% CO_2 we are unlikely to have an isothermal condition, which lowers the mass transfer rate somewhat.

The mass-transfer coefficient k can be divided into the film and pore mass-transfer coefficients, denoted by k_f and k_p, respectively.[21] They are related by:

$$\frac{1}{k} = \frac{1}{k_f} + \frac{1}{k_p} \tag{13}$$

where

$$k_f = \frac{D_m \cdot Sh}{b} \tag{14}$$

$$k_p = \frac{6 D_e}{t} \tag{15}$$

And again t is the width of the laminate wall, b is the pore minor axis, D_m and D_e are the molecular and effective diffusion coefficients, respectively, and Sh is the Sherwood number. The value of $D_m = 1.72 \times 10^{-5}$ m²/s was taken for CO_2 in N_2 at 303 K from Massman et al.,[47] and the Sherwood number for a laminate structure is expressed by:

$$Sh = A \left(1 + 0.139 \ Sc \ Re \frac{b}{L_c} \right)^{0.81} \tag{16}$$

where A is a parameter relating to the pore channel shape, 2.70 for a laminate system was used, and L_c is the length of the column, 0.15 m. The Schmidt number Sc, which relates the kinematic viscosity (the root of dynamic viscosity and density) to the molecular diffusivity, is determined by:

$$Sc = \frac{\mu_d}{D_m \rho} \tag{17}$$

where the density of the gas mixture at 303 K is $\rho = 0.1 \times \rho_{Co_2} + \rho_{N_2} = 0.117 \ Kg/m^3$, and the dynamic viscosity μ_d for a 1:9 CO_2:N_2 mixture is obtained by the Wilke equation:[48]

$$\mu_d = \frac{\mu_1}{1 + \frac{(x_2/x_1)[1+(\mu_1/\mu_2)^{1/2}(M_2/M_1)^{1/4}]^2}{(4/\sqrt{2}[1+(M_1/M_2)]^{1/2}}}$$
$$+ \frac{\mu_2}{1 + \frac{(x_1/x_2)[1+(\mu_2/\mu_1)^{1/2}(M_1/M_2)^{1/4}]^2}{(4/\sqrt{2}[1+(M_2/M_1)]^{1/2}}} \tag{18}$$

Where the values of $\mu_1 = 1.50 \times 10^{-5}$ Ns/m² and $\mu_2 = 1.79 \times 10^{-5}$ Ns/m² for CO_2 and N_2 were used, respectively, and $\mu_d = 2.25 \times 10^{-5}$ Ns/m². This results in $Sc = 11.2$. The Reynolds number Re was calculated from:

$$Re = \frac{(\rho u^2)}{(\mu_d u / L)} \tag{19}$$

Where the superficial velocity $u = 7.96 \times 10^{-3}$ m/s and the characteristic length L is expressed as the equivalent hydraulic diameter of a rectangular channel with the dimensions of the average lamellar pore, $L = 2ab/(a+b) = 1.10 \times 10^{-5}$ m. Thus $Re = 4.55 \times 10^{-4}$, which is well within the laminar flow region. Solving Eq. (16), since both b and Re are so small, the Sherwood number is dominated by the shape parameter A, and $Sh = 2.70$. Equation (14) then gives $k_f = 7.63$ m/s, and inserting that into Eq. (13) we obtain, for the three potassium contents 0%, 10.2% and 17.6% NaKA, three values of k_p, 0.32, 0.30 and 0.17 m/s, respectively. Equation (15) then gives us the respective effective diffusivities $D_e = 2.33 \times 10^{-7}$, 2.17×10^{-7}, and 1.26×10^{-7} m²/s.

Appendix B. Supplementary data

Supplementary data associated with this article can be found, in the online version, at doi:10.1016/j.jeurceramsoc. 2015.03.001.

References

1. D'Alessandro DM, Smit B, Long JR. Carbon dioxide capture: prospects for new materials. *Angew Chem Int Ed Engl* 2010;**49**:6058–82.
2. Hedin N, Chen L, Laaksonen A. Sorbents for CO_2 capture from flue gas – aspects from materials and theoretical chemistry. *Nanoscale* 2010;**2**:1819–41.
3. Samanta A, Zhao A, Shimizu GKH, Sarkar P, Gupta R. Post-combustion CO_2 capture using solid sorbents: a review. *Ind Eng Chem Res* 2012;**51**:1438–63.
4. Wang Q, Luo J, Zhong Z, Borgna A. CO_2 capture by solid adsorbents and their applications: current status and new trends. *Energy Environ Sci* 2011;**4**:42.
5. Tuinier MJ, van Sint Annaland M, Kramer GJ, Kuipers JAM. Cryogenic capture using dynamically operated packed beds. *Chem Eng Sci* 2010;**65**:114–9.
6. Rochelle GT. Amine scrubbing for CO_2 capture. *Science* 2009;**325**:1652–4.
7. Hedin N, Andersson L, Bergström L, Yan J. Adsorbents for the post combustion capture of CO_2 using rapid temperature swing or vacuum swing adsorption. *Appl Energy* 2013;**104**:418–33.
8. Mason JA, Sumida K, Herm ZR, Krishna R, Long JR. Evaluating metal-organic frameworks for post-combustion carbon dioxide capture via temperature swing adsorption. *Energy Environ Sci* 2011;**4**:3030.
9. McDonald TM, et al. Capture of carbon dioxide from air and flue gas in the alkylamine-appended metal-organic framework mmen-Mg2(dobpdc). *J Am Chem Soc* 2012;**134**:7056–65.
10. Ma J, Liu Q, Chen D, Zhou Y, Wen S. Carbon dioxide adsorption using amine-functionalized mesocellular siliceous foams. *J Mater Sci* 2014;**49**:7585–96.
11. Hahn MW, Steib M, Jentys A, Lercher JA. Tailoring hierarchically structured SiO_2 spheres for high pressure CO_2 adsorption. *J Mater Chem A* 2014;**2**:13624.
12. Cheung O, et al. CO_2 selective NaMg-CTS-1 and its structural formation from the titanium silicate based molecule sieve NaMg-ETS-4. *Microporous Mesoporous Mater* 2014;**198**:63–73.
13. Du N, et al. Polymer nanosieve membranes for CO_2-capture applications. *Nat Mater* 2011;**10**:372–5.
14. Lu W, et al. Porous polymer networks: synthesis, porosity, and applications in gas storage/separation. *Chem Mater* 2010;**22**:5964–72.
15. Meng QB, Weber J. Lignin-based microporous materials as selective adsorbents for carbon dioxide separation. *ChemSusChem* 2014;**7**:3312–8, http://dx.doi.org/10.1002/cssc.201402879.
16. Hao G-P, Li W-C, Qian D, Lu A-H. Rapid synthesis of nitrogen-doped porous carbon monolith for CO_2 capture. *Adv Mater* 2010;**22**:853–7.
17. Hao W, Björkman E, Lilliestråle M, Hedin N. Activated carbons prepared from hydrothermally carbonized waste biomass used as adsorbents for CO_2. *Appl Energy* 2013;**112**:526–32.

18. Cheung O, Hedin N. Zeolites and related sorbents with narrow pores for CO_2 separation from flue gas. *RSC Adv* 2014;**4**:14480.
19. Akhtar F, Andersson L, Ogunwumi S, Hedin N, Bergström L. Structuring adsorbents and catalysts by processing of porous powders. *J Eur Ceram Soc* 2014;**34**:1643–66.
20. Rezaei F, Webley PA. Structured adsorbents in gas separation processes. *Sep Purif Technol* 2010;**70**:243–56.
21. Rezaei F, Webley PA. Optimum structured adsorbents for gas separation processes. *Chem Eng Sci* 2009;**64**:5182–91.
22. Rezaei F, et al. The effect of wall porosity and zeolite film thickness on the dynamic behavior of adsorbents in the form of coated monoliths. *Sep Purif Technol* 2011;**81**:191–9.
23. Ojuva A, Akhtar F, Tomsia AP, Bergström L. Laminated adsorbents with very rapid CO_2 uptake by freeze-casting of zeolites. *ACS Appl Mater Interfaces* 2013;**5**:2669–76.
24. Akhtar F, Liu Q, Hedin N, Bergström L. Strong and binder free structured zeolite sorbents with very high CO_2-over-N_2 selectivities and high capacities to adsorb CO_2 rapidly. *Energy Environ Sci* 2012;**5**:7664.
25. Gibson LJ, Ashby MF. *Cellular solids structures and properties*. 2nd ed. Cambridge University Press; 1997.
26. Ashby MF, Medalist RFM. The mechanical properties of cellular solids. *Metall Mater Trans A* 1983;**14**:1755–69.
27. Donius AE, Liu A, Berglund LA, Wegst UGK. Superior mechanical performance of highly porous, anisotropic nanocellulose-montmorillonite aerogels prepared by freeze casting. *J Mech Behav Biomed Mater* 2014;**37C**:88–99.
28. Porter MM, Imperio R, Wen M, Meyers MA, McKittrick J. Bioinspired scaffolds with varying pore architectures and mechanical properties. *Adv Funct Mater* 2014;**24**:1978–87.
29. Wegst UGK, Bai H, Saiz E, Tomsia AP, Ritchie RO. Bioinspired structural materials. *Nat Mater* 2014:1–14, http://dx.doi.org/10.1038/nmat4089.
30. Bouville F, Maire E, Deville S. Lightweight and stiff cellular ceramic structures by ice templating. *J Mater Res* 2014;**29**:175–81.
31. Hunger PM, Donius AE, Wegst UGK. Platelets self-assemble into porous nacre during freeze casting. *J Mech Behav Biomed Mater* 2013;**19**:87–93.
32. Hunger PM, Donius AE, Wegst UGK. Structure-property-processing correlations in freeze-cast composite scaffolds. *Acta Biomater* 2013;**9**:6338–48.
33. Tang Y, Miao Q, Qiu S, Zhao K, Hu L. Novel freeze-casting fabrication of aligned lamellar porous alumina with a centrosymmetric structure. *J Eur Ceram Soc* 2014;**34**:4077–82.
34. Cheung O, Bacsik Z, Liu Q, Mace A, Hedin N. Adsorption kinetics for CO_2 on highly selective zeolites NaKA and nano-NaKA. *Appl Energy* 2013;**112**:1326–36.
35. Liu D-M. Particle packing and rheological property of highly-concentrated ceramic suspensions: ϕ_m determination and viscosity prediction. *J Mater Sci* 2000;**5**:5503–7.
36. Zhang J, Ashby MF. The out-of-plane properties of honeycombs. *Int J Mech Sci* 1992;**34**(6):475–89.
37. Gibson LJ. Modelling the mechanical behavior of cellular materials. *Mater Sci Eng A* 1989;**110**:1–36.
38. Maiti SK, Ashby MF, Gibson LJ. Fracture toughness of brittle cellular solids. *Scr Metall* 1984;**18**:213–7.
39. Bazant ZP, Gedolin L. *Stability of structures: elastic, inelastic fracture and damage theories*. World Scientific Publishing Co. Pte. Ltd.; 2010. p. 3–19.
40. Griffith AA. The phenomena of rupture and flow in solids. *Philos Trans R Soc London* 1921;**221**:163–98.
41. Weibull W. A statistical distribution function of wide applicability. *J Appl Mech* 1951;**18**:293–7.
42. Mosca A, Hedlund J, Ridha FN, Webley PA. Optimization of synthesis procedures for structured PSA adsorbents. *Adsorption* 2008;**14**:687–93.
43. Mosca A, Hedlund J, Webley PA, Grahn M, Rezaei F. Structured zeolite NaX coatings on ceramic cordierite monolith supports for PSA applications. *Microporous Mesoporous Mater* 2010;**130**:38–48.
44. Gupta A, Gaur V, Verma N. Breakthrough analysis for adsorption of sulfur-dioxide over zeolites. *Chem Eng Process Process Intensif* 2004;**43**:9–22.
46. Klinkenberg A. Heat transfer in cross-flow heat exchangers and packed beds. *Ind Eng Chem* 1954;**46**:2285–9.
47. Massman WJ. A review of the molecular diffusivities of H_2O, CO_2, CH_4, CO, O_3, SO_2, NH_3, N_2O, NO, and NO_2 in air, O_2 and N_2 near STP. *Atmos Environ* 1998;**32**:1111–27.
48. Wilke CR. A viscosity equation for gas mixtures. *J Chem Phys* 1950;**18**:517–9.

Publication V

PASSIVE RESONANCE SENSOR BASED METHOD FOR MONI-TORING PARTICLE SUSPENSIONS

by

Salpavaara Timo, Järveläinen Matti, Seppälä Sari, Yli-Hallila Teemu, Verho Jarmo, Vilkko Matti, Lekkala Jukka & Levänen Erkki

Passive resonance sensor based method for monitoring particle suspensions

Timo Salpavaara [a,*], Matti Järveläinen [b], Sari Seppälä [b], Teemu Yli-Hallila [a], Jarmo Verho [a], Matti Vilkko [a], Jukka Lekkala [a], Erkki Levänen [b]

[a] Department of Automation Science and Engineering, Tampere University of Technology, P.O. Box 692, FI-33101 Tampere, Finland
[b] Department of Materials Science, Tampere University of Technology, P.O. Box 589, FI-33101 Tampere, Finland

ARTICLE INFO

ABSTRACT

Control of particle suspensions is needed in several modern industrial processes. A reason for the difficulty in this task has been the lack of a fast and reliable measurement. In this study, we tested the measurement of particle suspension by using a method based on a passive resonance sensor. The relative amounts of dispersing agent and aluminium oxide in the suspension were varied. The studied method yielded signals which depended on the complex permittivity of the suspension. The results indicated that we were able to measure information that can be used as feedback for the suspension preparation process. In addition, the tested instrumentation was simple and robust and thus this method may allow online measurements directly from the industrial processes.

© 2015 Elsevier B.V. All rights reserved.

1. Introduction

Monitoring and controlling particle suspensions are essential parts of many modern industrial processes. One example is the manufacturing of technical ceramic components. The use of these components has increased in challenging applications due to their ability to withstand wear, high temperatures and corrosive environments better than traditional materials. These components are often manufactured via processes such as spray drying or slip casting where fine ceramic particles need to be suspended in liquid. The properties of the final components are highly dependent of the properties of the suspension [1]. It is important that the suspension is homogenous. In other words, the particles and additives have to be dispersed evenly in the suspension. Also, the solid content has to be as high as possible and the amounts of additives should be precisely at correct level. Thus, to increase efficiency and yield in processes that use suspensions, it is essential to develop industrially capable methods to characterize them.

Despite the fact that the slurry monitoring is an important part of the ceramic component manufacturing process, the commonly used quality assurance measurements are difficult and time-consuming. Usually a sample is taken and it is characterized in a laboratory. There are also measurement systems that have automatic sampling devices. Typical characterization methods are rheological measurements [2], centrifugal sedimentation tests [3], particle size and size distribution measurements and zeta potential analysis [4]. In addition to the challenges of getting representative samples from huge vessels, the transport to laboratories and the characterization tests take time. Thus, the results cannot be acquired in real time and cannot be used as effective feedback for the process. Hence there is a need for a non-invasive, inexpensive, rapid online-method that monitors qualities such as solid content, sedimentation and the effects of the additives. In addition to the traditional measurements, alternative methods have been developed based on ultrasound [5–7], microwaves [8] and electrical conductivity [9–11].

One other physical property of the materials that can be electrically measured is the relative electrical permittivity. This property describes how the electric field is affected by the dielectric medium compared with vacuum. The relative permittivity is calculated from a capacitance measurement. The typical form of the capacitive measuring element is a coaxial probe [12]. The probes are placed in the measured media and the measuring electronics or an amplifier has to be located in the close proximity of the probes to prevent noise pickup and parasitic capacitances. One other challenge of this method is to understand and control how the geometry of the

* Corresponding author at: Department of Automation Science and Engineering, Tampere University of Technology, P.O. Box 692, Korkeakoulunkatu 3, FI-33101 Tampere, Finland. Tel.: +358 40 7166528.
E-mail address: timo.salpavaara@tut.fi (T. Salpavaara).

capacitive probe affects the measured results. This can be problematic in industrial environments.

The dielectric or capacitive characterization techniques have been also tested for monitoring suspended particles [13–17]. In [14] Sjöblom et al. measured complex permittivity by using a dielectric sensor. The form of the sensor in these measurements was a capacitive coaxial probe. The dielectric sensor was measured by a computer controlled system that included a pulse generator and an oscilloscope. By using this method, the features like the sedimentation and volume fraction of Al_2O_3 were monitored. Despite the obvious advantages, this method, as such, is not popular in the ceramic industry to the best of our knowledge.

One variant of a dielectical measurement can be done using passive resonance sensors. The concept of passive resonance sensor has been known since the mid of the last century. In short, the principle of the method is to measure the behaviour of an LC circuit by using another coil [18]. When the reader coil is placed near to the LC circuit, an inductive link is formed. Because of this link, the resonance of the LC circuit can be detected when the impedance of the reader coil is measured. Different readout methods have been developed but the measurement of the complex impedance using an impedance analyser is one of the most common in the scientific studies [19–21]. The concept of passive resonance sensors has two notable advantages: it allows a short range wireless measurement and the structure of the actual sensor is very simple. The LC circuit can be measured through non-conductive materials like plastic or glass. However, it should be noted that this method does not allow making measurements through metallic container walls and the errors due the metallic objects in the measurement environment have to be investigated. The range of the measurement is relative to the dimensions of the coils, typically few centimetres. The simplicity of the sensor structure allows the use of nonconventional materials and makes the sensor durable and cheap to manufacture.

The applications of the passive resonance sensors range from simple pressure sensors to the measurement of chemical [20,22] and even biological variables [23]. The wide range of the applications is due to the fact that most of the typical measurement can be converted to the measurement of capacitance, resistance or inductance. All those quantities can be measured by using passive resonance sensors. A typical realization of this concept is a pressure sensor based on a pressure dependent capacitor [18,21,24]. Other tested applications are implantable sensors [18] and the measurement of moisture in sand and concrete [25]. The concept has also been used for measuring biopotential signals [26] and pH-value [20]. A new promising application for this concept is in biodegradable sensors [27,28].

The passive resonance sensors can be used to monitor the permittivity of their environment [19]. In [19] the real and imaginary parts of the complex permittivity have been calculated from the measured data with moderate success. This process requires and is dependent on accurate information of the sensor parameters and the constant that links the geometry of the sensor capacitor and the permittivity of the environment. The measurement of permittivity enables to detect the ratios of components in liquids [19] and gasses [29].

In this study, we investigate the possibilities of passive resonance sensors to monitor the preparation and composition of particle suspension. We selected aluminium oxide slurry as our test material since it is a common and well understood example of particle suspension. The tested slurry contains water, ceramic particles and additives. The proposed method combines the dielectric characterization techniques and a sensitive wireless measurement system. Thus we are able to measure slurry that can be used in a slip casting process without a complicated test arrangement. Also this method does not need excessive or expensive instrumentation and thus it may be transferred to the industrial environment in the future. The first goal of this work is to test if this method can be used to measure the volumetric ratio of ceramic particles dispersed in slurry. Secondly, since the use of dispersing agent is needed, its effects on the measurement are also studied. In this study, we verify the basic functioning of the measurement method.

2. Methods

The tested measurement method is based on the concept of passive resonance sensors. A magnetic field generated by a reader coil induces an electrical current to the sensor coil that creates an electrical field in the capacitor of the resonance circuit. The created electric field also partly passes through the measured substance, in this case slurry. The changes in the permittivity of the slurry will affect the equivalent capacitance of the sensor. In addition, the complex permittivity of the system will cause losses that can be measured.

2.1. Measurement setup

The cross-section of the measurement setup is shown in Fig. 1(a). The LC circuit tested in this work was made of a 7 μm thick etched aluminium pattern which was laminated between two 80 μm thick PET films. This pattern included a rectangular coil with three turns. The width of the coil wire was 0.6 mm. The diameter of the turns ranged from 14 mm to 21 mm. The pattern also had two rectangular 1 cm^2 surfaces which formed a parallel plate capacitor when the laminated film was folded in two and glued together. This structure encapsulates the LC circuit. The structure is durable, thin and easy to make. The capacitance and the resonance frequency of this kind of structure are sensitive to permittivity changes in its close proximity. The circuit was glued to the bottom of a glass container (borosilicate glass, diameter 115 mm, volume 500 ml) and then the sensor was embedded in the container by pouring a thin layer of epoxy on the bottom of the container (Fig. 1(b)). The thickness of the epoxy on top of the sensor was 0.3 mm. This layer was used to limit the effect caused by the measured substance on the resonance circuit. Without this layer, the conductivity of the slurry would cause excessive losses and the resonance of the sensor would be hard to detect. By using this configuration, the measurement
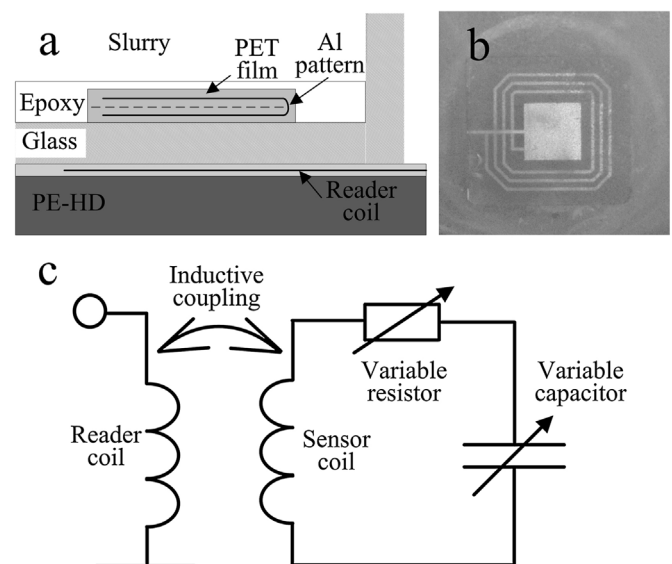
Fig. 1. (a) The cross-section of the encapsulated LC circuit in the measurement container. (b) Picture of the sensor embedded in epoxy. (c) The lumped element model of the measurement setup.
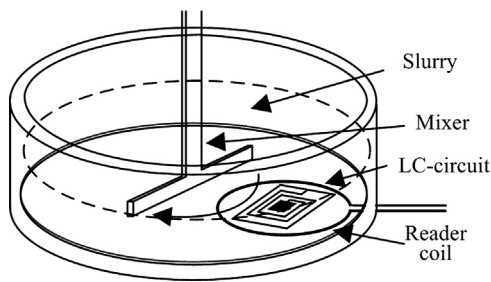
Fig. 2. The mixer was used to keep slurry homogenous on top of the sensor.

Fig. 3. Feature extraction process.

setup has no protruding parts and the stirrer can be used without the risk of the mixer blade hitting the sensor.

The resonance sensor was measured by a one-turn reader coil (diameter 40 mm) that was placed under the slurry container (Fig. 2). The reader coil was connected to a measuring device with a 20 cm RG-58C/U coaxial cable. The measurement was carried out with a custom-made reader device [24] that generates excitation and reference signals. The excitation signal was fed to the reader coil and compared against the reference. The device measures the magnitude ratio or gain/loss and the phase difference between two inputs. An in-house design was used instead of an impedance analyser for two reasons: the custom device allows more options for the sweep parameters and the sampling frequency, and the portability of the device allowed us to measure in premises where slurries are typically prepared and handled.

If a resonance sensor is placed near the reader coil, a resonance curve can be measured. The initial resonance curve and the resonance frequency of the sensor are defined by its dimensions and the materials that are used in the sensor. The permittivity of the tested material is altering the position of the resonance curve on the frequency axis. The measurements were done by using a 2000 point frequency sweep ranging from 70 MHz to 90 MHz and the sweep was repeated twice per second. By using this configuration and the selected frequency range, it is possible to measure materials whose permittivity range from air to water.

The electrical behaviour of the sensor in the measurement container can be modelled as a RLC circuit. A lumped element model of the measurement setup is shown in Fig. 1(c). The slurry is affecting the resistance and the capacitance of the model. The resistance represents both ohmic loss in the aluminium foil and the dielectric losses of the electric fields around and in the circuit. The capacitance in the model represents the parallel plate capacitor and the stray fields around the capacitor plates and the coil turns. The measured slurry mainly affects the resonator due to the electric fields between the coil turns and the other parts of the sensor. These electrical fields spread out to the environment through the non-conducting PET and epoxy layers. The electrical behaviour of nearly similar situation has been modelled by Ong et al. in [19]. The main difference between the measurement setups are that, in [19], the permittivity of the material is measured with an interdigital capacitor and the electrical field which interacts with materials is predominantly located near to the capacitor digits.

2.2. Feature extraction

The required signal processing for a resonance sensor measurement depends on the measured quantity, the measurement configuration and the reader device. A feature extraction process is used to capture the essential information from the measured data. One of the typical methods is to measure the complex impedance spectrum with an impedance analyser. Then the frequency of the maximum of the real part or the zero-reactance frequency can be identified [19]. The background subtraction can be used to remove
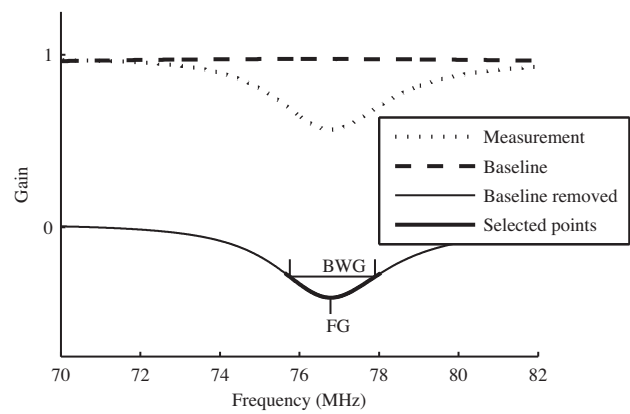
the impedance of the reader coil [19]. Another common method is to measure the phase of the impedance and to find the frequency of the phase minimum [21]. The relation between the extracted features can be analyzed, for example, by using the principal components analysis [29].

In this study, the measurement data consisted of gain response curves (GRC). An example of measured GRC is shown in Fig. 3. Each curve contained a set of gain values at discrete frequencies. A polynomial regression models were used to describe the essential areas of these curves. By using these models the place and form of the curves could be characterized as features. The goal was to link the changes of the measurands to the changes of characterized features. The data are expressed as dimensionless gain values because the form of the curve fits better to a polynomial regression model. The measured slurry or any other substance in the measurement container alters these curves, thus the proposed method is based on the measurement of the difference compared with the initial situation.

The measured gain response curve is seen as a dip on the frequency axis (Fig. 3). The dip was characterized by two features: the frequency (FG) and the bandwidth of the dip (BWG). These features were extracted from the polynomial model of the dip. The steps of the feature extraction process are illustrated in Fig. 3. First, the measured baseline (GRC of the reader coil without the presence of the resonance sensor) is subtracted from the GRC. The values that have an absolute value more than 65% of the absolute value of the measured minimum are selected. Then a 3rd order polynomial was fitted to the selected data points. A 3rd order polynomial can be fitted to selected data and the data set is still long enough to calculate the bandwidth of the dip. The absolute values were used because the dip has negative values. The 3rd order polynomial has been found to be a relatively robust and generalized model to describe the peaks and dips in frequency response data. The 3rd order polynomial is used instead of 2nd order polynomial to take into account the dissymmetry of the dip.

The feature FG is defined as the frequency where the polynomial model obtains its minimum value. The feature BWG is defined by using the identified polynomial model as a difference of the frequencies that have the same gain value as the value estimated at the frequency of FG divided by $\sqrt{2}$. This procedure mimics a typical process to define -3 dB bandwidth. The FG is strongly affected by the relative permittivity of the measured media. The BWG is affected by the losses in the resonator and the dielectric losses in the tested media. The extracted features may also have weak coupling between them.

2.3. Aluminium oxide slurry preparation

The measurement method was designed to monitor particle suspensions. To test this idea, the method was used to measure
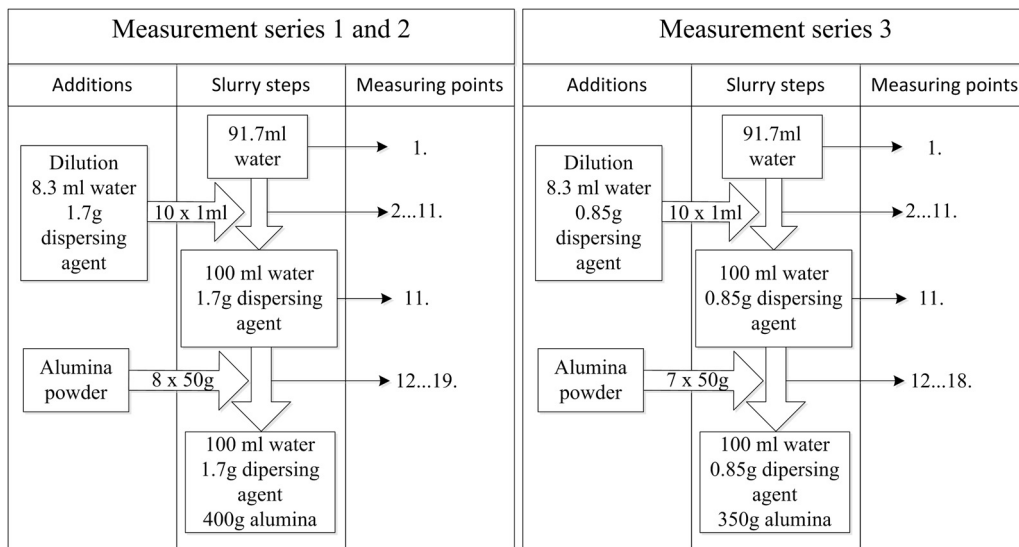
Fig. 4. The slurry preparation processes and the corresponding measurement points. The measurement series 1 monitors changes caused by the increasing dispersing agent concentration (points 2–11) and the increase of solid content (points 12–19). Series 2 is a repeat of series 1. Series 3 is identical to series 1 and 2, but only a half of the dispersing agent was used this time.

aluminium oxide slurry preparation. The slurries were made of Al_2O_3 powder, deionized water, and dispersing agent. First dispersing agent (Dispex A40, BASF SE) was dissolved to a small amount of water to ease the dosing of viscous liquid. Then the mixture was added to the remaining water in small increments. The dispersing agent worked as a stabilizer in the slurry. Then alumina powder (Martoxid MR70, Al_2O_3, Martinswerk) was added to the mixture in small increments. The alumina powder had a particle distribution where the majority of the particles are between 0.1 μm and 3 μm. The mixture was continuously stirred with a plastic blade in order to maintain its homogeneity. The plastic blade or the stirring speed had no significant effect on the measurement made with deionized water. Three slurry series were measured. The first two series were representing a typical slurry preparation process. In the third series, only a half of dispersing agent was used in order to test its effect on the measurement. Before each series, isopropanol was measured to test the repeatability of the measurement. The measurement points of the slurry preparation are illustrated in Fig. 4. The points were chosen solely to test the measurement method at discrete intervals. All measurements were done in room temperature 23 °C.

As a reference, a rheometer (Haake Rheostress RS150, Germany) was used to measure the viscosity of slurry. Because this reference viscosity measurement requires sampling (6 ml) which reduces the material, an identical slurry was prepared and the samples corresponding to the measurement points 15, 17 and 19 in Fig. 4 were taken. Since the viscosity of the tested material changes dramatically during the process, the test points were selected at high volumetric ratios of aluminium oxide in order to use the same measurement configuration for all tested samples. The corresponding reference viscosities measured at the shear rate of 10 1/s were 0.03 Pa s, 0.06 Pa s and 1.2 Pa s. The tested slurry was shear thinning material whose viscosity decreases as the shear rate increase.

3. Results

The gain response curves were measured during the preparation of the aluminium oxide slurry. The process contains two separate phases: the first phase is the addition of dispersing agent and the second phase is the addition of aluminium oxide. Separate procedures were used to calculate the results of each phase. The results of the first phase are compared with deionized water (Step 4a)

and the results of second phase are compared with the deionized water/dispersing agent mixture (Step 4b).

The results are obtained with following steps:

Step 1: A new sample is prepared.

Step 2: 100 gain response curves are measured and averaged.

Step 3: Features FG and BWG are extracted.

Step 4a: Features of the comparison point (deionized water, measurement point 1 in Fig. 4) are subtracted from the results.

Step 4b: Features of the comparison point (deionized water/dispersing agent mixture, measurement point 11 in Fig. 4) are subtracted from the results.

3.1. Measurement of dispersing agent

The results of the first process phase are presented in Fig. 5. Each point (except starting points) represents the situation after new portion of dispersing agent is added and fully mixed. The
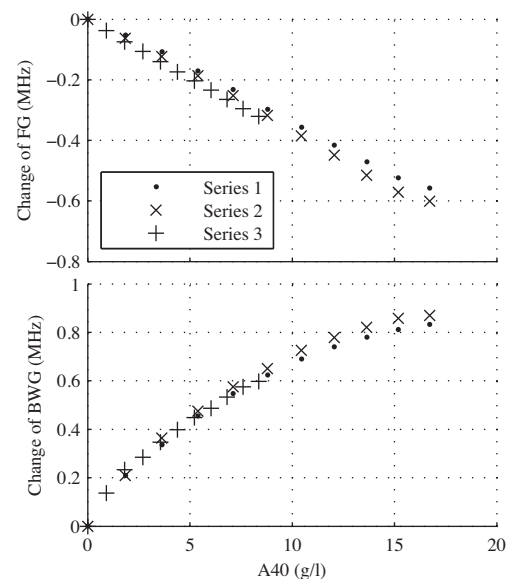
Fig. 5. The changes of the extracted features as the proportional amount of the dispersing agent in water was increased.
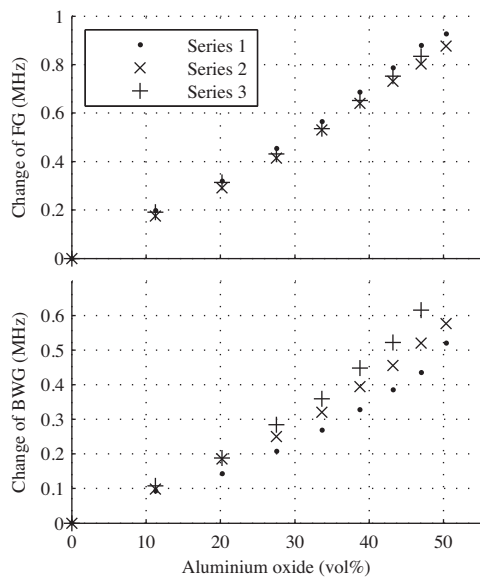
Fig. 6. The changes of the features FG and BWG as the volumetric ration of the aluminium oxide in the slurry was increased.

feature FG was decreasing as more dispersing agent was added. Within the tested range, the change of the FG was almost directly proportional to the concentration. The slope of the linear regression model for all measured data was −35 kHz/(g/l). The relation between the concentration of the dispersing agent and the BWG was non-linear. Repeatability of the features was good in both cases. One of the likely reasons for the noticed differences was the variation in the proportioning of the dispersing agent.

3.2. Measurement of aluminium oxide

The extracted features when aluminium oxide was added are presented in Fig. 6. The relation between the FG and the volumetric ratio of aluminium oxide in the slurry was almost linear. The average slope of the increase of FG in all these measurements was 18 kHz/vol%. According to these results with two tested concentrations, the amount of the dispersing agent only changed the starting point of the aluminium oxide measurement (Fig. 7, point 11). The
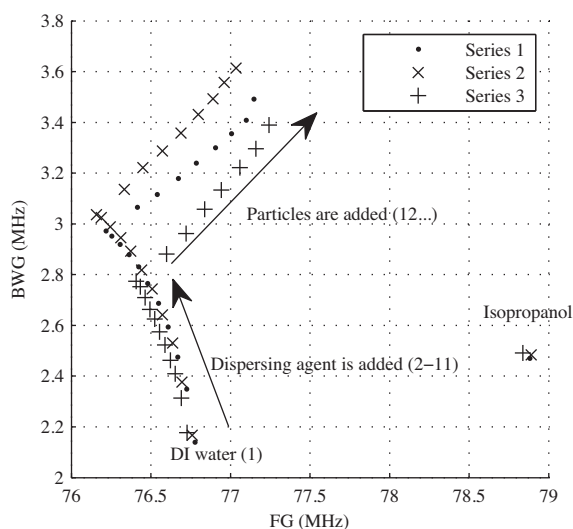
Fig. 7. The measured slurry preparation processes illustrated in a 2-dimensional map of the features FG and BWG. The features of isopropanol were measured as a reference.

behaviour of the FG was similar between all the three test series. The largest differences between the linear regression model and the measured data occur at the higher volume ratios. This may be caused by the non-homogeneity of slurry. The feature BWG cannot be used as an indicator of the volumetric ratio of the aluminium oxide in the slurry since the amount of dispersing agent will affect its behaviour.

3.3. Visualization of slurry preparation process

The preparation of aluminium oxide slurry can be visualized as a 2D map, where the axes are the features FG and BWG. Fig. 7 presents the extracted FG and BWG values of the three test series and isopropanol that was used as a reference material. This map also provides the means to study the repeatability of the measurement method. There is an offset in the features measured in plain deionized water and isopropanol reference between the test series. This may occur due to the changes in the placement of the measurement setup, contaminants in the liquids (especially deionized water) or changes in the measurement electronics.

An increase in the dispersing agent concentration decreases the FG and increases the BWG. Each increment is clearly distinguishable even if the added amount is small in comparison with the total amount of water. The overall behaviour of the measured features is similar between the series when aluminium oxide is added. The addition increases both extracted features. The series 1 and 2 are similar but not identical. In the third series, only half of the amount of the dispersing agent was used and the difference can be seen since the increase of the FG begins from a clearly different point.

4. Discussion

The long polarized molecules of the dispersing agent may explain the decrease of the feature FG when dispersing agent was added. The dispersing agent also increased the dielectric losses which were seen as the increase of the feature BWG. The aluminium oxide in water-dispersing agent solution increased the features FG and BWG. The increase of the FG may be explained by the fact that the aluminium oxide ($\varepsilon_r \approx 8$–10) has much lower relative permittivity than water ($\varepsilon_r \approx 80$). Thus slurry with a high volume fraction of aluminium oxide has lower relative permittivity and in this measurement it led to higher resonance frequency of the sensor and higher value of the FG. The increase of BWG may relate to the fact that the dispersing agent molecules attached themselves electrically on the aluminium oxide particle's surface and the formed combination interacted with the electrical field as a whole. As a summarization, the results suggest that the origin of the found changes in the measured features was caused by charging of molecules and surfaces and their interaction.

The more detailed electrical model of the measured media and the sensor and their interaction is left for further studies. The task has two major phases. The first one is to create a model that predicts the complex permittivity of the measured media based on the parameters of the particle suspension such as the volume ratio of particles and the used materials. Modelling of a complex of water–alumina–dispersant suspension is a hefty conundrum since even a dielectric model of two-component particulate suspension is a classic problem [13]. This kind of model would help to understand which parameters of suspension can be monitored by measuring its complex permittivity. The second phase is to create a model that predicts the extracted features based on complex permittivity. The electrical interaction between the sensor and the media is dependent on the geometry of the measurement capacitor and thus the optimization and modelling should be done when the measurement method is scaled up for the industrial use. Even as

such, the presented method can be used for clustering, classification and general quality assessment of particle suspensions as an online measurement method.

5. Conclusions

The advantage of the presented method is the simple and robust structure of the sensor. This may ease the installation and maintenance of the measurement. In this experimental application, the embedded sensor setup enabled to use the mixer in the vicinity of the sensor helping to maintain the homogeneity of the suspension. These usability features are an advantage when this method is transferred to industrial applications. The presented method shows potential as a tool for monitoring suspensions. The sensitivity of the method is adequate to measure even delicate changes in the amount of the dispersing agent and aluminium oxide. Thus the presented method can provide information that can be used to improve slurry preparation processes. In this study, interesting relations between the measurement features and the important parameters of slurry were found. In the following research, these relations should be further studied and modelled. Another task in the future is to measure a more extensive set of slurries with the presented method and to compare the results with reference methods like viscosity measurements and impedance spectroscopy.

Acknowledgements

References

[1] A. Tsetsekou, C. Agrafiotis, I. Leon, A. Milias, Optimization of the rheological properties of alumina slurries for ceramic processing applications. Part II. Spray-drying, J. Eur. Ceram. Soc. 21 (4) (2001) 493–506.

[2] B. Bitterlich, C. Lutz, A. Roosen, Rheological characterization of water-based slurries for the tape casting process, Ceram. Int. 28 (6) (2002) 675–683.

[3] J. Tsubaki, M. Kato, M. Miyazawa, T. Kuma, The effects of the concentration of a polymer dispersant on apparent viscosity and sedimentation behavior of dense slurries, Chem. Eng. Sci. 56 (2001) 3021–3026.

[4] R. Wäsche, M. Naito, V.A. Hackley, Experimental study on zeta potential and streaming potential of advanced ceramic powders, Powder Technol. 123 (2002) 275–281.

[5] J.A. Bamberger, M.S. Greenwood, Measuring fluid and slurry density and solids concentration non-invasively, Ultrasonics 42 (April (1–9)) (2004) 563–5677.

[6] J.A. Bamberger, M.S. Greenwood, Using ultrasonic attenuation to monitor slurry mixing in real time, Ultrasonics 42 (April (1–9)) (2004) 145–1488.

[7] M.S. Greenwood, J.A. Bamberger, Measurement of viscosity and shear wave velocity of a liquid or slurry for on-line process control, Ultrasonics 39 (August (9)) (2002) 623–630.

[8] F.E.I. Yuan, R. Pal, Measurement of solids concentration in aqueous slurries using a microwave technique, Chem. Eng. Sci. 50 (22) (1995) 3525–3533.

[9] H.A. Nasr-El-Din, R.S. Mac Taggart, J.H. Masliyah, Local solids concentration measurement in a slurry mixing tank, Chem. Eng. Sci. 51 (8) (1996) 1209–1220.

[10] M. Liu, T. Wang, W. Yu, J. Wang, An electrical conductivity probe method for measuring the local solid holdup in a slurry system, Chem. Eng. J. 132 (August (1–3)) (2007) 37–46.

[11] M. Špidla, V. Sinevič, M. Jahoda, V. Machoň, Solid particle distribution of moderately concentrated suspensions in a pilot plant stirred vessel, Chem. Eng. J. 113 (October (1)) (2005) 73–82.

[12] A.P. Gregory, R.N. Clarke, Dielectric metrology with coaxial sensors, Meas. Sci. Technol. 18 (May (5)) (2007) 1372–1386.

[13] V.A. Hackley, J. Texter (Eds.), Handbook on Ultrasonic and Dielectric Characterization Techniques for Suspended Particles, The American Ceramic Society, Ohio, 1998, pp. 47–74.

[14] B. Pettersen, E. Nodland, J. Sjöblom, A multivariate analysis on the sedimentation of aqueous silica suspensions as studied by means of time domain dielectric spectroscopy, J. Colloid Interface Sci. 214 (June (1)) (1999) 1–7.

[15] A.D. Hollingsworth, D.A. Saville, A broad frequency range dielectric spectrometer for colloidal suspensions: cell design, calibration, and validation, J. Colloid Interface Sci. 257 (1) (Jan. 2003) 65–76.

[16] P.J. Beltramo, E.M. Furst, Dielectric spectroscopy of bidisperse colloidal suspensions, J. Colloid Interface Sci. 380 (August (1)) (2012) 34–41.

[17] P.J. Beltramo, R. Roa, F. Carrique, E.M. Furst, Dielectric spectroscopy of concentrated colloidal suspensions, J. Colloid Interface Sci. 408 (October (1)) (2013) 54–58.

[18] C.C. Collins, Miniature passive pressure transenter for implanting in the eye, IEEE Trans. Biomed. Eng. 14 (April (2)) (1967) 74–83.

[19] K.G. Ong, C.A. Grimes, C.L. Robbins, R.S. Singh, Design and application of a wireless, passive, resonant-circuit environmental monitoring sensor, Sens. Actuators A: Phys. 93 (August (1)) (2001) 33–43.

[20] B.E. Horton, S. Schweitzer, A.J. DeRouin, K.G. Ong, A varactor-based, inductively coupled wireless pH sensor, IEEE Sens. J. 11 (April (4)) (2011) 1061–1066.

[21] M.A. Fonseca, J.M. English, M. von Arx, M.G. Allen, Wireless micromachined ceramic pressure sensor for high-temperature applications, J. Microelectromech. Syst. 11 (August (4)) (2002) 337–343.

[22] R.A. Potyrailo, N. Nagraj, C. Surman, H. Boudries, H. Lai, J.M. Slocik, N. Kelley-Loughnane, R.R. Naik, Wireless sensors and sensor networks for homeland security applications, Trends Anal. Chem. 40 (November (4)) (2012) 133–145.

[23] M.S. Mannoor, H. Tao, J.D. Clayton, A. Sengupta, D.L. Kaplan, R.R. Naik, N. Verma, F.G. Omenetto, M.C. McAlpine, Graphene-based wireless bacteria detection on tooth enamel, Nat. Commun. 3 (January) (2012) 763.

[24] T. Salpavaara, J. Verho, P. Kumpulainen, J. Lekkala, Readout methods for an inductively coupled resonance sensor used in pressure garment application, Sens. Actuators A: Phys. 172 (December (1)) (2011) 109–116.

[25] J.B. Ong, Z. You, J. Mills-Beale, E.L. Tan, B.D. Pereles, K.G. Ong, A wireless, passive embedded sensor for real-time monitoring of water content in civil engineering materials, IEEE Sens. J. 8 (December (12)) (2008) 2053–2058.

[26] J. Riistama, E. Aittokallio, J. Verho, J. Lekkala, Totally passive wireless biopotential measurement sensor by utilizing inductively coupled resonance circuits, Sens. Actuators A: Phys. 157 (February (2)) (2010) 313–321.

[27] S.-W. Hwang, H. Tao, D.-H. Kim, H. Cheng, J.-K. Song, E. Rill, M. a Brenckle, B. Panilaitis, S.M. Won, Y.-S. Kim, Y.M. Song, K.J. Yu, A. Ameen, R. Li, Y. Su, M. Yang, D.L. Kaplan, M.R. Zakin, M.J. Slepian, Y. Huang, F.G. Omenetto, J. a Rogers, A physically transient form of silicon electronics, Science 337 (September (6102)) (2012) 1640–16444.

[28] T. Salpavaara, J. Lekkala, S. Khan, V. Ellä, M. Kellomäki, Biodegradable encapsulation for inductively measured resonance circuit, in: 2012 IEEE 12th International Conference on Bioinformatics & Bioengineering (BIBE), November, 2012, pp. 11–13.

[29] R.A. Potyrailo, W.G. Morris, T. Sivavec, H.W. Tomlinson, RFID sensors based on ubiquitous passive 13. 56-MHz RFID tags and complex impedance detection, Wirel. Commun. Mob. Comput. 9 (10) (2009) 1318–1330.

Biographies

Timo Salpavaara received his M.Sc. degree in electrical engineering from Tampere University of Technology, (TTY), Finland, in 2005. Since 2005 he has been working as a research scientist at the department of automation science and engineering at Tampere University of Technology. Currently he is working on his PhD thesis. His research activities include inductively coupled resonance sensors, capacitive sensing and readout electronics.

Järveläinen M.Sc. majored in materials science and minored in industrial management from which he earlier graduated as a BSc. He works in Tampere University of Technology as a project manager and a researcher where he's interdisciplinary work aligns at the interface of industry and academy. He's projects deal with complicated measurements involving characterization methods, usually applicable for industrial components used in harsh environments.

Sari Seppälä M.Sc. is a researcher in department of materials science at Tampere University of Technology (TUT), Finland. She received her B.Sc. in metallic materials and M.Sc. in material research in TUT. Since then she has been working with non-destructive testing (NDT) methods of ceramic material characterization. Her research focuses on understanding dielectric materials' behaviour in an electric field, polarization mechanisms and their exploitation in development of frequency response based NDT methods.

Teemu Yli-Hallila received his M.Sc. degree in 2013 from the department of automation science and engineering, Tampere University of Technology (TUT), where he is currently working as a researcher. His current research interests include system identification, analysis and process control.

Jarmo Verho is a research assistant with the department of automation science and engineering, Tampere University of Technology, Tampere, Finland. He is specialized in low-noise electronics design and embedded systems. His current research interests include sensor networks, radio networks, short-range inductive links, and capacitive sensing techniques.

Matti Vilkko received the M.Sc. and Lic.Tech. degrees in electrical engineering and the Dr.Tech. degree in automation engineering from the Tampere University of Technology (TUT), Tampere, Finland, in 1989, 1993, and 1999, respectively. He was a researcher with the Institute of Automation and Control, TUT, from 1989 to 1999, where he is currently a professor with the department of automation science and engineering. He was involved in research on scheduling and optimization of hydrothermal power production. From 2000 to 2003, he held research and development management positions with Patria Ailon, Inc. and Ailocom, Inc. His current research interests include modelling, simulation, system identification, and process control.

Jukka Lekkala is a professor of automation engineering at Tampere University of Technology (TUT), Tampere, Finland. He received his M.Sc.(Eng) degree in electronics and D.Sc.(Eng) degree in biomedical engineering from TUT, in 1979 and 1984, respectively. Currently, he is the Head of the department of automation science and engineering (ASE) and also leads the research group of Sensor Technology and Biomeasurements. Prof. Lekkala has more than 130 international referee papers and ten patents. Lekkala's main research activities include sensors, biosensing systems, sensor materials, instrumentation, and modelling.

Prof. Erkki Levänen Dr. Tech. Professor of ceramics materials and head of department at department of materials science at Tampere University of Technology, Tampere Finland. Professor Levänen's research interests are in functional ceramics especially at the energy and environmental applications. His work ranges from material synthesis to novel processing techniques and advanced characterization methods as well as application oriented research. The nanoparticle and thin film synthesis include sol–gel, supercritical carbon dioxide assisted synthesis and pyrolysis methods aiming to multifunctional materials with enhanced durability and self-recovery.

Publication VI

THERMAL FLOW PERMEAMETRY - A RAPID METHOD FOR FINDING LOCAL CHANGES IN FLOW CHANNELS

by

Järveläinen Matti, Keskinen Lassi, Heinonen Saara, Kaleva Aaretti & Levänen Erkki

Thermal flow permeametry – A rapid method for finding local changes in flow channels

Matti Järveläinen [*], Lassi Keskinen, Saara Heinonen, Aaretti Kaleva, Erkki Levänen

Department of Materials Science, Tampere University of Technology, Tampere, P.O. Box 589, FIN-33101, Finland

ABSTRACT

Solid bodies with flow channels can have very heterogeneous structure, whose local variations are difficult to analyze. Yet, this can play an important role affecting characteristics, such as, fluid flow property, strength and heat conductivity. This article presents a method named thermal flow permeametry (TFP) that is applicable for a quick analysis of variations in flow channels, even in meter-sized structures. For illustrating the method, we analyzed the local permeability levels of a large and extremely complex fiber structure. In TFP, hot air is ejected through a structure, while thermal camera measures local surface temperature variations during heating. Gray values of the thermal image are then plotted versus the structures local thickness, density and permeability. We showed that gray values link with local permeability, affected by thickness, density and flow channel tortuousness. We also found out that TFP is very sensitive to local changes in flow channels.

© 2015 Elsevier Ltd. All rights reserved.

1. Introduction

Structures that contain flow channels are important in various applications such as composites and functional ceramics. In the former, the type and homogeneity of flow channels affect the matrix infiltration. This can be modelled [1,2], or studied with in situ-methods such as [3], and it has an effect in the final properties of the composite [4–8]. The latter group – functional ceramics include, for example, hot gas filters [9] where the porosity must be homogenous in order to reach even flow characteristics and good mechanical integrity. The latter characteristics are important in all structures with flow channels but especially in filters because they affect the filtration features [10], ease of cleaning the filter [11], and even the mechanical properties [12] of the component. However, these components often contain large variations in their permeability which arise from their manufacturing method, for example vacuum molding of flocked slurry [13], that may induce changes in wall thickness, bulk density, pore structure, and fiber orientation [14]. These changes can be difficult to measure during or after the manufacturing process, and for instance, solely the fiber orientation affects the mechanical properties [15] and permeability of the component [16–18]. Because the variations will have a large impact on the final properties, both permeability

and strength, it is of great importance to be able to both reduce their appearance and detect and quantify them in the final product.

Predicting the permeability has been studied before [19–25]. Conventionally, permeability measurements [26–28], have been used for analyzing the flow resistance of components with flow channels, and while the traditional permeameters are suitable for measuring the overall permeability, they cannot easily give information about the structural anisotropy of a measured component. The same applies for many of the new and innovative methods for measuring permeability or characterizing flow channels in different situations [29–35]. Although the referenced methods, as well as [36], can be precise and closer to quantifiable results in similar use, another method capable to quickly and non-destructively analyze local properties of large components with flow channels using gas as a measuring medium is needed. This would be beneficial, especially for application where gas flow characteristics dominate and that is the reason we developed thermal flow permeametry (TFP). TFP can be used to locate the permeability variances by inducing a hot air stream through the structure causing its outer surface to heat faster in areas where there is a higher flow. The component's surface is monitored in situ with an infra-red camera [37], and variations in the heating rate are constantly measured. The temperature differences on the surface of the measured structure are mostly caused by differences in its local permeability levels, which are determined by the pore structure. This gives a real-time image of the component where regions of high permeability are highlighted as bright areas contrary to dark areas

---

* Corresponding author.
    E-mail address: matti.jarvelainen@tut.fi (M. Järveläinen).

with low permeability. Even minute, and otherwise almost unmeasurable changes in pore structure can have significant effects to the permeability as the calculations in Section 4.2 show.

In our earlier study [38], we showed how a permeable structure heats faster in certain areas when hot air was blown through it, and related that with wall thickness and density, measuring structures with different density and constant wall thickness, and conversely. In this article, we continue from that by correlating local surface temperature with local wall thickness and density, and also show how the local permeability of a fibrous filter element correlates with the new method using a permeability tester for comparison. We also provide means, based on image analysis, for spatially locating the local differences in permeability. The presented method is intended for all structures with flow channels, especially when the local permeability plays a crucial role.

This is an opening article on TFP technique where we show the technique's functionality with a complex fibre network representing a typical flow porous structure whose variations in local permeability needs to be found. The method being able to locate the changes in this highly tortuous and heterogeneous structure will thus undoubtedly work with those having simpler flow channels.

2. Material and methods

2.1. Ceramic fibre component

A cylindrical hot gas filter made of alumina silicate fibers was used to demonstrate the applicability of the TFP-method. It was chosen because it had a highly variable pore structure and was composed of non-oriented fibers with un-fiberized areas (improperly molten fibers called 'shots') at the tips of some of the fibers. In other words the structure was one of the most heterogeneous ones we could find and had highly tortuous flow channels. A representative image of the investigated structure is seen in the scanning electron microscope image (Fig. 1) that was obtained with a Phillips XL-30 microscope. For the image, a representative piece was prepared by cutting it with a scalpel and mounting it on a sample pin with carbon cement and coating it with a thin layer of carbon. The structure composed of amorphous alumina silicate fibers with crystalline regions. The fibers were bound together with silica. Composition of the fibers, needed for calculations in Section 4.2, was given by a manufacturer, and supported by our own analysis, as 45–60 weight percent SiO_2 and 40–55 weight percent Al_2O_3. This composition was used to estimate the proportion of silica used as a structural binder in the fiber network. The mass fraction for Si in the fibers was calculated based on the mass fraction of aluminum obtained from Energy-dispersive X-ray Spectroscopy (EDS) analysis that was done to several areas
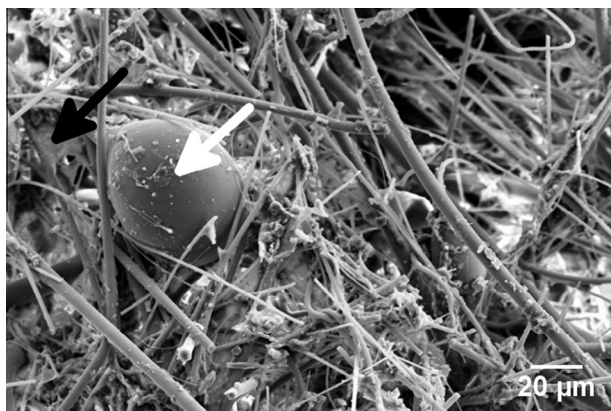
Fig. 1. SEM micrograph of the studied fiber structure. Black arrow pointing a binder sheet, white arrow pointing an unfiberized tip, i.e. "shot", of a fiber.

containing both fibers and binder. After a careful EDS analysis of single fibers and large areas, we estimate that the structure contained 3 weight percent of binding SiO_2 when compared to the total mass of the filter element.

Due to the heterogeneity and large size of the investigated component, the characteristics in Table 1, and below contain significant variations. The fiber diameters varied at 1–10 μm while the diameters of un-fiberized parts at the tips of the fibers varied from 10 μm to 300 μm. Fiber lengths varied from 100 μm to 800 μm. Mean flow pore size, measured with a PMI flow porometer (Porous Materials Inc., Ithaca, NY, USA), was 4 μm, and the average pore diameter, measured with a mercury porosimeter (Micromeritics poresizer 9320, Micromeritics Instrument Corporation, USA), was also 4 μm indicating that all the pores in the average range go through the structure. The largest flow channel, measured with a flow porometer, was 39 μm in diameters, and open porosity, measured with a mercury porosimeter, was 80 percent.

Thermal diffusivity was measured using NETZSCH 457 Micro-Flash (NETZSCH GmbH, Germany) in order to ensure that the surface heating was not caused by heat conduction. The obtained value, 0.3 mm^2/s is in the same order as for common wood [39, pp. 4–12], so conduction is very slow and later, in Section 4.3, we also experimentally show that the conduction has very minimal effect for the heating in TFP-experiments.

Thickness of the component was measured by a digital micrometer screw (Mitytoyo 293–240, Japan), and the density was measured by cutting and weighing sections from the filter element, and measuring their area with image-analyzing software ImageJ (version 1.47v, [40]). The latter method was used instead of a mechanical measuring tool in order to reach high accuracy with the compressible and concave samples.

2.2. TFP and other methods

A complete filter element was measured using TFP-method, followed by cutting it into nine cylinders, each 250 mm in length and

Table 1
Characteristics of the studied structure.

Filter element dimensions	Length (m)	2.4
	Outer diameter (m)	0.15
	Element wall thickness (m)	0.02
	Bulk density $\left(\frac{kg}{m^3}\right)$	410[a]
Microstructure	Fiber diameter (μm)	1–10
	Fiber length (μm)	<1000
	Diameter of un-fibrized fiber tips (μm)	10–500
Composition	Relative amounts	97% fibers 3% inorganic binder
	Fiber composition (by weight)	0.40–0.55 Al_2O_3 0.45–0.60 SiO_2
	Inorganic binder composition	Amorphous SiO_2
Pore characteristics	Mean flow pore size (μm)	4[b]
	Average pore size (μm)	4[c]
	Largest through-pore (μm)	39[b]
	Porosity (%)	80[c]–85[d]
Thermal diffusivity	(mm^2/s)	0.253 @ 100 °C[e] 0.266 at 200 °C

^a Measured mass per external dimensions.
^b Porous Materials Inc., capillary flow porometer.
^c Micromeritics poresizer 9320.
^d Calculated from measured mass per external dimensions and composition weighed densities using theoretical densities of 2850 $\frac{kg}{m^3}$ for Al_2SiO_5 fiber and 2203 $\frac{kg}{m^3}$ for SiO_2.
^e NETZSCH 457 MicroFlash.

further cutting out the sections of the cylinders that were imaged with thermal camera. Each cylinder section's thickness was measured and then their bulk density [41] was calculated by weighing and using image analysis to accurately measure the dimensions. Finally, their permeability was measured individually with a permeability testing unit described below. The three variables: thickness, density, and permeability were then correlated with gray values to see how they correlate.

2.2.1. Thermal flow permeability measurement

The thermal imaging setup consisted of a thermal camera (FLIR Thermacam PM595, FLIR Systems, Inc., USA) with an accuracy of ±2 percent of the reading, a length scale (scale 20 cm) made of metallic rods that are visible in IR-images, and an adjustable gas inlet able to feed air up to 2000 l/min. Air at room temperature (approximately 25 °C) flowed through a heater and finally through the monitored structure. The heater unit could be heated to 400 °C. A schematic presentation of the setup is presented in Fig. 2.

The air flow was set to 1000 Nl/min (norm liters), and the air heating unit was set to 100 °C. The heated air at the sample level was measured with thin k-type thermocouples and determined to be homogenous and at the heater set temperature after 80 s.
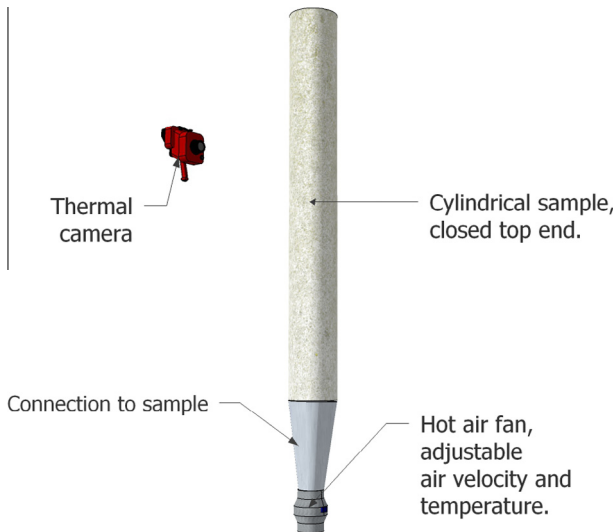
Fig. 2. Schematic presentation of thermal flow permeametry setup. Thermal camera was fixed on a tripod, 7 m from the imaged component. (For interpretation of the references to colour in this figure legend, the reader is referred to the web version of this article.)

An example of a thermal image is presented in Fig. 3. Temperatures in the measured surfaces ranged from 23–72 °C, average being close to 50 °C.

2.3. Quantification of surface temperature

Thermal images, in which the temperatures are exhibited as brightness variations, were converted to grayscale and their gray value – a unitless indicator of the luminescence, or brightness, of a pixel varying from 0 (black) to 254 (white) – was calculated with image analysis software, ImageJ [40]. Thus, the gray value relates directly to the surface temperature of the imaged component at the selected point or a selected area. An example of an imaged surface, both in color and grayscale, together with plotted gray value, is presented in Fig. 3. Presented Gray values are the average values from each position along the horizontal axis of the sample.

2.4. Classical air permeability measurement

Permeability measurements were conducted using a measuring probe connected to the open end of the measured component. A schematic presentation of the device can be seen in Fig. 4. The measuring probe had a gate valve to adjust the flow velocity and a flow velocity meter (Schmidt SS30.302, SCHMIDT Technology), with ±3 percent gain and plus 0.3 percent offset, and a connection to a hand-held micromanometer (DP measurement TT570SV, UK), with gain of ±1 percent and offset of ±1.

Air permeability was measured by drawing air through the component while the pressure drop over the studied component was adjusted with the gate valve. Air flow velocity was measured in a flow (after a laminar flow filter) that caused the same pressure drop, measured by the manometer, over all the measured components, and the flow was divided with the outer surface area of the component to calculate its facial velocity, which is independent of component size. Thus the permeabilities could be measured and compared between the complete component and sections cut from it.

The total measuring error of the permeability testing unit was experimentally found to be 10 percent, which is acceptable because the measured permeability variations were two times higher.

3. Results

In the present study a fibrous filter element with flow through it's structure (presented in Fig. 1 and Table 1) was measured by TFP to show that the method can be used to analyze differences in local
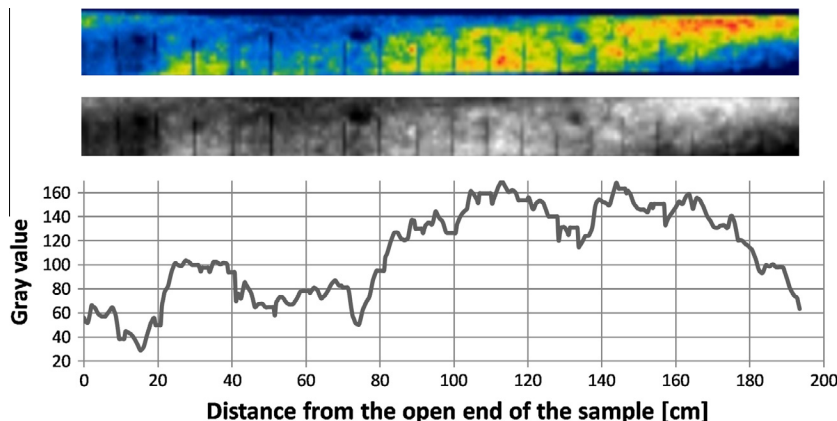
Fig. 3. Thermal image of measured surface in color and grayscale together with plotted gray value. White/red is hot, black/blue is cold.
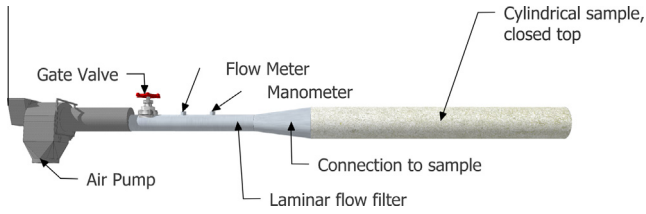
permeability and to investigate the method's sensitivity. In this chapter, the gray values are compared with the element's local wall thickness, porosity and facial velocity which, owing to the manufacturing method, had more variation in axial direction. These results aim to show how the parameters compare with the gray values. The parameters were measured from 25 cm tall sections cut from a complete element. The reported numbers are measured from the area of the thermal image. The use of air permeability for correlation was chosen as TFP-method also used air and liquid extrusion or intrusion techniques might have led to discrepancies in comparison.

3.1. Gray value and thickness

In order to relate the wall thickness to variations in the gray value, the filter element was cut into 25 cm long sections, and the wall thicknesses were measured from both sides of each section on the center line of the imaged surface. The gray values and wall thicknesses were then plotted against the distance in the element, Fig. 5, it could be seen that the gray value increased as the wall got thinner, indicating they have a higher surface temperature in comparison to thicker areas.

3.2. Gray value and porosity

Fig. 6 shows the gray value and local porosity of the component plotted versus the distance in the element. In areas of high porosity, the gray value is higher, indicating a higher surface temperature. Note that the porosity variation is very small. The porosity is calculated by subtracting from 1 the ratio of the measured density of the porous 25 cm cut sections of size equal to the thermal image and the density of a respective dense material (see Table 1).

3.3. Gray value and facial velocity

The air flow through the 25 cm sections was then measured with the permeability testing unit (Section 2.4) forcing the flow through the imaged area of the cylindrical sample by blocking the other areas with plastic film. In the experiment, the air flow was adjusted to incur 4 kPa pressure drop, as compared to atmospheric pressure, and the corresponding face velocity was calculated based on the flow velocity results and the section's outer surface area. Fig. 7 shows the gray value and the measured facial
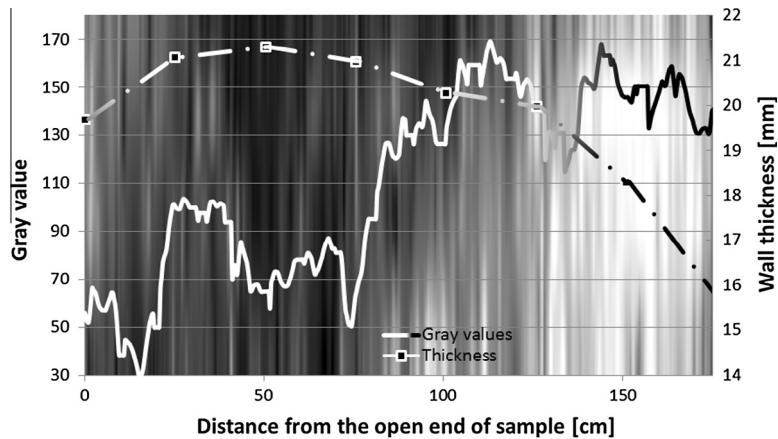
Fig. 5. Gray value vs. component wall thickness, with the thermal image in the background.
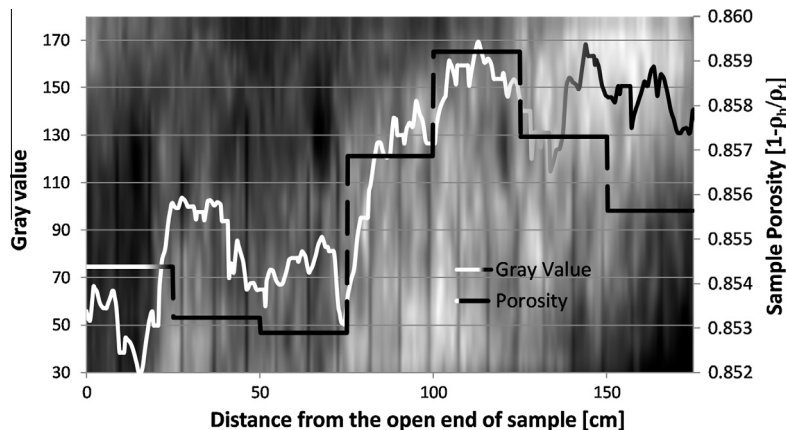
Fig. 6. Gray value vs. component porosity, with the thermal image in the background. ρ_b is measured bulk density, and ρ_t is the weighed average (in Table 1) of theoretical true densities of alumina silicate fiber and silica-binder.
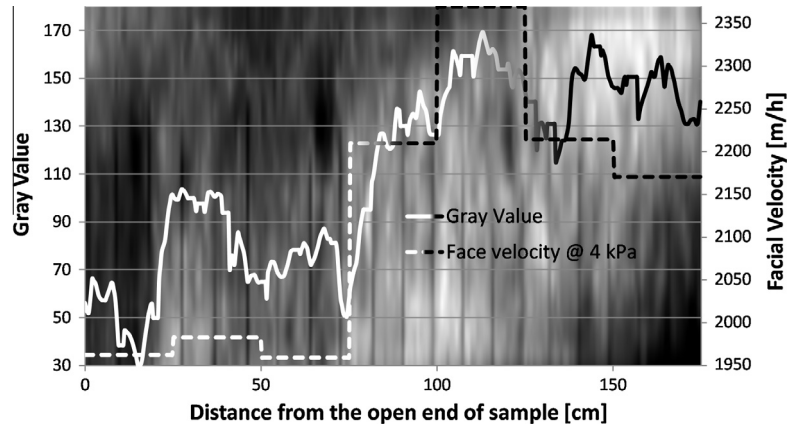
Fig. 7. Component gray value vs. facial velocity, with thermal image of the component in the background.
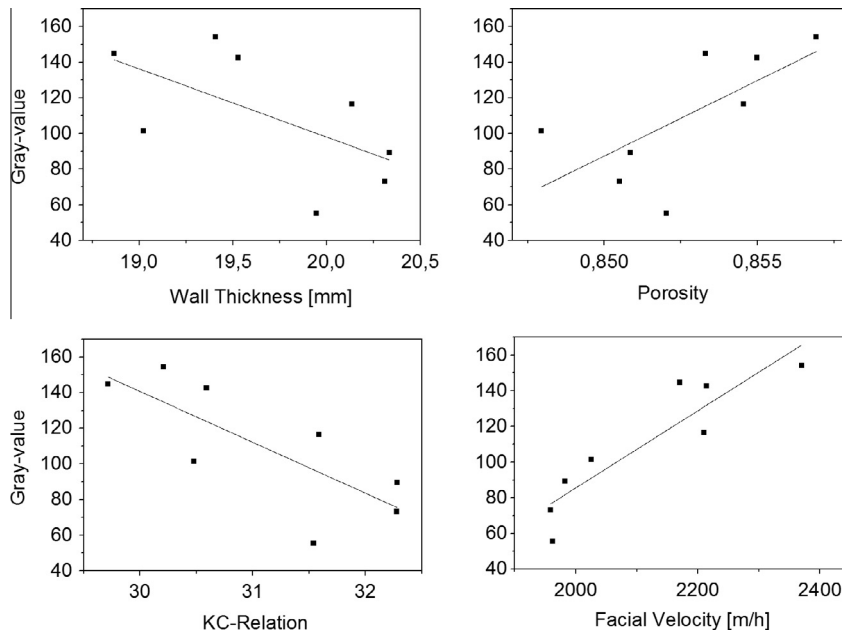

Fig. 8. Linear trend with correlation efficiency (R^2), between gray value and wall thickness, porosity, Kozeny–Carman relation, and facial velocity.

velocity versus the distance in the element. In sections of high facial velocity, the gray value is also higher.

4. Discussion

4.1. The relative importance of measured properties to the gray value

In the following, we show linear correlations between the gray value and the locally measured quantities: thickness, porosity, and facial velocity. The aim in this is to find out if the factors are linked with surface heating, not to describe or model the link.

We found out that the gray value, obtained from TFP measurements, is the most sensitive to local permeability presented here as facial velocity in constant pressure drop. The permeability is partly affected, but not determined, by wall thickness and porosity. Coincidental contribution of the two variables is evident as the correlation with gray value is higher if the variables are combined using Eq. (3) that in Appendix A is presented in its original form. In the equation, fluid dynamic viscosity (μ), specific surface area per unit

volume S_v, and Kozeny–Carman constant (K) were set constants leading to a relation that shows how the component's permeability depends on its thickness and porosity:

$$\frac{\Delta P}{U_0} \sim \frac{L\varepsilon^2 - 2L\varepsilon + L}{\varepsilon^3} \tag{1}$$

In other words, the relation from Kozeny–Carman equation can be used to see if the temperature differences, generated on the surface, are affected by both the component wall thickness and porosity.

The linear fittings are evaluated by adjusted R-squared and Pearson's correlations, which both indicate the same trends that can be seen in Table 2. Only a weak correlation between the wall thickness and gray value exists. Correlations between the porosity and the gray value are higher yet the R-square of 0.37 is still very weak. Correlation increases to 0.52 with the KC-relation that combines the wall thickness and porosity, but the highest correlation of 0.79 is found with the facial velocity. This shows that the differences in surface heating velocities are dominated by local

Table 2
Correlations calculated from Fig. 8 linear fittings.

	Wall thickness	Porosity	KC-relation	Facial velocity
Pearson's relation	0.61	0.68	0.77	0.91
Adjusted R-square	0.26	0.37	0.52	0.79

air permeability of the element, and other than wall thickness and permeability, there must also be variables affecting the surface heating rate. These must consist of pore structure or pore size distribution that change the flow channels' tortuousness. For instance in the case of fibrous filters the these characteristics are affected by the binder [42]. Also the amount of fibre volume fraction has an effect on the heating through thermal conductivity [43] but this is countered with high enough air flow velocity as is seen in Section 4.3.

As a summary; considering how the correlation to surface temperature increases in each step from wall thickness, through density, towards permeability, it is clearly evident that the presented TFP method primarily gives information about the local permeability of the structure, furthermore, it is so sensitive that the other methods, such as the classical air permeability measurement cannot be unambiguously used as a reference.

4.2. Sensitivity of TFP

As was shown in the previous section, TFP-method can locate permeability differences of a structure. The permeability is affected by shape, tortuosity and size of flow channels and is thus linked with local porosity. In general, permeability reduces with increasing fiber volume fraction [3]. To elucidate this and to numerically approximate the TFP-method's sensitivity to changes in local porosity, a calculation with Kozeny–Carman equation can be used, though it must be noted that Kozeny–Carman, especially in fibrous structure, is only a coarse predictor of quantified results. It can still be used to show how a minute, and many times undetectable, change of porosity can remarkably affect the local permeability, which in turn can be measured with TFP.

The Kozeny–Carman Eq. (3) [44, chap. 3], shows that in addition to the environmental parameters consisting of facial velocity (U_0), and fluid dynamic viscosity (μ); the structure's porosity (ε), specific surface area per unit volume (S_v), and thickness (L) are also controlling the pressure drop. The S_v is affected by the pore structure and size, which in our case is difficult to measure or predict, because the fiber structure is heterogeneous with uneven fiber diameter and the uneven shape, distribution, and size of binder sheets affecting it. The permeability is also affected by the tortuousness and shape of the flow channels, which are taken into account with the constant K in the formula. Keeping these in mind the equation is applied in Appendix A leading to an approximation that a porosity decrease from 0.85 to 0.80 would cause the pressure drop, at constant face velocity, to increase more than twofold from 4.00 kPa to 9.83 kPa. This emphasizes that the TFP-method, although affected by multiple factors related to flow pores, is above all highly sensitive to a relatively small changes in porosity.

4.3. Cause of surface temperature gradients during heating

As we have demonstrated via case study, the surface of a structure containing flow channels heats heterogeneously while hot air is ejected through it. This is because its local permeability varies with the local changes in its pore structure. The temperature increase is caused mainly by the high volume flow of hot air through the areas with high permeability, and the difference to
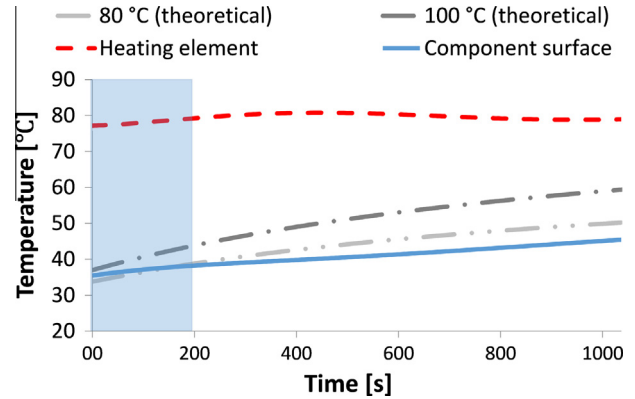
Fig. 9. Temperature of a heating element touching the inner surface of the component in dashed red and the component's outer surface temperature in blue. Theoretical heating curves in dashed gray at 80 and 100 °C calculated with Eq. (2). (For interpretation of the references to colour in this figure legend, the reader is referred to the web version of this article.)

areas with low permeability are promoted by the air cooling down while taking a longer route through the more tortuous path in the high density areas.

The heat conduction through the structure is not an issue, which can be shown by a simple experiment where the inner surface of the component was placed against a 80 °C surface while plotting the component's outer surface temperature together with the heating element's temperature. The result is shown in Fig. 9. During the over 15-min measurement the heating element could increase the component's outer surface temperature from 35 °C to 40 °C and when taking into account that the TFP measurements were carried out within first 3 min, marked by blue area in the figure, the effect of conduction can clearly be neglected. The total temperature increase in TFP measurement was approximately 25 °C as compared to plain conduction causing a change less than 2 °C. The figure also displays the theoretical heating rates caused by conduction, based on the structure's thermal diffusivity. The theoretical temperature curves were calculated with Eq. (2) [45, chap. 6.4], where, in this case, T_i is the initial temperature of the surface, T_s is the temperature of the heating element, $erf(x)$ is the Gauss error function, x is the structure's wall thickness, α is the measured thermal diffusivity at 100 °C and t is time.

$$T(x,t) = T_s + (T_i - T_s) \cdot erf\left(\frac{x}{2\sqrt{\alpha t}}\right) \tag{2}$$

The theoretical and experimental heating curves are in good agreement, especially in the area where the TFP-measurements were carried out. The overestimation at higher temperatures in the theoretical curve is caused by cooling of the structures surface, which is not taken into account in the equation.

5. Conclusions

The above experiments have helped to form a basis for thermal flow permeametry. Compared to conventional permeametry, it can locate local differences within the analyzed area without needing to seal off any areas of the measured component. It is also faster and capable of finding smaller differences than conventional methods, provided that the measuring parameters, mainly air temperature and flow velocity, are chosen correctly.

The method can be applied with little effort for several uses, such as ensuring an even production quality or analyzing local changes in specimen whose specific permeability levels have to be studied with gas, for instance when the specimen cannot

withstand liquids. Particularly this can work as an in situ-method to ensure the quality of a composite pre-preg before infiltration and may gain synergy when coupled with other methods, such as [3], or it can be used to study more complex structures such as fibrous filter elements that need homogeneous flow channels.

The experiments presented in this article were conducted for silica-based fibrous ceramics with a low density and thermal diffusivity. The method would undoubtedly also work for other structures, as long as the ratio between the component's permeability and thermal diffusivity is high enough. If the ratio is too low, the heat conducting through the structure might affect the results. Even in this case, the method might be applicable when using low air temperature and high flow velocity combined with a surface coating, such as graphite, that would promote heating caused by the air flowing through the structure. Notable is also that the structure used for measuring had exceptionally complex flow channels alluding that simpler structures can also be measured. The next step in development of this method is linking the surface heating rate with local pore size, followed by a model that corrects the rate with flow channels' tortuosity and shape, thus enabling quantifiable results. This should be carried out with structures that have more defined flow channels.

Acknowledgements

Appendix A. Sensitivity estimation with Kozeny–Carman equation

In Section 4.2 the effect of porosity changing from 0.85 to 0.80 causing the permeability to double was based on an estimation with Kozeny–Carman equation:

$$\frac{\Delta P}{L} = \mu \left[\frac{K(1-\varepsilon)^2 S_v^2}{\varepsilon^3} \right] U_0 \tag{3}$$

For the structure under investigation the S_v can be approximated with Eq. (3), where the variables, collected in Table 3, are the measured average values presented in results, μ is the air dynamic viscosity at the measuring temperature and K is the tortuosity for fibrous structure given as a constant in [46]. The equation yields $722 \frac{m^2}{m^3}$ for S_v. It is to be noted that assuming the K a constant is not accurate, except in highly porous systems, such as the one under inspection where K should not be a dominating factor [47].

Now, using the fiber densities presented earlier and $722 \frac{m^2}{m^3}$ for S_v, the approximate size of a fiber-binder block separating the flow channels, i.e. the area of material between an average sized flow channel, can be approximated. This is done by calculating how much material the structure contains based on the measured bulk

density (ρ_b) and weighed mean theoretical densities of aluminum silicate fiber and amorphous silicon dioxide in the component. With the given S_v, assuming a cylindrical fiber-binder block with radius (r) in a component weighing (m), by using $\frac{2 * m}{\pi * r}$, yields a diameter of 402 μm. This is a rough approximation of the average radius of a continuous section between the flow channels where the air cannot pass through.

The sensitivity of TFP-method to changes in porosity can now be seen by a simple calculation showing how much the permeability changes if the porosity would slightly decrease, for instance from 0.85 to 0.80. Firstly, this would change the ρ_b from $410 \frac{kg}{m^3}$ to $431 \frac{kg}{m^3}$ leading, with the same computation principle, to a change of S_v from $722 \frac{m^2}{m^3}$ to $1204 \frac{m^2}{m^3}$. Now using Eq. (3) again, the pressure drop, with constant face velocity, more than doubles from 4.00 kPa to 9.83 kPa. In fact, the change would be even higher due to the tortuosity, now assumed constant for the sake of simplicity, that in reality increases with decreasing porosity.

References

[1] Simacek P, Advani S. Simulating tape resin infiltration during thermoset pultrusion process. Compos Part A: Appl Sci Manuf 2015;72:115–26. http://dx.doi.org/10.1016/j.compositesa.2015.01.020. <http://linkinghub.elsevier.com/retrieve/pii/S1359835X15000317>.

[2] Sas HS, Wurtzel EB, Simacek P, Advani SG. Effect of relative ply orientation on the through-thickness permeability of unidirectional fabrics. Compos Sci Technol 2014;96:116–21. http://dx.doi.org/10.1016/j.compscitech.2014.03.007.

[3] Cender Thomas A, Simacek Pavel, Advani Suresh G. Resin film impregnation in fabric prepregs with dual length scale permeability. Compos Part A: Appl Sci Manuf 2013;53:118–28. http://dx.doi.org/10.1016/j.compositesa.2013.05.013.

[4] Levy A, Kratz J, Hubert P. Air evacuation during vacuum bag only prepreg processing of honeycomb sandwich structures: In-plane air extraction prior to cure. Compos Part A: Appl Sci Manuf 2015;68:365–76. http://dx.doi.org/10.1016/j.compositesa.2014.10.013. <http://linkinghub.elsevier.com/retrieve/pii/S1359835X1400325X>.

[5] Allaoui S, Cellard C, Hivet G. Composites: Part A effect of inter-ply sliding on the quality of multilayer interlock dry fabric preforms. Compos Part A 2015;68:336–45. http://dx.doi.org/10.1016/j.compositesa.2014.10.017.

[6] Qian C, Harper L, Turner T, Warrior N. Structural optimisation of random discontinuous fibre composites: Part 1 methodology. Compos Part A: App Sci Manuf 2015;68:406–16. http://dx.doi.org/10.1016/j.compositesa.2014.08.024. <http://linkinghub.elsevier.com/retrieve/pii/S1359835X14002577>.

[7] Qian C, Harper L, Turner T, Warrior N. Structural optimisation of random discontinuous fibre composites: Part 2 case study. Compos Part A: Appl Sci Manuf 2015;68:417–24. http://dx.doi.org/10.1016/j.compositesa.2014.09.004. <http://linkinghub.elsevier.com/retrieve/pii/S1359835X14002772>.

[8] Ivanov DS, Lomov SV. Compaction behaviour of dense sheared woven preforms: experimental observations and analytical predictions. Compos Part A: App Sci Manuf 2014;64:167–76. http://dx.doi.org/10.1016/j.compositesa.2014.05.002. <http://linkinghub.elsevier.com/retrieve/pii/S1359835X14001286>.

[9] Heidenreich S. Hot gas filtration a review. Fuel 2013;104:83–94. http://dx.doi.org/10.1016/j.fuel.2012.07.059. <http://linkinghub.elsevier.com/retrieve/pii/S0016236112006199>.

[10] Sharma SD, Carras JN. Fuels – hydrogen production-gas cleaning: barrier filters. In: Garche J, editor. Encyclopedia of electrochemical power sources. Amsterdam: Elsevier; 2009. p. 313–8.

[11] Kanaoka C, Amornkitbamrung M. Effect of filter permeability on the release of captured dust from a rigid ceramic filter surface. Powder Technol 2001;118(1–2):113–20. http://dx.doi.org/10.1016/S0032-5910(01)00301-1. <http://linkinghub.elsevier.com/retrieve/pii/S0032591001003011>.

[12] Westerheide R, von Der Wehd C, Walch A, Baumgarten J. Vibration behavior of ceramic hot gas filter elements: analysis and characterization of mechanical properties. Tech Rep; 2002.

[13] Zievers JS. Hot gas filter; 1990.

[14] Yu H, Potter K, Wisnom M. A novel manufacturing method for aligned discontinuous fibre composites (high performance-discontinuous fibre method). Compos Part A: Appl Sci Manuf 2014;65:175–85. http://dx.doi.org/10.1016/j.compositesa.2014.06.005. <http://linkinghub.elsevier.com/retrieve/pii/S1359835X14001705>.

[15] Baghaei B, Skrifvars M, Salehi M, Bashir T, Rissanen M, Nousiainen P. Novel aligned hemp fibre reinforcement for structural biocomposites: porosity, water absorption, mechanical performances and viscoelastic behaviour. Compos Part A: Appl Sci Manuf 2014;61:1–12. http://dx.doi.org/10.1016/j.compositesa.2014.01.017. <http://linkinghub.elsevier.com/retrieve/pii/S1359835X14000311>.

[16] Meyer KJ, Hofmann JT, Baird DG. Prediction of short glass fiber orientation in the filling of an end-gated plaque. Compos Part A: Appl Sci Manuf 2014;62:77–86. http://dx.doi.org/10.1016/j.compositesa.2013.12.013. <http://linkinghub.elsevier.com/retrieve/pii/S1359835X13003503>.

Table 3
Material parameters used in calculation.

L	0.020 m
μ	1.983 Pa s[a]
K	12.81
ε	0.85
U_0	0.44 m/s[b]
ρ_b	$410 \frac{kg}{m^3}$
ρ_t	$2850 \frac{kg}{m^3}$ for Al_2SiO_5 fiber and $2203 \frac{kg}{m^3}$ for SiO_2 binder

[a] Air dynamic viscosity at 25 °C.
[b] Avg. superficial velocity on the sample surface in the experiments.

[17] Notta-Cuvier D, Lauro F, Bennani B. An original approach for mechanical modelling of short-fibre reinforced composites with complex distributions of fibre orientation. Compos Part A: Appl Sci Manuf 2014;62:60–6. http://dx.doi.org/10.1016/j.compositesa.2014.03.016. <http://linkinghub.elsevier.com/retrieve/pii/S1359835X14000888>.

[18] Tsuda T, Ogasawara T, Moon S-Y, Nakamoto K, Takeda N, Shimamura Y, et al. Three dimensional orientation angle distribution counting and calculation for the mechanical properties of aligned carbon nanotube/epoxy composites. Compos Part A: Appl Sci Manuf 2014;65:1–9. http://dx.doi.org/10.1016/j.compositesa.2014.05.009. <http://linkinghub.elsevier.com/retrieve/pii/S1359835X14001444>.

[19] Liu HL, Hwang WR. Permeability prediction of fibrous porous media with complex 3D architectures. Compos Part A: Appl Sci Manuf 2012;43(11):2030–8. http://dx.doi.org/10.1016/j.compositesa.2012.07.024. <http://linkinghub.elsevier.com/retrieve/pii/S1359835X12002254>.

[20] Papathanasiou T. Flow across structured fiber bundles: a dimensionless correlation. Int J Multiphase Flow 2001;27:1451–61. <http://www.sciencedirect.com/science/article/pii/S0301932201000131>.

[21] Chen Z-R. Permeability predictions for woven fabric preforms. J Compos Mater 2009;44(13):1569–86. http://dx.doi.org/10.1177/0021998309355888. <http://jcm.sagepub.com/cgi/doi/10.1177/0021998309355888>.

[22] Lundstrom TS. Modeling of power-law fluid flow through fiber beds. J Compos Mater 2005;40(3):283–96. http://dx.doi.org/10.1177/0021998305055187. <http://jcm.sagepub.com/cgi/doi/10.1177/0021998305055187>.

[23] Lundstrom TS, Frishfelds V, Jakovics A. A statistical approach to permeability of clustered fibre reinforcements. J Compos Mater 2004;38(13):1137–49. http://dx.doi.org/10.1177/0021998304042079. <http://jcm.sagepub.com/cgi/doi/10.1177/0021998304042079>.

[24] Kuentzer N, Simacek P, Advani SG, Walsh S. Permeability characterization of dual scale fibrous porous media. Compos Part A: Appl Sci Manuf 2006;37(11):2057–68. http://dx.doi.org/10.1016/j.compositesa.2005.12.005. <http://linkinghub.elsevier.com/retrieve/pii/S1359835X05004306>.

[25] Lundström T. The permeability of non-crimp stitched fabrics. Compos Part A 2000;31:1345–53. <http://www.sciencedirect.com/science/article/pii/S1359835X00000373>.

[26] ASTM F778. Standard methods for gas flow resistance testing of filtration media. ASTM; 2007. http://dx.doi.org/10.1520/F0778-88R07. <http://www.astm.org/Standards/F778.htm>.

[27] Arbter R, Beraud J, Binetruy C, Bizet L, Bréard J, Comas-Cardona S, et al. Experimental determination of the permeability of textiles: a benchmark exercise. Compos Part A: Appl Sci Manuf 2011;42(9):1157–68. http://dx.doi.org/10.1016/j.compositesa.2011.04.021. <http://linkinghub.elsevier.com/retrieve/pii/S1359835X11001357>.

[28] Vernet N, Ruiz E, Advani S, Alms J, Aubert M, Barburski M, et al. Experimental determination of the permeability of engineering textiles: benchmark II. Compos Part A: Appl Sci Manuf 2014;61:172–84. http://dx.doi.org/10.1016/j.compositesa.2014.02.010. <http://linkinghub.elsevier.com/retrieve/pii/S1359835X14000505>.

[29] LeBel F, Fanaei AE, Ruiz E, Trochu F. Experimental characterization by fluorescence of capillary flows in dual-scale engineering fabrics. Text Res J 2013;83(15):1634–59. http://dx.doi.org/10.1177/0040517512471742. <http://trj.sagepub.com/cgi/doi/10.1177/0040517512471742>.

[30] Lundström T, Gebart B, Sandlund E. In-plane permeability measurements on fiber reinforcements by the multi-cavity parallel flow technique. Polym Compos 20(1). <http://onlinelibrary.wiley.com/doi/10.1002/pc.10342/abstract>.

[31] Demaria C, Ruiz E, Trochu F. In-plane anisotropic permeability characterization of deformed woven fabrics by unidirectional injection. Part I: experimental results. Polym Compos. http://dx.doi.org/10.1002/pc.20107/abstract. <http://onlinelibrary.wiley.com/doi/10.1002/pc.20107/abstract>

[32] Sharma S, Siginer DA. Permeability measurement methods in porous media of fiber reinforced composites. Appl Mech Rev 2010;63(2):020802. http://dx.doi.org/10.1115/1.4001047. <http://appliedmechanicsreviews.asmedigitalcollection.asme.org/article.aspx?articleid=1399595>.

[33] Wu X, Li J, Shenoi RA. A new method to determine fiber transverse permeability. J Compos Mater 2006;41(6):747–56. http://dx.doi.org/10.1177/0021998306067012. <http://jcm.sagepub.com/cgi/doi/10.1177/0021998306067012>.

[34] Stadtfeld HC, Erninger M, Bickerton S, Advani SG. An experimental method to continuously measure permeability of fiber preforms as a function of fiber volume fraction. J Reinf Plast Compos. http://dx.doi.org/10.1177/073168402128987518.

[35] Nedanov P, Advani S. A method to determine 3D permeability of fibrous reinforcements. J Compos Mater. http://dx.doi.org/10.1106/002199802021462. <http://jcm.sagepub.com/content/36/2/241.short>.

[36] Cender TA, Šimáček P, Advani SG. A method to determine open pore volume with pulse decay. Appl Phys Lett 2014;105(13):134101. http://dx.doi.org/10.1063/1.4896854. <http://scitation.aip.org/content/aip/journal/apl/105/13/10.1063/1.4896854>.

[37] Chrzanowski K, Park S. Evaluation of thermal cameras for non-destructive thermal testing applications. Infrared Phys Technol 2001;42(2):101–5. <http://www.sciencedirect.com/science/article/pii/S1350449500000621>.

[38] Järveläinen M, Keskinen L, Levänen E. Use of thermal imaging in characterization of ceramic fiber structures. In: 2nd International conference on competitive materials and technological processes, IOP Conf series: materials science and engineering, vol. 47. Miskolc; 2013. <http://iopscience.iop.org/1757-899X/47/1/012062>.

[39] Ross RJ. F. P. Laboratory. Wood handbook: wood as an engineering material. Tech Rep; 2010. <http://www.fpl.fs.fed.us/documnts/fplgtr/fpl_gtr190.pdf>.

[40] National Institutes of Health. ImageJ; 2013. <http://rsbweb.nih.gov/ij/index.html>.

[41] Webb P. Volume and density determinations for particle technologists. Micromeritics Instrument Corp (February). <http://www.anime.micrx.com/Repository/Files/Volume_and_Density_determinations_for_Particle_Technologists.pdf>.

[42] Fernando JA, Chung DDL. Pore structure and permeability of an alumina fiber filter membrane for hot gas filtration. J Porous Mater 2002;9(3):211–9. <http://apps.isiknowledge.com/full_record.do?product=WOS&search_mode=GeneralSearch&qid=5&SID=Q1ciIkA8El8jK@GNm@7&page=1&doc=2>.

[43] Yu H, Heider D, Advani S. Prediction of effective through-thickness thermal conductivity of woven fabric reinforced composites with embedded particles. Compos Struct 2015;127:132–40. http://dx.doi.org/10.1016/j.compstruct.2015.03.015. <http://linkinghub.elsevier.com/retrieve/pii/S0263822315001877>.

[44] Holdich RG. Fundamentals of particle technology. Loughborough: Midland Information Technology and Publishing; 2002. <http://www.particles.org.uk/particle_technology_book/particle_book.htm>.

[45] Rathore MM, Kapuno RR. Engineering heat transfer. 2nd ed. Sudbury, MA: Jones & Bartlett Learning; 2011.

[46] Li J, Gu Y. Coalescence of oil-in-water emulsions in fibrous and granular beds. Sep Purif Technol 2005;42(1):1–13. http://dx.doi.org/10.1016/j.seppur.2004.05.006. <http://linkinghub.elsevier.com/retrieve/pii/S138358660400139X>.

[47] Yazdchi K, Srivastava S, Luding S. On the validity of the Carman–Kozeny equation in random fibrous media. In: II International conference on particle-based methods, Barcelona; 2011. <http://doc.utwente.nl/80382/>.

Publication VII

COMPRESSION CURVE ANALYSIS AND COMPRESSIVE STRENGTH MEASUREMENT OF BRITTLE GRANULE BEDS IN LIEU OF INDIVIDUAL GRANULE MEASUREMENTS

by

Järveläinen Matti, Kaleva Aaretti, Kaitajärvi Annikka, Laakso Jarmo, Kanerva Ulla & Levänen Erkki

ARTICLE IN PRESS

Compression curve analysis and compressive strength measurement of brittle granule beds in lieu of individual granule measurements

Matti Järveläinen [a,*], Aaretti Kaleva [a], Annikka Kaitajärvi [b], Jarmo Laakso [a], Ulla Kanerva [b], Erkki Levänen [a]

[a] *Department of Materials Science, Tampere University of Technology, PO Box 589, FIN-33101 Tampere, Finland*
[b] *VTT Technical Research Centre of Finland, Sinitaival 6, PO Box 1300, FI33101 Tampere, Finland*

ARTICLE INFO

ABSTRACT

Powders in granulated form are used in various processes to facilitate convenient usage. The durability of the formed granules is a crucial parameter, typically evaluated by the compressive strength of the granules. However, especially for granules with a diameter in the order of tens of microns, statistically relevant testing of individual granules is not a feasible alternative, and in such cases uniaxial bed compression is required.

There has not been consensus on whether uniaxial compression of a granule bed can be used to study the fracture of micron size or brittle granules. In our case study of a bed of sintered kaolinite granules with diameters under $100\,\mu m$, we show how the compressive strength of individual granules can be obtained from the compressive measurement of the entire bed by plotting the relative density versus the logarithmic pressure scale.

We compressed the kaolinite powder with different loads; microscopy confirmed that below the analyzed strength the granules are intact, though the granules start to fracture in the curved region on the compression curve. We found that angle-fitting can be used to locate the average compressive strength on the compression curve and to follow the evolution of strength with sintering temperature. The experiments in unison demonstrate that compression curve analysis is applicable for strength analysis of brittle granules.

© 2016 Chinese Society of Particuology and Institute of Process Engineering, Chinese Academy of Sciences. Published by Elsevier B.V. All rights reserved.

Introduction

Materials in granular form are used in process industries, among others, in the production of mineral, concrete, metallurgical (Huang, Yi, & Jiang, 2012), pharmaceutical (Yohannes et al., 2015), and food products (Kwan, Wong, & Fung, 2015). Granules are also used as adsorbents, catalysts (Couroyer, Ning, & Ghadiri, 2000; Subero-Couroyer, Ghadiri, Brunard, & Kolenda, 2003), and in ceramic production, pesticides, fertilizers (Leszczuk, 2014), nuclear fuels, and sludges (Antonyuk, Tomas, Heinrich, & Mörl, 2005; Carneim & Messing, 2001). Granulation is needed to improve the flow properties of a powder and at the same time to prepack the powder to increase its processability (Richerson, Richerson, & Lee, 2005). Lower flowability in non-granulated powders as compared to granules is due to spontaneous agglomeration and relatively higher interaction forces between each particle (Briscoe & Özkan, 1997). Granulation also makes it possible to limit a powder's dusting (Leszczuk, 2014), and control properties such as: shape, chemical composition, size distribution, porosity, internal surface area (Antonyuk et al., 2010), and rate of dissolution (Rahmanian, Ghadiri, Jia, & Stepanek, 2009). Granulation also allows the processor to mix a binder with the granules before compaction, in the earliest processing steps (Müller, Russell, & Tomas, 2015; Terpstra, Pex, & De Vries, 1995). The binders provide lubrication and green-state strength prior to densification (Briscoe & Özkan, 1997).

The mechanical durability of a granule determines how well it can endure stresses that are induced during manufacture, e.g., collisions to spray dryer walls, transport, and during use (Antonyuk et al., 2005). However, the granulate is not always the final desired form; for instance in ceramic production a controlled breakage via pressing of the granules is needed for homogeneous products (Terpstra et al., 1995). Should the granules not break in an orderly form during compaction, the end-product will contain voids and local density changes (Honda & Nonaka, 1998). The granule

* Corresponding author. Tel.: +358 408490194.
   E-mail address: matti.jarvelainen@tut.fi (M. Järveläinen).
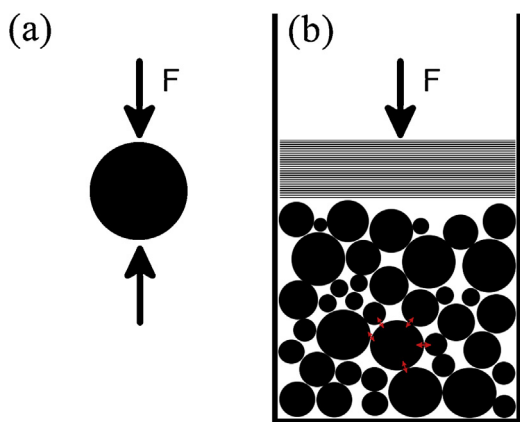
Fig. 1. Compression of (a) a single granule, and (b) a bed of granules. Red arrows show the force distribution of a granule. (For interpretation of the references to color in this figure legend, the reader is referred to the web version of this article.)

durability is usually tuned with additives, such as binders and lubricants, and careful control of the processing parameters. The durability of powder agglomerates (granulates) can also be important for processes such as injection molding, where powders in their as-synthesized form may aggregate and cause discontinuities in the final product. In such cases, the durability of the agglomerates must be known and accommodated, to ensure that the preprocessing will deagglomerate the powder (Song & Evans, 1994).

Mechanical durability of granules can be analyzed with functional measurements such as impact testing (Antonyuk et al., 2010), Pfosta-apparatus (Leszczuk, 2014), or drop weight testing (Salman & Tomas, 2014). For general analysis, the compressive strength of granules can be modeled (Antonyuk et al., 2010; Müller & Tomas, 2014; Schilde, Burmeister, & Kwade, 2014), and is often measured by compressing a single granule (Cheong, Adams, Hounslow, & Salman, 2009; Müller et al., 2015; Rahmanian et al., 2009; Rahmanian & Ghadiri, 2013), such as in Fig. 1(a). However, measuring a statistically representative amount of single granules may be prohibitive due to large variations in their size, strength, and shape. Very small granules, below 0.5 mm, are particularly difficult to measure even with special tools (Pitchumani, Zhupanska, Meesters, & Scarlett, 2004) or nanoindenters (Raichman, Kazakevich, Rabkin, & Tsur, 2006; Schilde et al., 2014), so these materials are more conveniently measured in packed beds, as shown in Fig. 1(b).

Measurement of a bed instead of individual granules also gives a better understanding of the uniformity of industrially produced granules. The bed strength represents the overall strength of an average granule, although the result is affected by the often-uneven force distribution in the bed, which in turn results from the granule strength, size distribution, and the uniaxial nature of the compression. Still, the same principles apply in bed and single granule compression: size, porosity, and roughness of the granules affects the strength (Antonyuk et al., 2005) together with the granule shape (Pitchumani et al., 2004) and internal imperfections (Subero-Couroyer et al., 2003). In bed compression, the result is also affected by the granule size distribution and granule friction (Kwan et al., 2015; McDowell & de Bono, 2013). Granule strength can be affected by cyclic loading (Salman & Tomas, 2014) in a fatigue mechanism where a repeated force below the granule's strength induces microcracks (lowering its strength (Pitchumani et al., 2004)), or causes hardening (increasing its strength (Antonyuk et al., 2010)); the atmosphere also affects granule strength (Cheong et al., 2009; Müller et al., 2015).

Both measuring methods (bed and single compression) for granule strength are justified. In single-granule compression, a statistically reliable number of granules is needed to measure
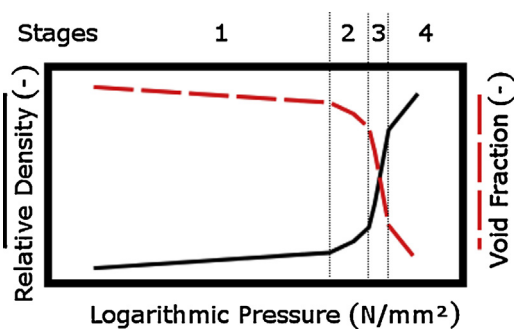
Fig. 2. Schematic illustration of a compression curve showing the four stages.

the average granule strength (Subero-Couroyer et al., 2003); even with easily measured large granules, it is laborious to achieve consistent compressive strength values, although some applicable approaches are now available (Pitchumani et al., 2004; Subero-Couroyer, Ghadiri, Brunard, & Kolenda, 2005). In bed compression, a large number of granules is measured simultaneously, providing the appropriate statistical characteristics on the first experiment; however, predicting the average properties of a single granule from these results is not straightforward due in part to the non-uniform strain that results from uneven load distribution of a randomly packed granule bed and a uniaxial compression tool.

In bed compression, the type of granule also has an effect on the yielding behavior of the bed. Some authors (e.g., Antonyuk et al., 2005, 2010; Aryanpour & Farzaneh, 2015; Briscoe & Özkan, 1997; Meyer & Faber, 1997; Subero-Couroyer et al., 2005) have studied large (over 1 mm) granules or granules that behave elastically or plastically, such as metals (Thyagarajan, Cantin, Kashyap, & Bettles, 2015), where the shear stresses have an important role in bed compression. Even otherwise brittle ceramic powders often include a binder (Carneim & Messing, 2001) in the granules that causes plastic deformation. Given the above, there is a lack of published information on brittle granules, which would break instantaneously without a significant plastic deformation. Here we show, through a case analysis, that bed compression curve-analysis is applicable for brittle granules with a diameter below 100 μm, and we present a systematic approach to interpreting the compression testing results.

Theoretical background

Compression stages

The behavior of granules during compression of a bed, including deformation and breakage, exhibits four stages (Briscoe & Özkan, 1997; Mort, Sabia, Niesz, & Riman, 1994) that are shown in Fig. 2. The stages appear in steady-state compression due to the increase in pressure that can be identified using a semi-logarithmic plot; presenting the compression behavior either by the relative density or the void fraction versus the logarithmic pressure, the effect of the pressure increase can be distinguished. The density change is very small until the onset of breakage in stage three, when it becomes logarithmic, enabling a linear fitting on a half-logarithmic scale (Song & Evans, 1994).

During stage 1, the granules deform elastically, pack, and rearrange. The packing density is governed by the shape and size distribution of the granules and influenced by different effects (Kwan et al., 2015), which are beyond the scope of this article. When the rearrangement takes place, the relative density increases as the granules achieve more dense packing.

During stage 2, the compressive strength of the granules is exceeded and they fracture. Some researchers (see especially

Carneim & Messing, 2001) divide stage 2 into initial and massive granule yield regimes; in the initial yield regime, compaction rate slows after the rearrangement ends. The compaction rate, i.e., pressure change in relation to density change, is calculated (see Mort et al., 1994) by deriving the compression curve where the average crushing strength would be the derivative maximum. Another method (Briscoe & Özkan, 1997), used in this paper, is to find the most-curved region of the half-logarithmic compression curve by angular fitting (presented in the Interpretation of the compression curve section).

The compressive strength of a granule is controlled by the size and orientation of intragranular discontinuities such as primary particle boundaries, binder-particle interfaces, pores, and cracks, which function as stress condensers. According to Pitchumani et al. (2004) the two most important breaking mechanisms are fracture (caused by normal forces), and attrition (caused by tangential forces); a model by McDowell and de Bono (2013) predicts that the various fracture mechanisms do not significantly affect measured average compressive strength.

The steepness and length of the second stage curve is related to the Weibull modulus, size distribution (Song & Evans, 1994), order, and homogeneity of the granules. In principle, granules of smaller size surrounding a larger one can divide the stress more evenly and the average number of granule contacts between large and small granules is reduced during compression, while the number of contacts with granules of the same size or larger stays constant. Continuing with the reasoning by McDowell and de Bono (2013) and McDowell (2002), the small granules are exposed to the highest stresses due to fewer contact points, however, the granules also become stronger according to the Griffith's weakest-link theory known in brittle materials (Pitchumani et al., 2004; Subero-Couroyer et al., 2003), which states that strength is defined by the pre-existing flaws in a brittle material. High Weibull modulus, small size distribution, and high packing density lead to a steep and short stage 2; the granules all break at the same load (Song & Evans, 1994).

Because of the above relationships, the changes in a bed compression curve are smooth when compared with the compression curve of a single granule, as granule breakage in a bed only causes the force to be divided more evenly to nearby granules. The punch geometry (Laity, 2014) and the granule friction against other granules and the die walls (Berg, Jonsén, & Häggblad, 2010) will also affect the measured compressive strength. During compression, stress is highest close to corners of the die and close to the compressing punch. According to Güner, Cora, and Sofuoğlu (2015), the friction between the die wall and the granules is a more dominant feature than granule–granule friction, which can lead to unequal force distribution creating local regions of high-stress areas (Aryanpour & Farzaneh, 2015). The aspect ratio of the compacts (Briscoe & Özkan, 1997) also affects the force distribution.

During stage 3, the fractured granules rearrange under similar laws as in stage 1, with the distinction that the electrostatic and van der Waals forces are more significant because of the decreased particle size.

During stage 4, the bed has no or few voids left, and the primary particles have been compressed close to the theoretical limit of packing density (Briscoe & Özkan, 1997). When the load is removed, the relief of pressure causes the release of elastic transformation, leading to a small decrease in compact density (Carneim & Messing, 2001).

Force distribution in a bed of granules

In single granule compression, force is transmitted to the granule in a uniform manner, whereas in a bed compression the load division is governed by how the force field is distributed across the granules. In general, the granule is in the most stressed
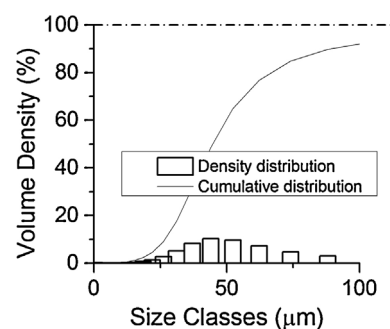

Fig. 3. The granule size distribution measured with laser diffractometer. Before the measurement, the granules were heat-treated at 930 °C for 1 h.

condition when the force is carried to it from neighboring granules of the same size, as that allows the loading on the opposite poles of the granule (McDowell & de Bono, 2013). Song and Evans (1994) found the strength of a packed bed of particles to be approximately 50% greater than the strength of a single particle, but expressing this relation is quite complex as multiple factors affect the force distribution. Thus, our experiments focused on development of a systematic approach to analyzing granules using bed compression, and on showing the method's applicability in finding the average value for granule breakage.

Materials and methods

Granules used for testing the method

The focus of this study was to determine how well the average compressive strength of brittle granules could be determined from the uniaxial pressing of a granule bed. For our case study, we chose a common industrially spray-dried material, granulated kaolinite powder.

The granules were received in a green state and they were heat-treated with different parameters to achieve comparative test materials; all testing was done on heat-treated samples, with the exception of several control samples in the sintering experiments, detailed in the Sintering experiment section. The heat treatment temperatures chosen based on sintering behavior of the powder is discussed further in the Sintering experiment section. The kaolinite granules were heated at 100 °C/h in a furnace (Entech ECF 20/18, Sweden) and held for 1 h at 560, 780, 830, 880, 930, and 980 °C in air atmosphere.

The size distribution of a sample powder was nearly the same after heat treatments as before, as shown in Fig. 3.

Characterization

The size distribution of the granules (PSD, particle-size distribution) before and after compression was determined by laser diffractometer (LD, Lecotrac LT100, Germany, or Malvern Master sizer 3000, UK) with an accuracy of ±0.6%. Tap water was used as the dispersing medium and ultrasound was used for 60 s for dispersing. The concentration of the suspensions was kept within 1–10%. Dispersing time with ultrasound was determined by measuring the optical concentration during the treatment; at 60 s optical concentration was no longer changing. The reference granule sizes measured from scanning electron microscope (SEM, Jeol JSM 6360LV, Japan) images agreed with the PSD measurements via LD, verifying the results. Powders from compressed granular beds were obtained by first crushing the bed with a spatula.

The morphological features of the kaolinite granules were characterized by SEM and a field emission scanning electron microscope
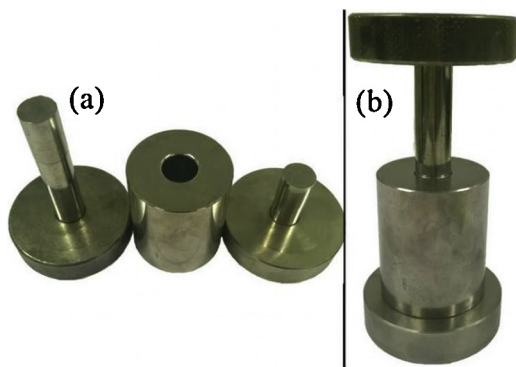
Fig. 4. The compression tool (a) disassembled into top punch (left), cylindrical die (middle), and lower punch (right), and (b) in the assembled state.

(FESEM, ULTRAplus, Carl Zeiss Microscopy GmbH, Germany), data is given in Appendix A. The samples prepared from compressed powder disks were obtained by cutting off the outmost edge of the disc to eliminate the possible effect caused by cylindrical wall friction and pouring of the powder onto a carbon tape. The powder was then coated with gold using a sputter coater (S150 Sputter Coater, Edwards, UK).

The sintering behavior of kaolinite was studied via dilatometer (AdamelLhomargy, DI-24, France), by heating a gently compacted green-state granule tab with a diameter of 1.0 mm and length of 2.69 mm up to 980 °C with a rate of 5 °C/min.

Compressive strength

Considering the factors discussed in the Compression stages section, in the present study we used the same compression tool for all measurements, and worked with a granule size in relation to die diameter that was very small, to decrease the influence of wall friction. We also collected all samples from granule compacts from the same area at the center of the compact, to avoid the local high-stress regions.

The granule bed compression tests, with the exception of the sintering experiments discussed in the Sintering experiment section, were carried out with an Instron 5967 (Illinois Tool Work Inc., USA) materials tester using a load cell with a maximum load capacity of 30 kN and accuracy of ±0.1%. The compression tests in the Sintering experiment section were carried out with Instron 4505 (Instron Industrial Products, UK) materials tester with a load cell that had a maximum capacity of 100 kN and an accuracy of ±0.25% of the output. The results from different devices were not compared with each other.

The granules were compressed with linear plate heads with a uniaxial compression tool shown in Fig. 4. The apparatus consisted of a top punch, bottom punch, and a cylindrical die with a diameter of 19.5 mm, where the tested material was poured. The moving surfaces of the tool were first sprayed with silicone (saBesto, Würth) and wiped to control wall friction. The mechanical yield of the compression tool in the studied range up to 10 kN was negligible, and it did not affect the measured yield behavior of the bed.

For each compression test, a sample of 1 g of heat-treated kaolinite granules was measured, and the precise mass determined using a precision scale (Mettler AE163, GWB, Switzerland, accuracy 0.01 mg). The sample was poured into the cylindrical die on top of the lower punch, and the tool was tapped to achieve a smooth powder bed surface. During the compression test, the lower punch stayed stationary and the top punch was pressed with a flat steel plate attached to the load cell. Different maximum forces were used and the sample was compressed at a constant speed of 1.00 mm/min.
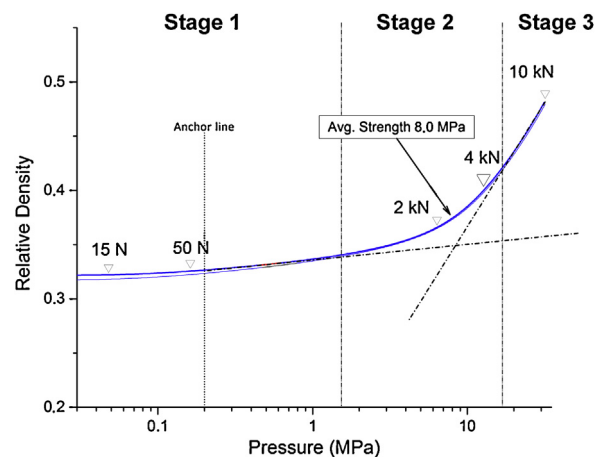

Fig. 5. 10 kN compression curve of granulated kaolinite powder sintered at 930 °C, showing the average strength (arrow); the stage 1 and stage 3 asymptotes (dashed lines), anchored at 0.2 MPa and maximum pressure; and marking the places for the compression limits of 15 N, 50 N, 2.0 kN, and 4.0 kN. The first three compression stages, as described in the Compression stages section, are also highlighted.

The compression speed has an effect on the measured stress. Antonyuk et al. (2010) used a lower velocity in single granule compression of elastic or plastic granules. However, according to Briscoe and Özkan (1997), in bed compression with non-elastic granules, the measured strength does not depend on the compression speed, provided that the measurements are carried out in the speed range of 1–10 mm/min.

The relative density of the granule bed was obtained by calculating the bulk density of the powder bed from bed height, the diameter of the die, and the bed weight, then dividing the bulk density by the theoretical density of kaolinite, 2.6 g/cm³. Observational error of the measurement was studied experimentally and is presented in Appendix B.

Results and discussion

To examine the feasibility of determining the compressive strength of an average brittle granule from a bed compression experiment, we devised two sets of experiments. In the first experiment (the Interpretation of the compression curve section) the maximum compressive force was varied and the compressed samples were characterized with SEM and LD to determine how well the fracture behavior coincided with the force predicted from the compression curve. In the second experiment (the Sintering experiment section) the granules were heat-treated at different temperatures and compressed with a force that exceeded the fracture threshold. This was done to further elucidate the robustness of the measurement method; the granules should become stronger at higher sintering temperatures and the method should accurately describe that trend. A short fractioning experiment (Appendix A) was also carried out to determine the effect of different size fractions on the measured strengths.

Interpretation of the compression curve

The granulated kaolinite samples sintered at 930 °C were compressed with five different maximum forces: 15 and 50 N, which were lower than the compressive strength; 2.0 and 4.0 kN, which had been determined to be close to the compressive strength; and, 10 kN, well above the compressive strength. The 10 kN compression curve, and the forces used in the lower force compression steps, are shown in Fig. 5 (two parallel compression curves are plotted). The
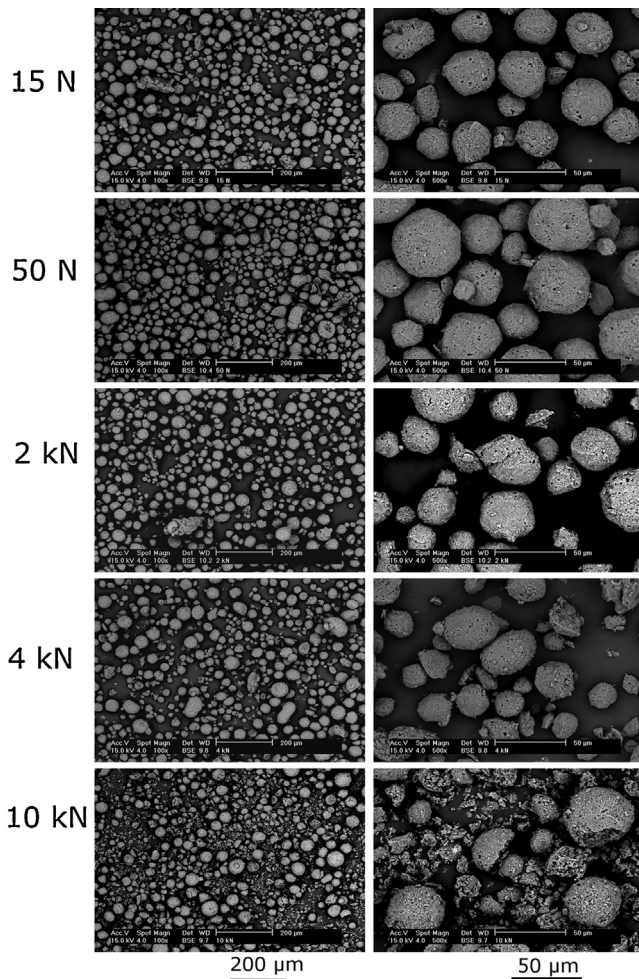
Fig. 6. SEM-images at two different magnitudes of kaolinite granules heat-treated at 930 °C after the compressive strength test with five different forces.

Fig. 7. The differential size distributions of granulated powder heat-treated at 930 °C after the compressive strength test with five different forces.

increase. At 4.0 kN, which is above the average crushing strength measured from the curve, LD data show that the small size fractions increase and simultaneously the number of average-size fractions diminishes, showing that the granules have broken. The fracture marks evident in the SEM images suggest fracturing by normal forces or attrition, which supports the theory by Pitchumani el al. (Pitchumani et al., 2004) that was presented earlier.

The granules fracture at a certain force range during stage 2. According to theory presented earlier (McDowell & de Bono, 2013; McDowell, 2002) this is caused by the size differences of the granules: larger granules can withstand higher loads because they are shielded by the smaller ones. This is evident by the relatively lower decrease in the amount of granules in the size range above 60 μm. Also, the relatively higher fracture probability of larger granules has an effect on the length of the second stage, but in this case it appears to be recessive. The four stages of the compression curve

purpose of this test was to show that the compression curve can be used to inspect the fracture strength of a brittle granule bed.

The compressive strength was measured from the relative density vs. log pressure curve in Fig. 5 by locating the spot where the curve has the steepest curvature. With a constant compression speed, this spot marks the place where the relative density increases the most rapidly while pressure increase is the slightest. This is the pivoting point where the granule bed is yielding, which in fragile materials can be directly interpreted as the point of fracture, i.e., compressive strength. The spot was located from the curve by extrapolating the linear regressions from compression stages 1 and 3 and finding their intercept. To reduce experimental noise, the first linear regression line was anchored to the relative density at 0.2 MPa. The second was anchored to the relative density at the maximum pressure. The intercept of the two regression lines was taken as the average compressive strength of the granule bed, as indicated in Fig. 5.

After the compression tests, each powder compact was imaged with SEM (Fig. 6) and characterized with LD. The initial granule size of the powder, presented in Fig. 3, is essentially the same as the particle size in a powder compressed with 15 N force, presented together with the other particle size fractions in Fig. 7.

The SEM images, Fig. 6, together with the LD results, Fig. 7, show that, below the measured compressive strength of 8.0 MPa, at the 15 and 50 N points, the granules are intact and their size fractions are similar, whereas granule shreds start to appear at 2.0 kN and the number of particles in the small size range starts to
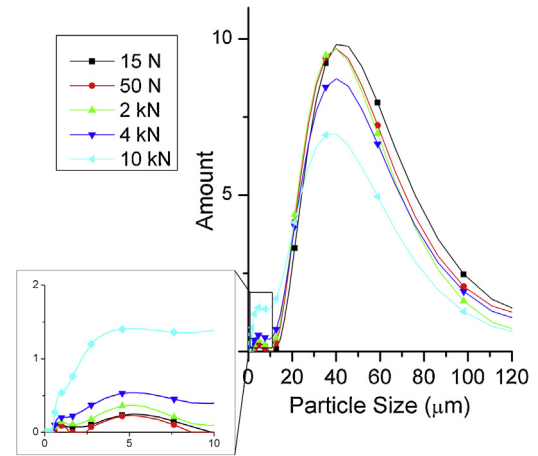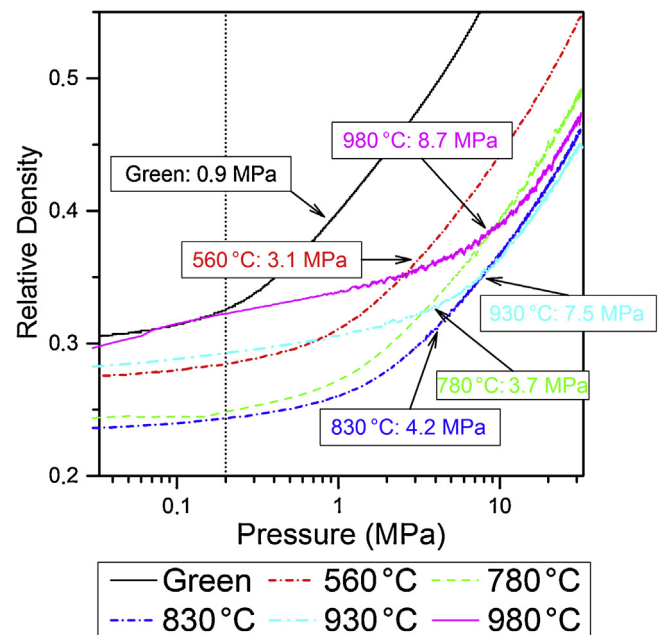

Fig. 8. The relative density versus the logarithmic experimentally applied pressure for kaolinite granule beds heat-treated at different sintering temperatures, and the as-received granule bed for reference ("Green", shown as a solid black line). The curves represent the average of three individual measurements, and the arrows show the fracture point obtained by the method explained in the Interpretation of the compression curve section.
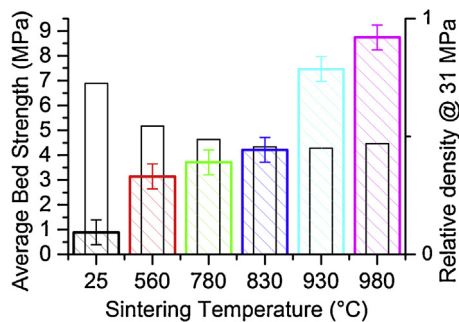
Fig. 9. The compressive strengths measured from kaolinite granules sintered at different temperatures (striped wide bars, observational error as calculated in Appendix B), and the relative densities after compressing with 31 MPa pressure (empty narrow bars).

(Fig. 2) are more distinct in brittle compression than in plastic compression; in plastic granule beds, rearrangement and yielding take place simultaneously, which is not the case with compression of brittle granules.

Obviously the granules fracture within a certain range of compression, but the following sintering experiment shows that the average point of fracture can be used to follow the changes in compressive strength.

Sintering experiment

Green-state kaolinite was heat-treated at five different temperatures: 560, 780, 830, 930, and 980 °C. The heat-treated kaolinite was then compressed with 10 kN force, well above its compressive strength. The compression curves are presented in Fig. 8, and the average point of fracture for each powder bed is also noted on the curves, obtained by the method described in the Interpretation of the compression curve section. For each of the presented curves, 3–5 compression experiments were completed, and the presented curves are averages calculated from the point averages of the individual compressions. Finally, the curves were smoothed using a 10 pts moving average.

Fig. 8 shows that, although the absolute position and the shape of the curve may change between experiments, the average strength, indicated by the arrows, increases consistently with sintering temperature. This temperature-related increase in compressive strength, along with the change in the relative density with temperature of sintering, is summarized in Fig. 9, and the observed strength increase with increasing sintering temperature shows the validity of our method for granule bed strength measurement. The sintering behavior is briefly analyzed below.
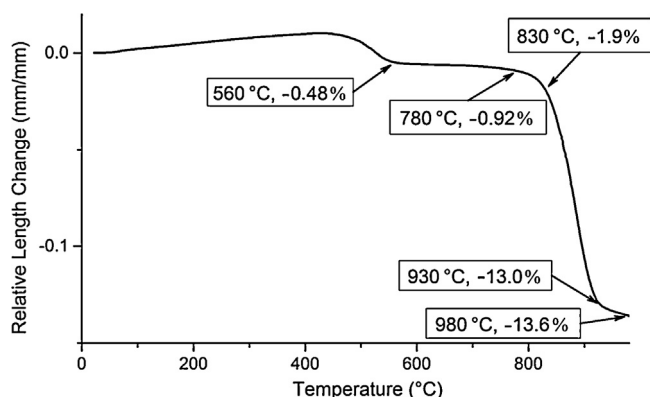
Fig. 10. Dilatometer curve of granulated kaolinite powder under heating, showing the relative sintering shrinkages at the temperatures at which the compressive tests were carried out.

Although not the focus of this article, a short investigation of the nonlinear evolution of sintering strength vs. temperature of kaolinite granules was carried out to show the feasibility of the measurement method. Fig. 10 shows that the sintering shrinkage in the isothermal experiment was nonlinear, which explains the nonlinear strength increase—these two properties are known to be linked (Hu & Wang, 2010). The figure shows two shrinkage steps, one at 400–500 °C, and another above 800 °C; in Flank (1979) these shrinkage steps are interpreted as a dehydroxylation step and phase change, respectively. In Appendix C, the sintering shrinkage and bed strength are correlated.

Conclusions

The difference between plastic granules (such as metals, polymers, and green state ceramics) and brittle ones (such as sintered ceramic powders) is the large deformation of plastic granules during uniaxial compression. The deforming behavior has an effect on the compression curve, but this study shows that the brittle granules can still be estimated using a similar approach to that of the plastic granules. Brittle granule compression has distinctive stages for each compression phenomenon (stage 1 particle rearrangement, stage 2 particle fracture, stage 3 fractured particle rearrangement, and stage 4 maximum compression), although the fracturing can take place in a wide pressure range.

We have shown via a case study of kaolinite powder that the compressive mechanical measurement of a bed of brittle, small granules (below 100 μm) can be used to determine the strength of an average granule. The study involved two experiments:

- In the first experiment, a granule bed was compressed at constant speed with different maximum forces, and the fracture of granules was analyzed after the compression with scanning electron microscope and LD particle size measurements. The experiment showed that by plotting the relative density versus the logarithmic pressure, the fracture regime of the granules can be determined and an average compressive strength can be estimated by extrapolating the constant density increase rates both before and after the fracture regime.
- In the second experiment, the average strength of a consolidated kaolinite bed was analyzed using our proposed method, i.e., by plotting the relative density versus the logarithmic pressure. This experiment showed that although the absolute placement of the curves may vary, and the granules fracture at a range of loads, the average strength, i.e., the flexural spot on the curve located with an angle fitting, can be used to follow the changes in granule strength.

These experiments validate earlier results on compressive bed strength by our group (Kanerva, Suhonen, Lagerbom, & Levänen, 2015). In addition to the main experiments, the effect of size fractions on compressive strength (Appendix A), observational error of the method (Appendix B), and correlation of sintering shrinkage to the bed strength (Appendix C) were analyzed.
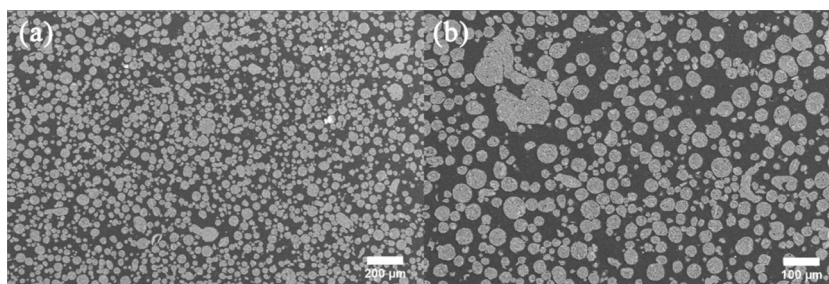
Appendix A. Fractioning experiment

Green-state kaolinite powder was heat-treated at 930 °C and sieved into two fractions using sieves (Retsch, Germany) with opening sizes of 25 and 45 μm and a sieving machine (Fritsch, Germany).

Fig. A1. SEM images of cross-sectional cuts of kaolinite granules heat-treated at 930 °C, at two different magnifications.

Table A1
Image analysis results from Fig. A2 showing the standard deviation (SD).

Section	Circularity (Fig. A2(a))	Aspect ratio (Fig. A2(a))	Gray value (Fig. A2(b))
25–45 μm	0.710 (SD 0.189)	1.444 (SD 0.468)	154.8 (SD 28.3)
45 μm	0.391 (SD 0.210)	1.907 (SD 0.664)	154.3 (SD 28.5)

Sieving time of 20 min was used to obtain a middle fraction that was between 25 and 45 μm, and a large fraction that was above 45 μm. These fractions were compressed and their average strengths were analyzed in the same manner as in the Interpretation of the compression curve section. Strength of the middle fraction was 8.9 MPa and strength of the large fraction was 8.1 MPa. This difference is larger than the observational error.

The variation in granule bed load carrying capability is not solely dependent on the granule size but may be caused by their shape and density in the different granule fractions (Rahmanian et al., 2009). The shape affects the flowability and force distribution, and density affects their individual capability in carrying load (Berg et al., 2010; Huang et al., 2012). To compare the shapes and densities of the two size ranges, cross-sectional samples of the granules were prepared and imaged with field emission scanning electron microscopy (FESEM, ULTRAplus, Carl Zeiss Microscopy GmbH, Germany) in secondary electron mode. The samples were analyzed as polished cross sections of granules after they were cold mounted in epoxy (Struers Epofix) in 30-mm-diameter mounting cups. Cold mounting was done in a vacuum impregnator (Struers Epovac) to decrease air bubbles. To dismiss the charging effect, the sample was coated with carbon (Agar turbo carbon coater, model 2090).

The SEM images were analyzed to find out if the two size ranges vary in granule shape or apparent density (ImageJ version 1.48 v), using Fig. A1(a) as a baseline. To analyze the shape, the baseline image was converted to binary form with automatic thresholding and the granules were partitioned from the images as is seen in Fig. A2(a). Granules that had a cross-sectional area the same as a circle having a diameter between 25 and 45 μm were marked with rastered red, and correspondingly those with an area larger than a 45-μm diameter circle were marked with black. Then, the average circularities ($4\pi \times$ [Area]/[Perimeter]^2, unity resembles a perfect circle) and aspect ratios (unity is a perfect circle) of the two sections were analyzed omitting the granules extending past the image borders. The results are presented in Table A1 and they, together with the SEM image, clearly show that the higher fraction was less round. The intragranular density was estimated from the SEM image in Fig. A1(b), by similarly sectioning the small and large fractions, which are circled in Fig. A2(b) with dashed red and black, respectively. The average gray values (the sum of the gray values of all the pixels in the selection divided by the number of pixels) were then calculated and are presented in Table A1. Considering the amount of standard deviations, the average gray values of the two sections were effectively equal, indicating there was no difference in the densities of the two fractions.

Based on these two analyses, it was concluded that the larger fraction being weaker (having lower compressive strength) was dominantly caused by the fraction's more uneven shape, which led to a more heterogeneous force field distribution during the compression. Some of the strength variation was possibly also caused by lower relative density at the beginning of compression. This lower relative density is caused by the larger volume of voids that the fractured bits of granules can later fill (de Bono & McDowell, 2015), and can be induced for instance by uneven granule shape or removal of finer granule fractions that decreased the relative density at the
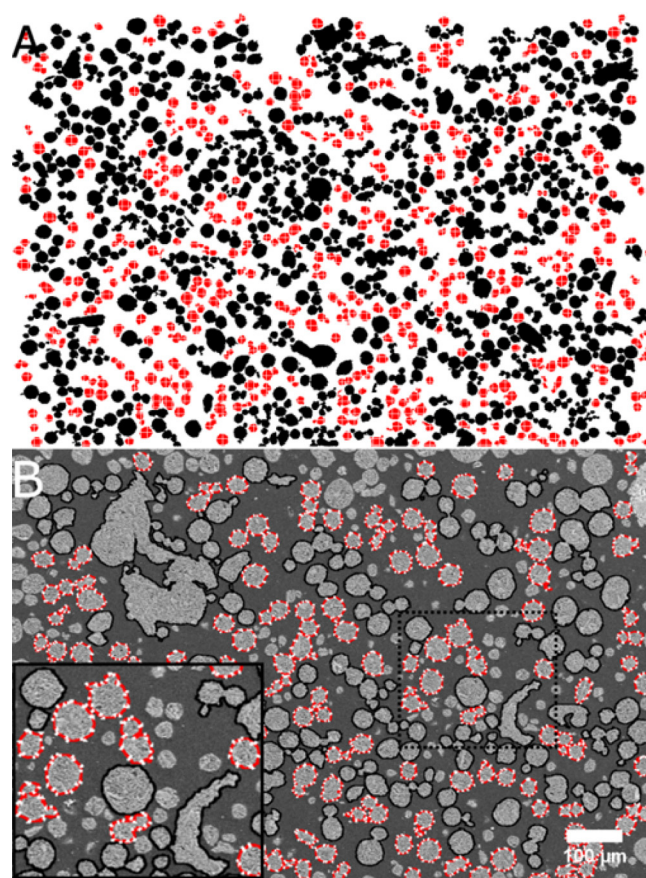
Fig. A2. . Images that were used to analyze the shape (a) and density (b) difference of two size ranges of kaolinite granules.
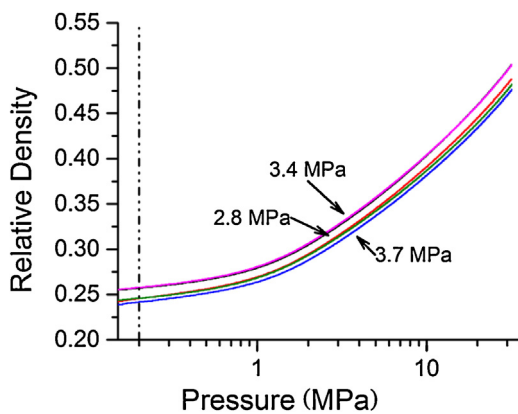
Fig. A3. Five compression curves of kaolinite samples heat-treated at 780 °C, compared to discern observational error.

beginning of compression (Yohannes et al., 2015). In our test the final relative densities are effectively the same.

Appendix B. Observational error in compressive bed strength measurement

The observational error was found to be close to ±0.5 MPa by testing the same granulated kaolinite powder that was heat-treated at 780 °C, five times and dissembling and assembling the experimental setup between each compression. Average compressive strength was found to be 3.3 MPa while the maximum and minimum were 3.7 and 2.8 MPa, respectively. The five comparison curves are presented in Fig. A3. The acquired error margin is used in each test. Compressive strength was located by the method explained in the Interpretation of the compression curve section.

Appendix C. Correlation of sintering shrinkage and average bed strength

The evolution of bed strength in relation to sintering shrinkage is seen in Fig. A4, where the result obtained from 980 °C is omitted because of the phase change seen in the sintering curve. Similarly to describing the relation between porosity and strength (Subero-Couroyer et al., 2003), this relationship can be described with a simple allometric exponential fitting that has a form of $\sigma = ax^b$ where a and b are experimental variables, σ is the average bed strength and x is the sintering shrinkage. When a is set to 3.7119 and b to 0.26989, the chi-square is 0.0295 and correlation
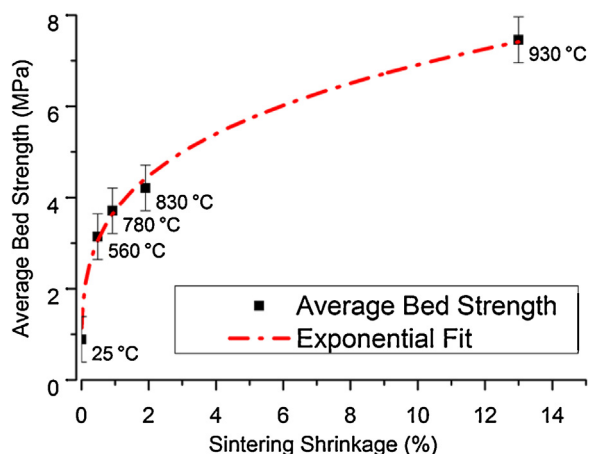
Fig. A4. Sintering shrinkage versus average bed strength with exponential fitting.

coefficient (R^2) 0.99213. The exceptionally good fitting, although with a limited number of experiments, gives a clear indication that the variables are exponentially linked. The magnitude of experimental variables a and b are possibly related to sintering kinetics and could be linked with specific surface area and chemical composition.

References

Antonyuk, S., Heinrich, S., Tomas, J., Deen, N. G., Van Buijtenen, M. S., & Kuipers, J. A. M. (2010). Energy absorption during compression and impact of dry elastic-plastic spherical granules. *Granular Matter, 12*(1), 15–47.

Antonyuk, S., Tomas, J., Heinrich, S., & Mörl, L. (2005). Breakage behaviour of spherical granulates by compression. *Chemical Engineering Science, 60*, 4031–4044.

Aryanpour, G., & Farzaneh, M. (2015). Application of a piston equation to describe die compaction of powders. *Powder Technology, 277*, 120–125.

Berg, S., Jonsén, P., & Häggblad, H. Å. (2010). Experimental characterisation of CaCO₃ powder mix for high-pressure compaction modelling. *Powder Technology, 203*(2), 198–205.

Briscoe, B. J., & Özkan, N. (1997). Compaction behaviour of agglomerated alumina powders. *Powder Technology, 90*, 195–203.

Couroyer, C., Ning, Z., & Ghadiri, M. (2000). Distinct element analysis of bulk crushing: Effect of particle properties and loading rate. *Powder Technology, 109*, 241–254.

Carneim, R. D., & Messing, G. L. (2001). Response of granular powders to uniaxial loading and unloading. *Powder Technology, 115*, 131–138.

Cheong, Y. S., Adams, M. J., Hounslow, M. J., & Salman, A. D. (2009). Microscopic interpretation of granule strength in liquid media. *Powder Technology, 189*(2), 365–375.

de Bono, J. P., & McDowell, G. R. (2015). An insight into the yielding and normal compression of sand with irregularly-shaped particles using DEM. *Powder Technology, 271*, 270–277.

Flank, W. H. (1979). Behavior of kaolinite pellets at elevated temperatures. *Clays and Clay Minerals, 27*(I), 11L 18.

Güner, F., Cora, Ö. N., & Sofuoğlu, H. (2015). Numerical modeling of cold powder compaction using multi particle and continuum media approaches. *Powder Technology, 271*, 238–247.

Honda, T., & Nonaka, H. (1998). Granulated powder for producing silicon nitride sintered body. U.S. Patent No. 5,854,156.

Hu, L., & Wang, C.-A. (2010). Effect of sintering temperature on compressive strength of porous yttria-stabilized zirconia ceramics. *Ceramics International, 36*(5), 1697–1701.

Huang, Z., Yi, L., & Jiang, T. (2012). Mechanisms of strength decrease in the initial reduction of iron ore oxide pellets. *Powder Technology, 221*, 284–291.

Kanerva, U., Suhonen, T., Lagerbom, J., & Levänen, E. (2015). Evaluation of crushing strength of spray-dried MgAl₂O₄ granule beds. *Ceramics International, 41*(7), 8494–8500.

Kwan, A. K. H., Wong, V., & Fung, W. W. S. (2015). A 3-parameter packing density model for angular rock aggregate particles. *Powder Technology, 274*, 154–162.

Laity, P. R. (2014). Effects of punches with embossed features on compaction behaviour. *Powder Technology, 254*, 373–386.

Leszczuk, T. (2014). Evaluation of the fertilizer granules strength obtained from plate granulation with different angle of granulation blade. *Acta Mechanica et Automatica, 8*(3), 141–145.

McDowell, G. R. (2002). On the yielding and plastic compression of sand. *Journal of the Japanese Geotechnical Society: Soils and Foundation, 42*(1), 139–145.

McDowell, G. R., & de Bono, J. P. (2013). On the micro mechanics of one-dimensional normal compression. *Géotechnique, 63*, 895–908.

Meyer, L. W., & Faber, I. (1997). Investigations on granular ceramics and ceramic powder. *Journal de Physique, IV*(07(C3)). C3–565–C3–570.

Mort, P. R., Sabia, R., Niesz, D. E., & Riman, R. E. (1994). Automatted generation and analysis of powder compaction diagrams. *Powder Technology, 79*, 111–119.

Müller, P., Russell, A., & Tomas, J. (2015). Influence of binder and moisture content on the strength of zeolite 4A granules. *Chemical Engineering Science, 126*, 204–215.

Müller, P., & Tomas, J. (2014). Simulation and calibration of granules using the discrete element method. *Particuology, 12*(1), 40–47.

Pitchumani, R., Zhupanska, O., Meesters, G. M. H., & Scarlett, B. (2004). Measurement and characterization of particle strength using a new robotic compression tester. *Powder Technology, 143–144*, 56–64.

Thyagarajan, R., Cantin, G. M. D., Kashyap, B. P., & Bettles, C. J. (2015). Modelling compaction behaviour of nickel–phosphorus and nickel–boron electroless coated titanium powders. *Powder Technology, 274*, 53–61.

Rahmanian, N., & Ghadiri, M. (2013). Strength and structure of granules produced in continuous granulators. *Powder Technology, 233*, 227–233.

Rahmanian, N., Ghadiri, M., Jia, X., & Stepanek, F. (2009). Characterisation of granule structure and strength made in a high shear granulator. *Powder Technology, 192*(2), 184–194.

Raichman, Y., Kazakevich, M., Rabkin, E., & Tsur, Y. (2006). Inter-nanoparticle bonds in agglomerates studied by nanoindentation. *Advanced Materials, 18*(15), 2028–2030.

Richerson, D., Richerson, D. W., & Lee, W. E. (2005). *Modern ceramic engineering: Properties, processing, and use in design* (3rd ed.). New York, NY: CRC Press.

Salman, Aman S., & Tomas, J. (2014). Breakage probability of stressed granules using a degradation model. *Chemical Engineering & Technology*, *37*(11), 1949–1958.

Schilde, C., Burmeister, C. F., & Kwade, A. (2014). Measurement and simulation of micromechanical properties of nanostructured aggregates via nanoindentation and DEM-simulation. *Powder Technology*, *259*, 1–13.

Song, J.-H., & Evans, J. R. G. (1994). A die pressing test for the estimation of agglomerate strength. *Journal of the American Ceramic Society*, *77*(3), 806–814.

Subero-Couroyer, C., Ghadiri, M., Brunard, N., & Kolenda, F. (2003). Weibull analysis of quasi-static crushing strength of catalyst particles. *Chemical Engineering Research and Design*, *81*, 953–962.

Subero-Couroyer, C., Ghadiri, M., Brunard, N., & Kolenda, F. (2005). Analysis of catalyst particle strength by impact testing: The effect of manufacturing process parameters on the particle strength. *Powder Technology*, *160*(2), 67–80.

Terpstra, R. A., Pex, P. P. A., & De Vries, A. (1995). *Ceramic processing*. New York, NY: Springer Science & Business Media.

Yohannes, B., Gonzalez, M., Abebe, A., Sprockel, O., Nikfar, F., Kang, S., et al. (2015). The role of fine particles on compaction and tensile strength of pharmaceutical powders. *Powder Technology*, *274*, 372–378.